

ORDER-BY-DISORDER PHENOMENA IN COLD ATOMIC GASES

A THESIS PRESENTED FOR THE DEGREE OF
DOCTOR OF PHILOSOPHY OF IMPERIAL COLLEGE LONDON
AND THE
DIPLOMA OF IMPERIAL COLLEGE
BY
MATJAŽ PAYRITS

DEPARTMENT OF MATHEMATICS
IMPERIAL COLLEGE
180 QUEEN'S GATE, LONDON SW7 2BZ

OCTOBER 2016

I certify that this thesis, and the research to which it refers, are the product of my own work, and that any ideas or quotations from the work of other people, published or otherwise, are fully acknowledged in accordance with the standard referencing practices of the discipline. Chapters 2 to 4 and Chapters 9 to 10 are partly based on previous publications, Refs. [94] and [95], respectively. I am the author of the great majority of both publications' texts and figures and have also implemented all of the numerical procedures.

Signed: _____

COPYRIGHT

The copyright of this thesis rests with the author and is made available under a Creative Commons Attribution Non-Commercial No Derivatives licence. Researchers are free to copy, distribute or transmit the thesis on the condition that they attribute it, that they do not use it for commercial purposes and that they do not alter, transform or build upon it. For any reuse or redistribution, researchers must make clear to others the licence terms of this work.

Order-by-disorder phenomena in cold atomic gases

ABSTRACT

This thesis presents novel theoretical results on two cold atomic systems with particular emphasis on the order-by-disorder mechanism that they exhibit. The latter selects one or a number of classically degenerate states of lowest energy as the true ground states on the basis of Helmholtz free energy contributions of fluctuations about the classical solutions. It has traditionally played an important role in solid-state systems but has so far not been conclusively observed.

The first system considered is that of cold bosons hopping in the two-dimensional dice lattice in the presence of an artificial gauge field, tuned to provide half an elementary flux per plaquette. The single-particle band structure consists entirely of flat bands. Many-particle behaviour is captured by a Bose-Hubbard model with contact interactions. Mean-field analysis yields a large degeneracy of classical ground states which is lifted through Order by Disorder. A closer analysis yields a picture of free-energy-mediated interactions between domain walls separating distinct, classically degenerate regions.

The second system is that of spin-2 species in a tightly confining spatial potential, with a generalised quadratic-Zeeman coupling. It is analysed by means of an exact mapping of the many-body Hamiltonian onto that of a five-dimensional rotor. The new Hamiltonian is in general non-Hermitian, but Hermitianising transforms may be found in a number of regimes. Analytical results for the ordinary quadratic Zeeman potential are presented and shown to yield qualitatively different behaviour from the mean-field analysis. In particular, there are no signs of a fluctuation-induced phase transition, predicted by mean-field theory. Motivated by this, an alternative potential,

Thesis advisor: Dr. Ryan Barnett

Matjaž Payrits

breaking less symmetry, is considered within the rotor framework and shown to display microscopic parallels of Order by Disorder.

To everything fluffy.

ACKNOWLEDGMENTS

I would like to thank the bright, cheerful people whom I had the fortune to meet and surround myself with during my PhD years at Imperial College. If it weren't for your impossible optimism, the English weather would have surely got to me. I would also like to thank my supervisor for the excellent tutelage I have received over the course of the last four years, and for curbing my occasional drift-offs into algebraic geometry. I am confident that the back-of-the-envelope skills I've developed during our meetings are priceless in comparison. Thanks also go to the Department of Mathematics. You take really good care of your students, even if they're physicists by heart, which I really appreciate. My friends and family back in Slovenia have also played a vital role in keeping me motivated and never losing a sense of purpose, for which I will be forever grateful. Finally, I have thoroughly enjoyed, and benefited from discussions with fellow mathematicians from my department and fellow physicists from all over the world. Thank you for all the ideas you have given me. This thesis would have been blank without them.

LIST OF FIGURES

1.1	The energy-level splittings for ^{87}Rb arising from the Zeeman effect.	24
2.1	Geometry of the dice lattice.	32
2.2	The dice lattice at half-flux.	36
2.3	Localised states of the lowest and highest bands of the dice lattice at half-flux.	38
3.1	The four small unit-cell periodic mean-field ground states of the dice lattice.	44
3.2	Schematic representation of a type I domain wall insertion. . .	47
4.1	The dice lattice Bogoliubov spectrum at $U_* = U_\Delta, t = 2U_*$, and $n_* = 6$	50
4.2	Free energy differences between small unit-cell states.	53
4.3	Dice lattice condensate depletion at $n_* = 6, U_* = U_\Delta$, and $T = t/10$	55
4.4	Zero-point energy per particle for large unit-cell periodic states with two domain walls of the same type per unit cell.	56
5.1	Spin-1 mean-field $q - c_1 n$ phase diagram.	66
5.2	Spin-2 mean-field $c_1 - c_2$ phase diagram at $p = q = 0$	67
5.3	Evolution of the Majorana representation of nematic states with η	68
5.4	Mean-field spin-2 phase diagram at negative q	69
5.5	Mean-field spin-2 phase diagram at positive q	70
5.6	Evolution of the non-inert mixed phase's Majorana representation with q	71

5.7	Evolution of the non-inert cyclic phase's Majorana representation with q	71
5.8	Spin-2 nematic Bogoliubov zero-point energy density with respect to η	73
9.1	Schematic representation of the tightly confined spin-2 ground state rotor wave function at large positive Nq	121
9.2	Schematic representation of the tightly confined spin-2 ground state rotor wave function at large negative Nq	123
9.3	Overlaps of finite- q spin-2 ground states with the large- $ q $ limiting states and their asymptotic convergence.	128
10.1	An illustration of the disparity between mean-field and exact spin-2 results.	133
10.2	Numerically computed limiting-state overlaps and spin-sublevel occupation values, supporting Order by Disorder in the tightly confined spin-2 condensate.	148
A.6	Honeycomb lattice images of different mean-field states.	169

CONTENTS

1	INTRODUCTION	2
1.1	Bose-Einstein condensation	7
1.1.1	Non-interacting systems	7
1.1.2	Interacting systems	9
1.1.3	BEC order parameters	11
1.1.4	Historical overview	13
1.2	Optical traps and lattices, the Bose-Hubbard model	13
1.2.1	The Stark effect	14
1.2.2	The Bose-Hubbard model	16
1.3	Effective interactions and spinor condensates	17
1.3.1	Effective spinor interactions	19
1.4	The Zeeman effect	21
1.5	Order-by-disorder	25
1.5.1	Bogoliubov theory	25
1.5.2	Effects of fluctuations: Order-by-Disorder	29
2	GEOMETRY AND SINGLE-PARTICLE PROPERTIES OF THE DICE LATTICE	31
2.1	\mathcal{T}_3 geometry and the Bose-Hubbard model	31
2.2	Single-particle spectrum	34
2.3	Single-particle spectrum at half-flux	35
3	MEAN-FIELD PROPERTIES OF THE BOSE-HUBBARD MODEL ON THE DICE LATTICE	40

3.1	Mean field calculation of sublattice densities	42
3.2	Mean field periodic ground states	45
4	EXCITATION SPECTRUM AND ORDER BY DISORDER IN THE BOSE-HUBBARD MODEL ON THE DICE LATTICE	48
4.1	Collective Excitation Spectrum	49
4.2	Computation of Degeneracy Lifting	52
4.3	The Condensate Depletion	54
4.4	Domain wall interactions	55
5	MEAN-FIELD PHASES OF SPINOR CONDENSATES	58
5.1	Cold spinor gas Hamiltonians	60
5.2	Mean-Field Phase Diagrams	63
5.2.1	Majorana Representation	63
5.2.2	Phase Diagrams	64
5.3	Nematic Order by Disorder	69
6	THE SINGLE MODE APPROXIMATION	74
6.1	Exact spin-1 eigenstates and spectra at $q = 0$	76
6.2	Spin-1 spectra and dynamics at $q > 0$	77
6.3	Exact spin-2 eigenstates and spectra at $q = 0$	79
7	HAMILTONIAN MAPPINGS AND THE ROTOR MAPPING	81
7.1	Common features	82
7.1.1	Mappings from overcomplete bases	82
7.1.2	Physical subspace	84
7.2	The Segal-Bargmann representation	86
7.3	Rotor mappings	91
7.3.1	Calculus on the n -sphere	93
7.3.2	Physical subspace	96

7.3.3	The T map	99
8	LOW-DIMENSIONAL APPLICATIONS OF THE ROTOR MAPPING	103
8.1	The double-well Bose-Hubbard model	104
8.2	Tightly confined spin-1 condensates	108
8.3	Tightly confined spin-2 condensates	110
9	EFFECTS OF THE QUADRATIC ZEEMAN EFFECT ON TIGHTLY CONFINED SPIN-2 ATOMS	115
9.1	Exact diagonalisation	116
9.2	Hermitianising transform at $g_1 = 0$	116
9.3	Large $N q $ limits	117
9.3.1	Large positive Nq regime	117
9.3.2	Large negative Nq regime	120
9.4	Wave function overlaps	123
10	AN EXACT MANIFESTATION OF ORDER BY DISORDER IN TIGHTLY CONFINED SPIN-2 ATOMS	131
10.1	Lack of fluctuation effects for the quadratic Zeeman potential in the single mode approximation	132
10.2	Continuum Order by Disorder	134
10.3	Rotor treatment	136
10.4	Ground-state overlaps with limiting nematic states	141
10.4.1	Limiting-state overlaps at $\eta_0 = \pi/2$	144
10.4.2	Limiting-state overlaps at $\eta_0 = 0$	147
10.5	Magnetic sublevel occupations	151
11	CONCLUSION	155
	APPENDIX A ENUMERATION OF POSSIBLE VORTEX-LATTICE STATES IN THE DICE LATTICE	160

A.1 Terminology	161
A.2 Korshunov states consist of vortex chains of length three . . .	163
A.3 Exhaustive list of Korshunov states	166
REFERENCES	192

CONVENTIONS

The following conventions are employed throughout this thesis:

- All equations employ units in which $\hbar = 1$, unless otherwise specified.
- Repeated indices imply the Einstein summation convention, except when explicitly stated otherwise and when a repeated index appears with different multiplicities on two sides of an equation.
- Operators are denoted by hats, except for differential operators, such as ∂_i and ∇^2 . Operators of multiplication by a coordinate are denoted by the same symbol as the coordinate, with an added hat. When a relation between coordinate operators is also true for the underlying coordinates, it is typically stated in terms of the latter. Finally, when a term or expression contains a differential operator as its rightmost factor, the remaining coordinate factors are understood to represent operators, even if unhatted.
- Vectors are represented in boldface. Matrices have no special formatting but are typically represented by capital letters. When there is need for vectors of vectors, the secondary-level vectors are represented by underlined symbols, and the secondary-level matrices by twice underlined capital letters.

1

INTRODUCTION

The final decades of the previous millennium saw rapid advances in cooling technology that have enabled unprecedented access to large-scale quantum phenomena in the laboratory. Being able to reliably maintain temperatures in or below the micro-Kelvin range allowed for the construction of particle ensembles in which the majority of particles occupied low-lying, highly wave-like quantum states. Nowhere was this demonstrated as clearly as with the realisation of a Bose-Einstein condensate of an atomic gas,^{26,5,18} arguably the main drive behind the technological advances. Cold atomic gases have since proven to be extremely amenable to precise and robust experimental control, particularly in combination with optical trapping methods. Besides being analysed in their own right, they have been utilised to cleanly simulate solid-state systems, with much smaller amounts of disorder than would have been possible in the original setting.⁷¹ The simulation efforts have recently resulted in the realisations of such iconic systems as the Hofstadter-Harper model^{83,3} and the topological Haldane model,⁵⁵ and are even likely to expand into the high-energy physics domain.¹⁴¹ Together, these developments have firmly established an entire new field of condensed-matter physics, referred to as the study of *(ultra)cold atomic* or *quantum gases*, or often simply *(ultra)cold*

atoms.

The present thesis attempts to further our theoretical understanding of two many-body quantum systems that have become experimentally viable with the rise of cold-atoms techniques. While the systems may seem at first glance to be entirely distinct and connected only by the previous fact, another important shared attribute crops up in the course of their analysis. A self-consistent mean-field analysis of both systems leads to a large ground-state degeneracy, with members of the degenerate set not related to each other by geometrical symmetry. In such a setting, quantum fluctuations play a vital role. In both of the systems considered, zero-point energies of the fluctuations conclusively select a preferred ground state, and this selection is further consolidated by thermal contributions to the Helmholtz free energy at finite temperatures. This phenomenon is commonly referred to in the literature as *Order by Disorder*^{134,113,45,46} and has traditionally played an important role in frustrated magnetic systems of solid-state physics. Experimental searches for the phenomenon have focused on such systems, but remain contentious.^{105,99} Recent theoretical work has, however, shown the phenomenon to be ubiquitous in the field of cold atoms, suggesting it may be experimentally realised within its context.

The present introductory chapter aims to give a broad technical and, to a lesser extent, historical overview of the field of cold atoms, as well as its subfields particularly pertinent to the pair of systems analysed. Before outlining the field of cold atoms, however, the following couple of paragraphs outline the structure of this thesis.

Chapters 2 through 4 are dedicated to the Bose-Hubbard model on the dice lattice in the presence of an effective magnetic field such that each lattice plaquette is threaded by half of an elementary flux quantum. In particular, Chapter 2 introduces the geometrical properties of the dice lattice and considers the single-particle spectra of tight-binding models in it. Properties at arbitrary magnetic fields are briefly reviewed. The case of half-an-elementary flux per plaquette stands out as particularly distinguished as it features eigenstates localised to a finite number of sites by destructive interference of Aharonov-Bohm phases, and yields an entirely flat single-particle

spectrum. In such a setting, the importance of inter-particle interactions is vastly enhanced for many-body systems. This is the subject of Chapter 3, which applies a hydrodynamic mean-field analysis to the many-body problem. A large set of geometrically inequivalent ground states is found. These can be characterised as vortex lattices, induced by phase windings around individual plaquettes. Following previous ideas of Korshunov regarding the XY model on the dice lattice,^{62,61,63} the concept of a zero-energy domain wall is introduced. This is used to systematically classify the degenerate mean-field ground-state manifold. Chapter 4 asks whether beyond-mean-field fluctuations lift the degeneracy, ultimately arriving at a positive answer. The Bogoliubov spectra of four mean field states, possessing the smallest unit cells and the most symmetric descriptions in terms of zero-energy domain walls of the previous chapter, are derived. They are shown to lead to the conclusive selection of one of the states, at both zero and finite temperature, through Order by Disorder. Another class of spectra is calculated for two domain walls at a variable distance. The results can be interpreted as fluctuation-mediated interactions between domain walls. This is used to argue that the previously obtained state is not selected only among the high-symmetry mean-field states, but among all of them.

Chapters 5 through 10 are dedicated to the other system of interest, a condensate of spin-2 atoms. Chapters 5 to 8 cover the background and methods that are used to derive the main results in Chapters 9 and 10. In detail, Chapter 5 introduces the mean-field properties of spin-1 and spin-2 condensates, and considers their phase diagrams with respect to atomic scattering lengths and external field. Throughout the expository chapters of the latter part of this thesis, the spin-1, and sometimes the even simpler double-well system, are used to make analogies with the spin-2 system. This allows clarifying the origin of effects that might be obscured within a direct treatment of the geometrically and algebraically much less intuitive spin-2 setting. The geometrical Majorana scheme for classifying spin- F states is reviewed. Additionally, the lifting of an accidental nematic degeneracy in the continuum is summarised, so that it can later be contrasted with the drastically different outcome of the full quantum treatment. Chapter 6 considers the tight binding, or sin-

gle mode approximation, and how it allows one to go beyond the mean-field regime. It summarises the properties of spin-1 condensates, derived within its context, and of spin-2 condensates in the absence of a quadratic Zeeman field. Similarities and differences from the mean-field phase diagrams are discussed throughout, and it is described how the validity of the mean-field approximation can be partially quantified. Chapter 7 then delves into the mathematical structure and properties of general Hamiltonian mappings and particularly the rotor mapping. The latter has been used to great effect in the spin-1 setting and is the main analytical tool of later chapters. It consists of mapping an arbitrary d -mode particle-conserving many-body Hamiltonian onto an equivalent Hamiltonian of a d -dimensional quantum rotor or, equivalently, of a particle moving on the $(d - 1)$ -sphere. The spin-1 and spin-2 mappings utilise the $d = 3$ and $d = 5$ versions of the mapping, respectively, while Chapter 7 considers arbitrary dimension. Specific low- d applications are the subject of Chapter 8. As well as reviewing mappings relevant to the double-well Bose-Hubbard Hamiltonian and the tightly-confined spin-1 system, and identifying further common features discernible from them, the formalism relevant to the spin-2 setting is introduced. This is then applied in Chapter 9 to study the response of a tightly confined spin-2 condensate to an applied quadratic Zeeman field. The spectra in different parameter regimes are derived. They are shown to agree with Bogoliubov-theory predictions, where these are stable. The rotor mapping can, however, also successfully be applied in a region where the ground state is a fragmented condensate. This implies a zero spin-mixing mode that drives up the depletion, making Bogoliubov theory inapplicable. The rotor mapping, on the other hand, remains stable within this region. Analytical expressions for the ground-state wave functions, in particular the overlaps with ground states in the limit of large positive and negative quadratic Zeeman field, are derived. One of the main features observed in the ground-state structure is that it seems to retain no trace of a continuum phase transition, induced by fluctuations. This is attributed to the fact that the quadratic Zeeman field breaks too much of the original Hamiltonian's symmetry, and in Chapter 10, an alternative potential that breaks less symmetry is considered. This time, the rotor Hamiltonian may be partitioned into parts of different orders and treated by means of

perturbation theory. The low-energy variable does not appear in the zeroth-order Hamiltonian at all, leading to an effective Hamiltonian for it. In terms of sublevel occupation fluctuations, the obtained states are qualitatively different from the mean-field states selected by a Bogoliubov analysis of the same spin potential. However, their sublevel occupation expectation values agree with it, demonstrating a microscopic, fully quantum parallel of Order by Disorder. This represents the second central result of this thesis, whose final conclusions are stated in Chapter 11.

As stated earlier, the main goal of the present chapter is to introduce the general field of cold atoms and some of its subfields particularly pertinent to the above topics. To that end, this Introduction is structured as follows: in Sec. 1.1, the phenomenon of Bose-Einstein condensation that gave rise to the field of cold atoms is reviewed. Condensation is first illustrated in the conceptually clear non-interacting setting in subsection 1.1.1. Some of the most iconic effects of Bose-Einstein condensation, related to superfluidity, however arise only in interacting systems. The methodology and features of the interacting regime are considered in subsection 1.1.2. Subsection 1.1.3 then introduces two commonly used order parameters, used to define a BEC in a general setting. Subsection 1.1.4 concludes the overview of BEC physics with a very brief historical account of condensation efforts. Moving on, Section 1.2 introduces some of the most frequently utilised experimental tools of cold atomic physics, optical traps and lattices. These rely on the atoms' self-polarisabilities, which induce an electric-field-dependent energy shift of the atomic ground state. This is known as the Stark shift, and its derivation is outlined in Sec. 1.2.1. Bosons confined to a periodic optical potential, via the Stark shift, have been shown to be described by an effective Bose-Hubbard Hamiltonian,⁵¹ whose properties are the subject of the brief Sec. 1.2.2. Section 1.3 then describes how the scattering properties of cold atomic gases yield simple many-body interaction Hamiltonians, a subject of utmost importance for the later chapters of this thesis, and sketches the derivation of their forms. Another important aspect of cold spinful species is their interaction with magnetic fields. The field-induced energy shifts are known as the Zeeman effect. At low, experimentally relevant fields, these have a regime of

pronounced non-linearity, due to the presence of the hyperfine interaction. The latter, as well as the explicit form of the energy shifts, are the subject of Sec. 1.4. In the final section, Sec. 1.5, the unifying phenomenon of Order by Disorder is introduced in more detail. First, in subsection 1.5.1, the primary means of going beyond mean-field theory, Bogoliubov theory, is reviewed. For finite systems, or even subsystems, this has remarkably elegant algebraic properties, which, in the author's experience, do not seem to be universally known. The surprising accuracy of the ground-state energy obtained with the formalism is demonstrated on an exactly solvable example. Finally, in subsection 1.5.2, the effects of fluctuations, leading to the lifting of accidental degeneracies, are discussed within the Bogoliubov theory framework, giving concrete form to the idea of Order by Disorder.

1.1 BOSE-EINSTEIN CONDENSATION

First predicted by Einstein in 1924,^{28,29} following up on previous ideas by Bose,¹⁷ the phenomenon of Bose-Einstein condensation, or BEC, is possibly the most profound manifestation of the mantra that several bosons can occupy the same quantum state. It states that, for suitable systems at low enough temperatures, a macroscopic fraction of particles will occupy the quantum ground state. The following subsections aim to yield an overview of the rich field that has grown out of this simple idea, starting with the simplest example of a non-interacting condensate.

1.1.1 NON-INTERACTING SYSTEMS

The concepts of condensation may be most concisely presented in a non-interacting setting. Consider thus a non-interacting system with single-particle eigenstates of energy ε_i , where $i = 1, 2, \dots$ and $\varepsilon_i \leq \varepsilon_{i+1}$. Employing natural units $k_B = \hbar = 1$, the thermal expectation value of n_i , the i -th single-particle eigenstate's occupation number, at temperature T and

chemical potential μ , is given by the Bose-Einstein distribution:

$$\langle n_i \rangle = (e^{(\varepsilon_i - \mu)/T} - 1)^{-1}. \quad (1.1)$$

While there are rigorous definitions of BEC involving taking the thermodynamic limit $N \rightarrow \infty$, there is a simpler argument to demonstrate that something interesting is going on already at large but finite N . Taking the energy of the ground state to be 0, it is evident that the chemical potential μ must remain negative, lest the ground-state occupation become negative, and hence unphysical. At fixed temperature T , the sum $\sum_i \langle n_i \rangle \equiv N$ increases monotonically with increasing μ . For large particle numbers one may typically replace the sum by an integral over the single-particle energy:

$$N = \sum_i \langle n_i \rangle \approx \int_0^\infty d\varepsilon \frac{g(\varepsilon)}{e^{(\varepsilon - \mu)/T} - 1}, \quad (1.2)$$

where $g(\varepsilon)$ is the system's density of states. It turns out that, at low temperatures, this integral does not properly account for the ground state, about which the distribution is heavily peaked, but is satisfactory for calculating the number of particles in excited states. The density of states is typically of the form $g(\varepsilon) = C\varepsilon^\alpha$. When $\alpha > 0$, the above integral converges in the limit $\mu \rightarrow 0^-$, and the limiting value represents the largest number of particles that excited states can accommodate at the given temperature. If this quantity is less than N , the total number of particles, the remaining particles must occupy the ground state.* This additional ground-state occupation is due to Bose-Einstein condensation.

An elementary calculation shows that the coefficient α equals $d/2 - 1$ for a uniform gas in d dimensions, and $d - 1$ for a d -dimensional harmonic os-

*This may seem like a rather ad hoc statement, artificially concocted to resolve the particle-number discrepancy. It may be justified by noticing that the integral approximation of Eq. (1.2) may only fail considerably near the origin. Even though the density of states tends to zero, a single state, deep within the divergent regime of the Bose-Einstein distribution function (1.1), may yield an arbitrarily large total particle number. The correctness of the ground-state occupation claim can also be numerically verified by keeping the sum discrete and solving for the tiny non-zero chemical potential at a fixed particle number.

illator. According to the convergence criterion for integral (1.2), $\alpha > 0$, Bose-Einstein condensation in non-interacting gases is predicted to occur in three dimensions for the uniform potential, and in 2 or 3-dimensional harmonic oscillator potentials. In lower dimensions, condensation is predicted to occur only at zero temperature. The 1-dimensional harmonic oscillator is in fact rather delicate,^{25,69} and shows that the above discussion is not the full story, but overall, the convergent-excitation-number rule of thumb works rather well.

1.1.2 INTERACTING SYSTEMS

A discussion of non-interacting systems, while conceptually clear, fails to account for the remarkable superfluid properties of real condensates. Even the very weak inter-particle interactions in dilute gases turn out to profoundly affect the excitation spectrum and, through it, the condensate's macroscopic properties.

A typical first approach to interacting condensates is mean-field theory at zero temperature. In this regime, one may consider a trial wave function in which all of the particles occupy the same single-particle state. In a system of N particles, this would be

$$\Psi(\{\mathbf{r}_i\}) = \prod \phi_0(\mathbf{r}_i) \quad (1.3)$$

where \mathbf{r}_i is the i -th particle's position. Additionally, interactions are typically well approximated by a delta-function potential, i.e., $V(\mathbf{r}_i, \mathbf{r}_j) = U\delta^{(3)}(\mathbf{r}_i - \mathbf{r}_j)$ for some interaction constant U . The reasons for this are sketched in Sec. 1.3 of this introduction. Considering a scalar condensate, a typical Hamiltonian reads

$$\hat{H} = \sum_i^N \left(-\frac{1}{2m} \nabla_i^2 + V(\hat{\mathbf{r}}_i) \right) + U \sum_{i<j}^N \delta^{(3)}(\hat{\mathbf{r}}_i - \hat{\mathbf{r}}_j) \quad (1.4)$$

where m is the atomic mass, $\hat{\mathbf{r}}_i$ the i -th particle's position operator, ∇_i the gradient operator acting on \mathbf{r}_i , and U an interaction constant. The goal now

is to minimise the expectation value of Hamiltonian (1.4) with respect to the single-particle state ϕ_0 of Eq. (1.3). It is even more convenient to introduce a scaled quantity, $\psi(\mathbf{r}) = \sqrt{N}\phi_0(\mathbf{r})$, usually referred to as *the condensate wave function*, and minimise with respect to it. A Lagrange multiplier μ needs to be introduced to constrain the spatial integral of $|\psi(\mathbf{r})|^2$ to N .[†] The complete expression to be minimised is:

$$E[\psi] = \int d\mathbf{r} \left[\frac{1}{2m} |\nabla\psi(\mathbf{r})|^2 + (V(\mathbf{r}) - \mu) |\psi(\mathbf{r})|^2 + \frac{1}{2}U |\psi(\mathbf{r})|^4 \right]. \quad (1.5)$$

Demanding that this quantity be a minimum with respect to variations in $\psi^*(\mathbf{r})$ yields, through the calculus of variations, the Gross-Pitaevskii equation:

$$-\frac{1}{2m}\nabla^2\psi(\mathbf{r}) + V(\mathbf{r})\psi(\mathbf{r}) + U|\psi(\mathbf{r})|^2\psi(\mathbf{r}) = \mu\psi(\mathbf{r}). \quad (1.6)$$

The complex many-body problem has been reduced to solving a single non-linear differential equation. On account of its simplicity and wide applicability, the Gross-Pitaevskii equation, or GPE, is one of the main calculational tools with which condensates are analysed. Though arriving at it from an alternative argument, Chapter 3 utilises the GPE to obtain the mean-field ground states of the dice lattice.

Just like the ordinary Schrödinger equation, the GPE has a time-dependent version, in which the chemical potential μ on the right-hand side of Eq. (1.6) is replaced by $i\partial_t$. This presents one method of obtaining the excitation spectrum, by finding small deviations from the ground state, periodic in time, and may be justified on the basis of the microscopic Bogoliubov theory, discussed in Sec. 1.5.1.

The condensate wave function is a complex quantity, but the GPE is invariant under multiplying it by a phase. The ground state must hence spontaneously break symmetry in choosing a phase. In the continuum, the broken phase symmetry implies the presence of a gapless Goldstone mode. This also oc-

[†]Even though the particle number is fixed, μ may be interpreted as the chemical potential of a related system, identical in every respect, except that it is in chemical equilibrium with a particle reservoir, such that its particle-number expectation value is N . Indeed, an alternative widely used mean-field scheme and one of the definitions of the BEC order parameter, discussed in Sec. 1.1.3, work with this related system from the very beginning.

curs for the non-interacting system, but even rather weak interactions induce a critical difference. In the non-interacting case, the excitation spectrum is unaffected by the condensate, and remains quadratic. Interactions, however, linearise the long-wavelength dispersion ε_p , as can be derived with either the time-dependent Gross-Pitaevskii equation or Bogoliubov theory. There is then a famous argument by Landau^{64,65} that condensate flows at velocities $v < \min(\varepsilon_p/p)$, minimised over the entire spectrum, experience *no* dissipation. This impressive and experimentally rewarding property of condensates is considered one of their main hallmarks.

Superfluid behaviour in Bose-Einstein condensates has been experimentally verified four years after their initial realisations.^{102,80} The authors of Ref. [80] achieved this through engineering a superfluid vortex. When a condensate is rotated or stirred fast enough, several vortices appear and arrange themselves into an Abrikosov triangular lattice, named after Alexei Abrikosov, who studied the vortices in the context of type-II superconductivity.² These were realised soon after,^{77,78,102} and their experimentally obtained absorption images remain one of the most iconic results in the study of Bose-Einstein condensates.

1.1.3 BEC ORDER PARAMETERS

The previous section introduced the mean-field methodology, appropriate for calculations in the condensed regime. The variational ansatz that it considered was chosen with this in mind, and the resulting Gross-Pitaevskii wave functions thus hardly convey any information on behaviour at higher temperatures. In this short section, the two commonly used order parameters, that may be used to observe the condensation phase transition, are introduced.

The first involves the one-particle reduced density matrix, and is due to Penrose and Onsager.⁹⁶ For a scalar condensate in a pure many-body state $\psi(\mathbf{r}_1, \dots, \mathbf{r}_N)$, this is defined as

$$\rho(\mathbf{r}, \mathbf{r}') \equiv N \int d\mathbf{r}_2 \cdots d\mathbf{r}_N \psi^*(\mathbf{r}, \mathbf{r}_2, \dots, \mathbf{r}_N) \psi(\mathbf{r}', \mathbf{r}_2, \dots, \mathbf{r}_N) \quad (1.7)$$

with straightforward generalisations for mixed states and multi-component condensates. Viewed as an integral operator, i.e., $(\rho\varphi)(\mathbf{r}) \equiv \int d\mathbf{r}' \rho(\mathbf{r}, \mathbf{r}')\varphi(\mathbf{r}')$, one can define its eigenvalues and eigenfunctions. When there are eigenvalues of order N , the system is said to be Bose-Einstein condensed, and when there is one, and only one such eigenvalue, the resulting BEC is said to be simple. With more than one macroscopic eigenvalue, the BEC is said to be *fragmented*. We will encounter several cases of fragmented condensates in systems of tightly bound cold spinor atoms, considered from Chapter 6 onwards. Focusing on simple condensates for now and denoting the macroscopic eigenvalue by N_0 and its corresponding eigenfunction by $\chi_0(\mathbf{r})$, the order parameter Ψ may be defined as $\Psi(\mathbf{r}) = \sqrt{N_0}\chi_0(\mathbf{r})$. Note that when the condensate is in the wave function (1.3), the single-particle state ϕ_0 is an eigenvector of ρ with eigenvalue N , while all states orthogonal to ϕ_0 have eigenvalues 0. In this case, the condensate wave function agrees with the order parameter.

Even though the majority of experiments to date involve a fixed number of particles, the second definition, most commonly used in practice, requires one to consider the related system in chemical equilibrium with the same average number of particles. This is usually not seen as a problem, as fluctuations of the relative particle number scale as $N^{-1/2}$, and are hence negligible for typical experimental values of N . Considering the standard bosonic field operator $\hat{\psi}(\mathbf{r}, \lambda)$ that annihilates a particle in some internal state, parametrised by λ , at position \mathbf{r} , the order parameter, according to the second definition, is simply $\Psi(\mathbf{r}, \lambda) = \langle \hat{\psi}(\mathbf{r}, \lambda) \rangle$, a quantity that can never be non-zero with strictly conserved particle number.

The above order parameter is closely related to an alternative approach to mean-field calculations, in which the variational function is taken to be a coherent state. Not only does this yield non-zero expectation values of annihilation operators, it is also their simultaneous eigenstate. Besides algebraic simplicity, the choice of minimising among coherent states is also motivated by their semiclassical properties, as they approximately minimise the Heisenberg uncertainty between the hydrodynamic variables of density and phase. Furthermore, their N -particle components are of the type utilised in the

mean field treatment of the previous section, with all particles occupying the same single-particle state.

1.1.4 HISTORICAL OVERVIEW

The above definitions and examples far predate the initial experimental realisations of the condensate in a dilute atomic gas by the independent groups of Cornell and Wieman,⁵ Ketterle,²⁶ and Hulet¹⁸ in 1995. The concept has seen several milestones since it was first proposed in 1924,²⁸ the first of which might have been Fritz London's suggestion that a BEC is responsible for the superfluid behaviour of liquid ^4He .⁷⁵ While this hypothesis stood the test of time, liquid helium atoms are very strongly interacting, making the overall condensate fraction significantly less than 1, and complicating experimental investigation. The search was thus on for weakly interacting species that would remain gaseous to very low temperatures. Spin-polarised hydrogen emerged as a natural candidate,^{44,121} though experimental issues meant a condensate of hydrogen atoms was realised only three years after those of alkali species, in 1998.³³ Nevertheless, the technique of evaporative cooling developed along the way, combined with a stage of laser cooling, was a key step in the successful condensation experiments of 1995. These all used alkali atoms, which have remained the most widely utilised particles in condensation experiments to date,¹¹⁸ on account of their many favourable properties, but condensates of non-alkali atoms, such as metastable ^4He atoms,^{104,97} ytterbium,^{124,34} chromium,⁴² erbium,⁴ and dysprosium⁷⁶ have also been realised. Many successful condensation experiments with particles other than atoms have also been performed, some of which have ushered in entire new fields of physics.^{27,138}

1.2 OPTICAL TRAPS AND LATTICES, THE BOSE-HUBBARD MODEL

A variety of trapping techniques are used during different stages of cold-atom condensate experiments. The earliest traps were magnetic or magneto-optical and the latter are still routinely used during the cooling process. Ever since

the late 90's, final stages of experiments have largely been carried out in purely optical traps. This is, in part, due to their experimental versatility, as well as the fact that, when properly configured, they couple equally to different magnetic spin sublevels, to a very good approximation.¹¹⁸ This makes them very suitable for probing properties of spinor atoms. They are formed by interfering laser beams producing an electromagnetic standing wave whose nodes or crests attract atoms via the Stark effect, briefly outlined below. Using more than one pair of lasers in a spatial configuration allows for the realisation of complex two- or three-dimensional intensity patterns.⁸⁸ Using lower laser intensities, an amount of tunnelling between the individual centres of attraction can be achieved, leading to an effective Bose-Hubbard model on the corresponding lattice,⁵¹ from which analogies with real solid-state systems may be derived.

In the following, we focus on the periodic case with many traps. A simple quasi-one-dimensional lattice may already be constructed with a single pair of coherent interfering laser beams.⁸⁸ This is typically realised by reflecting a single laser beam, making it interfere with itself, or splitting the beam initially and guiding the two resulting beams into the appropriate spatial arrangement. The latter method allows for added versatility, as varying the phases or frequencies of individual beams separately enables one to realise setups such as a moving lattice. The case of an accelerating lattice simulates an additional longitudinal force.

In realising higher-dimensional lattices, care needs to be taken with respect to multiple-wave interference effects. For two pairs of lasers, the polarisations can be adjusted so as to reduce these effects. For more complex arrangements, laser pairs of differing frequencies are typically used, with frequency differences on the order of 10 MHz, washing out the interference but hardly influencing other lattice properties.⁸⁸

1.2.1 THE STARK EFFECT

Considering time averages of the rapidly oscillating electric fields, this creates a periodic intensity pattern. Atoms populating the effective lattice are then

attracted to either the maxima or minima of the intensity pattern, depending on the frequency of laser light, via the Stark effect. This can be understood as an effective energy shift of the atomic ground state within the framework of perturbation theory.⁹⁸ The perturbing Hamiltonian is taken to be

$$H' = -\hat{\mathbf{d}} \cdot \boldsymbol{\mathcal{E}} \quad (1.8)$$

where $\hat{\mathbf{d}} = e \sum_i \hat{\mathbf{r}}_i$, with the sum being over all electrons in the atom, is the electronic dipole moment operator, and $\boldsymbol{\mathcal{E}}$ is the electric field, in general time-dependent. Letting the field oscillate with frequency ω , i.e., $\boldsymbol{\mathcal{E}}(t) = \boldsymbol{\mathcal{E}}_\omega e^{-i\omega t} + \boldsymbol{\mathcal{E}}_\omega^* e^{i\omega t}$ a straightforward application of time-dependent perturbation theory yields an energy shift

$$\Delta E_g = -\frac{1}{2} \langle \boldsymbol{\mathcal{E}}^2 \rangle \sum_e \left| \langle e | \hat{\mathbf{d}} \cdot \mathbf{e}_\varepsilon | g \rangle \right|^2 \left(\frac{1}{E_e - E_g + \hbar\omega} + \frac{1}{E_e - E_g - \hbar\omega} \right) \quad (1.9)$$

where \mathbf{e}_ε is the unit vector along the electric field's polarisation, the ground state is denoted by g , and excited states by e . This can be vastly simplified when the radiation frequency is close to that of an atomic transition, as one may then neglect all other terms in the above sum, as well as keep only the denominator with negative frequency. Furthermore, one can avoid the divergence exactly at the transition frequency by taking into account the decay time of the excited state due to spontaneous emission. Phenomenologically, this consists of introducing a complex component of its energy, $E_e \rightarrow E_e - i\hbar\Gamma_e/2$. This turns the energy shift into a complex quantity as well, i.e., introduces a decay time due to induced excitations, while its real part may still be considered a real energy shift. Further introducing the *detuning* $\delta \equiv \omega - \omega_{eg}$, where $\omega_{eg} = (E_e - E_g)/\hbar$ is the transition frequency, and the transition's *Rabi frequency* $\Omega_R \equiv \left| \langle e | \hat{\mathbf{d}} \cdot \boldsymbol{\mathcal{E}}_\omega | g \rangle \right| / \hbar$ yields the simple expression for the real energy shift

$$\text{Re } \Delta E_g = \frac{\hbar \Omega_R^2 \delta}{\delta^2 + \Gamma_e^2/4}. \quad (1.10)$$

From this, one immediately sees that for positive detuning, also called blue detuning, atoms will be attracted to minima of the electric field, while for

negative or red detuning they will be attracted to the maxima.

1.2.2 THE BOSE-HUBBARD MODEL

At large numbers of atoms per lattice site, a mean-field approach is viable, and may be supplemented by the venerable Bogoliubov method of treating quantum excitations about the mean-field configuration. At lower fillings, however, single-site particle-number fluctuations become important. For deep lattices, in which the difference in energy between the first single-site excited state and the corresponding ground state is much bigger than the hopping matrix element, given by J in Eq. (1.14) below, the most straightforward manner of treating said fluctuations is to consider an effective Bose-Hubbard model,^{51,50} originally devised in the context of liquid helium in restricted geometries.³¹ From it, the mean-field energy functional can be reproduced as the energy expectation value in a tensor product of coherent states, with the annihilation-operator eigenvalues corresponding to the condensate wave function.

Consider, for simplicity, an effective Bose-Hubbard model on a Bravais lattice. To state its form concisely, let us first introduce the localised Wannier states. These are formed by a suitable superposition of lowest-band Bloch states of the non-interacting problem. Denoting the latter by $\phi_{\mathbf{q}}(\mathbf{x}) = e^{i\mathbf{q}\cdot\mathbf{x}}u_{\mathbf{q}}(\mathbf{x})$, where \mathbf{q} is a wave vector in the first Brillouin zone and the $u_{\mathbf{q}}(\mathbf{x})$ share the periodicity of the lattice, the Wannier state localised at \mathbf{R} is given by:

$$w_{\mathbf{R}}(\mathbf{x}) = \frac{1}{V_{\text{cell}}} \int d^d\mathbf{q} e^{-i\mathbf{R}\cdot\mathbf{q}} \phi_{\mathbf{q}}(\mathbf{x}) \quad (1.11)$$

where V_{cell} is the d -dimensional volume of the unit cell. Defining $w_{\mathbf{R}}(\mathbf{x}) \equiv w(\mathbf{x} - \mathbf{R})$ and considering the bosonic field operator $\hat{\varphi}(\mathbf{x})$ of the second-quantised many-body picture, the latter may be expanded as

$$\hat{\varphi}(\mathbf{x}) = \sum_i \hat{a}_i w(\mathbf{x} - \mathbf{R}_i) \quad (1.12)$$

where i is some index labelling lattice sites, \mathbf{R}_i is the centre position of the i -

th site, usually defined so that the Wannier states are as localised as possible, and \hat{a}_i an annihilation operator for a boson at that site. In the absence of an external potential one may then derive the effective Hamiltonian

$$\hat{H} = -J \sum_{\langle ij \rangle} \hat{a}_i^\dagger \hat{a}_j + \frac{1}{2} U \sum_i \hat{n}_i (\hat{n}_i - 1) \quad (1.13)$$

where $\hat{n}_i = \hat{a}_i^\dagger \hat{a}_i$ is the number operator for the i -th site, the first sum is over all pairs of neighbouring sites, and the quantities J and U are defined as:

$$\begin{aligned} J &= \int d^d \mathbf{x} w^*(\mathbf{x} - \mathbf{R}_i) \left[-\frac{1}{2m} \nabla^2 + V_0(\mathbf{x}) \right] w(\mathbf{x} - \mathbf{R}_j) \\ U &= \frac{4\pi a_s}{m} \int d^d \mathbf{x} |w(\mathbf{x})|^4 \end{aligned} \quad (1.14)$$

where, in the first line, the i and j label any two neighbouring sites, m is the atomic species' mass, and a_s its s -wave scattering length. The prototypical example of a result obtained through this model is the superfluid to Mott insulator transition,^{31,51} which has been experimentally observed soon after the observation of superfluidity in condensates itself.⁴¹ By gradually increasing the repulsive interaction strength between atoms, the condensate wave function and, in particular, its phase, stop being well defined and the resulting state becomes well described by a tensor product of Fock states for individual sites, exhibiting a gapped excitation spectrum.^{32,114,132,30}

1.3 EFFECTIVE INTERACTIONS AND SPINOR CONDENSATES

Besides their excellent experimental properties, an appealing theoretical characteristic of cold atoms is the applicability of a simple inter-atomic contact interaction. This section provides an overview of their scattering properties and how these give rise to the effective interactions, which are a central feature of a number of Hamiltonians in Chapters 5 to 10.

Consider an isolated pair of two identical colliding atoms. Their scattering properties may be inferred from the wave function of their relative motion, separated from the centre-of-mass motion. The incoming atom's motion is

represented by a plane wave, travelling along the z direction, while the scattered wave-function components travel in the radial direction. The potential is assumed to be symmetric with respect to the azimuthal angle. The outgoing wave-function component may be decomposed into a sum of partial waves, indexed by an integer ℓ , with the angular dependence of the spherical harmonic $Y_{\ell,m=0}$. For cold atomic setups, the most important of these is the $\ell = 0$, or s -wave component.

Neglecting the weak magnetic dipolar interaction, at large distances the atoms interact through the isotropic Van der Waals interaction, with a strength proportional to $1/r^6$. One may invoke results of classical scattering theory⁶⁶ to show that, at long wavelengths, the cross sections for such interactions are dominated by s -wave scattering, regardless of the short-distance details of the interatomic potential. In the cold atomic setting, characteristic collision momenta are typically so low that the scattering wave function can be approximated by $\psi \approx 1 - \frac{a}{r}$, where the constant a is called the scattering length.

Due to the weakness of the interactions, the Born approximation may be invoked. Denoting the functional form of the potential between two particles, at positions \mathbf{r} and \mathbf{r}' , by $V(\mathbf{r} - \mathbf{r}')$, the scattering length in the Born approximation is given by

$$a_{\text{Born}} = \frac{m_r}{2\pi} \int d\mathbf{r} V(\mathbf{r}), \quad (1.15)$$

where m_r is the reduced mass of the colliding pair, half of the single-particle mass for a pair with the same masses. Since the approximate low-energy form of the wave function $\psi \approx 1 - \frac{a}{r}$ depends only on the scattering length, the same low-energy behaviour should be obtained for an arbitrary form of the potential with the same spatial integral, the simplest of which, for present applications, is the delta function. Comparing with Eq. (1.15), the entire potential for a pair of spinless cold atoms may thus be approximated very well by:

$$\hat{V} = U \delta^{(3)}(\hat{\mathbf{r}} - \hat{\mathbf{r}}') \quad \text{with} \quad U \equiv \frac{4\pi a}{m} \quad (1.16)$$

where $\hat{\mathbf{r}}$ and $\hat{\mathbf{r}}'$ are the particles' position operators, a is the s -wave scatter-

ing length, and m the species' atomic mass. This effective form may also be justified in a more rigorous fashion by integrating out high-momentum components of the potential.⁹⁸

Through a straightforward application of the second-quantisation formalism, one then arrives at the many body interaction term

$$\hat{V}_{\text{2nd}} = \frac{1}{2}U \int d\mathbf{r} \hat{\psi}^\dagger(\mathbf{r})\hat{\psi}^\dagger(\mathbf{r})\hat{\psi}(\mathbf{r})\hat{\psi}(\mathbf{r}) = \frac{1}{2}U \int d\mathbf{r} : \hat{n}(\mathbf{r})^2 : \quad (1.17)$$

where $\hat{\psi}(\mathbf{r})$ annihilates a particle at position \mathbf{r} , $\hat{n}(\mathbf{r}) = \hat{\psi}^\dagger(\mathbf{r})\hat{\psi}(\mathbf{r})$ is the density operator at \mathbf{r} , and the colons denote normal ordering.

1.3.1 EFFECTIVE SPINOR INTERACTIONS

For spinful atoms, a series of approximations, typically valid in cold atomic systems, imply that one may still consider only the s -wave component of the relative-motion wave function.^{47,93,118} There are, however, several scattering lengths that need to be taken into account, one for each value of the colliding pair's total spin allowed by symmetry. Taking into account parity properties for a pair of identical particles in an orbital s -wave, the allowed values of total spin are seen to be even, for both bosons and fermions. For a pair of spin- F cold atoms, this leads, by analogy with Eq. (1.16), to the first-quantised pair potential

$$\hat{V}^{(F)} = \delta^{(3)}(\hat{\mathbf{r}} - \hat{\mathbf{r}}') \sum_{S=0}^F U_{2S}^{(F)} \hat{\mathcal{P}}_{2S} \quad (1.18)$$

$$U_S^{(F)} \equiv \frac{4\pi a_S^{(F)}}{m} \quad (1.19)$$

Where $\hat{\mathbf{r}}$ and $\hat{\mathbf{r}}'$ are the particles' position operators, and the $\hat{\mathcal{P}}_J$ are projectors onto the subspace of total spin J . In contrast to the scalar case, there are now several interaction constants $U_J^{(F)}$, one for each even value of total spin J , which may be expressed in terms of the corresponding scattering lengths $a_J^{(F)}$.

For species with $F = 1$ and $F = 2$, the latter being a main focus of this thesis, the second-quantised form of the above interaction can be expressed in a neat, compact form. To sketch its derivation, the right-hand side of Eq. (1.18) first has to be put into an alternative form, a linear combination of $\mathbb{1}$ and $\hat{\mathbf{F}} \cdot \hat{\mathbf{F}}'$ for spin-1 species, and additionally $\hat{\mathcal{P}}_0$ for spin-2 species. Here $\hat{\mathbf{F}}$ and $\hat{\mathbf{F}}'$ are the particles' vectors of spin operators. This involves inverting the system of equations

$$\begin{aligned} \mathbb{1} &= \sum_{S=0}^F \hat{\mathcal{P}}_{2S}, \\ \hat{\mathbf{F}} \cdot \hat{\mathbf{F}}' &= \sum_{S=0}^F [S(2S+1) - F(F+1)] \hat{\mathcal{P}}_{2S} \end{aligned} \quad (1.20)$$

for spin-1, along with the additional trivial identity $\hat{\mathcal{P}}_0 = \hat{\mathcal{P}}_0$ for spin-2. Solving these, Eq. (1.18) may be expressed as

$$\hat{V}^{(F)} = \delta^{(3)}(\hat{\mathbf{r}} - \hat{\mathbf{r}}') \left(c_0^{(F)} \hat{\mathbb{1}} + c_1^{(F)} \hat{\mathbf{F}} \cdot \hat{\mathbf{F}}' + (2F+1) c_2^{(F)} \hat{\mathcal{P}}_0 \right). \quad (1.21)$$

The $c_i^{(F)}$ are a set of constants that will be referred to throughout the second part of the thesis. Their values are found to be:

$$\begin{aligned} c_0^{(1)} &= \frac{4\pi}{3m} (a_0^{(1)} + 2a_2^{(1)}) & c_0^{(2)} &= \frac{4\pi}{7m} (4a_2^{(2)} + 3a_4^{(2)}) \\ c_1^{(1)} &= \frac{4\pi}{3m} (a_2^{(1)} - a_0^{(1)}) & c_1^{(2)} &= \frac{4\pi}{7m} (a_4^{(2)} - a_2^{(2)}) \\ c_2^{(1)} &= 0 & c_2^{(2)} &= \frac{4\pi}{5m} (a_0^{(2)} - a_4^{(2)}) + \frac{8\pi}{7m} (a_4^{(2)} - a_2^{(2)}). \end{aligned} \quad (1.22)$$

To consider the second-quantised form of Eq. (1.21), define operators $\hat{\psi}_\alpha(\mathbf{r})$ which annihilate a boson with magnetic number α at position \mathbf{r} . Below, the positional dependence of $\hat{\psi}_\alpha$ will be suppressed for clarity. Just like for the scalar condensate, the second-quantised interaction Hamiltonian density will have a term proportional to $:\hat{n}^2:$, where the total density is now defined as $\hat{n} \equiv \hat{\psi}_\alpha^\dagger \hat{\psi}_\alpha$, arising from the first term of the first-quantised interaction (1.21). The remainder of the interaction yields additional terms. Their significance

will become clearer as we begin to analyse specific spinor Hamiltonians from Chapter 5 onwards, but their form is presented here for completeness. Define the density of spin in the i -th direction $\hat{\mathcal{F}}^{(F)i} = \hat{\psi}_\alpha^\dagger F_{\alpha\beta}^{(F)i} \hat{\psi}_\beta$, where $F^{(F)i}$ is the i -th spin- F matrix. Also define $\hat{\mathcal{A}}^{(F)} = \hat{\psi}_\alpha^t \hat{\psi}_\alpha = \sum_{\alpha=-F}^F (-1)^\alpha \hat{\psi}_\alpha \hat{\psi}_{-\alpha}$, where the superscript t refers to time reversal. Further suppressing the species' spin superscripts (F), the second-quantised potential is found to be

$$\hat{V} = \frac{1}{2} \int d\mathbf{r} \left(: c_0 \hat{n}^2 + c_1 \hat{\mathcal{F}}^2 : + c_2 \hat{\mathcal{A}}^\dagger \hat{\mathcal{A}} \right) \quad (1.24)$$

where the colons again denote normal ordering.

1.4 THE ZEEMAN EFFECT

This section covers the energy shifts of low-lying atomic states in a magnetic field. These show qualitatively different behaviour depending on the field strength, but are known collectively as the Zeeman effect. This offers a versatile addition to the experimental toolbox and will play a key role in Chapters 5 and 6, considering mean-field and exact properties of condensates in external fields, as well as in Chapter 9, deriving new results for tightly confined spin-2 bosons in the presence of a quadratic Zeeman field.

We consider the shifts for the most experimentally relevant bosonic species, the alkali atoms. In order to be bosonic, these need to have an even number of neutrons, which is satisfied by a number of stable alkali isotopes.

The magnetic field couples to the magnetic momenta of the outer-shell electron and the atomic nucleus. These momenta are related to the particles' spin and orbital angular momenta through standard quantum-mechanical relations. The alkali atoms have a single electron in their outermost shell. It occupies the lowest-energy s -subshell and accordingly has orbital angular momentum $\mathbf{L} = 0$. The total angular momentum $\mathbf{J} = \mathbf{L} + \mathbf{S}$ is thus just its spin \mathbf{S} , of magnitude $S = 1/2$. This yields a total magnetic moment $\boldsymbol{\mu} = -g_s \mu_B \mathbf{S}$, where g_s is the absolute value of the electron g -factor, equal to 2 to a good approximation, and $\mu_B = e/2m_e$ is the Bohr magneton, one half the ratio of the elementary charge to the electronic mass, a convenient unit in

which to measure atomic magnetic momenta. The nuclear angular momentum yields a magnetic moment on the much smaller order of $\mu_N = e/2m_p$, the nuclear magneton, where m_p is the proton mass. The nuclear angular momentum of most experimentally relevant alkali species is $I = 3/2$, including ^{23}Na , ^{39}K , and ^{87}Rb .

The nuclear and electronic magnetic momenta also interact with each other. The interaction is phenomenologically taken into account through the Hamiltonian term

$$\hat{H}_{\text{hf}} = A \hat{\mathbf{I}} \cdot \hat{\mathbf{J}}, \quad (1.25)$$

where $\hat{\mathbf{I}}$ and $\hat{\mathbf{J}}$ are the total nuclear and electronic angular momentum operators, respectively. The order of magnitude of the constant A is smaller than those of fine-structure effects, such as the electronic spin-orbit coupling, by about the factor of $m_e/m_p \sim 10^{-3}$, the ratio of the electron's and proton's masses. On account of this, the Hamiltonian term (1.25) is called the hyperfine interaction.

At zero external field, eigenstates of Eq. (1.25) are eigenstates of the total angular momentum squared operator, $\hat{\mathbf{F}}^2 \equiv (\hat{\mathbf{I}} + \hat{\mathbf{J}})^2$, since $\hat{\mathbf{I}} \cdot \hat{\mathbf{J}}$ can be expressed as $\frac{1}{2} [\hat{\mathbf{F}}^2 - \hat{\mathbf{I}}^2 - \hat{\mathbf{J}}^2]$. For alkali atoms, where $J = S = 1/2$, rules of angular momentum addition dictate that F can take on the values of $I \pm 1/2$. Taking into account that the corresponding eigenvalues of $\hat{\mathbf{F}}^2$ are $F(F+1)$, and similarly for the other two angular momentum operators, the zero-field energy splitting between the $F = I \pm 1/2$ levels is seen to be

$$\Delta W = A \left(I + \frac{1}{2} \right). \quad (1.26)$$

The general form and order of magnitude of ΔW can be gleaned from a perturbative result for states with a single outermost s electron,⁶⁶

$$\Delta W = \frac{\mu_0}{4\pi} \frac{16\pi}{3} \mu_B \mu \frac{I + \frac{1}{2}}{I} |\psi(0)|^2, \quad (1.27)$$

where μ_0 is the vacuum permeability, $\mu \sim \mu_N$ the magnetic moment of the nucleus, and $|\psi(0)|^2$ the electron's probability density at the nucleus. It

may also be noteworthy that, due to screening effects, the hyperfine splitting scales approximately linearly with the atomic number Z .

In the presence of a magnetic field B , oriented along the z direction, interactions of the nucleus' and electron's magnetic moments with B are added to the Hamiltonian. Expressing $\hat{\mathbf{I}} \cdot \hat{\mathbf{J}} = \hat{I}_z \hat{J}_z + \frac{1}{2} (\hat{I}_+ \hat{J}_- + \hat{I}_- \hat{J}_+)$, where $\hat{I}_\pm = \hat{I}_x \pm i\hat{I}_y$ and likewise for \hat{J}_\pm , and taking into account $\hat{\mathbf{J}} = \hat{\mathbf{S}}$, the full magnetic Hamiltonian becomes

$$\hat{H}_{\text{hf}} = A\hat{I}_z\hat{S}_z + \frac{A}{2} (\hat{I}_+\hat{S}_- + \hat{I}_-\hat{S}_+) + g_s\mu_B B\hat{S}_z + g_I\mu_N B\hat{I}_z \quad (1.28)$$

where g_I is an appropriately defined nuclear g -factor. Working in the $|m_I, m_S\rangle$ basis, where the two labels represent the nuclear and electronic magnetic quantum numbers, respectively, one sees that Hamiltonian (1.28) only couples states of the same $m_F \equiv m_I + m_S$. This immediately yields energy shifts linear in B for the $|\pm I, \pm 1/2\rangle$ states, that do not couple to any other states. The $m_F = \pm 1, 0$ subspaces are all 2-dimensional, which reduces the problem of finding Eq. (1.28)'s eigenvalues to that of diagonalising 2-by-2 matrices. Introducing the quantity $\Delta\mu \equiv g_s\mu_B - g_I\mu_N$ and the dimensionless magnetic field $x \equiv B\Delta\mu/\Delta W$, the results of this straightforward diagonalisation may be expressed neatly as

$$\Delta E_{F=I\pm 1/2} = -\frac{\Delta W}{2(2I+1)} + g_I\mu_N m_F B \pm \frac{\Delta W}{2} \sqrt{1 + \frac{2m_F x}{I+1/2} + x^2}, \quad (1.29)$$

a result often referred to as the Breit-Rabi formula, named after its early investigators.¹⁹ The energy-level splittings arising from this formula are shown in Fig. 1.1 for rubidium. The notation is standard, but it should be noted that F are good quantum numbers only for small x . This is, in fact, the regime of many cold-atoms experiments. This warrants an expansion of Eq. (1.29) to quadratic order in x . Dropping constant terms and re-expressing x in terms

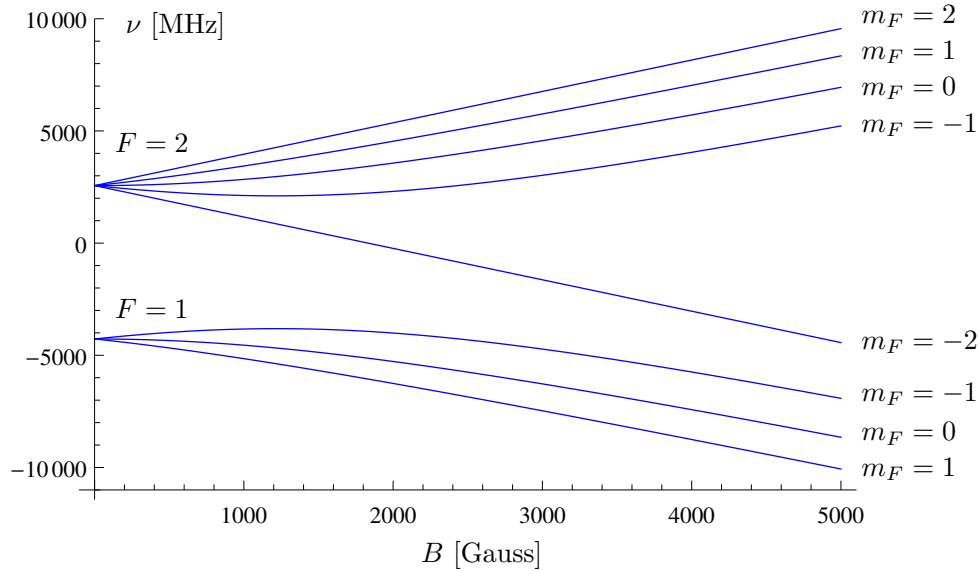


Figure 1.1: The energy-level splittings for ^{87}Rb arising from the Zeeman effect.

of B finally yields

$$\begin{aligned}
\Delta E_{F=I\pm 1/2} = & \pm \frac{1}{2} \left[\Delta W + \frac{(\Delta\mu)^2 B^2}{2\Delta W} \right] \\
& \pm \left[g_s \mu_B \pm 2 \left(I + \frac{1 \mp 1}{2} \right) g_I \mu_N \right] \frac{B m_F}{2I + 1} \\
& \mp \frac{(\Delta\mu)^2}{\Delta W (2I + 1)^2} B^2 m_F^2.
\end{aligned} \tag{1.30}$$

The coefficient of m_F is typically denoted by p and that of m_F^2 by q . Upon second-quantising, the term linear in m_F is proportional to \hat{F}_z , the z component of the total spin operator, while the quadratic term is proportional to \widehat{F}_z^2 . These terms are respectively called the linear and the quadratic Zeeman term.

It should be noted that the origin of such terms in actual experiments is not always magnetic. Cold-atomic setups allow for the engineering of a wide range of effective p and q values through electro-optical means, greatly extending the possible parameter ranges that may be probed.^{38,24,109,53}

1.5 ORDER-BY-DISORDER

A mean-field treatment is often the first line of investigation when analysing a quantum system with a large number of degrees of freedom. In cold atoms, this is often a very fruitful endeavour, yielding an intuitive, qualitatively, and often quantitatively correct picture of the system's properties. But there are, of course, cases where this is inadequate. One of the most frequently arising situations of the type is that of an accidental mean-field ground-state degeneracy. Here, accidental means that the degeneracy does not originate from broken symmetries of the Hamiltonian, and is thus not expected to be supported by a more exact, beyond-mean-field treatment.

Regardless, in most cases the correlations arising from a more exact treatment can simply be treated as perturbations to the mean field.[‡] This is the domain of Bogoliubov theory, whose elegant algebraic structure for bosonic systems is reviewed below. This gives rise to a set of non-interacting harmonic oscillator modes, whose zero-point energies and thermal contributions typically select a unique ground state among the accidentally degenerate family, constituting the mechanism of Order by Disorder.

1.5.1 BOGOLIUBOV THEORY

A central tenet of Bogoliubov theory is that one should replace the annihilation operators, appearing in the Hamiltonian of interest, by the sum of the complex mean-field c-numbers assigned to them, such as through the Gross-Pitaevskii equation, of order \sqrt{N} , and residual annihilation operators, naturally of order 1. Algebraically, one sets $\hat{a}_i = a_i + \delta\hat{a}_i$. Expanding the original Hamiltonian to second order in the $\delta\hat{a}$ operators yields a quadratic Hamiltonian that may always be transformed into a sum of noninteracting harmonic modes, and potentially a quadratic mode. This is achieved by per-

[‡]There are also cases when the mean-field assumption is simply wrong, and the exact and mean-field results are far removed from each other. A number of examples, arising in confined spin-1 and spin-2 condensates, are presented in Chapter 6. These regimes are experimentally challenging, as the validity of mean-field theory is rapidly restored with increasing particle number and external fields.

forming a *canonical transformation* of creation and annihilation operators.

This subsection considers properties of bosonic canonical transformations for the purposes of diagonalising quadratic Hermitian Hamiltonians, as obtained through the last paragraph's prescription. This section closely follows the exposition presented in the classic textbook by Blaizot and Ripka.¹⁵ The general form of the above type of Hamiltonian is

$$\hat{H} = \sum_{ij} \hat{a}_i^\dagger A_{ij} \hat{a}_j + \frac{1}{2} \sum_{ij} \left(B_{ij} \hat{a}_i^\dagger \hat{a}_j^\dagger + \hat{a}_j \hat{a}_i B_{ij}^* \right) \quad (1.31)$$

where A is a Hermitian matrix and B an arbitrary complex matrix. For simplicity, assume the indices of creation and annihilation operators run from 1 to a finite number n . It aids notation to introduce the vector of operators

$$\hat{\alpha} \equiv \left[\hat{a}_1, \hat{a}_2, \dots, \hat{a}_n, \hat{a}_1^\dagger, \hat{a}_2^\dagger, \dots, \hat{a}_n^\dagger \right]^T \equiv \left[\hat{\mathbf{a}}^T, \hat{\mathbf{a}}^\dagger \right]^T, \quad (1.32)$$

$$\hat{\alpha}^\dagger \equiv \left[\hat{a}_1^\dagger, \hat{a}_2^\dagger, \dots, \hat{a}_n^\dagger, \hat{a}_1, \hat{a}_2, \dots, \hat{a}_n \right] \equiv \left[\hat{\mathbf{a}}^\dagger, \hat{\mathbf{a}}^T \right]. \quad (1.33)$$

The defining properties of Fock-space creation and annihilation operators can then be succinctly expressed as

$$\left[\hat{\alpha}, \hat{\alpha}^\dagger \right]_c = \eta \equiv \begin{pmatrix} \mathbb{1}_{n \times n} & 0 \\ 0 & -\mathbb{1}_{n \times n} \end{pmatrix} \quad (1.34)$$

where the commutator has been denoted by square brackets with a subscripted c to differentiate it from plain square brackets enclosing vector components. In analogy with diagonalising a first-quantised Hamiltonian, one seeks to find a linear transformation of operators

$$\hat{\beta} = \left[\hat{\mathbf{b}}^T, \hat{\mathbf{b}}^\dagger \right]^T = T \hat{\alpha} \quad (1.35)$$

such that the Hamiltonian (1.31) takes on a simpler form with respect to the $\hat{\mathbf{b}}$ operators. Since these should also be legitimate annihilation operators, T must satisfy

$$\eta = \left[\hat{\beta}, \hat{\beta}^\dagger \right]_c = T \left[\hat{\alpha}, \hat{\alpha}^\dagger \right]_c T^\dagger = T \eta T^\dagger, \quad (1.36)$$

or equivalently

$$T^{-1} = \eta T^\dagger \eta. \quad (1.37)$$

A linear transformation satisfying this property is called a *canonical transformation*. Note that, in general, $\hat{\mathbf{b}}^\dagger$ from Eq. (1.35) need not be Hermitian conjugate to $\hat{\mathbf{b}}$, despite the notation. When diagonalising Hamiltonians of the type of Eq. (1.31), however, the two are genuinely Hermitian conjugate. A transformation T leading to this situation is also called a unitary canonical transformation.¹⁵

One may further rewrite Hamiltonian (1.31) as

$$\hat{H} = \frac{1}{2} \hat{\boldsymbol{\alpha}}^\dagger M \hat{\boldsymbol{\alpha}} - \frac{1}{2} \text{tr} A \quad \text{with} \quad M = \begin{pmatrix} A & B \\ B^* & A^* \end{pmatrix}. \quad (1.38)$$

Expressing everything in terms of $\hat{\boldsymbol{\beta}} = T \hat{\boldsymbol{\alpha}}$ yields

$$\hat{H} + \frac{1}{2} \text{tr} A = \frac{1}{2} \hat{\boldsymbol{\beta}}^\dagger (T^{-1})^\dagger M T^{-1} \hat{\boldsymbol{\beta}} = \frac{1}{2} \hat{\boldsymbol{\beta}}^\dagger \eta T \eta M T^{-1} \hat{\boldsymbol{\beta}} = \frac{1}{2} \hat{\boldsymbol{\beta}}^\dagger \eta D \hat{\boldsymbol{\beta}} \quad (1.39)$$

where T is to be chosen such that the matrix D , similar to ηM , is as simple as possible. A systematic treatment, as can be found in Chapter 3 of Blaizot and Ripka,¹⁵ shows that when ηM has no zero eigenvalues there exists a T and a positive-definite n -by- n diagonal matrix Ω such that[§]

$$D = \begin{pmatrix} \Omega & 0 \\ 0 & -\Omega \end{pmatrix} \quad (1.40)$$

[§]When there are zero eigenvalues present the situation is somewhat more complicated. Non-zero eigenvalues still come in opposite pairs, but ηM projected onto the orthogonal complement of all of their eigenvectors, sometimes called the zero sector, cannot in general be diagonalised. When it can be, it is identically equal to zero. Otherwise a zero eigenvector \mathbf{P} has an associated linearly independent vector \mathbf{Q} such that $\eta M \mathbf{Q} = -ic \mathbf{P}$ for some positive constant c . The contribution of the zero sector to the Hamiltonian is essentially that of a free particle in one dimension,¹⁵ a problem which admits no normalisable stationary solutions. Furthermore, every realistic BEC Bogoliubov Hamiltonian contains a broken-U(1) Goldstone zero mode. Lewenstein and You⁷⁰ have proposed interpreting the operator analogous to position as the condensate phase, and have predicted that the latter diffuses quadratically for short times. This has, however, not been observed in experiments.^{43,41,36} Recently, an alternative proposal, including higher than quadratic terms in the expansion of the zero sector, has been shown to yield a stationary ground state.⁹¹

so that the Hamiltonian (1.31) may finally be rewritten as

$$\hat{H} = \hat{\mathbf{b}}^\dagger \Omega \hat{\mathbf{b}} + \frac{1}{2} (\text{tr } \Omega - \text{tr } A), \quad (1.41)$$

a collection of *non-interacting* harmonic modes and a constant term.

In BEC systems one finally has to address the depletion of the condensate. This has to be small compared to the condensate occupation, so that expanding $\hat{a}_i = a_i + \delta\hat{a}_i$ and keeping second order terms in $\delta\hat{a}_i$ is justified. Note that here the $\delta\hat{a}_i$ play the role of \hat{a}_i of Eq. (1.31), so that $\hat{\beta} = T\delta\hat{\alpha}$. The depletion is defined as the expectation value $\mathcal{N}_{\text{ex}} = \langle \sum_i \delta\hat{a}_i^\dagger \delta\hat{a}_i \rangle$. Expressing everything in terms of \hat{b}_i and performing some simplifying algebra, one may separate the total depletion into a zero-temperature contribution \mathcal{N}_{q} and a temperature-dependent contribution \mathcal{N}_{th} with

$$\mathcal{N}_{\text{q}} = \frac{1}{4} \text{tr} [TT^\dagger (\mathbb{1} - \eta)] - \frac{n}{2} \quad (1.42)$$

$$\mathcal{N}_{\text{th}} = \frac{1}{2} \text{tr} [TT^\dagger f_{\text{BE}}(\eta D)] \quad (1.43)$$

where $f_{\text{BE}}(x) = (e^{x/T} - 1)^{-1}$ is the Bose-Einstein distribution at temperature T and zero chemical potential.

The most important aspect of Bogoliubov theory for the present discussion is that it allows one to determine the ground-state energy more accurately by adding the zero-point energies of the harmonic modes, corresponding to the traces term in Eq. (1.41), to the mean-field contribution. The zero-point contributions are typically orders of magnitude smaller than the energy scales determined by mean-field calculations, and the compound ground-state energy is usually remarkably accurate.

To illustrate this point, let us consider one of the rare examples of a system where an exact solution may be found and contrasted to that obtained in the Bogoliubov approximation, that of a two-site Bose-Hubbard Hamiltonian with hopping J and on-site interaction U . Its Hamiltonian is given by

$$\hat{H} = -J (\hat{a}_1^\dagger \hat{a}_2 + \hat{a}_2^\dagger \hat{a}_1) + \frac{U}{2} (\hat{a}_1^\dagger \hat{a}_1^\dagger \hat{a}_1 \hat{a}_1 + \hat{a}_2^\dagger \hat{a}_2^\dagger \hat{a}_2 \hat{a}_2). \quad (1.44)$$

The exact solutions may be found via the rotor mapping, introduced in Chapter 7 and applied to the double-well system in more detail in Sec. 8.1. It maps the above Hamiltonian onto that of a particle moving on a circle within a certain potential. Unlike the rotor theory, Bogoliubov theory is only stable when NJ is not much smaller than U , and it is in the stable regime that we draw the following comparison.

Even though expanding to second order in the $\delta\hat{a}$ operators means dropping terms of order \sqrt{N} , the difference between the Bogoliubov ground-state energy and the exact one turns out to be on the order of $N^{-1/2}$. This system further allows an intuitive decomposition of the total ground-state energy: the mean-field energy is the minimum of the potential energy on the associated circle and the Bogoliubov correction corresponds to the zero-point energy of oscillation about it, to within terms of order $N^{-1/2}$.

1.5.2 EFFECTS OF FLUCTUATIONS: ORDER-BY-DISORDER

As remarked in the opening paragraph of the present section, the situation in which there is a degenerate family of mean-field ground states is of particular interest. A typical source of degeneracies is symmetry-breaking, i.e., ground states not possessing the full symmetry of the Hamiltonian. For example, ground-states of a translationally invariant Hamiltonian may be localised, and applying the broken translation to such a state yields inequivalent states of the same energy. Such states will remain degenerate not only in the mean-field treatment but to all orders of approximation.

There is also a class of degeneracies that *do not* correspond to a breaking of a symmetry of the Hamiltonian. These are referred to as *accidental* degeneracies, reflecting the fact they are expected to be an artefact of the mean-field treatment. Such degeneracies are expected to be lifted by the Bogoliubov zero-point energies, a mechanism commonly dubbed *Order by Disorder*.

It should be noted that the mechanism appears in many guises. For instance, when the number of Bogoliubov modes about the mean-field is infinite, such as in the continuum, the summation of zero-point contributions

over all modes may not converge and a regularisation scheme is needed. Typically summing differences of mode-energies from those about a fixed mean-field configuration is sufficient. More generally, one may consider systems in thermal equilibrium at finite temperatures in which case the preferred mean field is selected by minimising the Helmholtz free energy, easily computable for a set of non-interacting boson modes with mode energies E_j as

$$F = \frac{1}{2} \sum_j E_j + \beta^{-1} \sum_j \ln(1 - e^{-\beta E_j}). \quad (1.45)$$

where $\beta = (k_B T)^{-1}$ and the mean-field energy has been subtracted. The first sum is over the zero-point contributions and is also present at zero temperature, while the second term is a thermal contribution that vanishes at absolute zero.

By far the most famous manifestation of the order-by-disorder principle is the Casimir-Polder force between two metal plates.²² While typically couched in different terminology, its traditional interpretation ascribes importance to the zero-point energies of electromagnetic standing-wave modes between the two plates. Their regularised sum decreases with decreasing plate separation, resulting in a net attractive force, proportional to the inverse fourth power of the separation. This effect has been successfully measured in experiments, in good agreement with quantitative predictions.^{20,84}

Besides the infamous Casimir-Polder force, the order-by-disorder mechanism has traditionally featured most prominently in elucidating the true ground states of frustrated magnetic systems, which typically feature a vastly degenerate ground-state manifold.^{134,113,45,46} Due to the Bogoliubov corrections to the GPE usually being several orders of magnitude smaller than mean-field energy scales, the effect in such systems has remained experimentally elusive, as it is typically dominated by disorder or other secondary effects.

Recently the phenomenon has, however, also received a spate of attention in the context of cold atoms.^{108,72,37,139,101,140,100,137,13,127,116,21,136} The experimental realities of cold atomic systems are hoped to finally provide a clean, definitive observation of the phenomenon in a condensed-matter setting.

2

GEOMETRY AND SINGLE-PARTICLE PROPERTIES OF THE DICE LATTICE

The following three chapters are dedicated to boson dynamics on the dice lattice. The present chapter first introduces the lattice's basic geometric properties, in Sec. 2.1, along with the single particle spectra in the presence of magnetic fields of various strengths, in Sec. 2.2. At exactly half-an-elementary-flux per plaquette an extreme localisation mechanism is induced,^{123,87} previously dubbed Aharonov-Bohm cages.¹³³ A more detailed derivation of the spectrum at this special field strength is presented in Sec. 2.3, which also includes a brief summary of work to date on dice-lattice tight-binding models. The following two chapters deal with the systematic description of the highly degenerate mean-field ground-state manifold and the ultimate lifting of degeneracies through Order by Disorder at the half-flux field strength.

2.1 \mathcal{T}_3 GEOMETRY AND THE BOSE-HUBBARD MODEL

The dice lattice, also referred to as the \mathcal{T}_3 lattice,¹³³ is a bipartite two-dimensional lattice. One of its alternating sublattices consists of six-fold co-

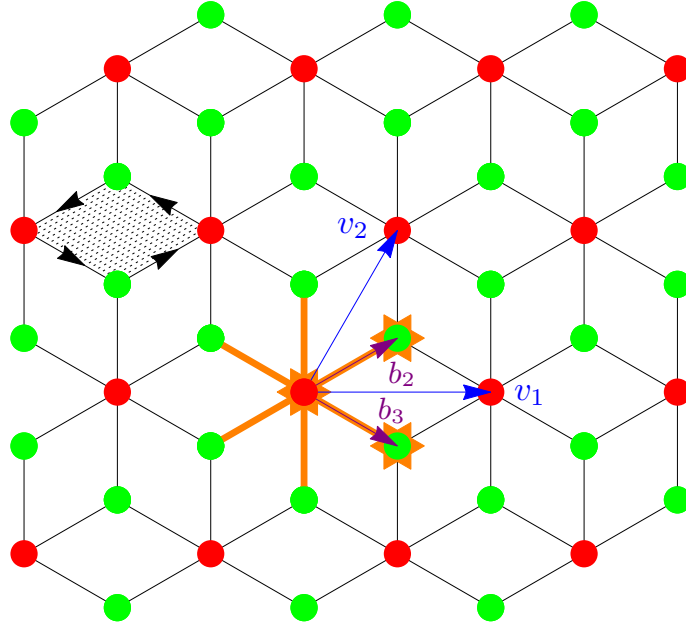


Figure 2.1: The basic geometrical properties of the dice lattice. There are two types of sites: hub sites with a coordination number of 6, shown in red, and rim sites with a coordination number of 3, shown in green. The links and sites outlined in orange comprise the unit cell in the absence of a gauge field. The shaded area shows a single plaquette, and the arrows on its surrounding links indicate the positive direction. The lattice vectors are $v_1 = (1, 0)$ and $v_2 = (1/2, \sqrt{3}/2)$, where the lattice constant has been set to unity for convenience. The lattice can thus be viewed as a triangular Bravais lattice with a three-fold basis. The basis vectors are $b_1 = \mathbf{0}$, $b_2 = (1/2, 1/2\sqrt{3})$, and $b_3 = (1/2, -1/2\sqrt{3})$.

ordinated sites, and the other of three-fold coordinated ones. In the absence of a magnetic field it has the translational symmetry of the triangular lattice and three sites per unit cell. All of its plaquettes are congruent rhombi. Its geometry is shown in Fig. 2.1. In experiments, the dice lattice may be realised as a Josephson junction array,^{1,112,126} in a heterostructure,¹³⁵ or as an optical lattice,^{85,21,14,103} utilising methods outlined in Sec. 1.2. We shall assume the latter in aspects of our analysis where experimental details are relevant.

The system that will be analysed is that of cold scalar bosons with repulsive interactions moving in the dice lattice potential, with a large average number of bosons per site. The kinetic part of the Hamiltonian is derived from a tight-binding model, and the interaction is taken to be on-site. At the quantum

level, the full system is then described by a Bose-Hubbard Hamiltonian, as introduced in Sec. 1.2.2.

The following labelling conventions are employed: the unit cells of the lattice are labelled by an integer n and the corresponding unit cell's location is denoted by \mathbf{R}_n . When the unit-cell/basis-vector decomposition is important, the site displaced from the origin of the n -th unit cell by the basis vector \mathbf{b}_γ is labelled with the pair (n, γ) . Otherwise each site is labelled by a single integer i and its location denoted by \mathbf{r}_i . Following Ref. [123], the six-fold coordinated sites are referred to as *hub* (*) sites, and the three-fold coordinated ones as *rim* (Δ) sites.

The system is considered in the presence of a synthetic gauge field with vector potential \mathbf{A} . In optical lattices these may be experimentally realised in a great variety of ways.⁴⁰ Later sections will focus particularly on the case where the line integral of \mathbf{A} around each plaquette equals π . Useful intuition about the configuration may be obtained through an analogy with electromagnetism: by considering the example of a particle of charge q in the presence of an electromagnetic potential \mathbf{A}_{EM} , \mathbf{A} is found to be analogous to $\frac{2\pi}{\Phi_0} \mathbf{A}_{\text{EM}}$ where $\Phi_0 = h/q$ is the charge- q elementary magnetic flux quantum. Likewise, $\int_{\mathcal{C}} \mathbf{A} \cdot d\mathbf{r}$, with \mathcal{C} a cyclic path along the edges of a plaquette, is analogous to the charged particle's corresponding Aharonov-Bohm phase.

In the continuum, electromagnetism is introduced into the Hamiltonian via minimal coupling, i.e., $\hat{\mathbf{p}} \rightarrow \hat{\mathbf{p}} - q\hat{\mathbf{A}}$. The tight-binding equivalent of this procedure is Peierls substitution, i.e., substituting pairs of creation and annihilation operators according to $\hat{a}_i^\dagger \hat{a}_j \rightarrow e^{iA_{ij}} \hat{a}_i^\dagger \hat{a}_j$, where \hat{a}_i is the annihilation operator for the i -th site and $A_{ij} = \int_{\mathbf{r}_j}^{\mathbf{r}_i} \mathbf{A}(\mathbf{r}) \cdot d\mathbf{r}$ is the line integral of the vector potential between sites j and i involved in the hopping. The noninteracting part of the Hamiltonian is thus $\hat{H}_0 = -t \sum_{\langle ij \rangle} (e^{iA_{ij}} \hat{a}_i^\dagger \hat{a}_j + \text{h.c.})$, where the sum is taken over all pairs of nearest neighbour sites.

The inter-site interactions are assumed to be negligibly weak. The interaction part of the Hamiltonian thus consists of terms of the form $\frac{1}{2} U_i \hat{a}_i^\dagger \hat{a}_i^\dagger \hat{a}_i \hat{a}_i$, where U_i is the positive on-site interaction. Keeping in mind the possible experimental realisation as an optical lattice, the hub and rim sites are assigned

independent interaction constants U_* and U_Δ , respectively. Introducing the chemical potential μ , the full Bose-Hubbard model on the dice lattice reads

$$\hat{H} = -t \sum_{\langle ij \rangle} \left(e^{iA_{ij}} \hat{a}_i^\dagger \hat{a}_j + \text{H.c.} \right) + \sum_i \left(\frac{1}{2} U_i \hat{a}_i^\dagger \hat{a}_i^\dagger \hat{a}_i \hat{a}_i - \mu \hat{a}_i^\dagger \hat{a}_i \right). \quad (2.1)$$

2.2 SINGLE-PARTICLE SPECTRUM

For completeness, this section briefly summarises the single-particle spectra in an arbitrary uniform perpendicular magnetic field as first derived in Ref. [133]. A useful means of expressing the field is through $f = \frac{\Phi}{2\pi}$, where Φ is the flux through a single plaquette, or equivalently the Aharonov-Bohm phase about its circumference. The spectrum can be seen to remain invariant under $f \rightarrow f + n$, $n \in \mathbb{N}$ and $f \rightarrow -f$, so that it is sufficient to consider only the range $0 \leq f \leq \frac{1}{2}$.

When f is rational, i.e., $f = p/q$, with p and q coprime, the unit cell consists of q hub sites and twice as many rim sites, and the spectrum consists of $3q$ bands. Of these, q are identically equal to 0, i.e., also degenerate and completely flat.* The non-zero negative-energy bands exactly coincide with the positive bands, mirrored across the zero-energy plane. The non-zero bands are related to those of the hexagonal lattice, with equal edge length, hopping strength t and magnetic field strength, by

$$\varepsilon_{\mathcal{T}_3, f}^{\pm n} = \pm t \sqrt{6 + 2 \frac{\varepsilon_{H, f}^n}{t} \cos \pi f}. \quad (2.2)$$

Here, $\varepsilon_{\mathcal{T}_3, f}^n$ is the energy of a dice-lattice state in the n -th band, when an elementary rhombus is threaded by f units of flux. $\varepsilon_{H, f}^n$ is defined similarly on the hexagonal lattice, where f is still defined as the number of elementary fluxes threading a region of the same area as an elementary rhombus of the \mathcal{T}_3 lattice, even though none are actually present in the hexagonal lattice skeleton.

*Vidal et al.¹³³ note an exception when $q = 3q'$; $q' \in \mathbb{N}$, when there are q' hub and $2q'$ rim sites in the unit cell, $3q'$ overall bands, and q' bands identically equal 0.

Plotting the support of the spectrum against f , a familiar Hofstadter-butterfly-like pattern emerges, displaying intricate nesting properties. Besides the vast degeneracy of the zero-energy states, several other curious properties can be discerned. For example, the spectrum at $f = 1/3$ is gapless. The following sections focus on the regime $f = 1/2$, also referred to as the “half-flux” regime, which, in a sense, exhibits the exact opposite of a gapless spectrum, as it contains merely three different energies with vast degeneracies.

The authors of Ref. [133] derived the above results in the Landau gauge. For our purposes, a more convenient gauge can be found for the half-flux regime.⁸⁵ Employing it, one may derive the $f = 1/2$ spectrum through a more conventional approach. This, and the discussion of eigenstates and localisation, is the subject of the next section.

2.3 SINGLE-PARTICLE SPECTRUM AT HALF-FLUX

To derive the spectrum at $f = 1/2$, first define the momentum-space annihilation operators $\hat{a}_{\mathbf{k}\gamma} = \frac{1}{\sqrt{N/2}} \sum_n \hat{a}_{n\gamma} e^{-i\mathbf{k}\cdot\mathbf{R}_n}$, where $N/2$ is the number of magnetic unit cells in the system.[†] The chosen gauge is shown in Fig. 2.2. One of its advantages is that it yields only real Peierls factors. Owing to the periodicity of the lattice, one can rewrite the non-interacting portion of the Hamiltonian in Eq. (2.1) as

$$\hat{H}_0 = \sum_{\mathbf{k}} \hat{\mathbf{a}}_{\mathbf{k}}^\dagger H_0(\mathbf{k}) \hat{\mathbf{a}}_{\mathbf{k}} \quad (2.3)$$

where $\hat{\mathbf{a}}_{\mathbf{k}} = [\hat{a}_{\mathbf{k}1}, \hat{a}_{\mathbf{k}2}, \dots, \hat{a}_{\mathbf{k}6}]^T$, $H_0(\mathbf{k})$ is a 6-by-6 Hermitian matrix, and the summation is over the first Brillouin zone. By inserting a full set of eigenvectors $\sum_{\gamma=1}^6 \mathbf{u}_{\mathbf{k}\gamma} \mathbf{u}_{\mathbf{k}\gamma}^\dagger$ on both sides of $H_0(\mathbf{k})$ in Eq. (2.3), one can express the Hamiltonian in terms of new quasiparticle operators $\hat{a}_{\mathbf{k}\gamma} = \mathbf{u}_{\mathbf{k}\gamma}^\dagger \hat{\mathbf{a}}_{\mathbf{k}}$ and

[†]The factor of one half is included as N , the number of *non-magnetic* unit cells, or equivalently hub sites, later turns out to be a more convenient measure of the system size.

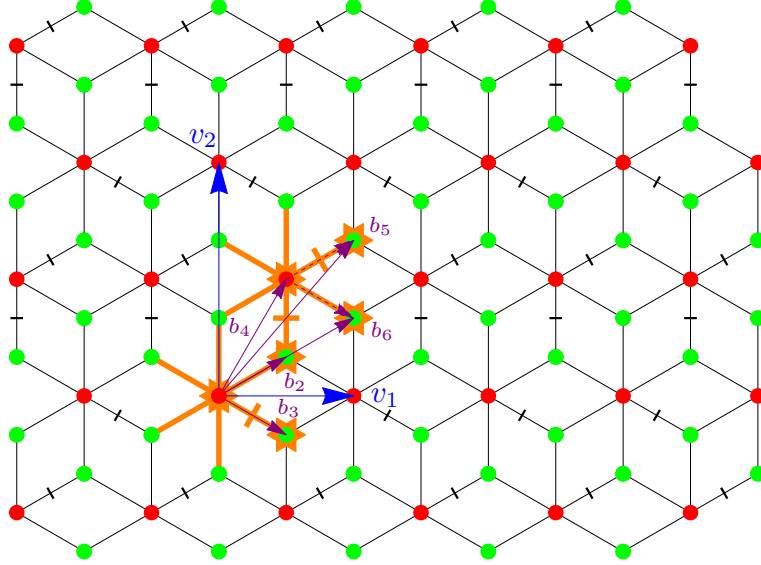


Figure 2.2: The dice lattice under an effective magnetic field using the gauge of Ref. [85]. The links and sites outlined in orange now comprise the half-flux-per-plaquette magnetic unit cell. Particles acquire a phase of π when hopping across crossed links and no phase when hopping across uncrossed links. The lattice vectors v_1 and v_2 can be chosen to be orthogonal, as in the figure, where $v_1 = (1, 0)$, $v_2 = (0, \sqrt{3})$, with a unit lattice constant. For this value of the field, the lattice can be viewed as a rectangular Bravais lattice with a 6-fold basis. The basis vectors are $b_1 = \mathbf{0}$, $b_2 = (1/2, 1/2\sqrt{3})$, $b_3 = (1/2, -1/2\sqrt{3})$, $b_4 = (1/2, \sqrt{3}/2)$, $b_5 = b_2 + b_4$, and $b_6 = b_3 + b_4$.

their corresponding eigenvalues $\lambda_{\mathbf{k}\gamma}$ as

$$\hat{H}_0 = \sum_{\mathbf{k}\gamma} \lambda_{\mathbf{k}\gamma} \hat{a}_{\mathbf{k}\gamma}^\dagger \hat{a}_{\mathbf{k}\gamma}. \quad (2.4)$$

The outcome is, as anticipated in the previous section, that the energies $\lambda_{\mathbf{k}\gamma}$ have no dispersion and remain constant throughout the Brillouin zone. There are three doubly degenerate bands with $\lambda_{\mathbf{k}\gamma} = \pm\sqrt{6}t, 0$. For the lowest and highest bands, this follows from the fact that their states can be expressed as a sum of completely localised eigenstates.

The Wannier functions, obtained from the Fourier transform of these extended Bloch wave functions, provide a particularly convenient basis for describing the single-particle states. For the highest and lowest energy bands, they are both eigenstates of the non-interacting Hamiltonian and completely

localised. For both of these bands, they span a hub site and its six surrounding rim sites. The amplitude on the hub is $1/\sqrt{2}$ and $1/\sqrt{12}$ on the rim sites. The phase of the rim site j relative to the central hub i is, in the gauge of Fig. 2.2, simply A_{ji} in the lowest band and $\pi - A_{ji}$ in the top band, i.e., either 0 or π in both cases. These features are shown in Fig. 2.3.

The existence of these localised states does not fall under any of the disorder-based localisation paradigms, such as Anderson localisation,⁶ but follows solely from destructive interference within the so-called Aharonov-Bohm cages on the lattice.¹³³ The Wannier functions corresponding to the zero-energy eigenstates, on the other hand, are only exponentially localised, so this simple explanation of flatness is not applicable for this case.

This yields an enormously degenerate ground state where the degeneracy is the number of non-magnetic unit cells N in the system. In the following chapter, the situation with many interacting bosons is considered. However, the strict single-particle localisation already allows one to infer the ground states of the full interacting problem for small fillings. Up to $N/3$ particles can be arranged on the dice lattice so that their localised states do not overlap. The degeneracy grows approximately as $\sim N^n/n!$ for $n \ll N$, where n is the number of particles, reaches a maximum for an intermediate value of n , and falls to 3 at $n = N/3$. With more particles, there is necessarily some overlap. In the regime $t \gg U_i$, one may however still consider dynamics arising solely from the lowest band and project Hamiltonian (2.1) onto it, as has been done by Möller and Cooper.⁸⁵ This yields a new effective Hamiltonian in which the single-particle localised ground states, living on a triangular lattice, now play the role of the Wannier states, and exhibit both contact and nearest-neighbour interactions. This analysis yields a Mott insulating state for $n = N$ particles and an exotic supersolid state for $n = N/2$, while for other values of n the system is predicted to separate into regions of the above phases, along with the $n = N/3$ state.

The following chapter considers mean-field theory at arbitrary values of $U_{*,\Delta}$ and t in the regime of a large average number of particles per site. Remarkably, though rooted in different geometric arguments, the mean-field ground-state degeneracy is still found to scale with the system area, as for a

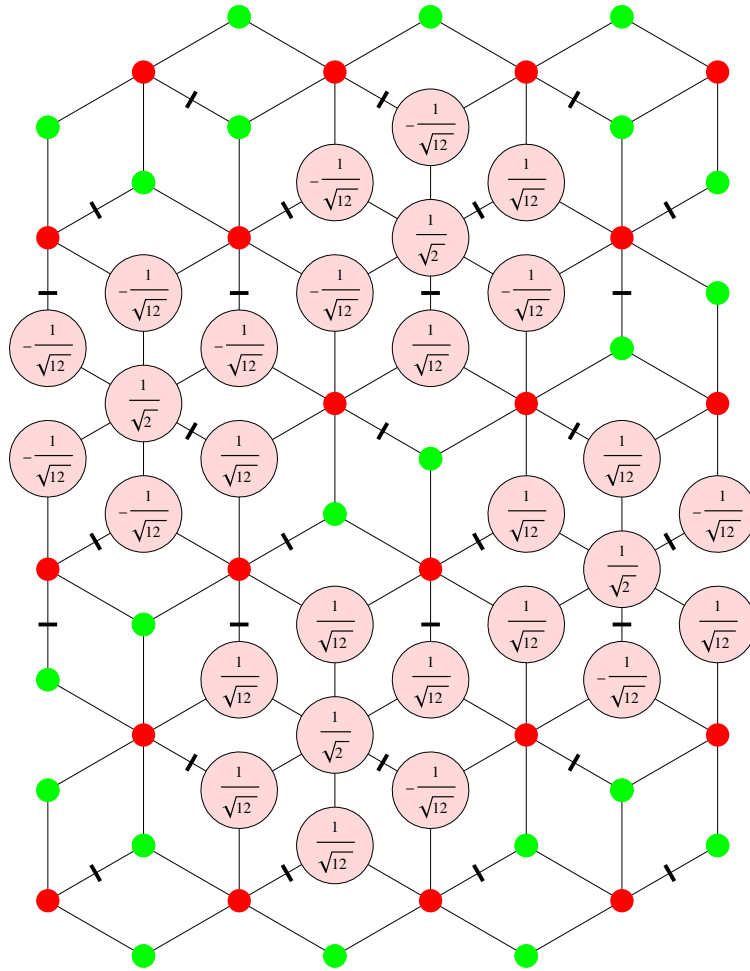


Figure 2.3: States of the lowest and highest bands of the dice lattice at half-flux. Each seven-site cluster represents a localised eigenstate whose wave function takes the circled values on the corresponding sites and is zero elsewhere. In each band, one can construct two orthogonal localised eigenstates within the same unit cell, centred on sites at the basis vectors $\mathbf{b}_1 = \mathbf{0}$ and \mathbf{b}_4 , in the notation of Fig. 2.2. The lowest band states are shown at the bottom of the figure and the highest band states at the top.

single particle.

Before moving on to the full mean-field analysis, let us briefly review previous work on the properties of tight-binding systems in the dice lattice, besides that already mentioned. The dice lattice's entirely flat spectrum has garnered attention in the context of fractional Chern insulators, for which systems with nearly flat bands are promising candidates.^{125,122,92} The other necessary condition, a non-zero Chern number, is not automatically realised in the dice lattice, but it has been found that it may be induced through the introduction of spin-orbit coupling,¹³⁵ at the cost of some dispersion. Many-body spectra at general flux have been studied in various regimes,^{23,103} and have been found, at half flux, to give rise to such phenomena as effective Dirac-Weyl fermions,¹⁴ and an exotic vortex-Peierls state²¹ close to the Mott-superfluid transition. Finally, there has been extensive work on the dice-lattice XY model by Korshunov,^{61,63,62} directly relevant to the calculations of the next chapter.

3

MEAN-FIELD PROPERTIES OF THE BOSE-HUBBARD MODEL ON THE DICE LATTICE

This chapter reintroduces interactions into Eq. (2.1) and finds the ground states at the mean-field level by solving the Gross-Pitaevskii equation. The calculation is outlined in Sec. 3.1 and the intricate mean-field ground-state manifold thus obtained is discussed in Sec. 3.2. The rest of this introductory section considers some calculational prerequisites and generalities.

As remarked in Sec. 1.1.3 of the introduction, a mean-field treatment is equivalent to assuming that the wave function can be written as a tensor product of independent coherent states for each site, allowing one to replace operators with c-numbers in expectation values, i.e.,

$$\hat{a}_i \rightarrow a_i = \sqrt{n_i} e^{i\theta_i} \quad (3.1)$$

with similar expressions for momentum-space quantities. Here n and θ are interpreted as the local density and phase variables.

Given the simple structure of the single-particle spectrum, it is reasonable to ask whether there exist any states that simultaneously minimise *both* the single-particle and the interaction part of the mean-field energy. The former is true when the state can be constructed as a linear combination of states in the lowest single-particle band and the latter when it gives rise to uniform densities n_* and n_Δ on the hub and rim sublattices, respectively. By writing the state as a linear combination of lowest-band eigenstates, one finds that such uniform densities can only be obtained when $U_\Delta/U_* = 2$. For future reference this parameter configuration will be referred to as the special point. Besides uniform densities, the state also has a simple phase picture. In particular, only three distinct magnitudes of *gauge invariant phase differences* are encountered. These are defined as

$$\Phi_{ij} = \theta_i - \theta_j - A_{ij} \tag{3.2}$$

and are indeed independent of the chosen gauge. Their values are derived in the next section.

We have conjectured that the states globally minimising the total mean field energy away from the special point retain uniform densities on both sublattices. This is motivated by the fact that the proposed states merge with what are provably the only global minima at the special point and by our failing to find a physically reasonable mechanism capable of breaking the density symmetry. In the following section, it is shown that the necessary condition of the states remaining local energy minima is satisfied. At the uniform sublattice density configurations one can furthermore follow Ref. [62] to show that the phase profiles minimising the energy are identical to those at the special point. These also coincide with the phase profiles obtained through a mean field analysis of Hamiltonian (2.1) projected into the lowest single-particle band when $nU_{*,\Delta} \ll t$,⁸⁵ where n is the average particle number per site.

3.1 MEAN FIELD CALCULATION OF SUBLATTICE DENSITIES

Carrying out the transformation in Eq. (3.1), the mean field energy of the Hamiltonian (2.1) is found to be

$$E = -2t \sum_{\langle ij \rangle} \sqrt{n_i n_j} \cos \Phi_{ij} + \frac{1}{2} \sum_i U_i n_i^2 - \mu \sum_i n_i \quad (3.3)$$

The equations of motion will be derived with the corresponding Lagrangian

$$L = \sum_i \left(-n_i \dot{\theta}_i \right) - E. \quad (3.4)$$

Expressed in terms of gauge invariant quantities, the Euler-Lagrange equations read

$$\dot{n}_i = 2t \sum_{j \in \mathcal{N}_i} \sqrt{n_i n_j} \sin \Phi_{ij} \quad (3.5)$$

$$\begin{aligned} \dot{\Phi}_{ij} &= t \sum_{i' \in \mathcal{N}_i} \sqrt{\frac{n_{i'}}{n_i}} \cos \Phi_{ii'} - t \sum_{j' \in \mathcal{N}_j} \sqrt{\frac{n_{j'}}{n_j}} \cos \Phi_{jj'} \\ &+ U_j n_j - U_i n_i. \end{aligned} \quad (3.6)$$

In this expression, \mathcal{N}_i denotes the set of all sites neighbouring site i . For the ground state we demand that the time derivatives on the LHS be zero.

The key assumption of uniform sublattice densities is now applied. Taking into account the overall geometry, the second equation yields

$$U_* n_* - U_\Delta n_\Delta = t \sqrt{\frac{n_\Delta}{n_*}} \sum_{i' \in \mathcal{N}_*} \cos \Phi_{*i'} - t \sqrt{\frac{n_*}{n_\Delta}} \sum_{j' \in \mathcal{N}_\Delta} \cos \Phi_{\Delta j'}. \quad (3.7)$$

As remarked before, the phase profiles occurring at the special point still solve the equations. To describe these, denote the three distinct phase difference magnitudes comprising them by $\Phi_l > \Phi_m > \Phi_s > 0$ (l, m, s for large, medium, small). Since the factor $\sqrt{n_i n_j}$ equals $\sqrt{n_\Delta n_*}$ for any neighbouring i and j , one can rewrite equation (3.5), the continuity equation, as $\sin \Phi_l = \sin \Phi_m + \sin \Phi_s$. The half-flux condition that the sum of phase differences around

a plaquette equal $\pm\pi$ imposes the restrictions $2\Phi_s + 2\Phi_l = \pi$ and $-\Phi_s + 2\Phi_m + \Phi_l = \pi$. This system of equations yields $\Phi_s \approx 9.74^\circ$, $\Phi_m \approx 54.74^\circ$ and $\Phi_l \approx 80.26^\circ$, along with the useful identity

$$e^{i\Phi_s} + e^{i\Phi_m} + e^{-i\Phi_l} = \sqrt{3}. \quad (3.8)$$

This phase configuration is identical to the one obtained by Korshunov for the dice lattice XY model,⁶¹ i.e., a mean-field model assuming *uniform* densities. This is so because the form of Eq. (3.5) is the same in both cases, as it does not depend on the local interaction terms of the Hamiltonian. Furthermore, the factor $\sqrt{n_i n_j}$ in Eq. (3.5) is constant for all pairs of neighbouring sites in both cases. It can thus be factored out when considering the ground state. In Ref. [61], this is due to the author's explicitly taking a uniform density across all sites, while in the present case it is due to the respectively uniform densities over the rim and hub sublattices comprising the bipartite dice lattice.

One can in fact easily determine the sublattice density values. Taking the features of the phase configuration and Eq. (3.8) into account, Eq. (3.7) simplifies to

$$U_* n_* - U_\Delta n_\Delta = \sqrt{3}t \frac{2n_\Delta - n_*}{\sqrt{n_\Delta n_*}}. \quad (3.9)$$

Given the two interaction strengths, this equation can be solved to determine the ratio of densities on the hub and rim sites, n_*/n_Δ . Note that at the special point, where $U_\Delta = 2U_*$, one has the simplest case $n_* = 2n_\Delta$, as expected from the fact that, at this parameter configuration, the interaction term of Eq. (3.3) is separately minimised. Finally, with this solution the chemical potential is found to be

$$\mu = U_* n_* - 2t \sqrt{\frac{3n_\Delta}{n_*}} = U_\Delta n_\Delta - t \sqrt{\frac{3n_*}{n_\Delta}} \quad (3.10)$$

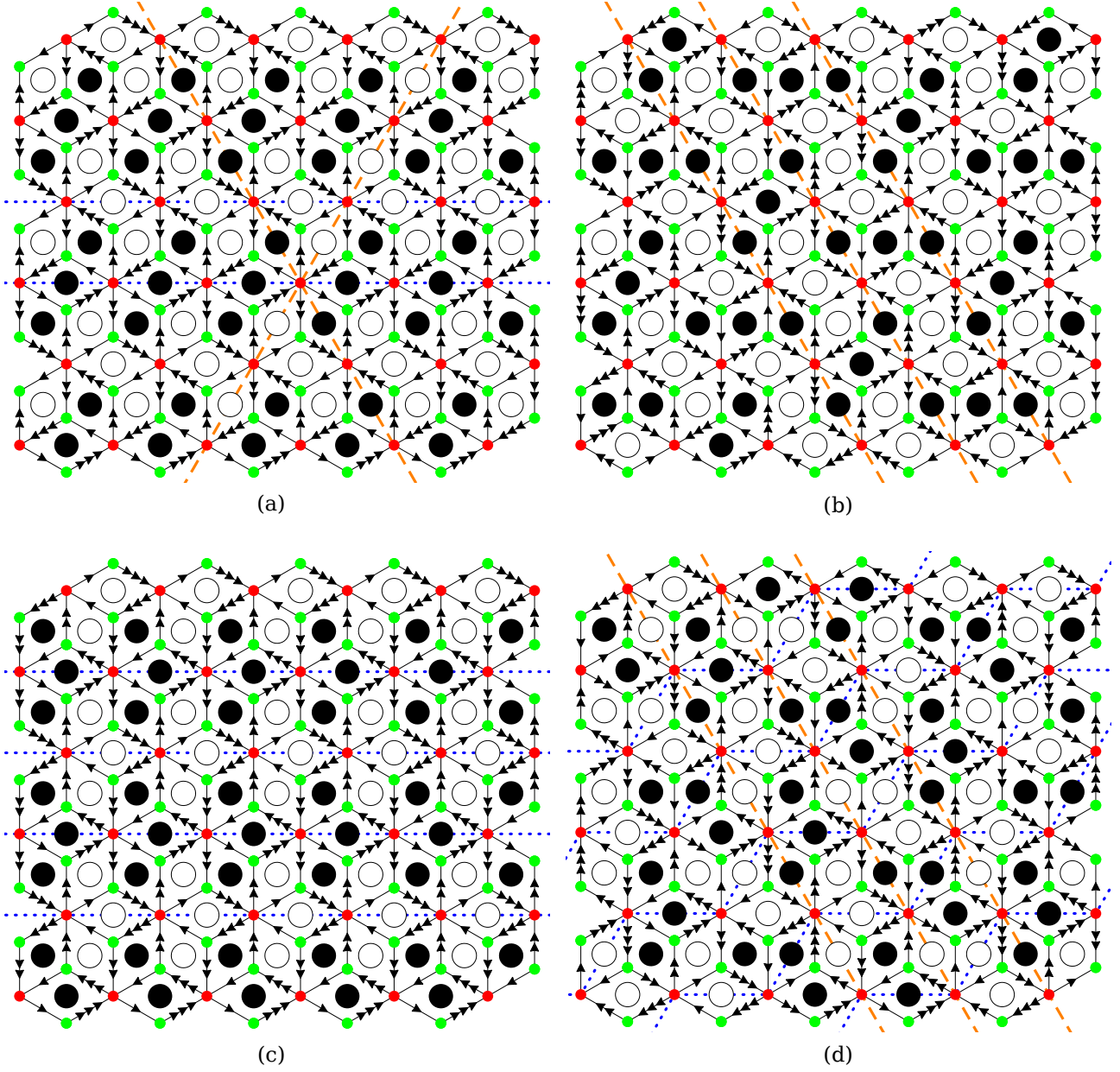


Figure 3.1: The four small unit-cell periodic mean field ground states. The single, double and triple arrows represent gauge invariant phase differences Φ_s , Φ_m and Φ_l across links, respectively, and the black (white) disks represent positive (negative) plaquette vorticities. The dashed and dotted lines signify locations of possible domain wall insertions (figure (a)) or domain walls themselves (all other figures). The dashed orange lines represent type-I domain walls while the blue dotted lines represent type-II domain walls.

3.2 MEAN FIELD PERIODIC GROUND STATES

One can assign to each plaquette a vorticity of either π or $-\pi$. For a rough qualitative picture, note that neutral superfluid vortices are known to have an approximately logarithmic interaction, attractive for vortices with opposite signs of vorticities and repulsive for those of like sign. Through a qualitative comparison of this vortex lattice with the two-dimensional Coulomb gas, which also exhibits logarithmic interactions, one can argue that the most energetically favourable configuration will have each vortex surrounded by as many neighbours of the opposite vorticity as possible. In a lattice the vortices are pinned to the sites of the dual lattice, which in this case is the Kagome lattice. The geometric frustration of the Kagome lattice prevents the possibility of a purely local prescription for the distribution of vortices minimising the energy. The vortex configurations of mean field ground states are demonstrably composed of *chains* of like-vortices of length three.*

Perhaps the simplest such state is shown in Fig. 3.1(a). All other applicable states with only the three gauge invariant phase differences introduced above may be obtained by rearranging the phase differences along a variety of infinite sequences of plaquettes in which every pair of neighbouring plaquettes shares just a single vertex. One can think of this process as the insertion of two types of *zero-energy domain walls* into state (a). The domain walls that can be inserted parallel to the dashed lines in Fig. 3.1(a) will be referred to as type I domain walls[†] and the ones that can be inserted parallel to the dotted lines as type II domain walls. Inserting a type I domain wall splits the lattice into two regions with orientations of the vortex triads not parallel to the wall differing by 60° . This is illustrated in the first two panels of Fig. 3.2. A type II domain wall bends the triads it crosses and establishes a mirror symmetry between both of its sides. Type II domain walls also bend by 60° whenever they cross a type I domain wall.[‡]

*With the exception of triangular clusters of like-vortices around rim sites which could be regarded as cyclic chains of length 3. These cannot occur.

[†]One can in fact only insert one of the type I domain walls shown and all walls parallel to it, but no two type I domain walls can be inserted at an angle.

[‡]Further details of the phase permutations comprising each type of domain wall and figures of single domain walls inserted into state (a) are given in Ref. [61], as well as in

The unit cell of vortex state (a) contains six lattice sites. It is twelvefold degenerate under the following geometric transformations that preserve the Hamiltonian, but not the state: translation by \mathbf{b}_4 , in the notation of Fig. 2.1, contributing a factor of 2 to the geometric degeneracy, the combination of time (arrow) reversal and spatial inversion, contributing another factor of 2, and $\pm 2\pi/3$ rotations about any site, contributing the final factor of 3. By inserting all possible type II domain walls into (a) we obtain another twelvefold degenerate state with six sites per unit cell, shown in Fig. 3.1(c), not related to state (a) by geometric symmetries. Inserting all possible type I domain walls into state (a), as is shown in Fig. 3.2, similarly yields the state shown in Fig. 3.1(b) with twelve sites per unit cell. Further inserting all possible type II domain walls into (b) yields the state shown in Fig. 3.1(d), also containing twelve sites per unit cell. States (b) and (d) have a fourfold translational degeneracy, so their total geometric degeneracy is 24-fold. Taking geometric multiplicities into account this yields a total of 72 small unit cell mean field periodic states, or SMPS's. All other uniform sublattice periodic mean field ground states can be obtained by gluing together the unit cells of the above four classes of SMPS's.⁶²

It should be noted that, given two asymptotically domain-wall-free regions, such that, for instance, the vortex lattice is one of the 72 SMPS's on the far left and a distinct SMPS on the far right, it is not in general possible to consistently interpolate between the two through a sequence of SMPS regions, i.e. state (a-d)-like regions, glued by zero-energy domain walls. This implies either the possibility of massive, i.e., energetically costly, domain walls and point defects, or global instabilities of such asymptotic configurations. The actual state of affairs is still an open question.

The geometric degeneracies discussed above originate from true symmetries of the Hamiltonian and will, as such, not be lifted by fluctuation effects, as discussed in Sec. 1.5.2 of the introduction. The degeneracy between states (a-d) of Fig. 3.1 is, however, accidental. Determining the effects of fluctuations on these, as well as more general states, is the subject of the next chapter.

appendix A.

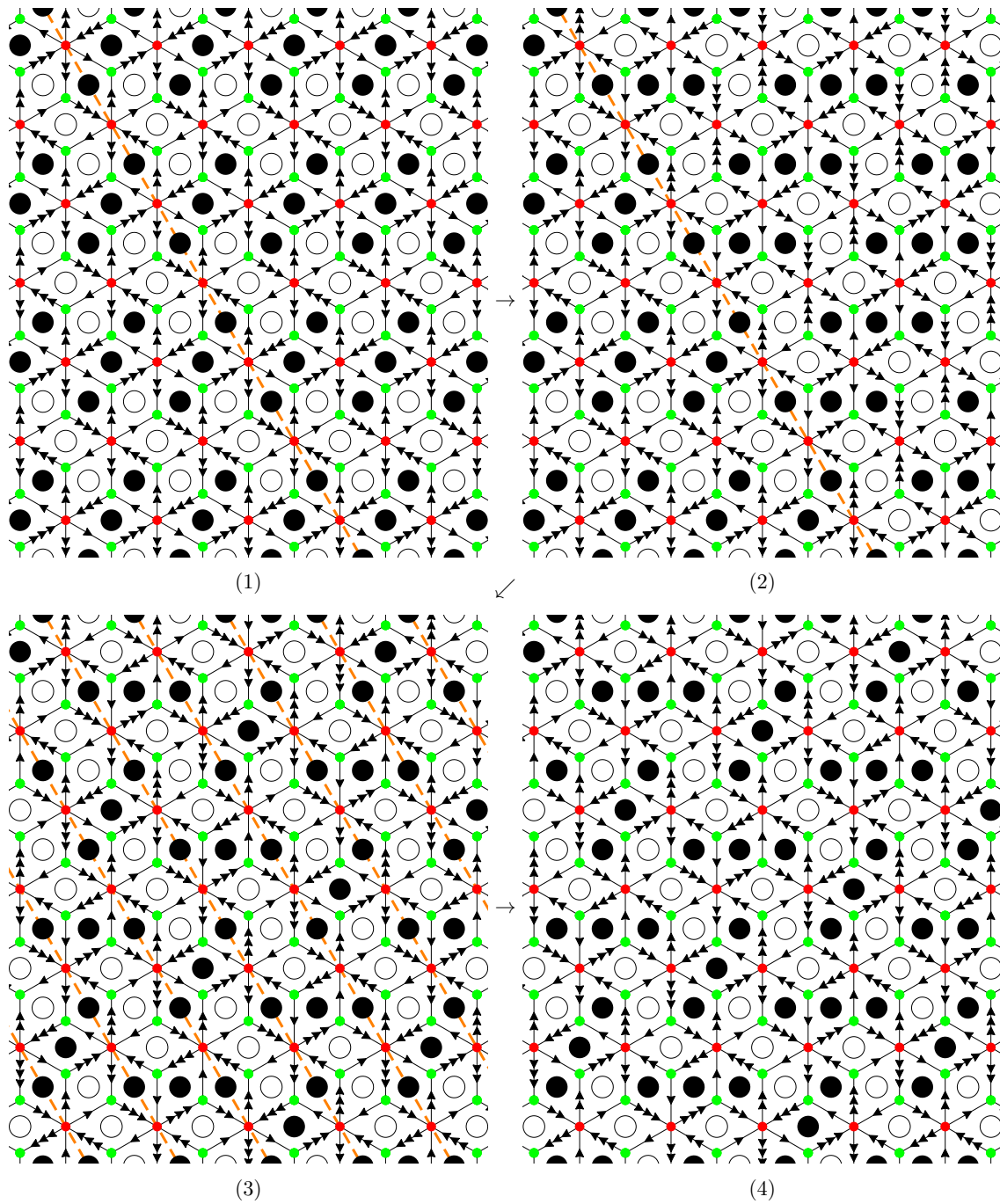


Figure 3.2: Schematic representation of the insertion of a single type-I domain wall into state (a), panels (1) → (2), and of all such parallel domain walls, panels (2) → (3), yielding state (b) in panel (4).

4

EXCITATION SPECTRUM AND ORDER BY DISORDER IN THE BOSE-HUBBARD MODEL ON THE DICE LATTICE

The rich mean-field ground-state manifold of the previous chapter displays a massive accidental degeneracy, parametrised by the set of possible type-I and type-II domain wall insertions, which scales with the system area. The present chapter investigates whether any of them is preferred due to Order by Disorder.

In quantitative terms, the state whose fluctuations yield the lowest Helmholtz free energy $F = -\frac{1}{\beta} \ln Z$, where $Z = \text{Tr}(e^{-\beta\hat{H}})$ is the partition function and $\beta = (k_B T)^{-1}$, is selected. At the level of Bogoliubov theory, the excitation spectrum is described by independent harmonic oscillators, yielding the

partition function

$$Z = \sum_{n_i} e^{-\beta \hbar \sum_j \omega_j (n_j + \frac{1}{2})} = \prod_j e^{-\frac{\beta E_j}{2}} \frac{1}{1 - e^{-\beta E_j}}. \quad (4.1)$$

and from this, the free energy

$$F = \frac{1}{2} \sum_j E_j + \beta^{-1} \sum_j \ln(1 - e^{-\beta E_j}). \quad (4.2)$$

The first term corresponds to the zero-point quantum contribution to the free energy and the second term to the contribution of thermal fluctuations. In the present case, the index j in Eq. (4.2) is a label for momentum and band index.

The next section outlines the derivation of the excitation spectrum, which is then applied to the central question of degeneracy resolution in Sec. 4.2. State (b) of Fig. 3.1 is found to be definitively selected at both zero and finite temperature. In Sec. 4.3 the depletion is evaluated, confirming the validity of the Bogoliubov approximation for an experimentally feasible range of parameters.

The analysis described is carried out within a restricted set of the mean-field ground-state manifold. Sec. 4.4 discusses preliminary results, indicating that, at least at zero temperature, mean-field domain walls display fluctuation-mediated interactions. Type-I domain walls exhibit attractive interactions, while type-II domain walls repel each other. The selected state should hence be that with the largest number of type-I domain walls, which is indeed what is found.

4.1 COLLECTIVE EXCITATION SPECTRUM

We now derive the collective excitation spectrum of Hamiltonian (2.1) at the level of Bogoliubov theory. This involves expressing the annihilation operators as $\hat{a}_i = a_i + \delta \hat{a}_i$, where a_i are the mean-field c-values from Eq. (3.1). The full Hamiltonian is expanded in $\delta \hat{a}_i$, keeping terms up to quadratic order.

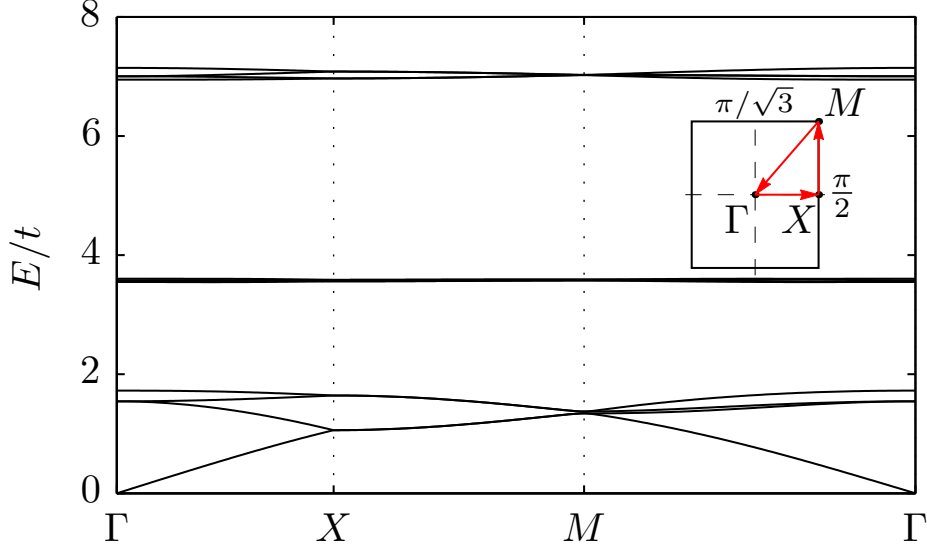


Figure 4.1: The twelve Bogoliubov modes about ground state (b) from Fig. 3.1 at $U_* = U_\Delta$, $t = 2U_*$ and $n_* = 6$. As the interaction strengths $U_{*,\Delta}$ decrease, the bands flatten and the gaps between them approach $\sqrt{6}t$. At $U_{*,\Delta} = 0$, the dispersionless degenerate single-particle spectrum is recovered.

The first order term always vanishes as the expansion is about a minimum (the very definition of a mean-field state) while the zeroth order term gives the degenerate mean-field energies. Thus the focus is on the second order contribution.

Substituting $\hat{a}_i = a_i + \delta\hat{a}_i$ into Eq. (2.1), and using the chemical potential given in Eq. (3.10), one finds the quadratic Hamiltonian

$$\begin{aligned} \delta\hat{H} = & -t \sum_{\langle ij \rangle} (e^{iA_{ij}} \delta\hat{a}_i^\dagger \delta\hat{a}_j + \text{H.c.}) + \sum_i (U_i n_i + G_i) \delta\hat{a}_i^\dagger \delta\hat{a}_i \\ & + \sum_i \frac{U_i}{2} \left(a_i^* a_i^* \delta\hat{a}_i \delta\hat{a}_i + a_i a_i \delta\hat{a}_i^\dagger \delta\hat{a}_i^\dagger \right) \end{aligned} \quad (4.3)$$

where $n_i = |a_i|^2$, $G_* = 2t\sqrt{\frac{3n_\Delta}{n_*}}$, and $G_\Delta = t\sqrt{\frac{3n_*}{n_\Delta}}$. It greatly simplifies the analysis to perform the gauge transformation $\delta\hat{a}_i \rightarrow e^{i\theta_i} \delta\hat{a}_i$ at this stage.

This results in the following *gauge invariant* Bogoliubov Hamiltonian:

$$\begin{aligned} \hat{H}_B = & -t \sum_{\langle ij \rangle} \left(e^{-i\Phi_{ij}} \delta \hat{a}_i^\dagger \delta \hat{a}_j + \text{H.c.} \right) \\ & + \sum_i \left[(U_i n_i + G_i) \delta \hat{a}_i^\dagger \delta \hat{a}_i + \frac{U_i n_i}{2} \left(\delta \hat{a}_i \delta \hat{a}_i + \delta \hat{a}_i^\dagger \delta \hat{a}_i^\dagger \right) \right]. \end{aligned} \quad (4.4)$$

The gauge invariant phase differences Φ_{ij} here are precisely those introduced in Sec. 3.1.

One can again define momentum space operators $\delta \hat{a}_{\mathbf{k}\gamma} = \sqrt{\frac{2}{N}} \sum_n \delta \hat{a}_{n\gamma} e^{-i\mathbf{k} \cdot \mathbf{R}_n}$ with $\gamma = 1, \dots, M$, where M is the number of sites per unit cell. This will be either 6 or 12 for states (a-d) from Fig. 3.1. By expressing the Hamiltonian in terms of these operators, one obtains, up to a constant energy shift (equal for all mean-field states), the Hamiltonian in the form

$$\hat{H}_B = \sum_{\mathbf{k}} \delta \hat{\alpha}_{\mathbf{k}}^\dagger H_B(\mathbf{k}) \delta \hat{\alpha}_{\mathbf{k}} \quad (4.5)$$

where $\delta \hat{\alpha}_{\mathbf{k}} = \left[\delta \hat{\alpha}_{\mathbf{k}}^T, \delta \hat{\alpha}_{-\mathbf{k}}^\dagger \right]^T$ with $\delta \hat{\alpha}_{\mathbf{k}} = [\delta \hat{a}_{\mathbf{k}1}, \dots, \delta \hat{a}_{\mathbf{k}M}]^T$, and

$$H_B(\mathbf{k}) = \left[\begin{array}{c|c} C_{\mathbf{k}} & D \\ \hline D & C_{-\mathbf{k}}^T \end{array} \right]. \quad (4.6)$$

Here D is a diagonal matrix with $U_* n_*$ ($U_\Delta n_\Delta$) entries for hub (rim) sites. To concisely describe $C_{\mathbf{k}}$, denote the part of \hat{H}_B appearing on the first line of Eq. (4.4) by \hat{H}_0 and let $\hat{H}_0 \equiv \sum_{\mathbf{k}} \delta \hat{\alpha}_{\mathbf{k}}^\dagger H_0(\mathbf{k}) \delta \hat{\alpha}_{\mathbf{k}}$. This is completely analogous to Eq. (2.3) of the single-particle spectrum calculation, with the matrix $H_0(\mathbf{k})$ adapted to the current gauge and unit-cell size. Then, $C_{\mathbf{k}} = H_0(\mathbf{k}) + G + D$ where G is finally a diagonal matrix containing the values G_* and G_Δ for hub and rim sites, respectively.

The creation and annihilation operators of the quasiparticle eigenstates of this quadratic Hamiltonian will, in general, be a sum of both particle annihilation and creation operators. As outlined in Sec. 1.5.1, they may be obtained by diagonalising each of $\eta H_B(\mathbf{k})$ as \mathbf{k} ranges over the Brillouin zone. The

following notation is adopted for the eigenvalue equations, also known as the Bogoliubov de-Gennes (BdG) equations:

$$\eta H_B(\mathbf{k})\phi_{\mathbf{k}\gamma\pm} = \pm E_{\mathbf{k}\gamma}\phi_{\mathbf{k}\gamma\pm} \quad (4.7)$$

where $E_{\mathbf{k}\gamma} \geq 0$ and $\eta = \begin{pmatrix} \mathbb{1}_{M \times M} & 0 \\ 0 & -\mathbb{1}_{M \times M} \end{pmatrix}$. The energies of the Bogoliubov modes are given by $E_{\mathbf{k}\gamma}$ where γ labels the band index. The quasiparticle operators which diagonalise \hat{H}_B are determined from the BdG eigenvectors as $\hat{\alpha}_{\mathbf{k}\gamma} = \phi_{\mathbf{k}\gamma+}^\dagger \eta \delta \hat{\alpha}_{\mathbf{k}}$. Note that normalising the $\phi_{\mathbf{k}\gamma\pm}$ such that $\phi_{\mathbf{k}\gamma\pm}^\dagger \eta \phi_{\mathbf{k}\gamma\pm} = \pm 1$ and arranging them into a matrix as $[\phi_{\mathbf{k}1+}, \dots, \phi_{\mathbf{k}M+}, \phi_{\mathbf{k}1-}, \dots, \phi_{\mathbf{k}M-}]$ yields T^{-1} , the inverse of the T matrix (1.35) of the introductory section 1.5.1, as appropriate for the Hamiltonian $\delta \hat{\alpha}_{\mathbf{k}}^\dagger H_B(\mathbf{k}) \delta \hat{\alpha}_{\mathbf{k}}$.

The excitation spectrum for a typical parameter set is shown in Fig. 4.1. It is seen that the interactions give dispersion to the excitation spectrum, which is completely flat at the single-particle level. The excitations about each vortex configuration yield a gapless Goldstone mode due to the broken U(1) superfluid phase. These have the dispersion $\sim \hbar \sqrt{(c_1 k_1)^2 + (c_2 k_2)^2}$ where $k_{1,2} = \mathbf{k} \cdot \mathbf{v}_{1,2}$ and $c_{1,2}$ is the speed of sound along the $\mathbf{v}_{1,2}$ lattice vectors shown in Fig. 2.2.

4.2 COMPUTATION OF DEGENERACY LIFTING

Having the excitation spectra at hand, the resulting degeneracy lifting can now be discussed. We have calculated the thermal and quantum contributions to the free energy in Eq. (4.2) at a range of values of the input parameters U_*/t , U_*/U_Δ , n_* and, for the thermal part, T/t . We have restricted ourselves to the four small unit-cell mean-field states shown in Fig. 3.1. One of these is intuitively expected to be selected on grounds of their high symmetry. A more physically motivated argument can be made in terms of domain wall interactions, discussed in Sec. 4.4. For each parameter configuration, the band energies were obtained by numerically diagonalising $H_B(\mathbf{k})$ from Eq. (4.6) at a uniformly spaced grid of momenta in the Brillouin zone. The grid was chosen so as to optimise convergence properties following a prescrip-

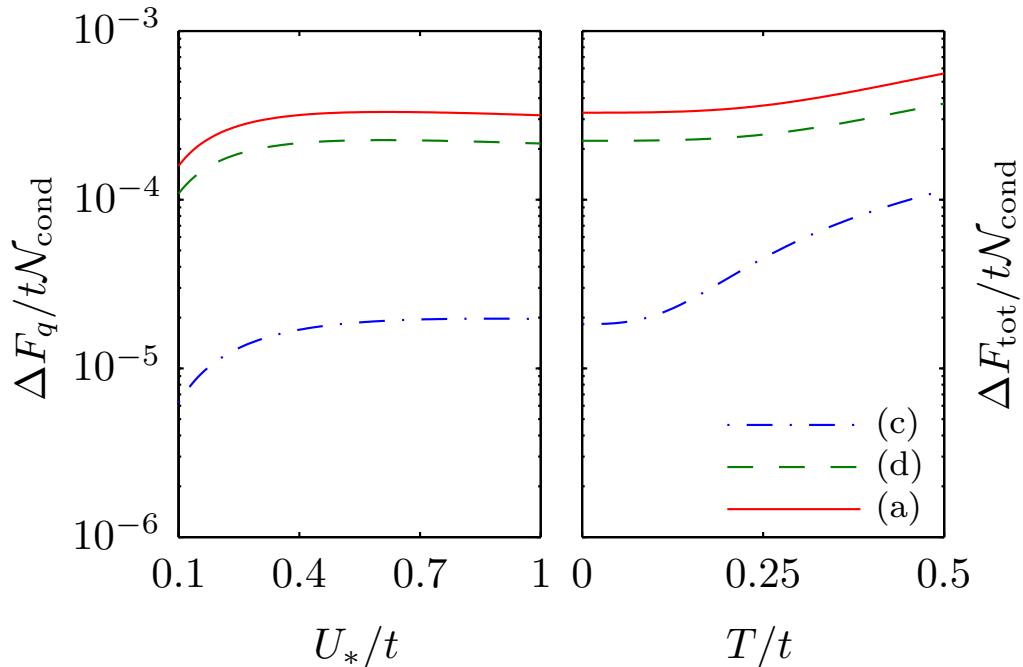


Figure 4.2: Left: Quantum free energy difference per condensed particle with respect to state (b) from Fig. 3.1 with $n_* = 6, U_* = U_\Delta$. Right: Total free energy difference at the same n_* and U_*/U_Δ , for finite temperature and $U_*/t = 0.5$.

tion by Monkhorst and Pack.⁸⁶ Convergence as a function of the grid spacing was checked for each parameter set.

Results for a range of parameters are shown in Fig. 4.2. We have plotted the differences of free energies of states (a), (c) and (d) with respect to state (b), $\Delta F_{a,c,d} = F_{a,c,d} - F_b$ using the labelling of Fig. 3.1. As seen in the left-hand side of the figure, the resulting free energy difference is always positive and so state (b) has the lowest free energy. Thermal fluctuations further enhance the degeneracy lifting as shown in the right-hand side of the figure.

In addition to determining the ground state, state (c) is observed to be universally the highest in free energy. States (a) and (d) are typically ordered as in Fig. 4.2 but cases were found in which their free energy curves cross. The geometric mean of the sound speeds along the two lattice vectors $\sqrt{c_1 c_2}$ is always lowest for (b) and highest for (c), which explains the ordering of the thermal contribution to the free energy at low temperatures.

4.3 THE CONDENSATE DEPLETION

Having established that state (b) has the lowest overall free energy, its stability must now be addressed. For Bogoliubov theory to be valid, the number of particles excited out of the condensate has to be small compared to the number of condensed particles, lest neglecting higher order $\delta\hat{a}_i$ terms become unjustified. The depletion, like the free energy, can be separated into a quantum and a thermal contribution, denoted by \mathcal{N}_q and \mathcal{N}_{th} , respectively. For the above analysis to be correct we must have $\mathcal{N}_{dep} = \mathcal{N}_q + \mathcal{N}_{th} \ll \mathcal{N}_{cond}$. From the solution of the Bogoliubov-de Gennes equation (4.7) the depletion can be expressed as

$$\mathcal{N}_q = \frac{1}{2} \sum_{\mathbf{k}\gamma} \phi_{\mathbf{k}\gamma+}^\dagger (\mathbb{1} - \eta) \phi_{\mathbf{k}\gamma+} \quad (4.8)$$

$$\mathcal{N}_{th} = \sum_{\mathbf{k}\gamma} \phi_{\mathbf{k}\gamma+}^\dagger \phi_{\mathbf{k}\gamma+} f_{BE}(E_{\mathbf{k}\gamma}) \quad (4.9)$$

where $f_{BE}(x) = (e^{\beta x} - 1)^{-1}$ is the Bose Einstein distribution function. Note that the above is again equivalent to Eq. (1.43) of the introduction, in terms of the appropriately normalised eigenvectors themselves rather than the canonical transformation matrix T .

While the quantum depletion converges, the thermal depletion integral has a logarithmic infrared divergence due to the Goldstone mode. Such divergences are typical for two-dimensional systems.⁸¹ Finite size effects will remove this divergence and can be crudely taken into account by using a small-momentum cut-off of $2\pi/L$ where L^2 is the system size. Consequently, the thermal depletion will scale as $\ln(L)$ for sufficiently large L .

Figure 4.3 shows the quantum and thermal contributions to the total depletion at experimentally feasible parameters. Quite interestingly, the total depletion exhibits a non-monotonic behaviour as a function of the Hubbard interaction parameters. In typical condensed systems, depletion increases monotonically as a function of the interactions.⁹⁸ A similar minimum was found for all parameter ranges tested. This can be attributed to the flatness of the non-interacting band structure. That is, as interactions are decreased,

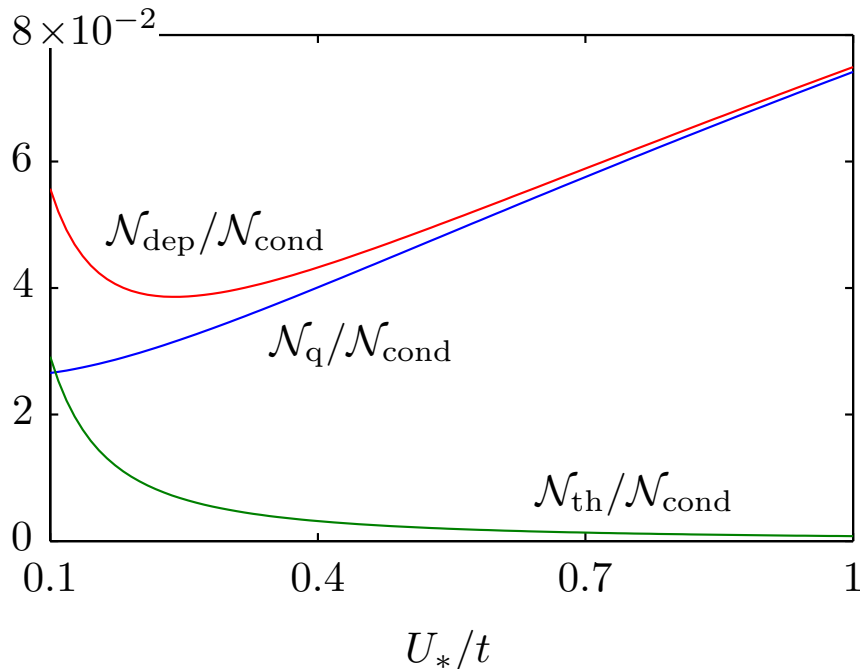


Figure 4.3: The quantum, thermal and total depletion per condensed particle for a system consisting of 20×20 unit cells at $n_* = 6$, $U_* = U_\Delta$, and $T = t/10$.

the Bogoliubov band structure (cf. Fig. 4.1) becomes flatter and thermal excitations are created more easily. When $U_* = U_\Delta = 0$ the Bogoliubov spectrum reduces to completely flat bands and the thermal depletion diverges. For the chosen parameters in this figure the depletion is always less than 10%. The depletion can be further decreased by choosing larger average density per site.

4.4 DOMAIN WALL INTERACTIONS

An assumption that still needs to be justified is that the mean-field state ultimately chosen by fluctuations is one of the highly symmetric configurations shown in Fig. 3.1. One of the most physically intuitive pictures that one might hope for is that of fluctuation-mediated domain-wall interactions, or equivalently a force between them. To that end, we have numerically calculated the spectra for a variety of configurations of domain walls of the same

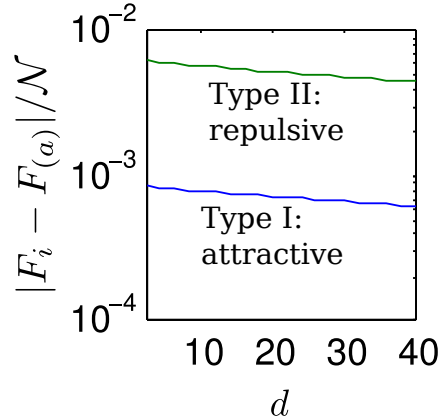


Figure 4.4: Zero-point energy differences with respect to state (a) per particle for large unit-cell periodic states with two domain walls of the same type per unit cell. These are negative for type-I domain walls and positive for type-II domain walls. They are plotted against the domain-wall separation d . The energy differences are measured in arbitrary but consistent units.

type inserted into state (a). To be able to reuse techniques of the previous calculations, the configuration was taken to be periodic. This requires an even number of domain walls per unit cell so that the edge state-(a) regions have the same orientation and may be identified. We have analysed the situation with two domain walls per unit cell, with a varying separation of d sites between them, with d much smaller than the periodicity. The idea behind this choice is that all interactions but that between the pairs of nearest domain walls may be neglected. Note that, should the interaction picture turn out to have merit, the effective interaction's magnitude should fall off quicker than the inverse power of d , as the free-energy density of states (b) and (c) could otherwise diverge.

Only very preliminary results were obtained, but they seem to support a picture in which type-I walls interact attractively and type-II walls repel each other. This is shown, with separations up to $d = 40$, in Fig. 4.4. Besides indicating why state (b), with the highest concentration of attractive type-I domain walls, is energetically preferred, this picture also explains the fact that state (c), with the highest concentration of repulsive type-II domain walls, is universally highest in energy.

Quite obviously, domain wall interactions could be subjected to an abundance of further quantitative investigations. The energetic contributions of interactions with next-nearest and further neighbours have not been adequately evaluated, and it is hard to discern anything but the sign of the interactions and that they do fall off with increasing separation from Fig. 4.4. Furthermore, studying the free energy at more general configurations and attempting to fit the results to the functional form of the interactions might be beneficial. In particular, smaller unit cells would greatly reduce the required computational time. With these technical issues out of the way, the behaviour at finite temperature and interactions between distinct-type domain walls would also be interesting to study.

This concludes the study of fluctuation effects in the deep superfluid regime of the Bose-Hubbard model on the dice lattice. The following chapters are dedicated to the behaviour of spinor condensates, particularly tightly confined ones, and the primary analytical tool used to study them, the rotor mapping. The results developed in them are ultimately applied to another instance of the Order-by-Disorder phenomenon in Chapter 10, along with the consistent parallel selection mechanism in the underlying microscopic Hamiltonian.

5

MEAN-FIELD PHASES OF SPINOR CONDENSATES

Cold quantum gases with internal spin degrees of freedom have been a topic of considerable interest since long before the successful condensation experiments of the mid-nineties. The reason for this is twofold: spinor condensates allow even greater versatility in the synthetisation of model Hamiltonians. Among other applications, they allow for the engineering of such novel phenomena as topological defects via spin textures.⁵⁶ The other reason are practical necessities, since species with zero-spin hyperfine states are an exception rather than the rule among stable alkali isotopes. The effective scalarity of condensates in the early days of experiments on Bose-Einstein condensates was a consequence of magnetic trapping methods which caused the gases to be spin-polarised, reducing their interactions to essentially those of a scalar condensate. With the advent of largely scalar optical traps, understanding the properties of spinor condensates became crucial for the development of new experimental protocols, in addition to studying them in their own right. A considerable amount of theory and experiment on the topic has amassed since then. For reviews see Refs. [119, 57, 130] and most recently Ref. [118].

A point in which spinor condensates differ particularly sharply from their scalar counterparts is that the former can form so called *fragmented* condensates.^{89,48} In the Penrose-Onsager definition of Bose-Einstein condensation for interacting systems,⁹⁶ briefly introduced in Sec. 1.1.3, such states exhibit more than one macroscopic eigenvalue of the reduced density matrix. This typically implies the presence of a zero Bogoliubov mode exchanging particles between the condensed components, driving up the depletion and thus invalidating use of Bogoliubov theory in its conventional form. Alternative means of calculating excitation spectra have to be found and in the present case it is employing one from a family of rotor mappings, introduced in Chapters 7 and 8.

The focus of the current work is on spin-2 condensates. To date the only experimental realisation of such a system are condensates of ^{87}Rb atoms in the upper hyperfine multiplet.* With increasing spin magnitude, the number of components of the order parameter steadily increases, as does the number of scattering lengths required to characterise interactions, so the study of higher-spin condensates takes on increasing levels of complexity. Hence, the most well studied cases are those of spin-1 and spin-2 condensates, for which we have a good analytical understanding of ground state structure and dynamics in both the continuum and the tightly confined setting, including many magnetic effects.^{129,93,90,67,59}

Several open questions on spin-1 and spin-2 condensates still remain. One of the goals of the second part of this thesis is elucidating the ground state structure of tightly confined spin-2 condensates, in the presence of a quadratic Zeeman field, at the full quantum level, rather than that of a mean-field analysis. It is nevertheless instructive to review the mean-field results, as these are valid in the vast majority of the range of physical parameters that enter the relevant Hamiltonian for intermediate or large particle numbers.¹²⁸ Finally, this will allow the exact quantum results to be contrasted with their mean-field counterparts and elucidate where mean-field theory fails. To that

* ^{23}Na atoms, whose $F = 1$ hyperfine multiplet physics has been thoroughly explored experimentally, unfortunately undergo hyperfine relaxation collisions at a significant rate. A number of other alkali and heavier radioactive isotope condensates awaiting experimental realisation might also provide access to $F = 2$ physics in the future.¹¹⁸

end, this chapter first introduces the general form of cold spinor Hamiltonians in Sec. 5.1 and moves on to discuss their mean-field phase diagrams, with respect to scattering lengths and the quadratic Zeeman fields, in Sec. 5.2. Besides the ground states' order parameters, these are also presented in terms of their Majorana representations, convenient graphical representations in which the states' symmetries are also manifest,^{79,10} whose generalities are the subject of Sec. 5.2.1.

In a particular region of the spin-2 phase diagram, called the *nematic* region, the mean field states possess an accidental continuous degeneracy. In the continuum, an order-by-disorder analysis may once again be carried out.^{127,116} This is seen to divide the nematic region into two subregions where two distinct higher-symmetry members of the degenerate mean-field ground-state manifold are selected, with a first order transition between them. On the other hand, an exact treatment at zero magnetic field suggests that the ground state is a condensate of singlet pairs across the entire nematic region, without any distinguishing features within the nematic subregions demarcated through Order by Disorder.^{60,131} To be able to further contrast it with later exact results, the order-by-disorder calculation of Refs. [127, 116] is outlined in Sec. 5.3.

5.1 COLD SPINOR GAS HAMILTONIANS

We begin by describing the Hamiltonian governing the underlying physical system, a collection of cold interacting spinful bosons in a scalar trapping potential[†] and a magnetic field, manifesting itself through a linear and a quadratic Zeeman term. The full first-quantised Hamiltonian is

$$\begin{aligned}\hat{H}_{\text{1st}} &= \sum_i^N \hat{H}_i^1 + \sum_{i<j} \hat{V}_{i,j}^2 \quad \text{with} \\ \hat{H}_i^1 &= \frac{1}{2m} \hat{p}_i^2 + V(\hat{\mathbf{r}}_i) + p\hat{F}_i^z + q(\hat{F}_i^z)^2.\end{aligned}\tag{5.1}$$

[†]By a scalar potential we mean one that couples to all magnetic sublevels approximately equally, such as the potential of an optical trap and unlike that of a magnetic trap.

Here N is the total particle number, m the atomic mass, V the external potential and \hat{p}_i , $\hat{\mathbf{r}}_i$ and \hat{F}_i^z the i -th particle's momentum, position and z -component of spin operators, respectively. p and q are the linear and quadratic Zeeman coefficients, respectively, as introduced in Sec. 1.4. The inter-particle potential $\hat{V}_{i,j}$ between the i -th and j -th particles is short-range and dominated by the s-wave component, i.e., it depends predominantly on the distance between the atoms. Its spatial part is well approximated by a delta function, multiplied by different prefactors, proportional to the scattering lengths, for each value of the interacting pair's total spin. Following the more detailed exposition of Sec. 1.3, \hat{V}_{ij}^2 of Eq. (5.1) may be identified with $\hat{V}^{(F)}$ of Eq. (1.21), that is,

$$\hat{V}^{(F)} = \delta^{(3)}(\hat{\mathbf{r}} - \hat{\mathbf{r}}') \left(c_0^{(F)} \hat{\mathbb{1}} + c_1^{(F)} \hat{\mathbf{F}} \cdot \hat{\mathbf{F}}' + (2F + 1) c_2^{(F)} \hat{\mathcal{P}}_0 \right), \quad (5.2)$$

upon identifying $\hat{\mathbf{r}}, \hat{\mathbf{F}} \rightarrow \hat{\mathbf{r}}_i, \hat{\mathbf{F}}_i$ and $\hat{\mathbf{r}}', \hat{\mathbf{F}}' \rightarrow \hat{\mathbf{r}}_j, \hat{\mathbf{F}}_j$. The projection operator $\hat{\mathcal{P}}_0$ onto the singlet subspace also refers to the i -th and j -th particles. The $c_i^{(F)}$ constants are expressed in terms of scattering lengths in Eq. (1.23). Hereafter, the species' spin will be considered fixed at either $F = 1$ or 2 and the superscripted (F) labels will be omitted.

Second-quantising Hamiltonian (5.1) above yields:

$$\hat{H}_{\text{2nd}} = \int d^3\mathbf{r} \left(\hat{\mathcal{H}}_0(\mathbf{r}) + \hat{\mathcal{H}}_q(\mathbf{r}) + \hat{\mathcal{H}}_I(\mathbf{r}) \right) \quad (5.3a)$$

$$\hat{\mathcal{H}}_0 = \hat{\psi}_\alpha^\dagger \left(-\frac{1}{2m} \nabla^2 + V(\mathbf{r}) \right) \hat{\psi}_\alpha \quad (5.3b)$$

$$\hat{\mathcal{H}}_q = p \hat{\mathcal{F}}^z + q \hat{\mathcal{Z}} \quad \text{with} \quad (5.3c)$$

$$\hat{\mathcal{F}}^i = \hat{\psi}_\alpha^\dagger F_{\alpha\beta}^i \hat{\psi}_\beta \quad \text{and} \quad \hat{\mathcal{Z}} = \hat{\psi}_\alpha^\dagger (F^z)_{\alpha\beta}^2 \hat{\psi}_\beta$$

$$\hat{\mathcal{H}}_I = : \frac{c_0}{2} \hat{n}^2 + \frac{c_1}{2} \hat{\mathcal{F}}^2 : + \frac{c_2}{2} \hat{\mathcal{A}}^\dagger \hat{\mathcal{A}} \quad \text{with} \quad (5.3d)$$

$$\hat{n} = \hat{\psi}_\alpha^\dagger \hat{\psi}_\alpha \quad \text{and} \quad \hat{\mathcal{A}} = \sum_{\alpha=-2}^2 (-1)^\alpha \hat{\psi}_\alpha \hat{\psi}_{-\alpha}$$

where $\hat{\psi}_\alpha(\mathbf{r})$ are the annihilation operators for bosons in the $m = \alpha$ magnetic sublevel at \mathbf{r} . $\hat{\mathcal{F}}^i(\mathbf{r})$ stands for the i -th component of the total spin density

operator whereas F^i is the i -th spin- F matrix. The positional dependence of creation/annihilation operators and densities has been suppressed above for brevity. The colon delimiters represent normal ordering. $\hat{\mathcal{H}}_0$ and $\hat{\mathcal{H}}_q$ are the second-quantised forms of single-particle operators from the second line of Eq. (5.1). $\hat{\mathcal{H}}_0$ originates from the potential and kinetic terms, and $\hat{\mathcal{H}}_q$ from the linear and quadratic Zeeman terms. $\hat{\mathcal{H}}_I$ is the second-quantised form of the two-particle interaction in Eq. (5.2). It is also worth noting that the operator $\hat{\mathcal{A}}$ may be loosely interpreted as an annihilation operator for a spin-singlet pair of bosons^{60,131} and that it is absent for spin-1 as $c_2^{(1)} = 0$.

For alkali atoms, except caesium,¹¹⁵ one may consider F_z , the eigenvalue of $\hat{F}^z \equiv \int d\mathbf{r} \hat{\mathcal{F}}^z$, as a conserved quantity as the spin relaxation time is longer than the typical trap lifetime.^{16,39} Mathematically, this manifests itself through \hat{F}^z commuting with the total Hamiltonian \hat{H} , $[\hat{H}, \hat{F}^z] = 0$, which also implies one can simultaneously diagonalise \hat{H} and \hat{F}^z . We will often restrict ourselves to a particular \hat{F}^z -eigenspace, particularly the experimentally relevant null space. When this is the case, the energetic contribution of the linear Zeeman term is constant and may thus be removed from the analysis.

We will mostly be concerned with two extremal potential profiles - either that of the continuum, i.e., $V(\mathbf{r}) = 0$, or of a very narrow trap, e.g. $V(\mathbf{r}) = \frac{1}{2}m\omega\mathbf{r}^2$ with $\hbar\omega$ far exceeding typical spin-excitation energies so that any spatial deviations from the ground state profile are effectively energetically prohibited. This is called the Single Mode Approximation, or SMA, and makes the spin dynamics effectively zero-dimensional.⁶⁷ Equivalently, these conditions can be phrased by saying that the spin coherence length should be much larger than the trap size and the density coherence length. For large particle numbers one may study both limits by mean-field methods, but the SMA offers several means of going beyond mean field as well. The single mode approximation is discussed in more detail in Chapter 6, and is further utilised from Chapter 8 onwards, while the focus of the present chapter is on the continuum.

To find the mean-field states, the annihilation operators of Eq. (5.3) are

replaced by *c*-numbers, i.e., $\hat{\psi}_\alpha \rightarrow \psi_\alpha$, a chemical potential is introduced, and the resulting expression is minimised with respect to ψ_α , in accordance with the mean-field calculations in sections 1.1.2 and 3.1. For the continuum, the potential is identically zero and the ground state is translationally invariant for repulsive interactions. This makes $\hat{\mathcal{H}}_0$ of Eq. (5.3b) identically zero, and the spatial integral in Eq. (5.3a) may be replaced by a multiplication with the system volume. Furthermore, the uniform density n factors out of $\hat{\mathcal{H}}_q$ of Eq. (5.3c), and its square n^2 factors out of the interaction Hamiltonian $\hat{\mathcal{H}}_I$ of Eq. (5.3d). This reduces the problem to minimising the resulting quantity \tilde{E} with respect to a single $(2F + 1)$ -component complex vector of unit norm $\boldsymbol{\chi}$, with the parameters $c_i n$, p , and q . \tilde{E} is given by:

$$\tilde{E} = \frac{c_1 n}{2} (\boldsymbol{\chi}_\alpha^* \mathbf{F}_{\alpha\beta} \boldsymbol{\chi}_\beta)^2 + \frac{c_2 n}{2} |\boldsymbol{\chi}^T T \boldsymbol{\chi}|^2 + q \boldsymbol{\chi}^\dagger (F^z)^2 \boldsymbol{\chi} + p \boldsymbol{\chi}^\dagger F^z \boldsymbol{\chi} \quad (5.4)$$

where T is a diagonal matrix with $T_{\alpha\alpha} = (-1)^\alpha$. Given the long spin-relaxation times, a conserved value of $F_z \equiv \langle \hat{F}^z \rangle$ may be taken into account through a Lagrange multiplier. In the following, however, we consider mean-field ground states for unconstrained F_z .

5.2 MEAN-FIELD PHASE DIAGRAMS

In this section, the mean-field phase diagrams of the spin-1 and spin-2 Bose gas in the continuum are presented. The geometric scheme used to classify the states is introduced first.

5.2.1 MAJORANA REPRESENTATION

A spin- $\frac{1}{2}$ particle can be represented by a point on the Bloch sphere. This direction can intuitively be understood as the direction of the spin expectation value. In the special case of spin- $\frac{1}{2}$, it so happens that this expectation value fully characterises the state. For larger magnitudes of spin one needs additional information, as can be seen from the fact that one can have a non-zero state with a zero spin expectation value, such as the \hat{F}^z zero eigenvector for a spin-1 particle. Fortunately, as first shown by Ettore Majorana,⁷⁹ one

need not leave the comfortable domain of the Bloch sphere to describe this information. Rather, any spin- F state may be described by $2F$ points on the Bloch sphere. In addition to extending tools known to most physicists in a simplistic manner, the utility of the representation also lies in the fact that the symmetries of the resulting polygon correspond to symmetries of the physical state.

The present elementary exposition of the Majorana-representation formalism follows Barnett et al.,¹⁰ who have applied the representation to classifying the zero- q phases of spin-2 condensates in the continuum. For a given spin- F state $|\phi\rangle = \sum_{\alpha=-F}^F A_{\alpha} |\alpha\rangle$, where $|\alpha\rangle$ are eigenstates of \hat{F}_z such that $\hat{F}_z |\alpha\rangle = \alpha |\alpha\rangle$, we wish to find the set of *fully polarised* states $|f\rangle$, orthogonal to $|\phi\rangle$. The fully polarised states are parametrised by the Bloch sphere, and the fully polarised state corresponding to the direction (θ, φ) , in standard spherical coordinates, is defined so that $\hat{\mathbf{F}} \cdot \mathbf{n}_{(\theta, \varphi)} |f(\theta, \varphi)\rangle = F |f(\theta, \varphi)\rangle$, where $\mathbf{n}_{(\theta, \varphi)}$ is the unit vector pointing in that direction. Letting ζ encode θ and φ as $\zeta = e^{i\varphi} \tan(\theta/2)$, one may conveniently express the unnormalised fully polarised state $|\zeta\rangle$ as

$$|\zeta\rangle = \sum_{\alpha=0}^{2F} \binom{2F}{\alpha}^{\frac{1}{2}} \zeta^{\alpha} |F - \alpha\rangle. \quad (5.5)$$

The orthogonality condition $\langle\phi|\zeta\rangle = 0$ then amounts to a polynomial equation in ζ , whose $2F$ complex roots determine the points on the Bloch sphere.

5.2.2 PHASE DIAGRAMS

We are now in a position to describe the mean-field phase diagrams. Most results of this section were first worked out in Refs. [93, 47]. At zero magnetic field, mean-field states may break the full rotational symmetry of the Hamiltonian, which results in a degenerate set of candidate ground states, related by the broken rotations. In the presence of a magnetic field in the z direction, the rotation symmetry about the z axis may be broken. In either case, some of the representative states yield particularly simple order parameters and it is in terms of these that the results are presented.

SPIN-1

For spin-1, the possible stationary states with respect to Eq. (5.4), along with their commonly used names, are as follows:

$$\Psi_f = (1, 0, 0)^T \text{ or } (0, 0, 1)^T \quad \text{ferromagnetic} \quad (5.6)$$

$$\Psi_{1p} = (0, 1, 0)^T \quad \text{longitudinal polar} \quad (5.7)$$

$$\Psi_{tp} = (1, 0, 1)^T / \sqrt{2} \quad \text{transverse polar} \quad (5.8)$$

An interesting property of all of the above is that they are *inert*, meaning that they remain energy extrema when the parameters of the Hamiltonian are varied. Their existence is guaranteed due to a group-theoretic theorem by Michel.⁸² There is an additional non-inert stationary state for $|q| < 2|c_1 n|$, where n is the particle number density and $c_1 = \frac{4\pi}{3m}(a_2 - a_0)$, as per Eq. (1.23). Namely

$$\Psi_{ba} = \left(\frac{\sin \theta}{\sqrt{2}}, \cos \theta, \frac{\sin \theta}{\sqrt{2}} \right)^T \quad \text{broken axisymmetric} \quad (5.9)$$

with $\sin \theta = \sqrt{1/2 + q/(4nc_1)}$.

The mean-field ground states' order parameters and Majorana representations are shown in their respective regions of the $q - c_1 n$ phase diagram at zero linear Zeeman field in Fig. 5.1.

SPIN-2

For spin-2, three stationary states may be identified already at $q = 0$. Their order parameters and common names are as follows:

$$\Psi_f = (1, 0, 0, 0, 0)^T \quad \text{ferromagnetic} \quad (5.10)$$

$$\Psi_t = \left(\sqrt{\frac{1}{3}}, 0, 0, \sqrt{\frac{2}{3}}, 0 \right)^T \quad \text{tetrahedral} \quad (5.11)$$

$$\Psi_n(\eta) = \left(\frac{\sin \eta}{\sqrt{2}}, 0, \cos \eta, 0, \frac{\sin \eta}{\sqrt{2}} \right)^T \quad \text{nematic} \quad (5.12)$$

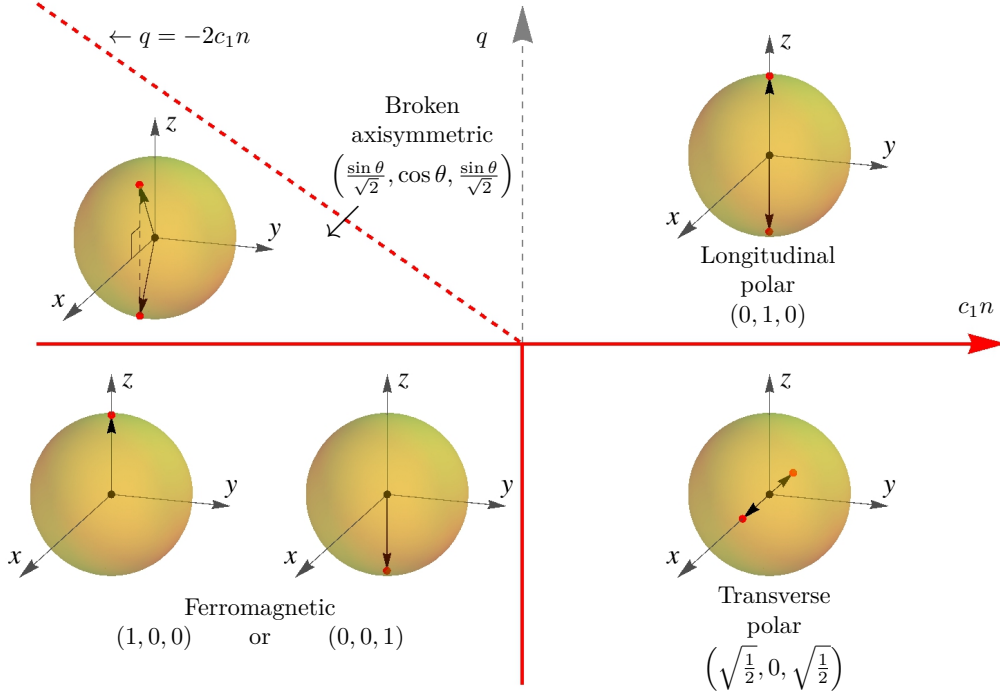


Figure 5.1: The ground-state phase diagram for spin-1 condensates with respect to the quadratic Zeeman coefficient q and $c_1 n$ at zero linear Zeeman field p , presented in terms of the ground states' order parameters and Majorana representations. n is the particle density and $c_1 = \frac{4\pi}{3m}(a_2 - a_0)$ with a_F the relevant s -wave scattering lengths.

The nematic states $\Psi_n(\eta)$ represent a degenerate family with respect to the continuous variable η . This is an *accidental* degeneracy, which is indeed lifted through Order by Disorder, as demonstrated in the next section. Two particular members of the family arise as preferred through both Order by Disorder at $q = 0$ and plain mean-field calculations at $q \neq 0$:

$$\Psi_{\text{un}} = \Psi_n(0) = (0, 0, 1, 0, 0)^T \quad \text{uniaxial nematic} \quad (5.13)$$

$$\Psi_{\text{bn}} = \Psi_n\left(\frac{\pi}{2}\right) = \left(\sqrt{\frac{1}{2}}, 0, 0, 0, \sqrt{\frac{1}{2}}\right)^T \quad \text{biaxial nematic} \quad (5.14)$$

As shown in the next section, the uni(bi)-axial state is selected for $c_1 > 0$ ($c_1 < 0$). The $q = 0$ phases are shown in Fig. 5.2. The general nematic state, or rather the evolution of its Majorana representation with η , is shown in

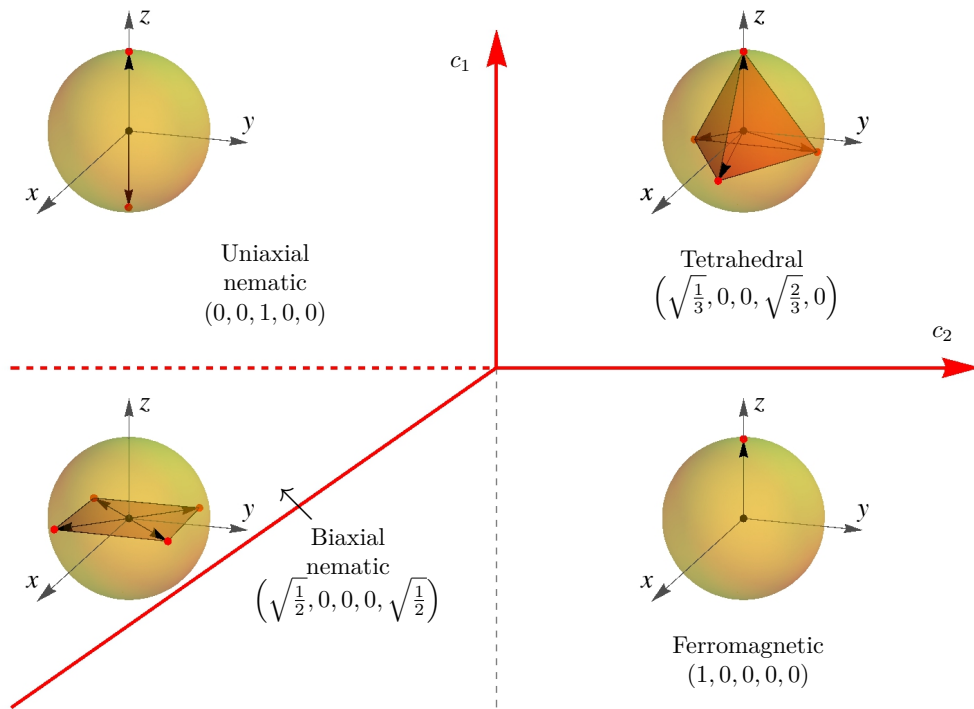


Figure 5.2: The ground-state phase diagram for spin-2 condensates with respect to the interaction constants c_1 and c_2 at zero external magnetic field, presented in terms of the ground states' order parameters and Majorana representations. A mean field analysis yields the degenerate family of nematic states, shown in Fig. 5.3, as possible ground states in the entire nematic region $c_2 < \min(0, 4c_1)$, but an order-by-disorder calculation, summarised in Sec. 5.3, shows that the true continuum ground states arise as shown, giving rise to the dashed phase boundary between the two nematic regions.

Fig. 5.3. It can be seen that all nematic states have rectangular representations and in general possess only reflection symmetry about planes spanned by any pair of coordinate axes. The uni/bi-axial states however possess more symmetry - the uniaxial state retains full $SO(2)$ rotational symmetry about the z axis and the biaxial state retains symmetry with respect to $\pi/2$ -rotations about the same axis.

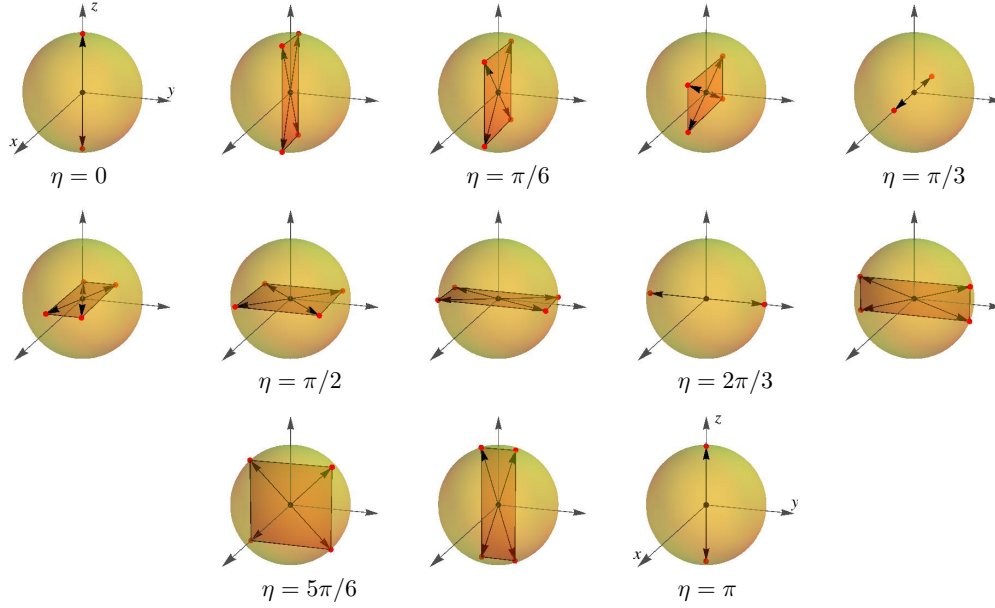


Figure 5.3: The evolution of the Majorana representation of a nematic state, as given by Eq. (5.14), with η , paramtrising the continuous degeneracy.

At $q \neq 0$ three additional non-inert stationary states appear:^{128,106}

$$\begin{aligned}
 \Psi_m &= (\cos \theta_m, 0, 0, \sin \theta_m, 0)^T & \cos \theta_m &= \sqrt{\frac{1}{3} - \frac{q}{3c_1 n}} & \text{mixed} \\
 \Psi_c &= \left(\frac{\sin \theta_c}{\sqrt{2}}, 0, -i \cos \theta_c, 0, \frac{\sin \theta_c}{\sqrt{2}} \right)^T & \cos \theta_c &= \sqrt{\frac{1}{2} + \frac{q}{c_2 n}} & \text{cyclic} \\
 \Psi_{ba} &= (a, b, c, b, a)^T & a, b, c & & \text{broken} \\
 & & \text{numerically} & & \text{axisymmetric} \\
 & & \text{determined} & & \\
 & & & & (5.15)
 \end{aligned}$$

The phase diagrams at negative and positive q are shown in Figs. 5.4 and 5.5, respectively. Note that Ψ_c and Ψ_m both become equivalent to a spatial rotation of the tetrahedral state Ψ_t at $q = 0$. The evolution of their Majorana representations with respect to q is shown in Figs. 5.6 and 5.7.

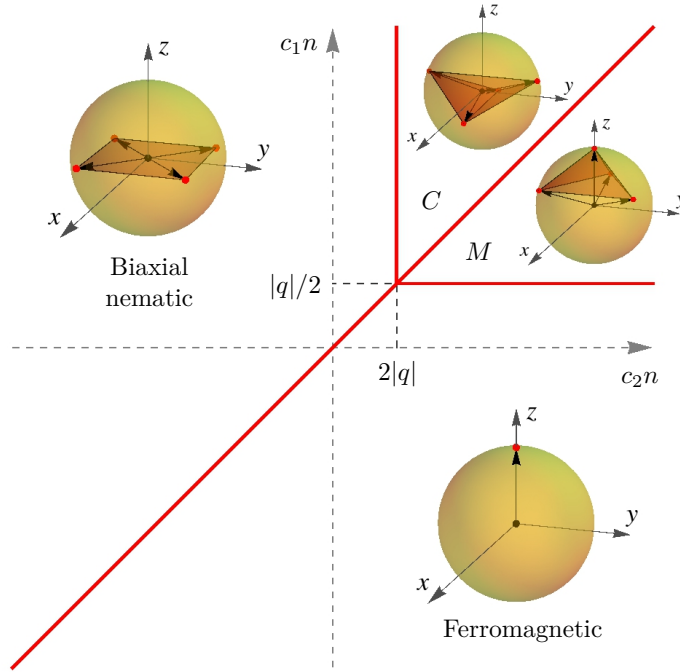


Figure 5.4: Mean-field spin-2 phase diagram at negative q . M and C denote the mixed and cyclic phases, respectively. The order parameters for these are given in Eq. (5.15).

5.3 NEMATIC ORDER BY DISORDER

The η -parametrised accidentally degenerate family of spin-2 mean-field ground states $\Psi_n(\eta)$, defined in Eq. (5.12), exhibits the phenomenon of Order by Disorder. This section summarises the main steps of the relevant calculation, following the detailed treatment of Ref. [127].

At any value of η , a Bogoliubov Hamiltonian may be obtained by considering small deviations from the homogeneous $\Psi_n(\eta)$ state, i.e., inserting $\hat{\psi}_\alpha = \sqrt{n_0}\Psi_{n\alpha}(\eta) + \delta\hat{\psi}_\alpha$, where n_0 is the condensate particle density, into Eq. (5.3a) and keeping terms up to second order in $\delta\hat{\psi}_\alpha$. Following steps akin to those of Sec. 4.1 for the dice lattice, one obtains a five-band spectrum. Since there is no unit cell in this problem, or rather, an arbitrarily small one could be chosen in the continuum, the Brillouin zone is unbounded.

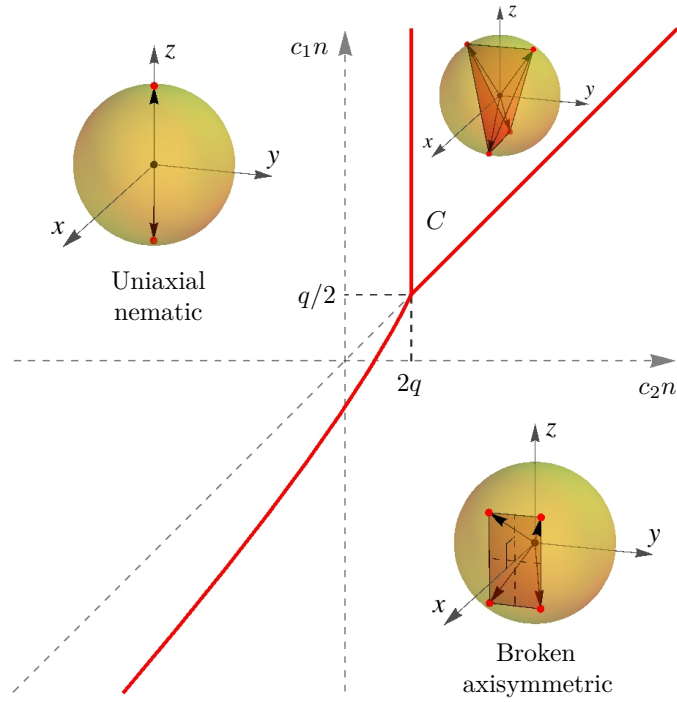


Figure 5.5: Mean-field spin-2 phase diagram at positive q . C denotes the mixed phase, as in Fig. 5.4. For the broken axisymmetric phase, qualitative features of its numerically determined Majorana representation and nematic-phase boundary are shown, summarised after Refs. [128, 118].

The band energies can be expressed in terms of a simple analytical expression:

$$E_j(\mathbf{k}) = k \sqrt{v_j^2 + \frac{k^2}{4m^2}} \quad (5.16)$$

where $j = 1, \dots, 5$ is the band index, v_j are the long-wavelength sound velocities for each band, and m is the species' atomic mass. The v_j can be expressed as:

$$v_j^2 = \frac{n_0}{m} \left(|c_2| + 4c_1 \sin^2 \left(\eta + \frac{2\pi}{3} j \right) \right) \quad \text{for } j = 1, 2, 3 \quad (5.17)$$

$$v_4^2 = \frac{n_0}{m} (c_0 - |c_2|) \quad (5.18)$$

$$v_5^2 = \frac{n_0}{m} |c_2| \quad (5.19)$$

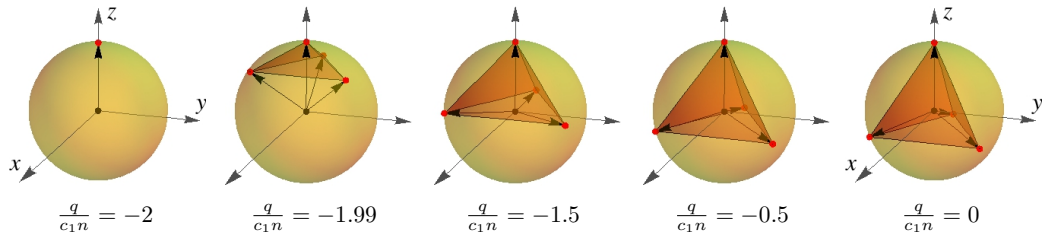


Figure 5.6: Evolution of the non-inert mixed phase's Majorana representation with q .

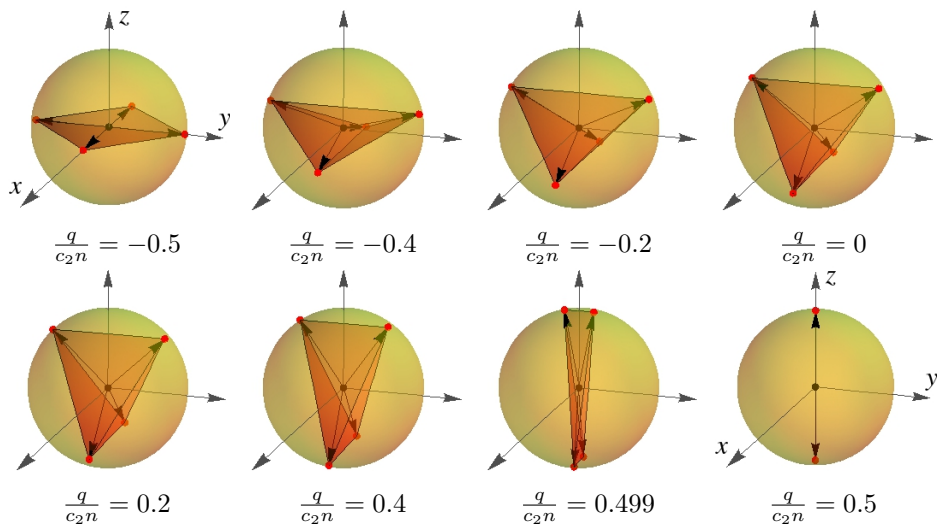


Figure 5.7: Evolution of the non-inert cyclic phase's Majorana representation with q .

Only the first three velocities explicitly depend on η so it is these whose Bogoliubov contributions one needs to consider. While the zero-point energy density integral over the unbounded Brillouin zone formally diverges, one may regularise it by subtracting the energy density of the limiting nematic state at $c_1 = c_2 = 0$ and any η . The difference is given by

$$\Delta\varepsilon \equiv \frac{\Delta E}{V} = \frac{8}{15\pi^2 m} (mn_0)^{\frac{5}{2}} \sum_{j=1}^3 \left(|c_2| + 4c_1 \sin^2 \left(\eta + \frac{2\pi}{3} j \right) \right)^{\frac{5}{2}}. \quad (5.20)$$

This is shown as a function of η , with its average value on the interval $[0, \pi]$ subtracted, for two different values of c_1 in Fig. 5.8. For $c_1 < 0$, the lowest energy is attained at $\eta = (2n + 1)\pi/6$; $n \in \mathbb{Z}$, the square biaxial states, and for $c_1 > 0$ at $\eta = n\pi/3$, the uniaxial states. In the absence of a magnetic field the energy lifting is insensitive to orientation, but an arbitrarily small positive (negative) quadratic Zeeman field q applied in the z direction will make the local energy minima closest to $\eta_0 = 0$ ($\eta_0 = \pi/2$) preferred. When q is of the same sign as c_1 the global minimum is unique. For small q of the opposite sign, there are two degenerate global minima, symmetric about η_0 , that draw closer together with increasing $|q|$, eventually reaching η_0 and coalescing at a $c_{1,2}$ -dependent critical value of $|q|$.¹²⁷

Thermal fluctuations further enhance the degeneracy lifting. As an illustration, in the regime with $\max(mv_i^2) \ll k_B T \ll k_B T_c$, where T_c is the condensate transition temperature,[†] the leading η -dependent term in T of the thermal free-energy density difference with respect to the limiting $c_1 = c_2 = 0$ state is

$$\frac{\Delta F_{\text{th}}}{V} = -\frac{2k_B T}{3\pi} (mn_0)^{\frac{3}{2}} \sum_{j=1}^3 \left(|c_2| + 4c_1 \sin^2 \left(\eta + \frac{2\pi}{3} j \right) \right)^{\frac{3}{2}}. \quad (5.21)$$

This contribution favours the same mean-field state as the zero-point energy density of Eq. (5.20).¹²⁷

[†]In a uniform condensate of particles with mass m at particle-number density n , the transition temperature is approximately $T_c \approx 3.3 \frac{n^{2/3}}{mk_B}$.⁹⁸

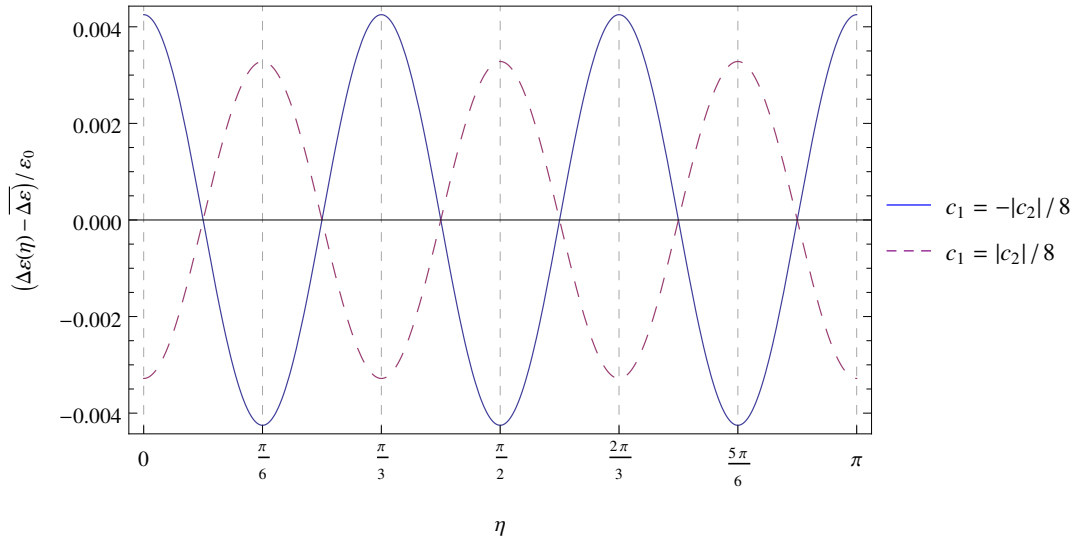


Figure 5.8: The Bogoliubov zero-point energy density obtained when expanding about the mean-field nematic state $\Psi_n(\eta)$, with its average value on the interval $[0, \pi]$ subtracted. Energy densities are measured in units of $\varepsilon_0 = \frac{8m^{3/2}}{15\pi^2}(n_0|c_2|)^{5/2}$.

6

THE SINGLE MODE APPROXIMATION

Besides the continuum, another extremal regime in which spinor condensates, and cold atomic systems with more general interactions, become particularly amenable to analytical techniques is that of tight confinement. To be concrete, this is usually taken to mean a potential profile whose walls are so steep that the energetic cost incurred by spatial fluctuations is far above the Boltzmann energy kT . This makes the system effectively zero-dimensional, as all of its particles occupy the lowest spatial mode. By dint of this last formulation, the approximation is most commonly referred to as the single mode approximation, or SMA.

Technically, the approximation implies that we can write the bosonic annihilation operators $\hat{\psi}_\alpha(\mathbf{r})$, appearing in Eqs. (5.3) of the previous chapter, as $\hat{\psi}_\alpha(\mathbf{r}) = \phi_0(\mathbf{r})\hat{a}_\alpha$ where $\phi_0(\mathbf{r})$ is the unit-normalised lowest spatial mode of the system and \hat{a}_α the annihilation operator for a boson in this lowest spatial mode with magnetic number $m = \alpha$. Substituting the $\hat{\psi}_\alpha$ as above and

integrating out the spatial components of the Hamiltonian Eq. (5.3) yields

$$\hat{H}_{\text{SMA}} = \frac{g_1}{2N} \hat{\mathbf{F}}^2 + \frac{g_2}{2N} \hat{A}^\dagger \hat{A} + q \hat{Z}. \quad (6.1)$$

plus constants. Here $g_i = n_0 c_i$ where $n_0 = N \int d\mathbf{r} |\phi_0(\mathbf{r})|^4$ and c_i are defined in Eq. (1.23). Recall again that $c_2^{(1)} = 0$ so that the $\hat{A}^\dagger \hat{A}$ term is not present for spin-1 species. The upper-case operators are obtained from their calligraphic density counterparts in Eq. (5.3) by letting $\hat{\psi}_\alpha \rightarrow \hat{a}_\alpha$, e.g., $\hat{F}^i = \hat{a}_\alpha^\dagger F_{\alpha\beta}^i \hat{a}_\beta = \hat{\mathbf{a}}^\dagger F^i \hat{\mathbf{a}}$ where F^i still represents the i -th spin matrix.

The Hamiltonians (5.3) and (6.1) evidently conserve total particle number \hat{N} and, as noted above, we consider it fixed at N . This allows one to drop terms arising from the spatial integrals of the scalar operators $\hat{\mathcal{H}}_0$ and $:\hat{n}^2:$ of Eq. (5.3), and to simplify the contribution of $\int :\hat{\mathcal{F}}^2: \propto :\hat{\mathbf{F}}^2: = \hat{\mathbf{F}}^2 - F(F+1)\hat{N}$ to $\hat{\mathbf{F}}^2$. Hamiltonian (6.1) further commutes with \hat{F}^z and can thus be simultaneously diagonalised. As in the continuum, we will often focus on fixed \hat{F}^z eigenspaces, particularly the null space, allowing us to drop the linear Zeeman term, as has already been done in Eq. (6.1).

The SMA can be combined with mean-field techniques. Like in the continuum, the ground-state order parameter factors into a spatial part and a spinor part. In the continuum this happens since the energy is obviously minimised for a spatially uniform configuration, while in the SMA it is since the spatial mode has been explicitly factored out at the very beginning. The spinor order parameters at fixed signs and ratios of $c_i n_0$ and the magnetic parameters p and q are the same in both cases. Additionally, when stable, the Bogoliubov spectrum in the SMA consists of continuum modes at zero quasimomentum, minus the density mode. As such, the combination of the two approximations serves to simplify calculations, when applicable, but yields no new information. We hence focus on exact many-body results derived within the SMA. Some of these will be expanded upon in the rotor treatment of later chapters.

6.1 EXACT SPIN-1 EIGENSTATES AND SPECTRA AT $q = 0$

This section follows the original treatment by Koashi and Ueda.⁶⁰ They demonstrated that the set of (unnormalised) states

$$|N_S, F, F_z\rangle \equiv \left(\hat{A}^\dagger\right)^{N_S} \left(\hat{F}^-\right)^{F-F_z} \left(\hat{a}_1^\dagger\right)^F |0\rangle \quad (6.2)$$

forms a complete orthogonal eigenbasis of Hamiltonian (6.1) for spin-1 atoms at $q = 0$, regardless of the sign of g_1 . Here $\hat{A} = \hat{a}_0^2 - 2\hat{a}_1\hat{a}_{-1}$ is the singlet annihilation operator and $\hat{F}^- = \hat{F}^x - i\hat{F}^y = \sqrt{2} \left(\hat{a}_0^\dagger\hat{a}_1 + \hat{a}_{-1}^\dagger\hat{a}_0\right)$ is the collective spin lowering operator. The quantum number $N_S = (N - F)/2$ can be interpreted as the number of singlet pairs, while $F(F + 1)$ and F_z are eigenvalues of the $\hat{\mathbf{F}}^2$ and \hat{F}^z operators. The energy of a member of the above basis is given in terms of these quantum numbers as

$$E = \frac{g_1}{2N} [F(F + 1) - 2N] + pF_z \quad (6.3)$$

where the linear Zeeman term $p\hat{F}^z$ has been reintroduced. This is helpful in demonstrating one of the main experimental obstacles in observing the singlet state. When $g_1 > 0, p = 0$, and, for simplicity, N is even, the true ground state of the system is given by $|N/2, 0, 0\rangle = \left(\hat{A}^\dagger\right)^{N/2} |0\rangle$, the singlet condensate. One of the consequences of the rotational invariance of singlet pairs is that all single-particle magnetic sublevels are equally occupied, that is, $\langle \hat{n}_i \rangle \equiv \langle \hat{a}_i^\dagger \hat{a}_i \rangle = N/3$ for $i = \pm 1, 0$. This is to be contrasted with the mean-field prediction. At exactly $p = 0$, there is in fact a continuous mean-field degeneracy among all rotations of the longitudinal polar state (5.7) or the transverse polar state Eq. (5.8), which are themselves spatial rotations of one another. However, keeping $q = 0$ and perturbing p by an arbitrarily small amount selects the transverse polar state, yielding the sublevel occupation expectation values $\langle \hat{n}_{\pm 1} \rangle = N/2$ and $\langle \hat{n}_0 \rangle = 0$. This shows that at extremely small values of $|p|$, mean field theory is inadequate. However, allowing for values of $|p|$ comparable to g_1 , $\langle \hat{n}_0 \rangle$ of the exact ground state is found to be

$$\langle \hat{n}_0 \rangle = \frac{N - |F_z|}{2|F_z| + 3} \simeq \frac{g_1 - |p|}{2|p| + 3g_1/N} \quad (6.4)$$

where the approximate equality holds when $|p| \leq g_1$ and we have $\langle \hat{n}_0 \rangle = 0$ otherwise. In both cases, the ± 1 sublevels each accommodate half of the remaining particles. This shows that particles from the zero sublevel are rapidly redistributed among the ± 1 sublevels with increasing $|p|$, approaching the mean-field distribution. At small magnetic fields B such that $1 \ll |F_z| \ll N$ in the ground state, the population of the $m = 0$ sublevel scales as $\langle \hat{n}_0 \rangle \sim c_1 n_0 / (2g\mu B)$,⁶⁰ where the unhatted n_0 is the average particle density in the trap and $g = p/\mu B$ is an effective g -factor. For ^{23}Na , g is equal to about $1/4$, as may be seen from Eq. (1.30), and $c_1/\mu_B \sim 10^{-22} \text{ cm}^3 \text{ G}$. For the typical experimental particle density of $n_0 \simeq 10^{18} \text{ m}^{-3}$,^{117,98} the observation of $\langle \hat{n}_0 \rangle$ on the order of 10^3 requires controlling the magnetic field on a sub- μG scale.⁶⁰

Equation (6.4) relies on the fact that the ground-state F and F_z quantum numbers change with increasing p , as may be verified from Eq. (6.3). It has previously been remarked that the spin-relaxation time is relatively long, often longer than the trap lifetime. In light of that, the above discussion may not seem too problematic, as the system may explicitly be prepared in an $F_z = 0$ state. Unfortunately, a similar situation occurs with the quadratic Zeeman field, favouring mean-field-like states within the same \hat{F}^z eigenspace,¹² as discussed in the following section.

6.2 SPIN-1 SPECTRA AND DYNAMICS AT $q > 0$

The results of this section were originally derived by Barnett et al.^{11,12} within the rotor framework that is extensively covered in the next two chapters. Notably, Sec. 8.2 presents the main steps of the pertinent calculation as it serves as a good basis for further work with the spin-2 rotor mapping. This section therefore primarily focuses on describing the results, obtained in the spin-1 setting. Refs. [11, 12] were written with the true magnetic realisation of the quadratic Zeeman field in the lower hyperfine multiplet of ^{23}Na in mind, and focused on the case $q > 0$ accordingly. A systematic rotor treatment of the $q < 0$ case would proceed similarly, but has not been carried out to date.

Transforming the SMA Hamiltonian (6.1) through the rotor mapping yields

the effective Hamiltonian

$$\hat{\mathcal{H}} = -\frac{g_1}{2N}\nabla^2 + q\left(N + \frac{3}{2}\right)\sin^2\theta + \frac{q^2N}{8g_1}\sin^2 2\theta \quad (6.5)$$

of a particle moving on the sphere, parametrised by the polar angle θ and the azimuthal angle φ . In Ref. [12] three regimes are considered, parametrised as

$$\begin{aligned} 1 &\ll q/g_1, \\ N^{-2} &\ll q/g_1 \ll 1, \quad \text{and} \\ q/g_1 &\ll N^{-2}, \end{aligned} \quad (6.6)$$

referred to as the Rabi, Josephson, and Fock regimes, respectively, in analogy with terminology used previously to describe the double-well Bose-Hubbard system.^{68,69} In the first two, the rotor is tightly localised about the poles of the sphere, but different terms of the potential dominate in each. Expanding the above Hamiltonian about the pole yields low lying spectra of the form $E = \Delta E(n_x + n_y)$, where $n_{x,y}$ are nonnegative integers, with $\Delta E = q$ for the Rabi regime and $\Delta E = \sqrt{2qg_1}$ for the Josephson regime. Both of these results agree with the spectra obtained through a Bogoliubov analysis.

Eigenstates of the Fock regime are spherical harmonics, delocalised about larger parts of the sphere. The energies, parametrised by an even (odd) integer ℓ between 0 and N for even (odd) N , equal $E_\ell = g_1\ell(\ell + 1)/2N$ and have degeneracies $2\ell + 1$. Transformed back into the operator picture, the ground state is the familiar condensate of singlet pairs, $(\hat{A}^\dagger)^{N/2}|0\rangle$. This state is doubly fragmented, i.e., features two macroscopically occupied single-particle states, and possesses a zero-energy spin mixing mode between the two condensate components. The Bogoliubov treatment is thus inapplicable as it suffers from a diverging depletion. The state is, however, very unstable to symmetry breaking perturbations, driving it towards a mean-field-like state, as outlined in the previous section for the linear Zeeman term, as the defining condition of the Fock regime, $q/g_1 \ll N^{-2}$, becomes increasingly difficult to satisfy in a controlled manner for macroscopic particle numbers. For typical

experimental values, the condition implies that the magnetic field would need to be kept at a value much smaller than $10 \mu\text{G}$. This, and the gap to the excited state scaling as N^{-1} , have so far prevented experimentally observing the singlet condensate, but there are proposals for adiabatically evolving an un-fragmented condensate of $m = 0$ atoms into the singlet condensate, which has been predicted to work for $\sim 10^2$ to $\sim 10^4$ particles in a trap.¹⁰⁷

The rotor mapping may also be fruitfully applied to study the dynamics of spin-1 condensates. A clear semiclassical picture emerges in terms of the Husimi distribution function⁴⁹ for the Rabi and Josephson regimes, in good agreement with performed experiments.^{74,73} For $q > 2g_1$, a potential minimum appears at the equator, which also affects dynamics. The general mapping has also been used to predict collapse-revival dynamics of the $m = 0$ magnetic sublevel occupation when quenching from an intermediate to a zero value of q .¹¹

6.3 EXACT SPIN-2 EIGENSTATES AND SPECTRA AT $q = 0$

At zero quadratic Zeeman field q , the exact spectrum of the tightly confined spin-2 condensate is also known and bears resemblances to the spin-1 case.^{60,131} Potentially degenerate eigenlevels can be labelled by the set $\{N_0, N_S, F, F_z\}$, where F_z is the eigenvalue of \hat{F}^z and F is such that the eigenvalue of \hat{F}^2 equals $F(F + 1)$. N_S can be interpreted as the number of spin-singlet pairs and $N_0 \equiv N - 2N_S$ as the number of bosons not in the singlet state. As mentioned before, this analogy is only a loose one, as \hat{A} and \hat{A}^\dagger do not obey bosonic commutation relations. However, the commutation relations of these and a third operator, which the authors of Ref. [131] denote by $\hat{S}_z \equiv \frac{1}{4}(2\hat{N} + 5)$, can be seen to be those of the Lie algebra $\mathfrak{su}(1, 1)$, closely related to $\mathfrak{su}(2)$, the spin algebra. This allows for an elegant derivation of the joint $\hat{A}^\dagger \hat{A}$ and \hat{S}_z eigenstates in analogy with the raising and lowering operator approach to the spin algebra. Technically, N_S and N_0 are defined such that the eigenvalue of $\hat{A}^\dagger \hat{A}$ equals $(N_0 + \frac{1}{2})(N_0 + \frac{5}{2})$ and $N_0 + 2N_S = N$. Explicitly constructing the complete but non-orthogonal basis of eigenstates is very algebraically involved and the interested reader is referred to the

original work in Ref. [131]. Their energies are, however, easily expressible in terms of the above quantum numbers and equal

$$E = \frac{g_1}{2} \left[\frac{F}{N} (F + 1) - 6 \right] + g_2 \frac{N_S}{N} (N + N_0 + 3). \quad (6.7)$$

The quantum numbers of the ground states may be easily inferred for different parameter configurations and show interesting parallels with the mean-field phase diagram. In the ferromagnetic region, the ground state N_S is zero and $F = 2N$ is maximised, while in the tetrahedral region the ground state N_S and F are both zero.

The nematic-region ground state is, however, less easily reconciled with its mean-field counterparts, as the ground state is non-degenerate and unique across the entire nematic region. It consists only of singlet pairs and potentially a singlet trio, maximising N_S and minimising F .

On the other hand, the case where $q \neq 0$ is much less well-understood analytically as N_S or N_0 are no longer good quantum numbers. Fortunately, analytical results can be obtained via the rotor mapping for this regime as well. The following two chapters introduce the general theory and basic applications of the rotor mapping, which is applied to the tightly confined spin-2 gas with $q \neq 0$ in Chapter 9.

7

HAMILTONIAN MAPPINGS AND THE ROTOR MAPPING

The spin-2 rotor mapping that is used to obtain analytical beyond-mean-field results for the tightly confined spinor problem builds on the examples of similar mappings for simpler systems. This chapter lays the mathematical foundation for a more general class of mappings which are referred to as Hamiltonian mappings and carefully defined in Sec. 7.1. The section further describes their general features and how one might go about calculating useful mapping-related quantities. Section 7.2 then illustrates these concepts on a slight extension of by far the most common mapping of the type, the Segal-Bargmann representation of second-quantised or Euclidean systems.

Finally, Sec. 7.3 contains a detailed exposition of the general features of the rotor mapping, which allows one to map a particle-conserving second-quantised many-body d -mode Hamiltonian onto that of a d -dimensional quantum rotor, or a particle moving on the $(d - 1)$ -sphere.

This chapter is fairly mathematical. A reader primarily interested in the applications of the rotor-mapping formalism may safely skip to the next chapter and refer back to specific results of this chapter as they are referenced.

7.1 COMMON FEATURES

Consider Hamiltonians \hat{H}_1 and \hat{H}_2 acting on Hilbert spaces S_1 and S_2 , respectively. Denote the spectrum of an operator \hat{A} by $\text{spec } \hat{A}$.^{*} Without loss of generality, let the size (cardinality) of $\text{spec } \hat{H}_2$ be larger or equal than that of $\text{spec } \hat{H}_1$.

A necessary condition for a mapping, in the sense about to be defined, between the Hamiltonians to exist is that $\text{spec } \hat{H}_1 \subseteq \text{spec } \hat{H}_2$. Consider first the case when $\text{spec } \hat{H}_1$ is a proper subset of $\text{spec } \hat{H}_2$. A mapping between the Hamiltonians is then an injective linear map between the two Hilbert spaces $T : S_1 \rightarrow S_2$ such that the \hat{H}_1 eigenspace with eigenvalue λ is mapped to a subspace of the λ -eigenvalue \hat{H}_2 eigenspace, possibly all of it. We refer to $T(S_1) \subset S_2$ as the *physical states* and the remainder of S_2 as *unphysical states*. One can define a pseudo-inverse map $T^\circ : S_2 \rightarrow S_1$ by letting $T^\circ T = \mathbb{1}_{S_1}$ and $T^\circ|_{S_2 \setminus T(S_1)} = 0$, i.e., T° maps all unphysical states to 0.

When the spectra are identical, the spaces S_1 and S_2 are isomorphic by construction. Identifying them, the Hamiltonian mapping is an automorphism T and $\hat{H}_2 = T\hat{H}_1T^{-1}$.

7.1.1 MAPPINGS FROM OVERCOMPLETE BASES

A particularly common type of Hamiltonian mapping as defined above arises when S_1 admits an overcomplete basis of states parametrised by some set \mathcal{M} , consisting of states $|z\rangle; z \in \mathcal{M}$. We limit ourselves to cases when \mathcal{M} is a smooth manifold as it is then straightforward to define differential operators on it, which is one of the main strengths of the mapping formalism. Choosing

^{*}Here we are slightly simplifying the mathematical concept of an operator spectrum. In particular, spaces S_1 and S_2 are assumed to have countable bases of their respective Hamiltonians' eigenstates. Then $\text{spec } \hat{H}_i$ is taken to be the set of *tagged* eigenvalues of the operator \hat{H}_i . By tagged we mean that, if an eigenvalue λ is g -fold degenerate, it features in $\text{spec } \hat{H}_i$ as g elements of the form (λ, j) where $j = 1, \dots, g$ is the "sequence number". Additionally note that all eigenvalues are required to be real for \hat{H}_i to be suitable Hamiltonians. They needn't be explicitly Hermitian but must be similar to Hermitian operators.

a positive measure $d\mu$ on \mathcal{M} , any state $|\psi\rangle \in S_1$ can be written as

$$|\psi\rangle = \int_{\mathcal{M}} d\mu(z) \psi(z) |z\rangle \quad (7.1)$$

where $\psi(z)$ uniquely determines $|\psi\rangle$ while the inverse mapping is defined up to unphysical states. The inner product of two states can be expressed as

$$\begin{aligned} \langle\phi|\psi\rangle &= \iint_{\mathcal{M}} d\mu(z_1)d\mu(z_2) \phi^*(z_1)\psi(z_2)\lambda(z_1, z_2) \\ &\equiv \int_{\mathcal{M}} d\mu(z) \phi^*(z) (\hat{\lambda}\psi)(z) \\ &= (\phi|\hat{\lambda}\psi). \end{aligned} \quad (7.2)$$

An integral operator $\hat{\lambda}$ has been introduced, both to compactify notation and to streamline later analysis. Here $\lambda(z_1, z_2) \equiv \langle z_1|z_2\rangle$ is the function, or integral kernel, used in the definition of $\hat{\lambda}$ through

$$(\hat{\lambda}\psi)(z_1) \equiv \int_{\mathcal{M}} d\mu(z_2) \lambda(z_1, z_2)\psi(z_2) \quad (7.3)$$

and $(\cdot|\cdot)$ is the standard square-integrable inner product with measure $d\mu$ such that $(\phi|\psi) = \int_{\mathcal{M}} d\mu(z) \phi^*(z)\psi(z)$. Note that $\lambda(z_2, z_1) = \lambda^*(z_1, z_2)$ and that this makes $\hat{\lambda}$ self-adjoint.

These definitions allow us to choose as the target space of our Hamiltonian mapping, the S_2 of the previous subsection, the space of complex functions f on \mathcal{M} with finite norm $(f|\hat{\lambda}f)^{1/2}$. In light of this, Eq. (7.1) constitutes the inverse map T° mapping a state $\psi \in S_2$ onto $|\psi\rangle \in S_1$. Finding a practical representation of T itself is more demanding and is the subject of the next subsection.

The space \mathcal{M} is typically chosen to have as many nice properties as possible. Two are particularly desirable:

- Per-parts integration with $d\mu$ over \mathcal{M} should yield no boundary terms.
- $\hat{H}_1 |z\rangle = \mathcal{H}_1(z, \partial_z) |z\rangle$ for every member $|z\rangle$ of the overcomplete basis

where \mathcal{H}_1 is some function of the coordinates z and derivatives with respect to them.

When these are satisfied, the target Hamiltonian of the mapping, \hat{H}_2 , acting on S_2 , may be found through the following sequence of steps:

$$\begin{aligned} \hat{H}_1 |\psi\rangle &= \int_{\mathcal{M}} d\mu(z) \psi(z) \hat{H}_1 |z\rangle = \int_{\mathcal{M}} d\mu(z) \psi(z) \mathcal{H}_1(z, \partial_z) |z\rangle \\ &\stackrel{\text{p.p.}}{\equiv} \int_{\mathcal{M}} d\mu(z) |z\rangle \mathcal{H}_2(z, \partial_z) \psi(z) \equiv \int_{\mathcal{M}} d\mu(z) \left(\hat{H}_2 \psi \right)(z) |z\rangle \end{aligned} \quad (7.4)$$

This also immediately implies that the spectrum of \hat{H}_1 is a subset of that of \hat{H}_2 .

7.1.2 PHYSICAL SUBSPACE

The previous subsection outlined how to find \hat{H}_2 without utilising the map $T : S_1 \rightarrow S_2$ at all. It did construct the map T° , in the very first equation, and this may in principle be inverted on the orthogonal complement of T° 's kernel to yield T . This is often too complicated to carry out directly. This section constructs the map T in a more pragmatic fashion and discusses helpful properties of the physical subspace.

The subspace of physical states coincides with the image of the operator $\hat{\lambda}$ of Eq. (7.2) and unphysical states correspond to its kernel. To see this, recall that unphysical states $\psi \in S_2$ are defined as states for which

$$|\psi\rangle = \int_{\mathcal{M}} d\mu(z) \psi(z) |z\rangle = 0. \quad (7.5)$$

This implies that as ϕ ranges over all of S_2 we have $\langle \phi | \psi \rangle = \left(\phi \left| \hat{\lambda} \psi \right. \right) = 0$ which is only possible if $\hat{\lambda} \psi = 0$. The remaining states are physical as it is a property of self-adjoint operators that their images coincide with the orthogonal complements of their kernels.

The restriction of $\hat{\lambda}|_{\text{im}(\hat{\lambda})}$ to the physical subspace then has no null space by definition and thus possesses an inverse $\hat{\lambda}^{-1}|_{\text{im}(\hat{\lambda})}$ which may be formally

extended to all of S_2 by letting it be zero on the unphysical subspace. It is easy to verify that this operator is also self-adjoint.

Since $\hat{\lambda}$ is an integral operator with kernel $\lambda(z_1, z_2)$, we have

$$\begin{aligned} (\hat{\lambda}\psi)(z) &= (\lambda_z|\psi); \\ \lambda_{z_1}(z_2) &\equiv \lambda^*(z_1, z_2). \end{aligned} \quad (7.6)$$

Using this property of $\hat{\lambda}$ and the existence of its inverse we find, for a physical state ψ ,

$$\psi(z) = (\hat{\lambda}\hat{\lambda}^{-1}\psi)(z) = (\lambda_z|\hat{\lambda}^{-1}\psi) = (\hat{\lambda}^{-1}\lambda_z|\psi) \equiv (\mathcal{J}_z|\psi). \quad (7.7)$$

This gives the physical subspace the structure of a reproducing kernel Hilbert space, or RKHS. Simply put, this is a Hilbert space of functions in which evaluation at a point z of *any* state corresponds to an inner product with a unique z -dependent state that is *not* a delta function. The name refers to the fact that there exists an integral operator $\hat{\mathcal{J}}$ with integral kernel $\mathcal{J}(z_1, z_2) = \mathcal{J}_{z_1}^*(z_2)$ that reproduces function values, i.e., $\psi(z_1) = \int_{\mathcal{M}} d\mu(z_2) \mathcal{J}(z_1, z_2)\psi(z_2)$. $\hat{\mathcal{J}}$ is, in fact, the identity operator.

Repeating the step again, one obtains the RKHS structure for the true inner product $(\cdot|\hat{\lambda}\cdot)$, since

$$\psi(z) = (\mathcal{J}_z|\psi) = (\mathcal{J}_z|\hat{\lambda}^{-1}\hat{\lambda}\psi) = (\hat{\lambda}^{-1}\mathcal{J}_z|\hat{\lambda}\psi) \equiv (\kappa_z|\hat{\lambda}\psi). \quad (7.8)$$

One may again consider a kernel $\kappa(z_1, z_2) = \kappa_{z_1}^*(z_2)$ and furthermore form the corresponding S_1 states

$$|\kappa_{z_1}\rangle = \int_{\mathcal{M}} d\mu(z_1) \kappa^*(z_1, z_2) |z_2\rangle \quad (7.9)$$

These then allow for the construction of the map $T : S_1 \rightarrow S_2$ as:

$$(T|\psi\rangle)(z) = \langle\kappa_z|\psi\rangle \quad (7.10)$$

In addition, this yields a resolution of the identity:

$$\mathbb{1} = \int_{\mathcal{M}} d\mu(z) |z\rangle \langle \kappa_z| \quad (7.11)$$

To summarise, finding T requires the following steps:

- Define an integral operator $\hat{\lambda}$ with integral kernel $\lambda(z_1, z_2) = \langle z_1 | z_2 \rangle$.
- Find the inverse $\hat{\lambda}^{-1}$ on $\hat{\lambda}$'s image.
- Define states $|\lambda_z\rangle$ with $\lambda_{z_1}(z_2) = \lambda^*(z_1, z_2)$.
- Define states $|\kappa_z\rangle = \hat{\lambda}^{-2} |\lambda_z\rangle$ and their corresponding S_1 states $|\kappa_z\rangle$.
- Then $(T|\psi\rangle)(z) = \langle \kappa_z | \psi \rangle$.

Finally note that, if $\hat{\lambda}^{-1/2}$ can be defined, one may form an auxiliary basis $|z_S\rangle \equiv \hat{\lambda}^{-1/2} |z\rangle$, in which the resolution of the identity is given by

$$\mathbb{1} = \int_{\mathcal{M}} d\mu(z) |z_S\rangle \langle z_S|. \quad (7.12)$$

Expressing states in this basis has the advantage that the induced inner product on S_2 becomes $(\cdot|\cdot)$, eliminating the need for double integrals, and that T can be found through $(T|\psi\rangle)(z) = \langle z_S | \psi \rangle$. The new basis might, however, spoil the second desired property listed on page 84. It therefore seems worth checking whether the property survives in a manageable form, as the absence of double integrals is quite desirable in itself, and working in the $|z_S\rangle$ basis from the beginning if it does.

7.2 THE SEGAL-BARGMANN REPRESENTATION

Arguably the most commonly encountered Hamiltonian mapping of the above type is the Segal-Bargmann representation^{9,111} of second-quantised systems.[†]

[†]It can also be applied to particles moving in Euclidean space by introducing annihilation operators $\hat{a} = \frac{1}{\sqrt{2}} \left(\frac{1}{\xi} \hat{x} + i\xi \hat{p} \right)$ where ξ is an arbitrary length scale. The choice of ξ is sometimes motivated by characteristic length scales, derivable from the Hamiltonian, e.g. the oscillator length $a_{\text{osc}} = (m\omega)^{-1/2}$ for a harmonic oscillator.

It consists of expressing states in the overcomplete basis of *coherent states* and features prominently in the coherent-state path integral,¹¹⁰ as well as finding applications in quantum optics^{58,35} and even classical signal processing.¹²⁰

This section uses the Segal-Bargmann representation to illustrate concepts introduced in the previous section on what is perhaps the simplest non-trivial Hamiltonian mapping, and certainly the most ubiquitous. The discussion is limited to that of a single-mode Hamiltonian, i.e., one that is a function of a single annihilation/creation operator pair, as the multi-mode generalisation is straightforward.

Coherent states have a number of remarkable properties, but for the present purposes it suffices to define them as eigenvectors of the non-hermitian annihilation operator \hat{a} . Its spectrum is all of the complex plane so the coherent states may be parametrised by an unbounded complex number z such that $\hat{a} |z\rangle = z |z\rangle$. It is well-known that they may be expressed as

$$|z\rangle = e^{z\hat{a}^\dagger} |0\rangle = \sum_{n=0}^{\infty} \frac{z^n}{\sqrt{n!}} |n\rangle \quad (7.13)$$

where $|n\rangle$ is the n -particle Fock state. The normalisation of the above states is one of two conventional ones, yielding states of norm $\exp(-|z|^2/2)$.

The integration measure used in the mapping is $d\mu(z) = \frac{1}{\pi} e^{-|z|^2} d^2z$. In analogy with Eq. (7.1), general states may therefore be expressed as

$$|\psi\rangle = \frac{1}{\pi} \int_{\mathbb{C}} d^2z e^{-|z|^2} \psi^*(z) |z\rangle \quad (7.14)$$

where the additional complex conjugation on ψ is another convention. As is simple to derive, $\lambda(z_1, z_2) = \langle z_1 | z_2 \rangle = \exp(z_1^* z_2)$. Following Eq. (7.2), this

yields the inner product

$$\begin{aligned}
\langle \phi | \psi \rangle &= \frac{1}{\pi^2} \iint_{\mathbb{C}} d^2 z_1 d^2 z_2 e^{-|z_1|^2 - |z_2|^2 + z_1^* z_2} \phi(z_1) \psi^*(z_2) \\
&= \frac{1}{\pi} \int_{\mathbb{C}} d^2 z e^{-|z|^2} \phi(z) \left(\hat{\lambda} \psi \right)^*(z) \\
\text{with } \left(\hat{\lambda} \psi \right)(u) &= \frac{1}{\pi} \int_{\mathbb{C}} d^2 z e^{-|z|^2} e^{uz^*} \psi(z)
\end{aligned} \tag{7.15}$$

A reader familiar with the Segal-Bargmann representation will notice that this inner product hardly resembles the one usually presented. This is due to our starting from the other end of the derivation and treating a slight extension of the representation. Notably, the original Segal-Bargmann mapping considers only *holomorphic* functions of z with finite norm. One way to think of these functions is as suitable linear combinations of the basis functions z^n for n a nonnegative integer. In our treatment the functions can also depend on z^* and hence not be holomorphic, though we do limit ourselves to functions with a series expansion for simplicity. This generalisation is useful as it allows the use of simple nonholomorphic trial wave functions, such as the Gaussian $\psi \sim \exp[-\alpha|z|^2]$.

Holomorphic functions do, however, represent the *physical subspace* of our mapping as introduced in the previous section. Overlaps, expectation values, and other physical results of working with a nonholomorphic function will be the same as when working with its projection onto the holomorphic physical subspace, but the algebra might be simpler. Restricting to the holomorphic physical subspace also recovers the standard Segal-Bargmann inner product, as will be demonstrated shortly.

To show the correspondence between physical states and holomorphic functions, consider the functions $f_{a,b}(z) \equiv z^a z^{*b}$ for integer a, b with $a + b \geq 0$. All functions of finite norm with a series expansion may be defined as sums of the $f_{a,b}$. Functions with $b = 0$ are holomorphic. Referring to the previous section, the physical subspace is defined to be the image of $\hat{\lambda}$. By expanding $\exp(uz^*)$ in a series and performing a few elementary integrations, one can

easily verify that

$$\hat{\lambda}f_{a,b} = \begin{cases} \frac{a!}{(a-b)!}f_{a-b,0} & a \geq b \\ 0 & a < b \end{cases} \quad (7.16)$$

which shows that the range of $\hat{\lambda}$ consists of all holomorphic functions.

Denoting the original Fock space by \mathcal{F} and the target extended Segal-Bargmann space by \mathcal{B} , we next seek to find the map $T : \mathcal{F} \rightarrow \mathcal{B}$. Following Sec. 7.1.2, we must invert $\hat{\lambda}$, restricted to its image. From Eq. (7.16) it can be seen, however, that $\hat{\lambda}$ acting on holomorphic functions with $b = 0$ simply returns the same functions and is thus the identity. In the language of Sec. 7.1.2 this also implies that $\lambda(u, z) = \exp(uz^*)$ is a reproducing kernel.

This implies a cascade of simplifications, particular to the Segal-Bargmann representation. For one, the inner product from Eq. (7.15) of two physical states ϕ and ψ becomes the more familiar

$$\langle \phi | \psi \rangle = \frac{1}{\pi} \int_{\mathbb{C}} d^2z e^{-|z|^2} \phi(z) \psi^*(z). \quad (7.17)$$

Following the steps of Sec. 7.1.2, the reproducing states $|\kappa_z\rangle$ of Eq. (7.9) are again found to be the coherent states $|z\rangle$ themselves, implying

$$(T|\psi\rangle)(z) = \psi^*(z) = \langle z | \psi \rangle \quad (7.18)$$

and yielding the resolution of the identity

$$\mathbb{1} = \frac{1}{\pi} \int_{\mathbb{C}} d^2z e^{-|z|^2} |z\rangle \langle z| \quad (7.19)$$

in analogy with Eq. (7.11). This resolution is typically the starting point of expositions of the Segal-Bargmann representation. We have opted to work in the opposite direction as the analogous resolutions for other Hamiltonian mappings are in general much more complicated. In contrast to the present situation, it might be virtually impossible to intelligently guess or derive their form by any other means.

Finally, the task of mapping a given Hamiltonian \hat{H}_1 , acting on the Fock

space \mathcal{F} , onto \hat{H}_2 , acting on the extended Segal-Bargmann space \mathcal{B} , which we take to consist of all finite norm functions of z and z^* with series expansions, must be addressed. It is sufficient to describe how the operators \hat{a} and \hat{a}^\dagger transform individually and then chain these transformations from right to left.

At this point it should be stated that the desirable properties listed near the end of Sec. 7.1.1 are both satisfied for the present space. Per-parts integration yields no boundary terms as $e^{-|z|^2}|\psi(z)|^2$ must tend to zero at large $|z|$ for ψ to be in \mathcal{B} . With regard to the other property, observe the following relations:

$$\hat{a}|z\rangle = z|z\rangle \quad \hat{a}^\dagger|z\rangle = \partial_z|z\rangle \quad (7.20)$$

where the first comes from the definition of coherent states and the second is easily verifiable through their form in Eq. (7.13). Using these relations, the fact that we can treat z and z^* as independent variables when integrating over \mathbb{C} , and that the states $|z\rangle$ do not depend on z^* , one can derive

$$\begin{aligned} \hat{a}|\psi\rangle &= \frac{1}{\pi} \int_{\mathbb{C}} dz^* dz e^{-|z|^2} \psi^*(z) z |z\rangle \\ &= -\frac{1}{\pi} \int_{\mathbb{C}} dz^* dz \left(\partial_{z^*} e^{-|z|^2} \right) \psi^*(z) |z\rangle \\ &\stackrel{\text{p.p.}}{=} \frac{1}{\pi} \int_{\mathbb{C}} dz^* dz e^{-|z|^2} \partial_{z^*} \psi^*(z) |z\rangle \\ &= \frac{1}{\pi} \int_{\mathbb{C}} dz^* dz e^{-|z|^2} (\partial_z \psi)^*(z) |z\rangle \end{aligned} \quad (7.21)$$

and

$$\begin{aligned} \hat{a}^\dagger|\psi\rangle &= \frac{1}{\pi} \int_{\mathbb{C}} dz^* dz e^{-|z|^2} \psi^*(z) \partial_z |z\rangle \\ &\stackrel{\text{p.p.}}{=} -\frac{1}{\pi} \int_{\mathbb{C}} dz^* dz \partial_z \left(e^{-|z|^2} \psi^*(z) \right) |z\rangle \\ &= \frac{1}{\pi} \int_{\mathbb{C}} dz^* dz e^{-|z|^2} (z^* \psi^*(z) - \partial_z \psi^*(z)) |z\rangle \\ &= \frac{1}{\pi} \int_{\mathbb{C}} dz^* dz e^{-|z|^2} ((\hat{z} - \partial_{z^*}) \psi)^*(z) |z\rangle. \end{aligned} \quad (7.22)$$

Thus \hat{H}_2 may be found by substituting

$$\hat{a} \rightarrow \partial_z \quad \text{and} \quad \hat{a}^\dagger \rightarrow \hat{z} - \partial_{z^*} \quad (7.23)$$

Note that ∂_{z^*} vanishes when acting on the holomorphic physical states. As an example, the simple Hamiltonian $\omega \hat{a}^\dagger \hat{a}$ would map to $\hat{H}_2 = \omega (\hat{z} \partial_z - \partial_{z^*} \partial_z)$. A rather beautiful property in this case is that a wave function with the physical Bargmann representation $\psi(z)$ at time $t = 0$ evolves into $\psi(e^{-i\omega t} z)$ at time t . Another useful property of the mapping is that an arbitrary function of operators $A(\hat{a}^\dagger, \hat{a})$, normal ordered or not, maps onto $A(\hat{z} - \partial_{z^*}, \partial_z)$. This is the primary reason that its resolution of the identity is used at every time step of the coherent-state path integral, as it is the most straightforward way to transform a second-quantised operator into a scalar quantity, in the appropriate sense.

7.3 ROTOR MAPPINGS

This section introduces the general formalism of the d -dimensional rotor mapping. This may be utilised quite generally for any second-quantised system with d modes (i.e. creation/annihilation operator pairs) and a conserved number of particles. It finds particular utility for Hamiltonians that may be “antisymmetrised,” in a sense that is addressed at the beginning of the following chapter. Such systems include tightly confined spinor condensates, to which the rotor mapping is applied in Chapters 8 to 10.

We will be working in the N -particle subspace of the d -mode Fock space, denoted \mathcal{F}_N . Further denoting the d annihilation operators by $\hat{a}_\alpha; \alpha = 1, \dots, d$, the overcomplete basis for the mapping consists of the states

$$|\mathbf{\Omega}\rangle = \frac{1}{\sqrt{N!}} (\mathbf{\Omega} \cdot \hat{\mathbf{a}}^\dagger)^N |0\rangle \quad \text{for} \quad |\mathbf{\Omega}| = 1 \quad (7.24)$$

where $\hat{\mathbf{a}}^\dagger = [\hat{a}_1^\dagger, \dots, \hat{a}_d^\dagger]$ is a vector of creation operators and $|0\rangle$ is the zero-particle vacuum state. $\mathbf{\Omega}$ is a d -dimensional *real* unit vector, i.e., belonging to the $(d-1)$ -sphere \mathcal{S}^{d-1} embedded in \mathbb{R}^d at unit radius. This implies our

mapping will be into a space of functions defined over the $(d - 1)$ -sphere.

Note that the vacuum state $|0\rangle$ is not a member of the overcomplete basis (7.24). This is in contrast with the Segal-Bargmann transform where $z = 0$, corresponding to the vacuum state, is accordingly set apart as a distinguished point in \mathbb{C} . Until one ascribes physical significance to the operators \hat{a}_α , the rotor basis (7.24) has no distinguished point $\mathbf{\Omega}$. Indeed, orthogonal transformations of the single-particle basis, and through it \hat{a}_α , simply rotate the member states, though more general unitary transformations have no such intuitive analogue. This motivates a rotationally invariant integration measure over \mathcal{S}^{d-1} , i.e., a constant one.

A general state $|\psi\rangle \in \mathcal{F}_N$ can thus be written as

$$|\psi\rangle = \int_{\mathcal{S}^{d-1}} d\mathbf{\Omega} \psi(\mathbf{\Omega}) |\mathbf{\Omega}\rangle \quad (7.25)$$

where ψ belongs to the space of complex functions defined over the $(d - 1)$ sphere of a certain finite norm. The norm is derived from the inner product, whose functional form is analogous to Eq. (7.2). Its explicit form in the rotor setting is stated below in Eq. (7.27). Denote the space of such finite-norm functions by \mathcal{R}_d . Note that Eq. (7.24) implies that $|-\mathbf{\Omega}\rangle = (-1)^N |\mathbf{\Omega}\rangle$, from which it follows that states $\psi \in \mathcal{R}_d$ of parity $(-1)^{N+1}$ are mapped to zero by Eq. (7.25), and are hence unphysical.

The overlap of two states is given by

$$\langle \mathbf{\Omega} | \boldsymbol{\rho} \rangle = (\mathbf{\Omega} \cdot \boldsymbol{\rho})^N \quad (7.26)$$

indicating that the basis is most evidently not orthogonal, though it becomes so to a good approximation for large N . It also seems intuitive that the basis should be complete. This will definitively be shown later, at the end of Sec. 7.3.2, by constructing the subspace of physical states.

We may now explicitly express the inner product, analogous to Eq. (7.2), as

$$\begin{aligned}
\langle \phi | \psi \rangle &= \iint_{\mathcal{S}^{d-1}} d\Omega d\boldsymbol{\rho} \phi^*(\boldsymbol{\Omega}) (\boldsymbol{\Omega} \cdot \boldsymbol{\rho})^N \psi(\boldsymbol{\rho}) \\
&= \int_{\mathcal{S}^{d-1}} d\Omega \phi(\boldsymbol{\Omega}) (\hat{\lambda}\psi)(\boldsymbol{\Omega}) \\
(\hat{\lambda}\psi)(\boldsymbol{\Omega}) &= \int_{\mathcal{S}^{d-1}} d\boldsymbol{\rho} (\boldsymbol{\Omega} \cdot \boldsymbol{\rho})^N \psi(\boldsymbol{\rho})
\end{aligned} \tag{7.27}$$

where we have proceeded in complete analogy with the general treatment of Sec. 7.1 and the Segal-Bargmann transform of Sec. 7.2.

Again referring to the desirable conditions near the end of Sec. 7.1.1, integration by parts is seen to yield no boundary terms as spheres (for $d > 1$) are closed manifolds. To find the Hamiltonian action on the $|\boldsymbol{\Omega}\rangle$, recall that the particle number is considered fixed, so the most elementary building block of a general Hamiltonian will be $\hat{a}_\alpha^\dagger \hat{a}_\beta$. One then finds

$$\hat{a}_\alpha^\dagger \hat{a}_\beta |\boldsymbol{\Omega}\rangle = \Omega_\beta (\nabla_\alpha + N\Omega_\alpha) |\boldsymbol{\Omega}\rangle. \tag{7.28}$$

The operator ∇ is the spherical gradient operator, discussed in the following subsection.

7.3.1 CALCULUS ON THE n -SPHERE

Throughout this section, \mathcal{S}^{d-1} will be parametrised by its d Cartesian coordinates Ω_α , with the constraint $\Omega_\alpha \Omega_\alpha = 1$. This seems to be considerably more elegant for abstract manipulations than working with an unconstrained set of coordinates, such as those of the stereographic projection or the arbitrary-dimensional generalisations of the polar and azimuthal angle,[‡] and also affords a concise representation of the physically important Laplacian eigenbasis.

Aside from the position operators $\hat{\Omega}_\alpha$, the most basic ones that may be defined are components of the spherical gradient, $\nabla_\alpha \equiv \mathbf{e}_\alpha \cdot \nabla$. The vector

[‡]Save for the derivation of the integration-by-parts rule, presented shortly.

∇ lies in the tangent plane at every point of the sphere and can be defined through the differential-geometric notions of exterior derivatives, pushforwards and pullbacks. A much simpler but equivalent approach involves arbitrarily extending the functions defined over \mathcal{S}^{d-1} to functions defined over a larger subset of \mathbb{R}^d , containing \mathcal{S}^{d-1} as a measure-zero subset. The extensions can truly be anything, as long as they are smooth at all points of the sphere and their restrictions to the sphere coincide with the original functions. Then ∇ is simply the projection of the ordinary Euclidean gradient ∂ onto the tangent space of the sphere:

$$\nabla_\alpha = \partial_\alpha - \hat{\Omega}_\alpha \hat{\Omega} \cdot \partial. \quad (7.29)$$

Using these definitions, the following useful relations may be found:

$$\begin{aligned} [\nabla_\alpha, \hat{\Omega}_\beta] &= \delta_{\alpha\beta} - \hat{\Omega}_\alpha \hat{\Omega}_\beta \\ \hat{\Omega}_\alpha \nabla_\alpha &= 0 \\ [\nabla_\alpha, \nabla_\beta] &= \hat{\Omega}_\alpha \nabla_\beta - \hat{\Omega}_\beta \nabla_\alpha \equiv i\hat{L}_{\alpha\beta}. \end{aligned} \quad (7.30)$$

The operators $\hat{L}_{\alpha\beta}$ are an arbitrary-dimensional generalisation of the three-dimensional angular momentum operators. That the latter can be labelled by a single index is a particularity of three dimensions. The single- and double-indexed operators in three dimensions are related by $\hat{L}_i = \frac{1}{2}\varepsilon_{ijk}\hat{L}_{jk}$ where ε is the Levi-Civita completely antisymmetric tensor.

The integration-by-parts rule for ∇_α is derived next. By rotational invariance, it suffices to find the rule for, say, ∇_1 . To that end, label a d -dimensional unit vector parametrising the $(d-1)$ sphere by $\Omega^{(d-1)}$ and parametrise it as $\Omega^{(d-1)} = (\cos\theta, \sin\theta\Omega^{(d-2)})$. We then have $\nabla_1 = -\sin\theta\partial_\theta$. Furthermore, the integration measure is schematically equal to $\int_{\mathcal{S}^{d-1}} d\Omega^{(d-1)} =$

$\int_0^\pi d\theta \sin^{d-2} \theta \int_{\mathcal{S}^{(d-2)}} d\Omega^{(d-2)}$. We find

$$\begin{aligned}
& \int_{\mathcal{S}^{d-1}} d\Omega^{(d-1)} f \nabla_1 g = - \int_{\mathcal{S}^{d-2}} d\Omega^{(d-2)} \int_0^\pi d\theta \sin^{d-1} \theta f \partial_\theta g \\
& \stackrel{\text{p.p.}}{=} \int_{\mathcal{S}^{d-2}} d\Omega^{(d-2)} \int_0^\pi d\theta g \partial_\theta \sin^{d-1} \theta f \\
& = \int_{\mathcal{S}^{d-2}} d\Omega^{(d-2)} \int_0^\pi d\theta \sin^{d-2} \theta g [(d-1) \cos \theta + \sin \theta \partial_\theta] f \\
& \int_{\mathcal{S}^{d-1}} d\Omega^{(d-1)} g [(d-1) \Omega_1 - \nabla_1] f
\end{aligned} \tag{7.31}$$

and by rotational symmetry it may be inferred that generally

$$\int_{\mathcal{S}^{d-1}} d\Omega f \nabla_\alpha g = \int_{\mathcal{S}^{d-1}} d\Omega g [(d-1) \Omega_\alpha - \nabla_\alpha] f. \tag{7.32}$$

Another important element of calculus on the sphere is the spherical Laplacian operator, given by

$$\nabla^2 = \frac{1}{2} \sum_{\alpha\beta} \hat{L}_{\alpha\beta}^2 = \nabla_\gamma \nabla_\gamma. \tag{7.33}$$

With the above properties, the action of the fundamental particle-conserving Hamiltonian building block on $|\Omega\rangle$ in Eq. (7.28) may easily be verified. With the integration-per-parts rule (7.32) at hand, the mapping onto an operator acting on \mathcal{R}_d may be concluded through the following steps:

$$\begin{aligned}
\hat{a}_\alpha^\dagger \hat{a}_\beta |\psi\rangle &= \int_{\mathcal{S}^{d-1}} d\Omega \psi(\Omega) \Omega_\beta (N \Omega_\alpha + \nabla_\alpha) |\Omega\rangle \\
& \stackrel{\text{p.p.}}{=} \int_{\mathcal{S}^{d-1}} d\Omega |\Omega\rangle [(N+d-1) \Omega_\alpha - \nabla_\alpha] \Omega_\beta \psi(\Omega) \\
& = \int_{\mathcal{S}^{d-1}} d\Omega |\Omega\rangle [(N+d) \Omega_\alpha \Omega_\beta - \Omega_\beta \nabla_\alpha - \delta_{\alpha\beta}] \psi(\Omega)
\end{aligned} \tag{7.34}$$

implying the general operator mapping

$$\hat{a}_\alpha^\dagger \hat{a}_\beta \rightarrow (N+d) \hat{\Omega}_\alpha \hat{\Omega}_\beta - \hat{\Omega}_\beta \nabla_\alpha - \delta_{\alpha\beta}. \tag{7.35}$$

One often deals with expressions of the form $\hat{a}_\alpha^\dagger Q_{\alpha\beta} \hat{a}_\beta \equiv \hat{\mathbf{a}}^\dagger Q \hat{\mathbf{a}}$, where Q is

an arbitrary matrix. Applying the above rule to such an expression yields:

$$\hat{\mathbf{a}}^\dagger Q \hat{\mathbf{a}} \rightarrow (N + d) \hat{\mathbf{\Omega}}^T Q \hat{\mathbf{\Omega}} - \hat{\mathbf{\Omega}}^T Q^T \nabla - \text{Tr } Q. \quad (7.36)$$

For completeness, we finally state the following less frequently used properties of calculus on the sphere:

$$\begin{aligned} [\hat{L}_{\alpha\beta}, \hat{L}_{\gamma\delta}] &= i \left(\delta_{\alpha\gamma} \hat{L}_{\beta\delta} + \delta_{\beta\delta} \hat{L}_{\alpha\gamma} - \delta_{\alpha\delta} \hat{L}_{\beta\gamma} - \delta_{\beta\gamma} \hat{L}_{\alpha\delta} \right) \\ [\hat{L}_{\alpha\beta}, \hat{\Omega}_\gamma] &= i \left(\delta_{\alpha\gamma} \hat{\Omega}_\beta - \delta_{\beta\gamma} \hat{\Omega}_\alpha \right) \\ [\nabla_\alpha, \hat{L}_{\beta\gamma}] &= i \left(\delta_{\alpha\gamma} \nabla_\beta - \delta_{\alpha\beta} \nabla_\gamma \right) - \left(\hat{\Omega}_\alpha \hat{L}_{\beta\gamma} + \hat{\Omega}_\beta \hat{L}_{\gamma\alpha} + \hat{\Omega}_\gamma \hat{L}_{\alpha\beta} \right) \\ [\nabla^2, \hat{\Omega}_\alpha] &= -(d-1) \hat{\Omega}_\alpha + 2 \nabla_\alpha \\ [\nabla^2, \nabla_\alpha] &= (d-3) \nabla_\alpha - 2 \hat{\Omega}_\alpha \nabla^2 \end{aligned} \quad (7.37)$$

7.3.2 PHYSICAL SUBSPACE

This subsection derives the range of the operator $\hat{\lambda}$, as defined in Eq. (7.27), corresponding to the physical subspace of the mapping. The author has found it easiest to characterise this in the eigenbasis of the Laplacian from Eq. (7.33), which is introduced next.

Members of the Laplacian's n -th eigenspace, for $n = 0, 1, 2, \dots$ are homogeneous polynomials of degree n in the coordinates $\Omega_\alpha; \alpha = 1, \dots, d$. They may be written in reduced form as

$$\psi_M^n(\mathbf{\Omega}) \equiv M_{\alpha_1 \alpha_2 \dots \alpha_n} \Omega_{\alpha_1} \Omega_{\alpha_2} \dots \Omega_{\alpha_n} \quad (7.38)$$

where M is a completely symmetric rank- n traceless tensor. By the latter we mean that contracting any two of its indices yields zero, regardless of the values of the other indices. The traceless condition ensures that no trivial factors of $\Omega_\alpha \Omega_\alpha = 1$ appear.

It is a relatively straightforward exercise in applying relations of the previous section to show that the functions in Eq. (7.38) are indeed eigenfunctions of ∇^2 with eigenvalues $\lambda_n = -n(d+n-2)$. The dimensions of the eigenspace

are determined by the number of independent components of the tensor M . This corresponds to the number of independent components of a completely symmetric d -dimensional rank- n tensor, which we will denote $P(d, n)$, minus the number of tracelessness constraints $P(d, n - 2)$, since the trace of a completely symmetric rank- n tensor is a completely symmetric tensor of rank $n - 2$ and the same dimension. $P(d, n) = \binom{n+d-1}{d-1}$ corresponds to the number of ways of distributing n elements among d bins. The n -th eigenlevel's dimension is thus

$$g_n = \binom{n+d-1}{d-1} - \binom{n+d-3}{d-1}. \quad (7.39)$$

We now turn to the action of the operator $\hat{\lambda}$, as defined in Eq. (7.27), on members of the Laplacian eigenbasis. Note that members of the n -th Laplacian eigenspace have parity $(-1)^n$, whereas the integral kernel of $\hat{\lambda}$, given by $\lambda(\boldsymbol{\Omega}, \boldsymbol{\rho}) = (\boldsymbol{\Omega} \cdot \boldsymbol{\rho})^N$, has parity $(-1)^N$ in both variables. This implies that $\hat{\lambda}$ maps states for which $n + N$ is odd to zero and that they are thus unphysical. Restricting to states with even $N + n$, we have

$$\begin{aligned} (\hat{\lambda}\psi_M^n)(\boldsymbol{\rho}) &= M_{\alpha_1 \dots \alpha_n} \int_{S^{d-1}} d\boldsymbol{\Omega} (\boldsymbol{\rho} \cdot \boldsymbol{\Omega}) \Omega_{\alpha_1} \cdots \Omega_{\alpha_n} \\ &= \frac{N!}{(N+n)!} M_{\alpha_1 \dots \alpha_n} \partial_{\alpha_1} \cdots \partial_{\alpha_n} \int_{S^{d-1}} d\boldsymbol{\Omega} (\boldsymbol{\chi} \cdot \boldsymbol{\Omega})^{N+n} \Big|_{\boldsymbol{\chi}=\boldsymbol{\rho}} \\ &= \frac{N!}{(N+n)!} \left(\int_{S^{d-1}} d\boldsymbol{\Omega} \Omega_1^{N+n} \right) M_{\alpha_1 \dots \alpha_n} \partial_{\alpha_1} \cdots \partial_{\alpha_n} (\boldsymbol{\chi} \cdot \boldsymbol{\chi})^{\frac{N+n}{2}} \Big|_{\boldsymbol{\chi}=\boldsymbol{\rho}} \end{aligned} \quad (7.40)$$

where the derivatives act with respect to $\boldsymbol{\chi}$ and we have used the fact that, due to rotational symmetry, the integral on the second line depends only on the size of $\boldsymbol{\chi}$, allowing us to proceed as if $\boldsymbol{\chi}$ was oriented along the Ω_1 axis. The integral on the third line can be evaluated in several ways, e.g. by transforming to the coordinates used to derive the integration-by-parts rule in Eq. (7.31), and equals

$$\int_{S^{d-1}} d\boldsymbol{\Omega} \Omega_1^{N+n} = 2\pi^{\frac{d-1}{2}} \frac{\Gamma\left(\frac{N+n+1}{2}\right)}{\Gamma\left(\frac{N+n+d}{2}\right)}. \quad (7.41)$$

As for the remainder of the last line of Eq. (7.40), carrying out the two rightmost derivations yields

$$\begin{aligned}
(\boldsymbol{\chi} \cdot \boldsymbol{\chi})^{\frac{N+n}{2}} &\rightarrow (N+n)(\boldsymbol{\chi} \cdot \boldsymbol{\chi})^{\frac{N+n}{2}-1} \chi_{\alpha_n} \\
&\rightarrow (N+n)(N+n-2)(\boldsymbol{\chi} \cdot \boldsymbol{\chi})^{\frac{N+n}{2}-2} \chi_{\alpha_{n-1}} \chi_{\alpha_n} \\
&\quad + (N+n)(\boldsymbol{\chi} \cdot \boldsymbol{\chi})^{\frac{N+n}{2}-1} \delta_{\alpha_{n-1}\alpha_n}.
\end{aligned} \tag{7.42}$$

The entire expression is, however, contracted with a traceless tensor, so any Kronecker delta tensors, such as on the last line of the above, contract to zero. This rule carries on through all n derivations: any derivative acting on any factor but the power of $\boldsymbol{\chi} \cdot \boldsymbol{\chi}$ yields a Kronecker delta and contracts to zero. This implies that after n steps we have

$$\begin{aligned}
M_{\alpha_1 \dots \alpha_n} \partial_{\alpha_1} \dots \partial_{\alpha_n} (\boldsymbol{\chi} \cdot \boldsymbol{\chi})^{\frac{N+n}{2}} \\
= 2^n \frac{\left(\frac{N+n}{2}\right)!}{\left(\frac{N-n}{2}\right)!} (\boldsymbol{\chi} \cdot \boldsymbol{\chi})^{\frac{N-n}{2}} M_{\alpha_1 \dots \alpha_n} \chi_{\alpha_1} \dots \chi_{\alpha_n} \propto \psi_M^n(\boldsymbol{\chi}).
\end{aligned} \tag{7.43}$$

Note that this expression is actually only true for $0 \leq n \leq N$. Since we are restricting to states where $\frac{N+n}{2}$ is a positive integer, the exponent of $(\boldsymbol{\chi} \cdot \boldsymbol{\chi})$ will eventually reach zero for $n \geq N$, and any further derivations will yield zero. Thus $\hat{\lambda}$ maps all $n > N$ states to 0, meaning that they are unphysical.

Combining Eqs. (7.40), (7.41) and (7.43) for a state with $n \leq N$ and even $n + N$ finally yields

$$\left(\hat{\lambda} \psi_M^n\right)(\boldsymbol{\rho}) = \frac{2^{1-N} \pi^{\frac{d}{2}} N!}{\Gamma\left(\frac{N+n+d}{2}\right) \left(\frac{N-n}{2}\right)!} \psi_M^n(\boldsymbol{\rho}). \tag{7.44}$$

Since the full Laplacian eigenbasis is complete, this fully determines the range of $\hat{\lambda}$. The physical states are thus spanned by eigenfunctions of the Laplacian of parity $(-1)^N$ for $n \leq N$.

Let us also write $\hat{\lambda}$ in the suggestive form

$$\hat{\lambda} = 2^{1-N} \pi^{\frac{d}{2}} \sum_{k=0}^N M_{Nk} \hat{\mathcal{P}}_k \quad \text{with} \quad M_{Nk} = \begin{cases} \frac{N!}{\Gamma\left(\frac{N+k+d}{2}\right) \left(\frac{N-k}{2}\right)!} & 2 \mid (N+k) \\ 0 & 2 \nmid (N+k) \end{cases} \quad (7.45)$$

where $\hat{\mathcal{P}}_k$ are the projectors onto the k -th Laplacian eigenspace. The notation M_{Nk} is suggestive of a further application in the following section.

We are now also in a position to rigorously show completeness of the set $\{|\Omega\rangle\}$. To do so, choose an arbitrary orthogonal basis $\psi_i^n; i = 1, \dots, g_n$, with respect to the ordinary inner product $(f|g) = \int_{\mathcal{S}^{d-1}} d\Omega f^*(\Omega)g(\Omega)$, for the n -th Laplacian eigenspace, restricting to ones of suitable parity. Also define the Fock space counterparts $|\psi_i^n\rangle = \int_{\mathcal{S}^{d-1}} d\Omega \psi_i^n(\Omega) |\Omega\rangle$. Recall that $\langle\phi|\psi\rangle = \left(\phi \middle| \hat{\lambda}\psi\right)$. Since Eq. (7.44) shows that $\hat{\lambda}$ merely scales each of the mutually orthogonal Laplacian eigenspaces, $(\psi_i^n|\psi_j^m) = 0 (\neq 0)$ implies $\langle\psi_i^n|\psi_j^m\rangle = 0 (\neq 0)$. Thus the $|\psi_i^n\rangle$ form an orthogonal set of states. There are $g_s + g_{s+2} + \dots + g_N$ states in the set where the g_i are given by Eq. (7.39) and s is the integer remainder of N divided by 2. Easily summing up the telescoping series shows that there are $\binom{N+d-1}{d-1}$ states in the set, which is exactly the dimension of the N -particle Fock space \mathcal{F}_N . Hence the set $\{|\psi_i^n\rangle\}$ is complete as well. Since all of its members are defined as superpositions of states from the set $\{|\Omega\rangle\}$, the latter also has to be complete.

7.3.3 THE T MAP

To conclude the general treatment of the rotor mapping, and introduce some of its most curious properties, let us construct the map T taking Fock states into the physical subspace of \mathcal{R}_d .

We follow the standard steps outlined in Sec. 7.1.2. We construct a family of states $\lambda_\Omega \in \mathcal{R}_d$ such that $\lambda_\Omega(\rho) = \lambda^*(\Omega, \rho) = (\Omega \cdot \rho)^N$, the derived states κ_Ω with $\kappa_\Omega(\rho) = \left(\hat{\lambda}^{-2}\lambda_\Omega\right)(\rho) \equiv \kappa^*(\Omega, \rho)$, and their Fock-space counterparts $|\kappa_\Omega\rangle = \int_{\mathcal{S}^{d-1}} d\Omega \kappa^*(\Omega, \rho) |\rho\rangle$. Specifically for the rotor mapping, these have

the curious property that

$$\begin{aligned}
|\kappa_{\Omega}\rangle &= \frac{1}{\sqrt{N!}} \int_{\mathcal{S}^{d-1}} d\Omega \kappa^*(\Omega, \rho) (\rho \cdot \hat{\mathbf{a}}^\dagger)^N |0\rangle \\
&= \frac{1}{\sqrt{N!}} \int_{\mathcal{S}^{d-1}} d\Omega \kappa(\Omega, \rho) \lambda(\rho, \hat{\mathbf{a}}^\dagger) |0\rangle
\end{aligned} \tag{7.46}$$

where we have anticipated the realness of $\kappa(\cdot, \cdot)$.

From the general results of Sec. 7.1.2, it may be verified that $\kappa(\cdot, \cdot)$ is the integral kernel of $\hat{\lambda}^{-1}$. Furthermore, the product of two integral operators with integral kernels $\alpha(\cdot, \cdot)$ and $\beta(\cdot, \cdot)$ is itself an integral operator, with an integral kernel given by $\int_{\mathcal{S}^{d-1}} d\Omega \alpha(\cdot, \Omega) \beta(\Omega, \cdot)$. From this and Eq. (7.46) it follows that

$$|\kappa_{\Omega}\rangle = \frac{1}{\sqrt{N!}} \mathcal{J}(\Omega, \hat{\mathbf{a}}^\dagger) |0\rangle \tag{7.47}$$

where $\mathcal{J}(\cdot, \cdot)$ is the reproducing kernel of Eq. (7.7).

To find this kernel, refer back to the expression of $\hat{\lambda}$ as a sum of Laplacian eigenspace projector operators in Eq. (7.45). $\hat{\lambda}$ is an integral operator with integral kernel $\lambda(\Omega, \rho) = (\Omega \cdot \rho)^N$, but the calculation deriving Eq. (7.45) would proceed completely analogously for operators with integral kernels $(\Omega \cdot \rho)^k$ for other nonnegative integers k , by simply replacing every occurrence of N with k . To formalize this, introduce a family of integral operators $\hat{\mu}_k; k = 0, 1, \dots, N$, with respective kernels $\mu_k(\Omega, \rho) \equiv 2^{k-1} \pi^{-\frac{d}{2}} (\Omega \cdot \rho)^k$, with the constants chosen for later convenience. Arrange these into a vector $\hat{\underline{\mu}} = [\hat{\mu}_0, \hat{\mu}_1, \dots, \hat{\mu}_N]^T$. Also define the vector of Laplacian-eigenspace projectors $\hat{\underline{\mathcal{P}}} = [\hat{\mathcal{P}}_0, \hat{\mathcal{P}}_1, \dots, \hat{\mathcal{P}}_N]^T$. The generalisation of Eq. (7.45) can then succinctly be written as $\hat{\underline{\mu}} = \underline{\underline{M}} \hat{\underline{\mathcal{P}}}$ where $\underline{\underline{M}}$ is a matrix with entries

$$M_{jk} = \begin{cases} \frac{j!}{\Gamma\left(\frac{j+k+d}{2}\right) \left(\frac{j-k}{2}\right)!} & 2 \mid (j+k) \text{ and } k \leq j \\ 0 & 2 \nmid (j+k) \text{ or } k > j. \end{cases} \tag{7.48}$$

By inverting this matrix, the projectors $\hat{\mathcal{P}}_j$ can be expressed as sums of the integral operators $\hat{\mu}_k$. This implies that the projectors themselves are integral operators, with kernels given by the corresponding sum of the $\hat{\mu}_k$ operators'

(7.51) yields

$$|\kappa_{\Omega}\rangle = \left(2\pi^{\frac{d}{2}}\sqrt{N!}\right)^{-1} \sum_{n=s}^N (-1)^{\frac{N+n}{2}} 2^n \frac{\Gamma\left(\frac{N+n+d}{2}\right)}{n! \left(\frac{N-n}{2}\right)!} (\hat{\mathbf{a}}^{\dagger} \cdot \hat{\mathbf{a}}^{\dagger})^{\frac{N-n}{2}} (\boldsymbol{\Omega} \cdot \hat{\mathbf{a}}^{\dagger})^n |0\rangle. \quad (7.52)$$

While seemingly computationally intense, this allows us to express any Fock N -particle Fock state $|\psi\rangle$ as a unique state $T|\psi\rangle$ in the physical subspace, again through the relation $(T|\psi\rangle)(\boldsymbol{\Omega}) = \langle\kappa_{\Omega}|\psi\rangle$.

This concludes the general treatment of the rotor mapping. In the next chapter we demonstrate how low-dimensional versions of it may be fruitfully applied to study well-known systems such as the Josephson model and tightly confined Bose-Einstein condensates of spin-1 and spin-2 species.

Before moving on to applications, it should be remarked that there are still some open questions about the abstract rotor mapping, which are the subject of ongoing research. A seemingly very promising direction is attempting to answer the question of whether performing calculations in the special basis, yielding the simple resolution of Eq. (7.12) in the rotor setting, is feasible. It is possible to express $\hat{\lambda}$ as a function of the Laplacian ∇^2 and identify linear combinations of Ω_{α} and ∇_{α} with simple commutation relations with respect to arbitrary functions of the Laplacian. This allows one to derive an analogue of the second desired property on page 84, which is expressed with respect to the original rotor basis in Eq. (7.28), for the new basis. At this preliminary stage it appears that the cost of the simple induced inner product is that the Hamiltonian picks up a somewhat complicated function of the Laplacian, but one that the aforementioned simple commutation relations nevertheless make surprisingly manageable.

8

LOW-DIMENSIONAL APPLICATIONS OF THE ROTOR MAPPING

In this chapter, the rotor mapping, whose abstract properties were introduced in Sec. 7.3 of the previous chapter, is applied to several well known systems with a small number of modes, in order to demonstrate the mapping's utility. The systems considered are the double-well Bose-Hubbard Hamiltonian, a tightly-confined condensate of spin-1 atoms, and one of spin-2 atoms, covered in successive sections of this chapter. The results of the spin-2 section also provide the foundation for the more specific treatments within Chapters 9 and 10.

Before turning to the concrete applications, it is advantageous to state a rule of thumb for finding the single-particle basis in which the rotor Hamiltonian is expected to take the simplest, most manageable form. As remarked in the discussion motivating the choice of integration measure above Eq. (7.25), single-particle bases related by orthogonal transformations induce overcomplete rotor bases related to each other by rotations, and can thus largely be considered equivalent, while there is no such simple picture for general unitary transformations. The choice of a basis up to orthogonal transformations

therefore appears rather important.

Consider now a d -mode Hamiltonian and arrange the annihilation operators into a vector $\hat{\mathbf{a}} = [\hat{a}_1, \hat{a}_2, \dots, \hat{a}_d]^T$. We will be dealing with particle-conserving Hermitian Hamiltonians. These may always be expressed as sums of products of building blocks of the form $\hat{\mathbf{a}}^\dagger H^i \hat{\mathbf{a}}$ with some matrices H^i . The rule of thumb then states that we should find a new basis $\hat{\mathbf{b}} \equiv U \hat{\mathbf{a}}$, with U a unitary matrix, such that as many as possible of the transformed matrices $A^i \equiv U H^i U^\dagger$ are as close as possible to completely imaginary and antisymmetric matrices. This is desirable as $\hat{\mathbf{a}}^\dagger A \hat{\mathbf{a}}$ with completely imaginary and antisymmetric A are mapped onto sums of well-behaved generalised angular-momentum operators, $\hat{L}_{\alpha\beta} = -i(\Omega_\alpha \nabla_\beta - \Omega_\beta \nabla_\alpha)$, under the rotor mapping. More complicated terms, for example squares of such bilinears, should generally be given priority.

In tightly-confined bosonic spin- F mappings, i.e., $F \in \mathbb{N}$, this turns out to be possible on representation-theoretic grounds. The most complicated term of the Hamiltonian is typically proportional to $\hat{\mathbf{a}}^\dagger F^i \hat{\mathbf{a}} \hat{\mathbf{a}}^\dagger F^i \hat{\mathbf{a}}$, with an implied summation over i . F^i are spin- F matrices. These are generators of the spin- F representations of $SU(2)$, the double cover of $SO(3)$. It is well known that the bosonic $SU(2)$ representations map points of $SU(2)$, corresponding to the same underlying element of $SO(3)$, to the same matrix. These representations can thus also be thought as those of $SO(3)$, a real group. By virtue of this they are guaranteed to admit a basis in which all the F^i generate orthogonal matrices, meaning that they themselves are imaginary and antisymmetric. In practical terms, familiar to most physicists, this basis may be constructed in analogy to transforming the three-dimensional spherical harmonics Y_{Fm} , with $m = -F, -F + 1, \dots, F$, into their everywhere-real superpositions.

8.1 THE DOUBLE-WELL BOSE-HUBBARD MODEL

Consider a system of N scalar particles with repulsive interactions in a pair of potential wells such that there is some tunnelling between them. In the context of condensates, this setup could be constructed by optical means, making the system well described by an effective Bose-Hubbard Hamiltonian,

as outlined in Sec. 1.2 of the introduction. We take the Hamiltonian to be

$$\hat{H} = \frac{U}{2} [\hat{n}_1 (\hat{n}_1 - 1) + \hat{n}_2 (\hat{n}_2 - 1)] - J (\hat{a}_1^\dagger \hat{a}_2 + \hat{a}_2^\dagger \hat{a}_1) \quad (8.1)$$

where \hat{a}_i are the annihilation operators for particles on the i -th site, $i = 1, 2$, $\hat{n}_i = \hat{a}_i^\dagger \hat{a}_i$ are the respective particle number operators, and U and J are positive constants parametrising the repulsive interaction and inter-site hopping, respectively.

Before tackling its spectrum through the rotor mapping, let us remark on the more traditional, low-energy treatment of the model. This consists of letting $\hat{a}_i = e^{i\hat{\varphi}_i} \sqrt{\hat{n}_i}$, either directly as operators or by first reverting to a classical Hamiltonian and subsequently imposing the commutation relations $[\hat{n}_i, \hat{\varphi}_j] = i\delta_{ij}$. The exact form of the Hamiltonian expressed with these hydrodynamic variables is not easy to work with, but keeping the highest-order terms in N when this is large yields

$$\hat{H}_J = -JN \cos 2\hat{\varphi} + \frac{U}{4}\hat{n}^2, \quad (8.2)$$

equivalent to the Hamiltonian of the Josephson model.^{54,7} Here $\hat{\varphi} \equiv \frac{1}{2}(\hat{\varphi}_1 - \hat{\varphi}_2)$ and $\hat{n} \equiv \hat{n}_1 - \hat{n}_2$, implying $[\hat{n}, \hat{\varphi}] = i$. By treating \hat{n} as $i\partial_\varphi$, finding the spectrum becomes equivalent to solving the one-dimensional Schrödinger equation for a particle with mass $2/U$ moving in a potential $V(\varphi) = -JN \cos 2\varphi$.

To find the periodicity condition for the resulting wave functions, first introduce the variable $\varphi_T \equiv \frac{1}{2}(\varphi_1 + \varphi_2)$. Wave functions can be considered as functions of either φ_1 and φ_2 , or φ and φ_T . Any wave function can be expanded in terms of a separable basis of states satisfying the constraint $\hat{n}_1 + \hat{n}_2 = i\partial_{\varphi_1} + i\partial_{\varphi_2} = N$. We denote its members by

$$\psi_{n_1, n_2}(\varphi_1, \varphi_2) = \exp[-i(n_1\varphi_1 + n_2\varphi_2)] = \exp[-i(N\varphi_T + n\varphi)] \quad (8.3)$$

where $n = n_1 - n_2$. Since the spectra of $\hat{n}_{1,2}$ consist of positive integers, any

wave function can be expanded, for a set of complex coefficients c_k , as

$$\begin{aligned}\psi(\varphi_1, \varphi_2) &= \sum_{k=0}^N c_k \psi_{k, N-k}(\varphi_1, \varphi_2) = e^{-iN\varphi_T} \sum_{k=0}^N c_k e^{i(N-2k)\varphi} \\ &\equiv e^{-iN\varphi_T} \psi_{\text{eff}}(\varphi).\end{aligned}\tag{8.4}$$

This completely fixes the φ_T dependence, effectively eliminating the variable from the problem, consistent with its absence from Hamiltonian (8.2). Furthermore, the definition of ψ_{eff} above indicates that an appropriate periodicity condition is $\psi_{\text{eff}}(\varphi + \pi) = (-1)^N \psi_{\text{eff}}(\varphi)$.

The spectrum of the above problem closely approximates that of the original double-well problem for large particle numbers N . The rotor mapping, however, is exact, regardless of particle number. It was first derived through a somewhat different procedure, akin to the Bargmann transform of Sec. 7.2, by Anglin et al.⁸ The present exposition will put more emphasis on the mechanics of the rotor mapping that may be generalised to arbitrary dimensions. Let us first transform Hamiltonian (8.1) into a form allowing us to make contact with the rule of thumb for finding an optimal single-particle basis for the mapping, set out in the opening of the chapter. Since $\hat{n}_1 + \hat{n}_2 = N$ is constant, the interaction term equals

$$\begin{aligned}\hat{H}_I &\equiv -\frac{UN}{2} + \frac{U}{2} [\hat{n}_1^2 + \hat{n}_2^2] = -\frac{UN}{2} + \frac{U}{4} [(\hat{n}_1 + \hat{n}_2)^2 + (\hat{n}_1 - \hat{n}_2)^2] \\ &= \frac{UN}{4} (N - 2) + \frac{U}{4} (\hat{\mathbf{a}}^\dagger \sigma_z \hat{\mathbf{a}})^2\end{aligned}\tag{8.5}$$

where $\sigma_z = \text{diag}(1, -1)$ is the third Pauli matrix and $\hat{\mathbf{a}} = [\hat{a}_1, \hat{a}_2]^T$. Up to a constant, the full Hamiltonian then reads

$$\hat{H} = \frac{U}{4} (\hat{\mathbf{a}}^\dagger \sigma_z \hat{\mathbf{a}})^2 - J \hat{\mathbf{a}}^\dagger \sigma_x \hat{\mathbf{a}}\tag{8.6}$$

where $\sigma_x = \begin{pmatrix} 0 & 1 \\ 1 & 0 \end{pmatrix}$ is the first Pauli matrix. According to the rule of thumb one should try to antisymmetrise the first term. A new single-particle basis

achieving this is readily found as*:

$$\hat{b}_x = \frac{\hat{a}_1 + \hat{a}_2}{\sqrt{2}} \quad \text{and} \quad \hat{b}_y = -i \frac{\hat{a}_1 - \hat{a}_2}{\sqrt{2}}. \quad (8.7)$$

In the new basis the Hamiltonian reads

$$\hat{H} = \frac{U}{4} \left(\hat{\mathbf{b}}^\dagger \sigma_y \hat{\mathbf{b}} \right)^2 - J \hat{\mathbf{b}}^\dagger \sigma_z \hat{\mathbf{b}}. \quad (8.8)$$

where $\sigma_y = \begin{pmatrix} 0 & -i \\ i & 0 \end{pmatrix}$ is the remaining second Pauli matrix. Employing the general formalism of the previous chapter and defining

$$|\mathbf{\Omega}\rangle \equiv \frac{1}{\sqrt{N!}} \left(\mathbf{\Omega} \cdot \hat{\mathbf{b}}^\dagger \right)^N |0\rangle \quad \text{and} \quad |\psi\rangle = \int_{S^1} d\mathbf{\Omega} \psi(\mathbf{\Omega}) |\mathbf{\Omega}\rangle, \quad (8.9)$$

where $\hat{\mathbf{b}} = [\hat{b}_x, \hat{b}_y]^T$ and $\mathbf{\Omega} = [\Omega_x, \Omega_y]^T$, allows one to apply the general mapping rule in Eq. (7.36) to obtain the rotor Hamiltonian

$$\hat{\mathcal{H}} = \frac{U}{4} \hat{L}_{xy}^2 - J(N+2) \hat{\mathbf{\Omega}}^T \sigma_z \hat{\mathbf{\Omega}} + J \hat{\mathbf{\Omega}}^T \sigma_z \mathbf{\nabla}. \quad (8.10)$$

After this stage, working with the constrained Euclidean coordinates $\mathbf{\Omega}$ does not really offer any advantages, due to the simplicity of the circle, and the above Hamiltonian simplifies when expressed with respect to the angular coordinate φ . One has $\mathbf{\Omega} = [\cos \varphi, \sin \varphi]^T$, $\mathbf{\nabla} = [-\sin \varphi \partial_\varphi, \cos \varphi \partial_\varphi]$ and $\hat{L}_{xy} = -i\partial_\varphi$. Furthermore, this implies $\hat{\mathbf{\Omega}}^T \sigma_z \hat{\mathbf{\Omega}} = \cos 2\varphi$ and $\hat{\mathbf{\Omega}}^T \sigma_z \mathbf{\nabla} = -\sin 2\varphi \partial_\varphi$, so that Hamiltonian (8.10) is equivalent to

$$\hat{\mathcal{H}} = -\frac{U}{4} \partial_\varphi^2 - J(N+2) \cos 2\hat{\varphi} - J \sin 2\hat{\varphi} \partial_\varphi. \quad (8.11)$$

At first sight the last term of $\hat{\mathcal{H}}$ does not look Hermitian. The truth is that the notion of Hermiticity depends on the inner product, and the last term indeed *is* Hermitian with respect to the induced rotor inner product,

*One may again follow representation-theoretic reasoning for the basis, although it is hardly illuminating in this case, given the simplicity of the problem. σ_z can be taken to generate a reducible representation of $U(1)$, a direct sum of the ± 1 representations. This is exactly the complexification of the fundamental real representation, so a similarity transform between the two may be found.

$\langle \phi | \psi \rangle = \iint d\varphi_1 d\varphi_2 \phi^*(\varphi_1) \cos^N(\varphi_1 - \varphi_2) \psi(\varphi_2)$. However, the spectrum of an operator does not depend on the inner product, so one is allowed to work with the simpler single-integral inner product when diagonalising $\hat{\mathcal{H}}$. The latter is *not* Hermitian with respect to the standard inner product, but in the case of the double-well rotor Hamiltonian, a simple Hermitianising transform may be found.⁸ Letting $\hat{S} = \frac{J}{U} \cos 2\hat{\varphi}$, the Hermitian Hamiltonian is obtained as

$$\hat{\mathcal{H}}' = e^{-\hat{S}} \hat{\mathcal{H}} e^{\hat{S}} = -\frac{U}{4} \partial_\varphi^2 - J(N+1) \cos 2\hat{\varphi} + \frac{U^2}{J} \sin^2 2\hat{\varphi} \quad (8.12)$$

The large- N limit of the above Hamiltonian can be seen to agree with the Josephson Hamiltonian of Eq. (8.2), and also possesses the same periodicity conditions, due to the general (anti)symmetrisation requirements of the rotor mapping. Hamiltonian (8.12) is, however, exact for arbitrary N .

8.2 TIGHTLY CONFINED SPIN-1 CONDENSATES

Tightly confined spin-1 condensates obey the SMA Hamiltonian introduced in Eq. (6.1). Due to the fixed number of particles N and the fact that $g_2 = 0$ for spin-1, the Hamiltonian may be rewritten as

$$\begin{aligned} \hat{H} &= \frac{g_1}{2N} \hat{\mathbf{F}}^2 - q \hat{a}_0^\dagger \hat{a}_0 \\ \hat{F}^i &\equiv \hat{\mathbf{a}}^\dagger F^i \hat{\mathbf{a}} \quad \text{for } i = x, y, z \end{aligned} \quad (8.13)$$

where $\hat{\mathbf{a}} = [\hat{a}_1, \hat{a}_0, \hat{a}_{-1}]$ and F^i are the spin-1 matrices, given by:

$$F^x = \frac{1}{\sqrt{2}} \begin{pmatrix} 0 & 1 & 0 \\ 1 & 0 & 1 \\ 0 & 1 & 0 \end{pmatrix} \quad F^y = \frac{i}{\sqrt{2}} \begin{pmatrix} 0 & -1 & 0 \\ 1 & 0 & -1 \\ 0 & 1 & 0 \end{pmatrix} \quad F^z = \begin{pmatrix} 1 & 0 & 0 \\ 0 & 0 & 0 \\ 0 & 0 & -1 \end{pmatrix}. \quad (8.14)$$

Applying the general basis-simplifying rule of thumb is particularly rewarding in this case. Choosing the new operators as

$$\hat{b}_x = -\frac{\hat{a}_1 - \hat{a}_{-1}}{\sqrt{2}}, \quad \hat{b}_y = -i \frac{\hat{a}_1 + \hat{a}_{-1}}{\sqrt{2}}, \quad \text{and} \quad \hat{b}_z = \hat{a}_0 \quad (8.15)$$

and arranging them into a vector $\hat{\mathbf{b}} = [\hat{b}_x, \hat{b}_y, \hat{b}_z]^T$ allows one to express $\hat{F}^i = \hat{\mathbf{b}}^\dagger M^i \hat{\mathbf{b}}$ with $(M^i)_{jk} = -i\varepsilon_{ijk}$, where ε is the Levi-Civita tensor. Even more concisely, $\hat{\mathbf{F}} = -i\hat{\mathbf{b}}^\dagger \times \hat{\mathbf{b}}$.

This also gives the overcomplete rotor basis $|\mathbf{\Omega}\rangle = \frac{1}{\sqrt{N!}}(\mathbf{\Omega} \cdot \hat{\mathbf{b}}^\dagger)^N |0\rangle$ an additional interpretation as the degenerate family of ground states at the mean-field level for an antiferromagnetic condensate at zero external field,⁸⁹ i.e., with $c_1 > 0$ and $p = q = 0$ in the notation of Eq. (5.4). In other words, members of the rotor basis correspond to the spatial rotations of the polar states (5.7) or (5.8).[†] Recalling that polar states have Majorana representations consisting of two diametrically opposite points, these can even be seen to be given by $\pm\mathbf{\Omega}$ for the state $|\mathbf{\Omega}\rangle$.

Under the rotor mapping, the \hat{F}^i map onto $-\hat{L}^i$, the i -th component of the three-dimensional angular momentum, and $\hat{\mathbf{F}}^2$ onto $\hat{\mathbf{L}}^2 = -\nabla^2$. Performing the mapping, in complete analogy with the previous section, we obtain

$$\hat{\mathcal{H}} = -\frac{g_1}{2N}\nabla^2 - q(N+3)\hat{\Omega}_z^2 + q\hat{\Omega}_z\nabla_z. \quad (8.16)$$

We will again benefit by changing to spherical coordinates with

$$\mathbf{\Omega} = (\sin\theta \cos\varphi, \sin\theta \sin\varphi, \cos\theta) \text{ and } \nabla_z = -\sin\theta \partial_\theta. \quad (8.17)$$

The final term is again not Hermitian with respect to the standard inner product on the sphere. Fortunately, in this case too there turns out to exist a simple Hermitianising similarity transform.¹² This time letting $\hat{S} = \frac{qN}{4g_1} \cos 2\hat{\theta}$, we obtain

$$\hat{\mathcal{H}}' = e^{-\hat{S}}\hat{\mathcal{H}}e^{\hat{S}} = -\frac{g_1}{2N}\nabla^2 + q\left(N + \frac{3}{2}\right)\sin^2\hat{\theta} + \frac{q^2N}{8g_1}\sin^2 2\hat{\theta} \quad (8.18)$$

[†]This can be seen from the mean-field energy expression in Eq. (5.4). Working in the present $\hat{\mathbf{b}}$ basis, the c-number vector $\boldsymbol{\chi}$ is replaced by $\mathbf{\Omega}$ and the spin expectation value becomes $\mathbf{F} = -i\mathbf{\Omega}^* \times \mathbf{\Omega} = 0$, where the last equality follows on account of $\mathbf{\Omega}$ being real. At zero external field the mean-field energy is simply equal to $\frac{c_1 n}{2}\mathbf{F}^2$. Since $c_1 > 0$ and $\mathbf{F}^2 \geq 0$, on account of $\hat{\mathbf{F}}$'s Hermiticity, the expression is obviously minimised by the $|\mathbf{\Omega}\rangle$ states.

where the final two terms represent an effective potential. Note that neither the Hamiltonian nor the similarity transform depend on the azimuthal angle φ . A derivative with respect to it appears in the Laplacian, $\nabla^2 = \sin^{-1} \theta \partial_\theta (\sin \theta \partial_\theta) + \sin^{-2} \theta \partial_\varphi^2$. \hat{F}^z can be shown to map onto $-\hat{L}_z = i\partial_\varphi$ under the rotor mapping, and restricting to an \hat{F}^z eigenspace with eigenvalue m allows one to replace the second term of the Laplacian by $-m^2 \sin^{-2} \theta$. This reduces the problem to a single dimension, parametrised by $\theta \in [0, \pi]$, vastly simplifying calculations.

Let us also remark that for the particular Hamiltonian (8.13), the first $(N+1)(N+2)/2$ lowest-energy eigenstates span the rotor's physical subspace, while all higher-energy eigenstates are unphysical and map to zero, as can be demonstrated by an elegant perturbative argument.¹²

Finally, the rotor mapping Hamiltonian (8.18) may be applied to finding the spectra in different regimes of the parameters N and q/g_1 . In accordance with the results presented in Chapter 6, for $N^{-2} \ll q/g$ the Hamiltonian may be expanded about the pole, $\theta = 0$, yielding an effective isotropic harmonic oscillator Hamiltonian. The mode energy is close to q when $q/g_1 \gg 1$ and close to $\sqrt{2g_1q}$ when $N^{-2} \ll q/g_1 \ll 1$. Both of these results may be derived through Bogoliubov theory.

The regime $q/g_1 \ll N^{-2}$ is, however, inaccessible to Bogoliubov theory due to the emergence of a very-low-energy mode, driving up the depletion. It is nevertheless treatable through the rotor mapping and yields, to a good approximation, the spectrum of the free rotor, $E_\ell = \frac{g_1}{2N} \ell(\ell+1)$ with degeneracies $2\ell+1$, for ℓ taking values of the same parity as N between 0 and N .

8.3 TIGHTLY CONFINED SPIN-2 CONDENSATES

In the spin-2 case, the single mode Hamiltonian retains its full form (6.1):

$$\begin{aligned} \hat{H} &= \frac{g_1}{2N} \hat{\mathbf{F}}^2 + \frac{g_2}{2N} \hat{A}^\dagger \hat{A} + q\hat{Z} \\ \hat{F}^i &\equiv \hat{\mathbf{a}}^\dagger \mathbf{F}^i \hat{\mathbf{a}} \quad \text{for } i = x, y, z, \end{aligned} \tag{8.19}$$

where $\hat{\mathbf{a}} = [\hat{a}_2, \hat{a}_1, \hat{a}_0, \hat{a}_{-1}, \hat{a}_{-2}]$ and F^i are now the spin-2 matrices. Recall from Eq. (5.3d) that $\hat{A} = 2\hat{a}_2\hat{a}_{-2} - 2\hat{a}_1\hat{a}_{-1} + \hat{a}_0\hat{a}_0$. The spin-2 matrices are given by

$$\begin{aligned}
F^x &= \frac{1}{2} \begin{pmatrix} 0 & 2 & 0 & 0 & 0 \\ 2 & 0 & \sqrt{6} & 0 & 0 \\ 0 & \sqrt{6} & 0 & \sqrt{6} & 0 \\ 0 & 0 & \sqrt{6} & 0 & 2 \\ 0 & 0 & 0 & 2 & 0 \end{pmatrix} & F^y &= \frac{i}{2} \begin{pmatrix} 0 & -2 & 0 & 0 & 0 \\ 2 & 0 & -\sqrt{6} & 0 & 0 \\ 0 & \sqrt{6} & 0 & -\sqrt{6} & 0 \\ 0 & 0 & \sqrt{6} & 0 & -2 \\ 0 & 0 & 0 & 2 & 0 \end{pmatrix} \\
F^z &= \begin{pmatrix} 2 & 0 & 0 & 0 & 0 \\ 0 & 1 & 0 & 0 & 0 \\ 0 & 0 & 0 & 0 & 0 \\ 0 & 0 & 0 & -1 & 0 \\ 0 & 0 & 0 & 0 & -2 \end{pmatrix}. & & (8.20)
\end{aligned}$$

The quadratic Zeeman operator is given by $\hat{Z} = \hat{\mathbf{a}}^\dagger (F^z)^2 \hat{\mathbf{a}}$.

The Cartesian basis, antisymmetrising the spin matrices, is given by:

$$\begin{aligned}
\hat{b}_1 &= \hat{a}_0 \\
\hat{b}_2 &= \frac{i}{\sqrt{2}} (\hat{a}_1 + \hat{a}_{-1}) & \hat{b}_4 &= \frac{i}{\sqrt{2}} (\hat{a}_{-2} - \hat{a}_2) \\
\hat{b}_3 &= \frac{1}{\sqrt{2}} (\hat{a}_{-1} - \hat{a}_1) & \hat{b}_5 &= \frac{1}{\sqrt{2}} (\hat{a}_2 + \hat{a}_{-2})
\end{aligned} \tag{8.21}$$

In the new basis, the spin operators become $\hat{F}^i = \hat{\mathbf{b}}^\dagger M^i \hat{\mathbf{b}}$, where the M^i are

given by

$$\begin{aligned}
M^x = -i \begin{pmatrix} 0 & \sqrt{3} & 0 & 0 & 0 \\ -\sqrt{3} & 0 & 0 & 0 & -1 \\ 0 & 0 & 0 & 1 & 0 \\ 0 & 0 & -1 & 0 & 0 \\ 0 & 1 & 0 & 0 & 0 \end{pmatrix} & \quad M^y = -i \begin{pmatrix} 0 & 0 & \sqrt{3} & 0 & 0 \\ 0 & 0 & 0 & 1 & 0 \\ -\sqrt{3} & 0 & 0 & 0 & 1 \\ 0 & -1 & 0 & 0 & 0 \\ 0 & 0 & -1 & 0 & 0 \end{pmatrix} \\
M^z = -i \begin{pmatrix} 0 & 0 & 0 & 0 & 0 \\ 0 & 0 & 1 & 0 & 0 \\ 0 & -1 & 0 & 0 & 0 \\ 0 & 0 & 0 & 0 & 2 \\ 0 & 0 & 0 & -2 & 0 \end{pmatrix}. & \quad (8.22)
\end{aligned}$$

We also denote $Q \equiv (M^z)^2 = \text{diag}(0, 1, 1, 4, 4)$. The quadratic Zeeman operator becomes $\hat{Z} = \hat{\mathbf{b}}^\dagger Q \hat{\mathbf{b}}$.

The matrices above, while imaginary and antisymmetric, display a lot less regularity compared to those of the spin-1 problem, and are somewhat more difficult to work with. This is likely due to the spin-1 representation being similar to the fundamental representation of $\text{SO}(3)$, which is also its adjoint representation, while the spin-2 representation is similar to the traceless symmetric representation, which is rather undistinguished.

We proceed as in the previous sections, namely by constructing the overcomplete basis

$$|\mathbf{\Omega}\rangle = \frac{1}{\sqrt{N!}} \left(\mathbf{\Omega} \cdot \hat{\mathbf{b}}^\dagger \right)^N |0\rangle \quad (8.23)$$

where $\mathbf{\Omega}$ is a norm-1 5-component real vector, i.e., belonging to the 4-sphere \mathcal{S}^4 .

Like in the spin-1 case, members of the basis minimise the mean-field energy in a certain region of the phase diagram. For spin-2 this turns out to be the nematic region, and members of the rotor basis are correspondingly the spatial rotations of nematic mean-field states, characterised by the order parameter $\Psi_n(\eta) = \left(\frac{\sin \eta}{\sqrt{2}}, 0, \cos \eta, 0, \frac{\sin \eta}{\sqrt{2}} \right)^T$ of Eq. (5.12). The connection with the Majorana representation is more obscure than for the spin-1 case,

but the following exact statement can be made: each distinct mean-field state with an order parameter of the form $R(g)\Psi_n(\eta)$ (where $g \in \text{SO}(3)$ ranges over all rotations and $R(g)$ is the matrix corresponding to g in the 5-dimensional representation), can be expressed in the form of Eq. (8.23) with Ω belonging to exactly one pair of diametrically opposite points on the 4-sphere.

Again taking into account the general bilinear rotor mapping rule in Eq. (7.36) we find

$$\begin{aligned}
\hat{F}^x &\rightarrow -\left(\sqrt{3}\hat{L}_{12} - \hat{L}_{25} + \hat{L}_{34}\right) \\
\hat{F}^y &\rightarrow -\left(\sqrt{3}\hat{L}_{13} + \hat{L}_{24} + \hat{L}_{35}\right) \\
\hat{F}^z &\rightarrow -\left(\hat{L}_{23} + 2\hat{L}_{45}\right) \\
\hat{A}^\dagger \hat{A} &\rightarrow \nabla^2 + N^2 + 3N
\end{aligned} \tag{8.24}$$

Assembling these transformations as appropriate for the full Hamiltonian (8.19) finally yields

$$\begin{aligned}
\mathcal{H} &= \frac{g_2}{2N}\nabla^2 + \frac{g_1}{2N}\hat{M}^2 + q(N+5)\hat{\Omega}^T Q \hat{\Omega} - q\hat{\Omega}^T Q \nabla, \\
\hat{M}^i &\equiv \hat{\Omega}^T M^i \nabla = -\frac{i}{2}M_{\alpha\beta}^i \hat{L}_{\alpha\beta} \quad \text{for } i = x, y, z.
\end{aligned} \tag{8.25}$$

When $q = 0$, the resulting Hamiltonian is Hermitian with respect to the standard inner product over the 4-sphere, with the ground state uniformly delocalised about the sphere. Given the previously derived spectrum at $q = 0$,^{60,131} summarised in Sec. 6.3, this is seen to correspond, loosely speaking, to a condensate of singlet pairs. It is interesting to comment on this result in light of the recent publication by Jen and Yip⁵² who pointed out that, even though naïve averaging of nematic states over rotations in all of $\text{SO}(3)$ produces the correct spin-singlet ground state for confined antiferromagnetic spin-1 bosons, extending this to spin-2 does not work, as the singlet is no longer unique in this case.[‡] The rotor mapping demonstrates

[‡]More precisely, for a given even number of particles there is a unique spin-1 many-body singlet state, composed of spin-singlet pairs. In the spin-2 setting, an additional building block for many-body singlets emerges, a spin-singlet trio. For a fixed particle number there are now generally several non-equivalent many-body singlet states, composed of different

that the correct state can in fact be obtained by averaging over the associated 4-sphere.

In the general case, the obtained Hamiltonian is not Hermitian with the standard inner product. Unlike with the double-well Bose-Hubbard Hamiltonian or the analogous spin-1 case, the angular momentum terms of the Hamiltonian appear too complicated for a simple Hermitianising similarity transform, depending only on the position operators $\hat{\Omega}_\alpha$, such as those of Eqs. (8.12) and (8.18), to exist. It may, however, be found exactly when $g_1 = 0$, and approximately when $N|q| \gg |g_{1,2}|$. This is the topic of the next chapter.

As remarked at the end of chapter 7, one may obtain a Hamiltonian, Hermitian with respect to the standard inner product, by working from the start in the special basis (7.12). This would also have the advantage that it would Hermitianise rotor Hamiltonians derived from *any* Hermitian Fock-space Hamiltonian. Working with the special basis is the subject of ongoing research. The corresponding algebra appears rather involved, but displays interesting features that may, hopefully, ultimately make the special basis feasible to work with.

numbers of spin-singlet pairs and trios.

9

EFFECTS OF THE QUADRATIC ZEEMAN EFFECT ON TIGHTLY CONFINED SPIN-2 ATOMS

In this chapter, analytical and numerical results elucidating the response of tightly confined spin-2 atoms to an applied quadratic Zeeman field are presented. The problem has previously evaded an analytical description. The latter is obtained through an application of the rotor mapping, whose abstract properties were introduced in Sec. 7.3 and example applications described in Chapter 8. This chapter also builds upon Sec. 8.3 of the previous chapter which introduces the necessary algebra for the tightly-confined spin-2 mapping.

The numerical results were obtained through a surprisingly successful exact-diagonalisation scheme, which is briefly presented first. In Sec. 9.2, the Hermitianising transform at $g_1 = 0$ is described. Then, in Sec. 9.3, the approximate Hermitianising transform for the $N|q| \gg |g_{1,2}|$ regime is introduced, separately for each sign of q . This yields effective low-energy spectra, and is further applied to finding ground-state overlaps with limiting large- $|q|$ ground

states in Sec. 9.4.

9.1 EXACT DIAGONALISATION

Due to the effective spatial 0-dimensionality of the tightly bound system our problem is that of diagonalising a five-mode many-body Hamiltonian. By further fixing N and F_z , the relevant Fock bases may be enumerated by three independent occupation numbers. The sizes of the bases hence scale as N^3 with particle number N , making it quite feasible to diagonalise Hamiltonian (8.19), or at least find the ground state and its energy, at fixed values of $g_{1,2}$, q , F_z and N with regular desktop hardware on timescales on the order of hours for up to about 300 particles.

Denoting Fock states by

$$|n_2, n_1, n_0, n_{-1}, n_{-2}\rangle \equiv \prod_{m=-2}^2 \frac{\hat{a}_m^\dagger{}^{n_m}}{\sqrt{n_m!}} |0\rangle, \quad (9.1)$$

one way of enumerating the entire Fock basis for fixed N and F_z is by considering n_2, n_1 and n_{-2} as independent variables and letting $n_0 = N + F_z - 3n_2 - 2n_1 + n_{-2}$ and $n_{-1} = 2n_2 + n_1 - 2n_{-2} - F_z$. The ranges of the independent n variables are cumbersome to state but can easily be found programmatically. What remains is expressing the terms of Hamiltonian (8.19) with respect to this basis and diagonalising the resulting sparse matrices, which can be accomplished with standard numerical packages.

9.2 HERMITIANISING TRANSFORM AT $g_1 = 0$

In this special case the Hamiltonian \mathcal{H} of Eq. (8.25) simplifies considerably as $\hat{\mathcal{M}}^2$, arguably its most complicated term, is not present. We assume the correct similarity transform is of the form $e^{\hat{S}}$ where $\hat{S} = S(\hat{\Omega})$ is a function of the position operators only. We seek S such that $\mathcal{H}_0^H \equiv e^{-\hat{S}} \mathcal{H} e^{\hat{S}}$ is Hermitian. The $\hat{\Omega}^T Q \hat{\Omega}$ term of Eq. (8.25) is invariant under this transformation. The Laplacian transforms as $e^{-S} \nabla^2 e^S = \nabla^2 + (\nabla^2 S) + |\nabla S|^2 + 2(\nabla S)^T \nabla$ and the

final non-Hermitian term of Eq. (8.25) picks up a Hermitian $-q\mathbf{\Omega}^T Q(\nabla S)$ term, where hats on operators were suppressed for clarity. Gathering the evidently non-Hermitian terms and demanding that their sum be zero yields the condition

$$\left(\frac{g_2}{N}(\nabla S)^T - q\mathbf{\Omega}^T Q\right)\nabla = 0. \quad (9.2)$$

While one could make progress by formally solving a differential equation for S on the 4-sphere derived from the above, we avoid the tedious aspects of doing so by positing that $S(\mathbf{\Omega}) = \mathbf{\Omega}^T X \mathbf{\Omega}$ for some matrix X . Inserting the ansatz into condition (9.2) and recalling that $\hat{\mathbf{\Omega}} \cdot \nabla = 0$, we see that $X = \frac{qN}{2g_2}Q$ indeed satisfies the condition. By defining $\rho_a \equiv \sqrt{\Omega_2^2 + \Omega_3^2}$ and $\rho_b \equiv \sqrt{\Omega_4^2 + \Omega_5^2}$ this may be put into simple terms as $S(\mathbf{\Omega}) = \frac{qN}{2g_2}(\rho_a^2 + 4\rho_b^2)$. After expanding out S in the remaining terms added by the transformation, the final Hamiltonian is found to be

$$\begin{aligned} \hat{\mathcal{H}}_0^H &= \frac{g_2}{2N}\nabla^2 + q\left(N + \frac{5}{2} - \frac{qN}{2g_2}\right)\hat{\rho}_a^2 \\ &+ 4q\left(N + \frac{5}{2} - \frac{2qN}{g_2}\right)\hat{\rho}_b^2 + \frac{q^2N}{2g_2}(\hat{\rho}_a^2 + 4\hat{\rho}_b^2)^2 \end{aligned} \quad (9.3)$$

9.3 LARGE $N|q|$ LIMITS

9.3.1 LARGE POSITIVE Nq REGIME

For large positive Nq , the dominant $q\hat{Z} = q\hat{a}_\alpha^\dagger(F^z)_{\alpha\beta}^2\hat{a}_\beta$ term in Hamiltonian (8.19) is minimised for the state

$$a_0^{\dagger N}|0\rangle = b_1^{\dagger N}|0\rangle = \frac{1}{2}\int_{\mathcal{S}^4}d^4\Omega(\text{sgn}\Omega_1)^N\prod_{i=2}^5\delta(\Omega_i)|\mathbf{\Omega}\rangle, \quad (9.4)$$

suggesting* that the low-lying exact eigenstates are tightly localised about the $\Omega_1 = \pm 1$ poles. As discussed in Sec. 7.3, the wave function has to have

*This state minimises the $q\hat{Z}$ term among all states with N particles, without regard to fixing F_z . The state obviously has $F_z = 0$, as does the limiting state (9.12) in the negative q regime, suggesting the \hat{F}_z null space as a particularly natural choice. We consider F_z to be fixed at 0 for the remainder of Sec. 9.3.

parity $(-1)^N$, so we may restrict our attention to the region about one of the poles and infer the wave function's behaviour about the other by symmetry. Choosing to expand about the $\Omega_1 = +1$ pole motivates the reparametrisation

$$\boldsymbol{\Omega} = (\sqrt{1 - \mathbf{x}^2}, \mathbf{x})^T. \quad (9.5)$$

The indices of \mathbf{x} are taken to run from 2 to 5 to avoid excessive arithmetic in subscripts. Next assume that low-lying states are of the form

$$\psi_n(\mathbf{x}) = h_n(\mathbf{x})e^{-\frac{N}{2}\mathbf{x}^T\Gamma\mathbf{x}} \quad (9.6)$$

where n is a generic (multi)index label, $\Gamma = \text{diag}(\gamma_2, \dots, \gamma_5)$ is some diagonal matrix, and h_n are some residual functions of sub-exponential growth, such as, for example, Hermite polynomials. The overall factor of N was extracted for later convenience. The diagonal elements of $N\Gamma$ can be interpreted as inverse squared oscillator lengths ξ_{i0} for the i -th direction, i.e., $N\gamma_i = \xi_{i0}^{-2}$. The assumption of tight localisation amounts to the condition $\xi_{i0} \ll 1$, which has to be checked for consistency at the end of the calculation. Since $\langle x_i^n \partial_j^m \rangle \lesssim \xi_{i0}^n / \xi_{j0}^m$,[†] this allows us to simplify the Hamiltonian (8.25) by keeping only the lowest ξ_{i0} terms multiplied by each of $\frac{q_{1,2}}{N}$, q , and Nq .

The goal now is to express Hamiltonian (8.25) in terms of x_i and $\partial_i \equiv \frac{\partial}{\partial x_i}$. The former follows from the coordinate definitions in Eq. (9.5), while the latter follows from computing the spherical gradient components ∇_α , as introduced in Sec. 7.3.1, expressed in terms of the new coordinate system. This leads to

$$\begin{aligned} \nabla_1 &= -\sqrt{1 - \mathbf{x}^2} \mathbf{x} \cdot \boldsymbol{\partial} \\ \nabla_i &= \partial_i - x_i \mathbf{x} \cdot \boldsymbol{\partial} \quad \text{for } i > 1 \end{aligned} \quad (9.7)$$

Carrying out the necessary index algebra and truncating at the lowest order

[†]Due to wave function parity such expectation values may be much less or even vanish, but the stated quantity is the upper limit on their order of magnitude.

ξ_{i0} terms yields the simple expressions

$$\begin{aligned}\nabla^2 &\simeq \boldsymbol{\partial} \cdot \boldsymbol{\partial} & \boldsymbol{\Omega}^T Q \boldsymbol{\Omega} &\simeq \mathbf{x}^T Q' \mathbf{x} \\ \mathbf{M}^2 &\simeq -3 (\partial_2^2 + \partial_3^2) & \boldsymbol{\Omega}^T Q \nabla &\simeq \mathbf{x}^T Q' \boldsymbol{\partial}\end{aligned}\quad (9.8)$$

where $Q' \equiv \text{diag}(1, 1, 4, 4)$ is Q with the first row and column omitted. Putting this all together and letting $\hat{p}_i = -i\partial_i$, we obtain an approximate Hamiltonian $\hat{\mathcal{H}}_+ = \sum_{i=2}^5 \hat{\mathcal{H}}_i$ where

$$\hat{\mathcal{H}}_i = \frac{A_i}{2N} \hat{p}_i^2 + \frac{NB_i}{2} \hat{x}_i^2 - iC_i \hat{x}_i \hat{p}_i. \quad (9.9)$$

The various constants in this Hamiltonian are as follows:

$$\begin{aligned}A_{2,3} &= 3g_1 + |g_2| & A_{4,5} &= |g_2| \\ C_{2,3} &= q & C_{4,5} &= 4q \\ B_i &= t_N C_i & \nu_i &\equiv C_i/A_i \\ t_N &\equiv 2 + 5/N\end{aligned}\quad (9.10)$$

The quantities t_N and ν_i are introduced for the purpose of later notation. This allows us to treat each direction individually. Following reasoning analogous to that of Sec. 9.2 and applying the similarity transform $\hat{\mathcal{H}}_+^H = e^{-\hat{S}} \hat{\mathcal{H}}_+ e^{\hat{S}}$ with $\hat{S} = -N \sum_i \nu_i \hat{x}_i^2/2$, we obtain a Hermitian sum of four independent harmonic oscillator Hamiltonians, i.e., a Hamiltonian with terms of the same form as Eq. (9.9), but with new constants $A'_i = A_i$, $B'_i = B_i + C_i^2/A_i$ and $C'_i = 0$.

This allows us to simply read off mode energies and oscillator lengths. They are given by

$$\begin{aligned}\Delta E_i &= C_i \sqrt{1 + t_N/\nu_i}, \\ \xi_i^{-2} &= N\nu_i \sqrt{1 + t_N/\nu_i}, \\ N\gamma_i = \xi_{i0}^{-2} &= N\nu_i \left(1 + \sqrt{1 + t_N/\nu_i}\right),\end{aligned}\quad (9.11)$$

where ξ_i are the oscillator lengths of the Hermitianised Hamiltonian whereas ξ_{i0} are those of the original non-Hermitian Hamiltonian. The solutions are

indeed of the form assumed in Eq. (9.6). Referring to Eq. (9.10) allows us to verify that $\xi_{i0} \ll 1$ and thus the consistency of our approach when $Nq \gg |g_{1,2}|$.

The obtained mode energies agree very well with the numerically obtained spectrum. As an illustration, the largest relative discrepancy among the 100 lowest analytically and numerically obtained energies at $N = 100$, $g_1 = |g_2|$, $q = 100|g_2|$ is 1.1 percent. The accuracy of the oscillator lengths, or rather the wave functions in general, is discussed in Sec. 9.4. A sketch of the large-positive- Nq rotor ground state is shown in Fig. 9.1.

It is interesting to note that the four modes agree exactly with the continuum Bogoliubov mode energies at zero momentum, minus the density mode.¹¹⁸ The author believes this to be a non-trivial result as the number of particles N does not necessarily have to be large. Nevertheless, the limiting state about which we are expanding is of the mean-field form.

The rotor framework is also capable of describing excitations about fragmented states. This is demonstrated in the following subsection. As stated previously, such excitations are outside the reach of conventional Bogoliubov analysis.

9.3.2 LARGE NEGATIVE Nq REGIME

For large negative values of Nq , i.e., when $-Nq \gg |g_{1,2}|$, the dominant $q\hat{Z}$ term in Hamiltonian (8.19) is minimised for the state

$$\begin{aligned} \left(\hat{a}_2^\dagger \hat{a}_{-2}^\dagger\right)^{N/2} |0\rangle &\propto \int d\varphi \left(e^{i\varphi} a_2^\dagger + e^{-i\varphi} a_{-2}^\dagger\right)^N |0\rangle \\ &\propto \int d\varphi \left(\cos \varphi b_4^\dagger + \sin \varphi b_5^\dagger\right)^N |0\rangle \\ &\propto \int d^4\Omega \delta(\Omega_1) \delta(\Omega_2) \delta(\Omega_3) |\mathbf{\Omega}\rangle \end{aligned} \quad (9.12)$$

Note that the first line of the above equation clearly demonstrates that we are working with a fragmented state, with two macroscopically occupied single-particle states for large N . As mentioned before, the rotor mapping is of

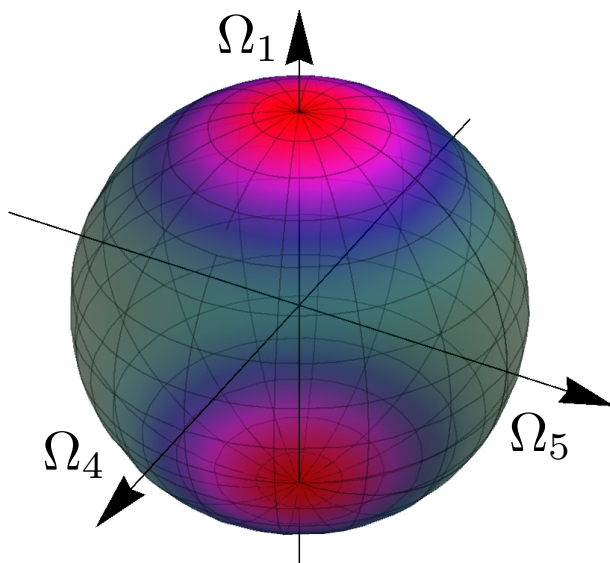


Figure 9.1: A schematic representation of the ground state wave function at large positive Nq . Brighter, more opaque colours represent areas of greater wave-function magnitude. The Ω_2 and Ω_3 coordinates are omitted and considered set to 0, but the wave function is localised in both of them as well.

particular utility here.

An appropriate reparametrisation in this case is

$$\begin{aligned}\Omega_i &= x_i && \text{for } i = 1, 2, 3, \\ (\Omega_4, \Omega_5) &= \sqrt{1 - \mathbf{x}^2} (\cos \varphi, \sin \varphi),\end{aligned}\tag{9.13}$$

where we have reused the label x from the $Nq \gg |g_{1,2}|$ case for three of the coordinates and introduced the angular variable φ as the fourth. Further reusing notation from the previous subsection, we assume low-energy states can be written as

$$\psi_n(\mathbf{x}, \varphi) = h_n(\mathbf{x}, \varphi) e^{-\frac{N}{2} \mathbf{x}^T \Gamma \mathbf{x}},\tag{9.14}$$

in analogy with Eq. (9.6) for large positive Nq . Here h_n is of subexponential growth in $|\mathbf{x}|$ and periodic in φ , and $\Gamma = \text{diag}(\gamma_1, \gamma_2, \gamma_3)$. We again assume the $\xi_{i0} \equiv (N\gamma_i)^{-1/2}$ are small, allowing us to keep only the lowest ξ_{i0} terms, multiplied by each of $\frac{g_{1,2}}{N}$, q and Nq . Additionally, we assume that the wave

function is not localised in the φ direction, so that $\partial_\varphi \equiv \frac{\partial}{\partial\varphi}$ is of order 1, in the sense that its matrix elements with low-lying states are at most of order 1.

Again let $\partial_i \equiv \frac{\partial}{\partial x_i}$ and define $\boldsymbol{\partial} \equiv (\partial_1, \partial_2, \partial_3)$. Note that $\boldsymbol{\partial}$ does not contain ∂_φ . The gradient components are found to be

$$\begin{aligned}\nabla_i &= \partial_i - x_i \mathbf{x} \cdot \boldsymbol{\partial} \quad \text{for } i = 1, 2, 3, \\ \nabla_4 &= -\sqrt{1 - \mathbf{x}^2} \cos \varphi \mathbf{x} \cdot \boldsymbol{\partial} - \frac{\sin \varphi}{\sqrt{1 - \mathbf{x}^2}} \partial_\varphi, \\ \nabla_5 &= -\sqrt{1 - \mathbf{x}^2} \sin \varphi \mathbf{x} \cdot \boldsymbol{\partial} + \frac{\cos \varphi}{\sqrt{1 - \mathbf{x}^2}} \partial_\varphi.\end{aligned}\tag{9.15}$$

Expressing components of Hamiltonian (8.25) in terms of \mathbf{x}, φ , and their partial derivatives, and truncating higher-order ξ_{i0} terms yields

$$\begin{aligned}\nabla^2 &\simeq \boldsymbol{\partial} \cdot \boldsymbol{\partial} & \Omega^T Q \Omega &\simeq -\mathbf{x}^T Q'' \mathbf{x} \\ \mathbf{M}^2 &\simeq -\partial_2^2 - \partial_3^2 & \Omega^T Q \nabla &\simeq -\mathbf{x}^T Q'' \boldsymbol{\partial}\end{aligned}\tag{9.16}$$

where $Q'' = \text{diag}(4, 3, 3)$ is $(4\mathbb{1} - Q)$ with the last two columns and rows omitted. This leads to $\hat{\mathcal{H}}_- = \sum_{i=1}^3 \hat{\mathcal{H}}_i$, with $\hat{\mathcal{H}}_i$ of the same form as in Eq. (9.9) and the relevant constants defined as:

$$\begin{aligned}A_1 &= |g_2| & A_{2,3} &= (g_1 + |g_2|) \\ C_1 &= 4|q| & C_{2,3} &= 3|q| \\ B_i &= t_N C_i & \nu_i &\equiv C_i/A_i\end{aligned}\tag{9.17}$$

with t_N as in Eq. (9.10). The rest of the calculation proceeds as in the previous section, again leading to Eq. (9.11) for $i = 1, 2, 3$, evaluated with the above constants, and a validation of our assumptions of localised states.

Again, the mode energies are in excellent agreement with the numerics, with the largest relative discrepancy among the first 100 lowest energies at $N = 100, g_1 = |g_2|, q = -100|g_2|$ equal to 0.16 percent. A sketch of the large-negative- Nq rotor ground state is shown in Fig. 9.2.

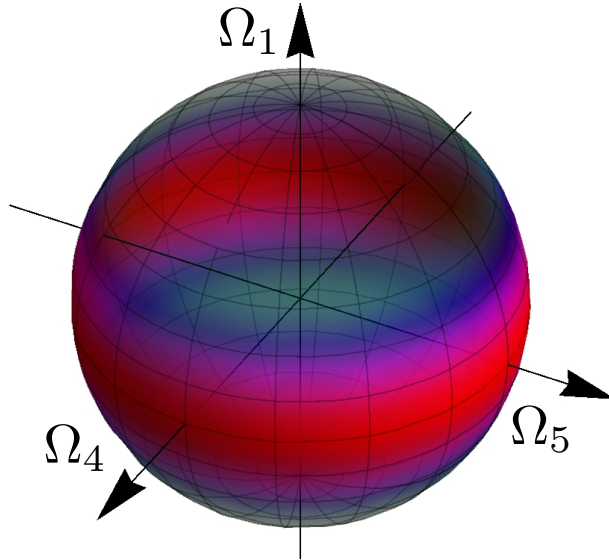


Figure 9.2: A schematic representation of the ground state wave function at large negative Nq . Like in Fig. 9.1, the wave function is concentrated in the brighter, more opaque areas, and is also localised in the omitted Ω_2 and Ω_3 directions.

9.4 WAVE FUNCTION OVERLAPS

Besides facilitating the analytical derivation of excitation energies, the rotor mapping also yields insightful information on the wave functions themselves. The associated 4-sphere often provides a more intuitive picture of the wave function than the original second-quantised operator picture.

In this section we investigate the overlap of the ground state wave functions, with arbitrary values of q , with wave functions in the limit of large $N|q|$. The ground states are computed in two ways: analytically through the rotor mapping, and numerically by means of the exact diagonalisation of Sec. 9.1 for modest values of the total particle number. We label the limiting large-

$N|q|$ ground-state wave functions as

$$\begin{aligned} |\psi_+^\infty\rangle &= \frac{1}{\sqrt{N!}}(\hat{a}_0^\dagger)^N |0\rangle, \\ |\psi_-^\infty\rangle &= \frac{1}{(N/2)!}(\hat{a}_2^\dagger\hat{a}_{-2}^\dagger)^{N/2} |0\rangle, \end{aligned}$$

which are appropriate for large positive and large negative Nq , respectively. The first state has a clear correspondence to the mean-field uniaxial nematic state oriented along the z -axis, as shown in Fig. 5.2. The second state is fragmented and can be viewed as an equal-weight superposition of all square biaxial nematic states lying in the xy plane, as is evident from Eq. (9.12). One may also view $|\psi_-^\infty\rangle$ as the $F_z = 0$ component of any of these mean-field ground states. For large positive or negative Nq , one expects a large overlap of the ground state with $|\psi_+^\infty\rangle$ or $|\psi_-^\infty\rangle$, respectively. On the other hand, for moderate Nq , one may ask if any relic of the order-by-disorder phenomenon present in the continuum case, as indicated in Fig. 5.2, remains.

The simplest expressions for the overlaps may be obtained in the regime where $N \gg 1$ and $|q|$ is not much smaller than either $|g_1|$ or $|g_2|$, to which we restrict in the following. This is slightly more restrictive than the condition of the previous section, namely, $N|q| \gg |g_{1,2}|$. For the case when $N|q| \gg |g_{1,2}|$, but N is not large compared to unity, the analysis is complicated by the interplay between asymptotic series convergence and the applicability of extending Gaussian integration limits to infinity.

Define the overlap of two possibly unnormalised states $|a\rangle$ and $|b\rangle$ as $(a|b) \equiv |\langle a|b\rangle| / \sqrt{\langle a|a\rangle \langle b|b\rangle}$. States are completely determined by their wave function in the overcomplete basis and we follow the usual convention of labelling states of the original Hamiltonian by the same label as their rotor wave functions, that is

$$|\psi\rangle \equiv \int_{\mathcal{S}^4} d\Omega \psi(\Omega) |\Omega\rangle. \quad (9.18)$$

Label the ground states as obtained through the rotor mapping by $|\psi_\pm^R\rangle$. The sign in the subscript indicates whether Hamiltonian (8.25) was expanded about the large-positive- or large-negative- Nq limiting state. Label the nu-

merically obtained ground states by $|\psi^N\rangle$.

While the overcompleteness of the basis did not manifest itself significantly in calculating the spectrum, it does affect calculations involving the eigenfunctions. In the thermodynamic limit, one can express this inner product in terms of delta functions on the four-sphere. However, for finite N , overlaps must be computed by means of the standard rotor inner product, discussed at length in Sec. 7.3, involving double integrals over the 4-sphere:

$$\langle\psi_a|\psi_b\rangle = \int_{S^4} d\Omega_1 \int_{S^4} d\Omega_2 \psi_a^*(\Omega_1)\psi_b(\Omega_2) (\Omega_1 \cdot \Omega_2)^N \quad (9.19)$$

CASE OF POSITIVE q

Here we reuse the \mathbf{x} coordinates of Sec. 9.3.1, as defined in Eq. (9.5). We integrate over only half of the 4-sphere, as this is less cluttered by trivial (anti)symmetrisations. The relevant wave functions in the rotor picture (9.18) are $\psi_+^\infty(\mathbf{x}) = \delta^{(4)}(\mathbf{x})$ and $\psi_+^R(\mathbf{x})$. The latter is of the form of Eq. (9.6) with h_n equal to 1, i.e., $\psi_+^R(\mathbf{x}) = \exp(-\frac{N}{2}\mathbf{x}^T\Gamma\mathbf{x})$, with $\Gamma = \text{diag}(\gamma_2, \gamma_3, \gamma_4, \gamma_5)$ and γ_i as expressed in Eq. (9.11), evaluated at the values given by Eq. (9.10).

In the new coordinates, we have $d\Omega = d\mathbf{x}/\sqrt{1-\mathbf{x}^2}$, and the dot product between vectors on the four sphere is expressed as

$$\Omega_1 \cdot \Omega_2 = \sqrt{(1-\mathbf{x}_1^2)(1-\mathbf{x}_2^2) + \mathbf{x}_1 \cdot \mathbf{x}_2}. \quad (9.20)$$

Assuming tight localisation about $\mathbf{x} = 0$, the main contribution to the integral (9.19) will come from that region and we may extend the boundary of integration from $|\mathbf{x}| = 1$ to $|\mathbf{x}| \rightarrow \infty$. The denominator of the new integration measure varies relatively slowly, so we may set it to its value at $\mathbf{x} = 0$.

Due to the simplicity of ψ_+^∞ , a straightforward calculation yields

$$\langle \psi_+^\infty | \psi_+^\infty \rangle = 1 \quad (9.21)$$

$$\begin{aligned} \langle \psi_+^\infty | \psi_+^R \rangle &= \int_{\mathbb{R}^4} d\mathbf{x} (1 - \mathbf{x}^2)^{\frac{N}{2}} e^{-\frac{N}{2} \mathbf{x}^T \Gamma \mathbf{x}} \\ &\simeq \int_{\mathbb{R}^4} d\mathbf{x} e^{-\frac{N}{2} \mathbf{x}^T (\Gamma + \mathbb{1}) \mathbf{x}} \\ &= \prod_{i=2}^5 \sqrt{\frac{2\pi}{N(\gamma_i + 1)}}. \end{aligned} \quad (9.22)$$

On the third line we approximated $1 - \mathbf{x}^2 \simeq e^{-\mathbf{x}^2}$, permissible on account of tight localisation.

Evaluation of $\langle \psi_+^R | \psi_+^R \rangle$ involves the approximation (valid due to the localised wave functions) $\boldsymbol{\Omega}_1 \cdot \boldsymbol{\Omega}_2 = \sqrt{(1 - \mathbf{x}_1^2)(1 - \mathbf{x}_2^2)} + \mathbf{x}_1 \cdot \mathbf{x}_2 \simeq 1 - \frac{\mathbf{x}_1^2}{2} - \frac{\mathbf{x}_2^2}{2} + \mathbf{x}_1 \cdot \mathbf{x}_2 = 1 - \frac{1}{2} (\mathbf{x}_1 - \mathbf{x}_2)^2 \equiv 1 - \mathbf{y}_2^2 \simeq e^{-\mathbf{y}_2^2}$ where we introduced new integration variables $\mathbf{y}_{1,2} \equiv (\mathbf{x}_1 \pm \mathbf{x}_2) / \sqrt{2}$. With these variables and the above approximation, the integrand becomes $\exp[-\frac{N}{2} (\mathbf{y}_1^T \Gamma \mathbf{y}_1 + \mathbf{y}_2^T (\Gamma + 2\mathbb{1}) \mathbf{y}_2)]$, leading to $\langle \psi_+^R | \psi_+^R \rangle = \prod_{i=2}^5 \frac{2\pi}{N} [\gamma_i (\gamma_i + 2)]^{-1/2}$.

Combining the results of the previous paragraph and Eq. (9.22), we find that the total overlap $\langle \psi_+^\infty | \psi_+^R \rangle$ can be expressed as a product of contributions from individual x_i -directions and that the i -th direction contributes a factor of $\left[\frac{\gamma_i (\gamma_i + 2)}{(\gamma_i + 1)^2} \right]^{1/4}$. Motivated by this, define

$$u_i^2 \equiv \frac{(\gamma_i + 1)^2}{\gamma_i (\gamma_i + 2)} = \frac{1}{2} \left(1 + \frac{\nu_i + 1}{\sqrt{\nu_i (\nu_i + 2)}} \right) \quad (9.23)$$

where the rightmost expression was derived by expanding γ_i in terms of ν_i as in Eq. (9.11) and letting $t_N \equiv 2 + 5/N \simeq 2$. The ν_i are defined in Eq. (9.10) and are summarised here for convenience:

$$\nu_a \equiv \nu_{2,3} = \frac{q}{3g_1 + |g_2|} \quad \nu_b \equiv \nu_{4,5} = \frac{4q}{|g_2|}. \quad (9.24)$$

Since each direction contributes a factor of $u_i^{-1/2}$, the total overlap is

$$(\psi_+^\infty | \psi_+^R) = u_a^{-1} u_b^{-1}. \quad (9.25)$$

The overlap $(\psi_+^\infty | \psi_+^R)$ is plotted in the main panel of Fig. 9.3 for $N = 200$ particles and $g_1 = |g_2|$. For comparison, the analogous overlaps $(\psi_\pm^\infty | \psi^N)$, computed with the numerically determined ground state $|\psi^N\rangle$ for the same parameter ranges, are also shown. As is expected, both the analytically and numerically obtained relevant overlaps approach unity for large $|q|$. To show that the two agree in more than just this obvious large- q limit, consider their asymptotic expansions. Let $f_\pm = (\psi_\pm^\infty | \psi_\pm^R) = 1 + \sum_{n=1}^\infty a_n q^{-n}$ and $g_\pm = (\psi_\pm^\infty | \psi^N) = 1 + \sum_{n=1}^\infty b_n q^{-n}$. Define $\Delta_\pm \equiv |f_\pm - g_\pm| = |\sum_{n=1}^\infty (a_n - b_n) q^{-n}|$. The inset of Fig. 9.3 shows that $q\Delta_+$ tends to zero with increasing q , implying that our analytical expressions agree with the numerics to at least the first order in the asymptotic expansion.

CASE OF NEGATIVE q

For this subsection, we reuse the \mathbf{x} and φ coordinates of Sec. (9.3.2), defined in Eq. (9.13). The limiting large-negative- Nq rotor wave function is $\psi_-^\infty(\mathbf{x}, \varphi) = \delta^{(3)}(\mathbf{x})$. The finite- q ground-state, as obtained in section 9.3.2, is $\psi_-^R(\mathbf{x}, \varphi) = \exp\left(-\frac{N}{2}\mathbf{x}^T\Gamma\mathbf{x}\right)$, with the matrix $\Gamma = \text{diag}(\gamma_1, \gamma_2, \gamma_3)$ as defined underneath Eq. (9.14), and the γ variables as defined in Eq. (9.11), evaluated at values from Eq. (9.17).

In the new coordinates, one has $d\Omega = d\varphi d\mathbf{x} / \sqrt{1 - \mathbf{x}^2} \simeq d\varphi d\mathbf{x}$, with the last approximation being permissible on account of localisation, as in the positive q case. As before, we may extend the \mathbf{x} integration boundaries to infinity. The range of integration in φ is from 0 to 2π . The dot product between vectors on the four sphere is $\boldsymbol{\Omega}_1 \cdot \boldsymbol{\Omega}_2 = \cos(\varphi_1 - \varphi_2) \sqrt{(1 - \mathbf{x}_1^2)(1 - \mathbf{x}_2^2)} + \mathbf{x}_1 \cdot \mathbf{x}_2$. Since the considered wave functions do not depend on the φ coordinate, we may simplify integration over $\varphi_{1,2}$ by a change of variables. Defining $\varphi \equiv \varphi_1 - \varphi_2$ and, say, $\varphi'_2 \equiv \varphi_2$ allows us to immediately perform the now

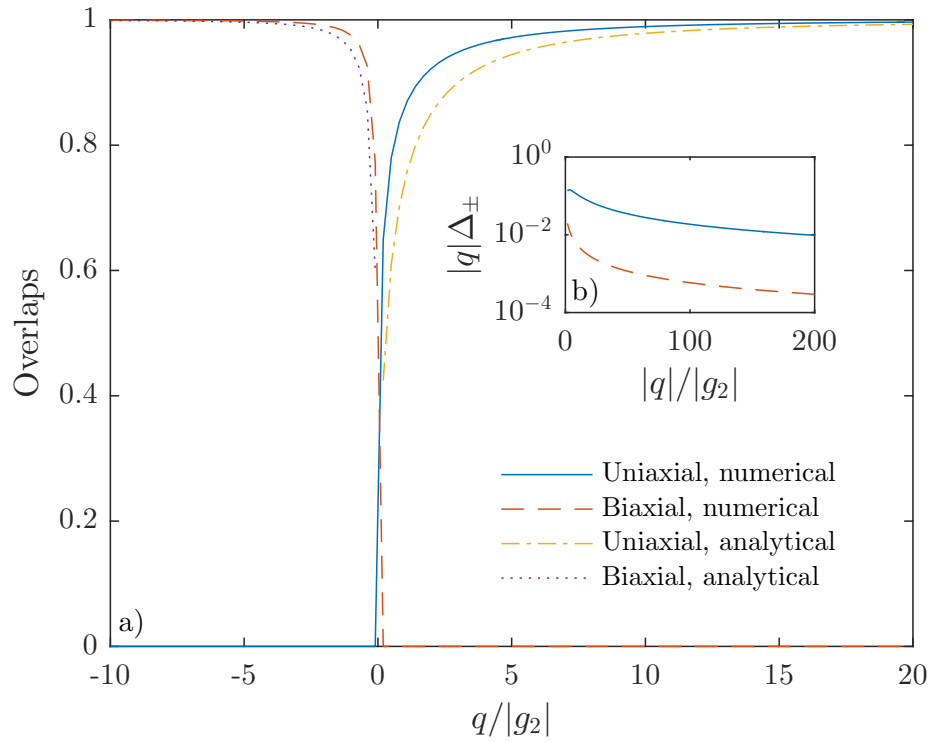


Figure 9.3: (a) Overlaps of finite- q ground states with the large- $|q|$ limiting states ψ_{\pm}^{∞} , at $g_1 = |g_2|$, with respect to $q/|g_2|$. The solid blue and dashed red lines show numerically obtained overlaps, $(\psi_{\pm}^{\infty}|\psi^N)$, with the uniaxial and biaxial limiting states, respectively. The dash-dotted yellow and dotted purple lines show the corresponding analytical estimates, $(\psi_{\pm}^{\infty}|\psi_{\pm}^R)$. For large $|q|/|g_2|$ both tend to one or zero. Inset (b) demonstrates that $|q|\Delta_{\pm}$, where Δ_{\pm} is defined under Eq. (9.25), tends to zero with increasing $|q|$, implying that our analytical and numerical expressions agree to at least first order in asymptotic expansion. The solid blue (dashed red) line refers to positive- q uniaxial-overlap (negative- q biaxial-overlap) quantities.

trivial φ'_2 integral to obtain

$$\langle \psi_a | \psi_b \rangle = 2\pi \int_0^{2\pi} d\varphi \iint_{\mathbb{R}^3} d\mathbf{x}_1 d\mathbf{x}_2 \psi_a^*(\mathbf{x}_1) \psi_b(\mathbf{x}_2) \times \left(\cos \varphi \sqrt{(1 - \mathbf{x}_1^2)(1 - \mathbf{x}_2^2)} + \mathbf{x}_1 \cdot \mathbf{x}_2 \right)^N \quad (9.26)$$

where $\psi_{a,b}$ are any wave functions that do not depend on the φ variable, such as ψ_-^∞ or ψ_-^R . Using this expression and approximations analogous to those of Eq. (9.22), the simpler integrals are found to be:

$$\langle \psi_-^\infty | \psi_-^\infty \rangle = 2\pi \int_0^{2\pi} d\varphi \cos^N \varphi \equiv \mathcal{N}_- \quad (9.27)$$

$$\begin{aligned} \langle \psi_-^\infty | \psi_-^R \rangle &\simeq \mathcal{N}_- \int_{\mathbb{R}^4} d\mathbf{x} e^{-\frac{N}{2} \mathbf{x}^T (\Gamma + \mathbf{1}) \mathbf{x}} \\ &= \mathcal{N}_- \prod_{i=1}^3 \sqrt{\frac{2\pi}{N(\gamma_i + 1)}}. \end{aligned} \quad (9.28)$$

To calculate $\langle \psi_-^R | \psi_-^R \rangle$, consider again the factor

$$f \equiv \left(\cos \varphi \sqrt{(1 - \mathbf{x}_1^2)(1 - \mathbf{x}_2^2)} + \mathbf{x}_1 \cdot \mathbf{x}_2 \right)^N \quad (9.29)$$

of Eq. (9.26). Due to the large exponent N , the significant contributions to the integral will come from regions of maximum $|\cos \varphi|$, that is for $\varphi \sim 0$ or π . In both regions, we may expand $\cos \varphi$ to quadratic order and extend integration boundaries to infinity, yielding a Gaussian integral in $\delta\varphi \equiv \varphi - \varphi_0$ where $\varphi_0 = 0$ or π . Also expanding the square roots and keeping lowest order terms in $\mathbf{x}_{1,2}$ and φ yields

$$f \simeq \exp \left[-\frac{N}{2} \left(\delta\varphi^2 + 2\mathbf{y}_r^2 + \sum_{i=1}^2 \mathbf{y}_i^T \Gamma \mathbf{y}_i^T \right) \right] \quad (9.30)$$

where $\mathbf{y}_{1,2} \equiv (\mathbf{x}_1 \pm \mathbf{x}_2) / \sqrt{2}$ as in the positive- q case. The label r equals 1 for the $\varphi_0 = \pi$ region and 2 for the $\varphi_0 = 0$ region. The integrals over $\mathbf{y}_{1,2}$ are equal in both cases, and twice the $\delta\varphi$ integral is in fact approximately equal

to \mathcal{N}_- of Eq. (9.28), as can be verified by applying the same approximate treatment of integration over φ to $\langle \psi_-^\infty | \psi_-^\infty \rangle$. This leads to $\langle \psi_-^R | \psi_-^R \rangle = \mathcal{N}_- \prod_{i=1}^3 \frac{2\pi}{N} [\gamma_i (\gamma_i + 2)]^{-1/2}$.

Combining the above results and expressing everything in terms of u_i , defined in Eq. (9.23) and evaluated at

$$\nu_c \equiv \nu_1 = 4 \left| \frac{q}{g_2} \right| \quad \nu_d \equiv \nu_{2,3} = \frac{3|q|}{g_1 + |g_2|}, \quad (9.31)$$

summarised after Eq. (9.17), ultimately yields

$$\langle \psi_-^\infty | \psi_-^R \rangle = u_c^{-\frac{1}{2}} u_d^{-1} \quad (9.32)$$

The main panel of Fig. 9.3 again demonstrates that both numerical and analytical overlaps tend to 1 with increasing $|q|$ while the inset shows that the convergence agrees to at least the first order in the asymptotic expansion.

10

AN EXACT MANIFESTATION OF ORDER BY DISORDER IN TIGHTLY CONFINED SPIN-2 ATOMS

One of the outcomes of the analysis in the previous chapter is the complete absence of the order-by-disorder phenomenon which is present for the continuum case.^{116,127} The present chapter briefly explains how and why this manifests itself through the ground-state overlaps with limiting large- $N|q|$ states, in Sec. 10.1, and then proposes subjecting the tightly confined condensate to an alternative potential, coupling only to single-particle sublevels with magnetic number $m = \pm 1$. A mean-field order-by-disorder selection is demonstrated for the continuum problem with this new potential in Sec. 10.2. Section 10.3 then analyses the low-lying spectrum of the tightly bound system in the presence of the new potential in the rotor framework. Through degenerate perturbation theory, an effective Hamiltonian for the classically degenerate η degree of freedom is derived. This is argued to be an exact, fully quantum parallel of the continuum order-by-disorder mechanism. Section 10.4 then considers rotor ground-state overlaps with the limiting nematic

mean-field states of the previous chapter, about which the ground states are localised, and demonstrates that they tend to zero with increasing particle number N , implying a stark departure from mean-field-like states. Finally, in Sec. 10.5, magnetic sublevel occupation expectation values are evaluated in the rotor formalism and shown to agree with the effects of the continuum order-by-disorder mechanism.

10.1 LACK OF FLUCTUATION EFFECTS FOR THE QUADRATIC ZEEMAN POTENTIAL IN THE SINGLE MODE APPROXIMATION

In the continuum with zero external field, an order-by-disorder mechanism selects different mean-field ground states in two nematic subregions of the spin-2 phase diagram, as shown in Sec. 5.3. Let us temporarily refer to the $c_1 > 0$ subregion as the uniaxial region, and the $c_1 < 0$ subregion as the biaxial region, after the states of Eq. (5.14) selected at zero field. Turning on a large enough positive (negative) quadratic Zeeman field q selects the uniaxial (biaxial) nematic state, regardless of the nematic subregion. However, when applying a positive q in the biaxial region or a negative q in the uniaxial region, this may only happen after q exceeds the scale of fluctuation-induced energy variation, i.e., the difference between the maximum and minimum values attained by the curves in Fig. 5.8. This is typically tiny in experimentally relevant settings.¹²⁷

Even though the exact tightly-bound ground state at $q = 0$ is known to be a spin singlet, based on the mean-field behaviour, one may expect to see signatures of the exact ground states approaching the limiting large-positive- Nq state faster with increasing q in the uniaxial region, and similarly for the large-negative- $N|q|$ limiting state in the biaxial region.

The numerically obtained overlaps, however, do not reflect this expectation. The smaller the value of $g_1/|g_2|$, the faster the wave function's approach to *both* limiting states with increasing magnitude of q . This is schematically shown in Fig. 10.1. The effect is completely smooth in the whole nematic region, without any qualitative change in behaviour at $g_1 = 0$, where a fluctuation-induced phase transition occurs in the mean-field analysis.

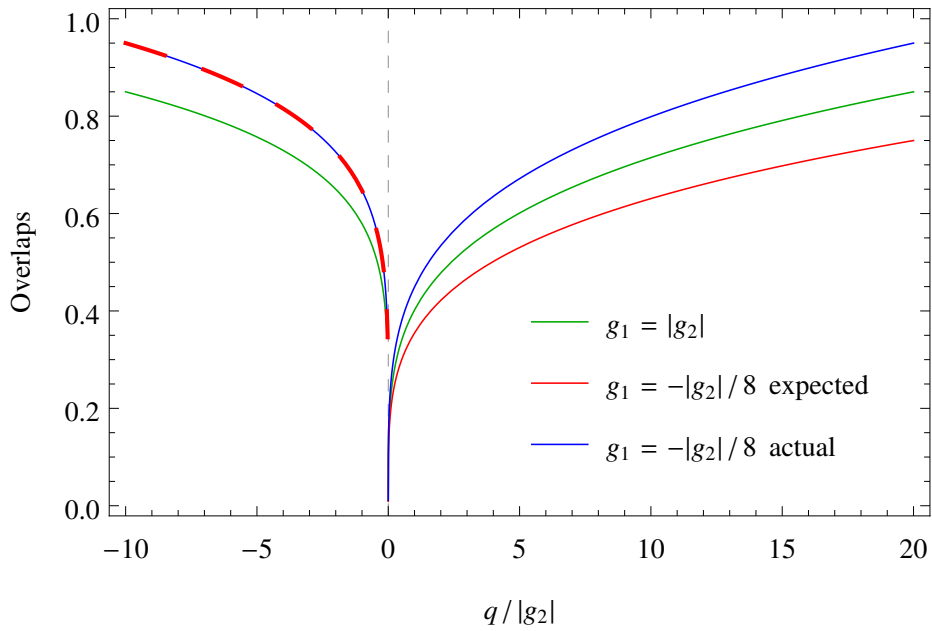


Figure 10.1: A qualitative illustration of the disparity between wave-function localisation behaviour at different values of g_1 , expected on the basis of a mean-field treatment, and the actual quantum results from exact diagonalisation. In the $q \geq 0$ ($q < 0$) section of the plot, the rotor ground-state overlap with the limiting positive- q (negative- q) ground state is shown. Moving from the uniaxial into the biaxial region, as determined by g_1 , one may expect the negative- q limiting state to be approached quicker with increasing $-q$, and the positive- q limiting state slower with increasing q , than in the uniaxial region, as argued in the main text. The former does happen, but the latter does not. Instead, both limiting states are approached quicker as one moves deeper into the biaxial region.

The lack of the order-by-disorder selection at the quantum single-mode level can be accounted for by the fact that the quadratic Zeeman potential breaks too much symmetry of the Hamiltonian (8.19). Motivated by this, we have considered an alternative external potential. Specifically, the new potential replaces

$$q\hat{Z} \rightarrow \lambda(\hat{a}_1^\dagger \hat{a}_1 + \hat{a}_{-1}^\dagger \hat{a}_{-1}) \quad (10.1)$$

in Hamiltonian (8.19). Such a potential could be realised by electro-optical means. Note that, within mean field theory, all nematic states of Sec. 5.2.2, whose order parameter is shown in Eq. (10.3) below, are degenerate under this external potential. Considering the rotor mapping rule in Eq. (7.35), one can see that the above change propagates through the mapping by changing the last two terms of Hamiltonian (8.25) to

$$\mathcal{H}_\lambda = \lambda \left((N + 5) (\Omega_2^2 + \Omega_3^2) - \Omega_2 \nabla_2 - \Omega_3 \nabla_3 \right). \quad (10.2)$$

The following section briefly summarises the degenerate mean-field ground-state manifold in the presence of such a potential and demonstrates that the degeneracy is lifted through Order by Disorder. Unlike with the quadratic Zeeman effect, this selection will be fully consistent with the outcome of the rotor calculations in Secs. 10.3 to 10.5.

10.2 CONTINUUM ORDER BY DISORDER

The new potential does not break the zero-field nematic degeneracy, and all of the states with nematic order parameters

$$\Psi_n(\eta) = \left(\frac{\sin \eta}{\sqrt{2}}, 0, \cos \eta, 0, \frac{\sin \eta}{\sqrt{2}} \right), \quad (10.3)$$

remain valid ground-state candidates. Like with the dice lattice calculation in Sec. 4.1 or the zero-field spin-2 calculation in Sec. 5.3, the first step in deriving the fluctuation-induced degeneracy lifting is calculating the modes about each of the mean-field degenerate nematic states $\Psi_n(\eta)$. Obtaining these involves a straightforward but lengthy Bogoliubov analysis. Adding

a chemical potential, letting $\hat{\psi}_\alpha(\mathbf{r}) = \sqrt{n}\Psi_{n\alpha}(\eta) + \delta\hat{\psi}_\alpha(\mathbf{r})$, where n is the uniform condensate density, expanding the Hamiltonian to quadratic order in $\delta\hat{\psi}_\alpha(\mathbf{r})$, and diagonalising the resulting quadratic Hamiltonian, one finds the mode energies of the usual form

$$E_{\mathbf{k},n} = \sqrt{\xi_{\mathbf{k},n}(\xi_{\mathbf{k},n} + 2\gamma_n)} \quad (10.4)$$

where the particular parameters for the five modes are

$$\xi_{\mathbf{k},1} = \xi_{\mathbf{k},2} = \varepsilon_{\mathbf{k}} + \lambda \quad (10.5)$$

$$\xi_{\mathbf{k},3} = \xi_{\mathbf{k},4} = \xi_{\mathbf{k},5} = \varepsilon_{\mathbf{k}} \quad (10.6)$$

and

$$\gamma_j = n \left(|c_2| + 4c_1 \sin^2 \left(\eta + \frac{2\pi}{3}j \right) \right) \quad \text{for } j = 1, 2, 3 \quad (10.7)$$

$$\gamma_4 = n(c_0 - |c_2|) \quad (10.8)$$

$$\gamma_5 = n|c_2| \quad (10.9)$$

Here, $\varepsilon_{\mathbf{k}} = \frac{k^2}{2m}$ is the free particle dispersion. Note that these modes are equivalent to those in the absence of an external field, as treated in Sec. 5.3, with the sole difference that $\varepsilon_{\mathbf{k}}$ is shifted to $\varepsilon_{\mathbf{k}} + \lambda$ for two of the η -dependent modes.

Proceeding in analogy with the zero-field case, the zero-point contribution of the Bogoliubov modes is found to be $\Delta E = \frac{1}{2} \sum_{\mathbf{k},n} (E_{\mathbf{k},n} - E_{\mathbf{k},n}|_{\eta=0})$ where $E_{\mathbf{k},n}|_{\eta=0}$ is subtracted to regularise the summation. It is found that, for sufficiently large $\lambda > 0$, the biaxial nematic state with $\eta = \pi/2$ is selected when $c_1 > 0$, while the uniaxial nematic state with $\eta = 0$ is selected when $c_1 < 0$.

We now proceed to show that a consistent result arises in the rotor framework for the tightly bound system. The initial steps of the rotor mapping proceed completely analogously to the previous chapter, but a rather different effective Hamiltonian on the 4-sphere soon emerges, with clear parallels to the order-by-disorder selection mechanism.

10.3 ROTOR TREATMENT

The results of this section are similar to the large- $N|q|$ limit in that, for sufficiently large λ and depending on the sign of g_1 , the rotor wave function is localised either about the Ω_1 poles or around the 4-5 equator of the 4-sphere. However, the localisation widths scale differently with N than in the quadratic Zeeman case, leading to important qualitative differences. Localisation at the poles (equator) also occurs at negative (positive) g_1 , which is in fact the opposite of the effect in the continuum in the absence of an external potential.

For the calculations of this section we introduce a third, more general coordinate system:

$$\boldsymbol{\Omega} = \begin{pmatrix} \cos \eta \sqrt{1 - \boldsymbol{x}^2} \\ x_1 \cos \varphi - x_2 \sin \varphi \\ x_1 \sin \varphi + x_2 \cos \varphi \\ \sin \eta \cos 2\varphi \sqrt{1 - \boldsymbol{x}^2} \\ \sin \eta \sin 2\varphi \sqrt{1 - \boldsymbol{x}^2} \end{pmatrix} \quad (10.10)$$

This can be put into a more compact form by using rotation matrices. In particular let $R_{\alpha\beta}(\varphi)$ be the matrix which rotates in the $\alpha\beta$ plane by angle φ from the positive α axis towards the positive β axis. Then the current coordinate system can be written as

$$\boldsymbol{\Omega} = R_{23}(\varphi)R_{45}(2\varphi)R_{14}(\eta) \left(\sqrt{1 - \boldsymbol{x}^2}, x_1, x_2, 0, 0 \right)^T. \quad (10.11)$$

Note that $R_{23}(\varphi)R_{45}(2\varphi) = \exp(-i\varphi M^z)$. Recalling that each point of the 4-sphere is associated with a spatial rotation of a mean-field nematic state, the η coordinate is seen to correspond exactly to the η parametrising the accidentally degenerate family of nematic states in Eq. (5.12), while φ and \boldsymbol{x} determine their spatial orientations.

An appropriate range of the coordinates is as follows: η takes values in the interval $[0, \pi]$ and \boldsymbol{x} in the unit disk. The wave functions are periodic in φ

with period 2π , with the additional constraint

$$\psi(\eta, \mathbf{x}, \varphi + \pi) = \psi(\eta, -\mathbf{x}, \varphi). \quad (10.12)$$

The integration measure is $2\sqrt{1-\mathbf{x}^2} \sin \eta$. To concisely state the spherical gradient components in the new coordinates, denote $\partial_i \equiv \frac{\partial}{\partial x_i}$, $\partial_\eta \equiv \frac{\partial}{\partial \eta}$, $\partial_\varphi \equiv \frac{\partial}{\partial \varphi}$, and let $\boldsymbol{\partial} \equiv (\partial_1, \partial_2)^T$. Let $R(\zeta)$ be the matrix of anti-clockwise rotation by ζ radians in the plane. Then we have

$$\begin{aligned} \nabla_1 &= -\frac{\sin \eta}{\sqrt{1-\mathbf{x}^2}} \partial_\eta - \cos \eta \sqrt{1-\mathbf{x}^2} \mathbf{x} \cdot \boldsymbol{\partial} \\ \begin{pmatrix} \nabla_2 \\ \nabla_3 \end{pmatrix} &= R(\varphi)(\mathbf{1} - \mathbf{x}\mathbf{x}^T) \boldsymbol{\partial} \\ \begin{pmatrix} \nabla_4 \\ \nabla_5 \end{pmatrix} &= \begin{pmatrix} \cos 2\varphi \\ \sin 2\varphi \end{pmatrix} \begin{pmatrix} \frac{\cos \eta}{\sqrt{1-\mathbf{x}^2}} \partial_\eta - \sin \eta \sqrt{1-\mathbf{x}^2} \mathbf{x} \cdot \boldsymbol{\partial} \\ \frac{1}{2 \sin \eta \sqrt{1-\mathbf{x}^2}} \begin{pmatrix} \sin 2\varphi \\ -\cos 2\varphi \end{pmatrix} (x_1 \partial_2 - x_2 \partial_1 - \partial_\varphi) \end{pmatrix} \end{aligned} \quad (10.13)$$

Finally, the coordinates of a point diametrically opposite to a reference point are given in terms of the reference point coordinates as

$$\begin{aligned} \mathcal{P}\Omega(\eta, \mathbf{x}, \varphi) &= \Omega\left(\pi - \eta, R\left(\frac{\pi}{2}\right)\mathbf{x}, \varphi + \frac{\pi}{2}\right) \\ &= \Omega\left(\pi - \eta, R\left(-\frac{\pi}{2}\right)\mathbf{x}, \varphi - \frac{\pi}{2}\right) \end{aligned} \quad (10.14)$$

with the last equality following on account of constraint (10.12).

As usual, we consider the \hat{F}^z null space, which in the present coordinates implies our wave functions will be independent of φ . Constraint (10.12) then also demands that the wave functions be even in \mathbf{x} . We also consider the regime of large particle number, $N \gg 1$. Since the potential in Eq. (10.1) is independent of η at the mean-field level, we may heuristically consider η as the low-energy coordinate and accordingly seek wave functions less localised in the η direction than in the \mathbf{x} coordinates.

By observing factors of N in Hamiltonian (8.25), expanded in current coor-

dinates, one finds that low-lying wave functions may be taken to be localised in \mathbf{x} about zero on a length scale of order $N^{-1/2}$, and in η about some value η_0 on a length scale of order $N^{-1/4}$, subject to some consistency conditions. This allows one to separate the Hamiltonian into two parts, $\hat{\mathcal{H}}_0$ of order 1 and $\hat{\mathcal{H}}_\eta$ of orders between $N^{-1/4}$ to $N^{-3/4}$, and we discard terms of higher order in $1/N$. For compact notation, introduce matrices

$$\begin{aligned} A(\eta) &\equiv \left(1 + \frac{2g_1}{|g_2|}\right) \mathbb{1} + B(\eta) \quad \text{with} \\ B(\eta) &\equiv \frac{g_1}{|g_2|} \text{diag} \left(\cos 2\eta + \sqrt{3} \sin 2\eta, \cos 2\eta - \sqrt{3} \sin 2\eta \right). \end{aligned} \quad (10.15)$$

Reusing notation introduced below Eq. (10.12), denote $\delta\eta \equiv \eta - \eta_0$ and let $\hat{L}_x \equiv -i(\hat{x}_1\partial_2 - \hat{x}_2\partial_1)$ and $\hat{T}_1 \equiv \hat{x}_1\partial_1 + \hat{x}_2^2\partial_1^2 - (1 \leftrightarrow 2)$. Then one may write

$$\begin{aligned} \hat{\mathcal{H}}_0 &= -\frac{|g_2|}{2N} A_{ij}(\eta_0) \partial_i \partial_j + \lambda N \hat{\mathbf{x}}^2 - \lambda \hat{\mathbf{x}} \cdot \boldsymbol{\partial} \\ \hat{\mathcal{H}}_\eta &= -\frac{|g_2|}{2N} \left[\partial_\eta^2 + (\cot \hat{\eta} - B'_{ij}(\eta_0) \hat{x}_i \partial_j) \partial_\eta \right. \\ &\quad \left. + \delta \hat{\eta} B'_{ij}(\eta_0) \partial_i \partial_j + \frac{1}{2} \delta \hat{\eta}^2 B''_{ij}(\eta_0) \partial_i \partial_j \right. \\ &\quad \left. - \frac{\csc^2 \hat{\eta}}{4} \hat{L}_x^2 \right] + \frac{g_1}{2N} \sqrt{3} \csc \hat{\eta} \hat{T}_1. \end{aligned} \quad (10.16)$$

The last line is of a non-negligible order only when the distance between η_0 and 0 or π is on the order of $N^{-1/4}$ or less.

Noting that $\hat{\mathcal{H}}_0$ does not depend on $\delta\hat{\eta}$, we may tackle the above with degenerate perturbation theory. First note that $\hat{\mathcal{H}}_0$ may be brought to Hermitian form by applying the similarity transformation $e^{-\hat{S}} \hat{\mathcal{H}}_0 e^{\hat{S}}$ where

$$\hat{S} = -\frac{N\lambda}{2|g_2|} \hat{\mathbf{x}}^T A(\eta_0)^{-1} \hat{\mathbf{x}}. \quad (10.17)$$

The transformed Hamiltonian has the ground state energy

$$E_0(\eta_0) = \lambda \left(1 + \frac{1}{2} \text{Tr} \sqrt{\mathbb{1} + \frac{2|g_2|}{\lambda} A(\eta_0)} \right) \quad (10.18)$$

and ground state eigenfunction

$$\begin{aligned}\psi_0(\mathbf{x}) &= (2\pi)^{-\frac{1}{2}} \det^{\frac{1}{4}} C(\eta_0) \exp \left[-\frac{N\lambda}{2|g_2|} \mathbf{x}^T C(\eta_0) \mathbf{x} \right]; \\ C(\eta_0) &\equiv A(\eta_0)^{-1} \sqrt{\mathbb{1} + \frac{2|g_2|}{\lambda} A(\eta_0)}.\end{aligned}\tag{10.19}$$

This yields a greatly degenerate zeroth-order ground-state subspace, consisting of wave functions ψ of η and \mathbf{x} that factor as $\psi(\eta, \mathbf{x}) = \phi(\eta)\psi_0(\mathbf{x})$. We can then project $e^{-\hat{S}}\hat{\mathcal{H}}_\eta e^{\hat{S}}$ into this low-energy subspace to obtain an effective Hamiltonian, acting only on the η coordinate, as

$$\hat{\mathcal{H}}_\eta^{\text{eff}} = \int d\mathbf{x} \psi_0^*(\mathbf{x}) e^{-\hat{S}} \hat{\mathcal{H}}_\eta e^{\hat{S}} \psi_0(\mathbf{x}).$$

Now observe the following expectation value:

$$M_{ij} \langle \partial_i \partial_j \rangle = -N \text{Tr} \left[M \left(\mathbb{1} + \frac{2|g_2|}{\lambda} A(\eta_0) \right)^{-\frac{1}{2}} \right]\tag{10.20}$$

where M is an arbitrary matrix. Observe that this case covers the coefficients of both the linear and quadratic $\delta\hat{\eta}$ terms in $\hat{\mathcal{H}}_\eta$, Eq. (10.16), by choosing M to be $-\frac{|g_2|}{2N} B'(\eta_0)$ and $-\frac{|g_2|}{2N} B''(\eta_0)$, respectively. At this point, note that should the expectation value of the linear $\delta\hat{\eta}$ term be of its natural order, order 1, completing the square in $\delta\hat{\eta}$ would yield another term of order 1, invalidating its placement into $\hat{\mathcal{H}}_\eta$, which is supposed to be of higher order in $1/N$. Note also that the coefficient of the linear $\delta\hat{\eta}$ term is exactly the derivative of the zeroth-order energy $E_0(\eta_0)$ from Eq. (10.18) with respect to η_0 . The above problem is avoided if we expand about a local extremum of $E_0(\eta_0)$, eliminating the linear term. For $\hat{\mathcal{H}}_\eta^{\text{eff}}$ to be bounded from below, the extremum must be a minimum. Note that we do not get any apparent order inconsistencies if we expand about an η_0 a distance of order $N^{-1/4}$ away from the local minimum, but the analysis is vastly simplified when the linear term is exactly zero, particularly for the last line of Eq. (10.16) when close to $\eta_0 = 0$, so we focus on expansions about zeroth-order energy minima from now on.

For large enough λ , these occur only at $\eta_0 = 0$ for negative g_1 and $\eta_0 = \pi/2$ for positive g_1 . The former corresponds to localisation about the Ω_1 poles, and the latter about the 4-5 equator, as anticipated in the opening paragraph of this section. In both of these cases, $A(\eta_0)$ is proportional to $\mathbb{1}$, so both $\psi_0(\mathbf{x})$ and $e^{\pm\hat{S}}\psi_0(\mathbf{x})$ are isotropic in x_1, x_2 . As is easy to verify, this makes the expectation values of the last line of Eq. (10.16) zero, eliminating those terms from $\hat{\mathcal{H}}_\eta^{\text{eff}}$. Additionally, we have $B'(\eta_0) \propto \text{diag}(1, -1)$. This, combined with isotropy in \mathbf{x} , leads to $B'_{ij}(\eta_0) \langle \hat{x}_i \partial_j \rangle = 0$ as well. Finally noting $B(0, \frac{\pi}{2}) = \pm \frac{g_1}{|g_2|} \mathbb{1}$ and $B''(\eta_0) = -4B(\eta_0)$ and evaluating the coefficient of the quadratic $\delta\hat{\eta}$ term via Eq. (10.20), we obtain

$$\hat{\mathcal{H}}_\eta^{\text{eff}} = -\frac{|g_2|}{2N} (\partial_\eta^2 + \cot \eta \partial_\eta) + 4|g_1| (1 + 2\mathcal{F}_{\eta_0})^{-\frac{1}{2}} \delta\hat{\eta}^2 \quad (10.21)$$

where \mathcal{F}_{η_0} equals $\mathcal{F}_0 = (|g_2| + 3g_1)/\lambda$ when expanding about the Ω_1 poles, that is $\eta_0 = 0$, and $\mathcal{F}_{\pi/2} = (|g_2| + g_1)/\lambda$ when expanding about the 4-5 equator, that is $\eta_0 = \pi/2$. Also note that $\cot \eta \partial_\eta$ is of lower order for $\eta_0 = \pi/2$ and may be neglected, while for $\eta_0 = 0$, $\partial_\eta^2 - \cot \eta \partial_\eta \simeq \eta^{-1} \partial_\eta \eta \partial_\eta$, the radial contribution to the two-dimensional Laplacian. In both cases, the low-lying eigenfunctions are those of a harmonic oscillator: unconstrained eigenfunctions of the one-dimensional oscillator for $\eta_0 = \pi/2$, and the isotropic, zero-angular-momentum eigenfunctions of the two-dimensional isotropic oscillator for $\eta_0 = 0$. The energy scale and the oscillator length have the same form in both cases when expressed in terms of the η_0 -dependent \mathcal{F}_{η_0} . For brevity, introduce another η_0 -dependent quantity, $\mathcal{B}_{\eta_0} \equiv \sqrt{\frac{8|g_1|}{|g_2|}} (1 + 2\mathcal{F}_{\eta_0})^{-1/4}$. The oscillator length then equals $\xi_\eta^{-2} = \sqrt{N} \mathcal{B}_{\eta_0}$ and the energy scale equals $\Delta E = N^{-1/2} |g_2| \mathcal{B}_{\eta_0}$.^{*} The n -th eigenlevel has energy $(n + \frac{1}{2}) \Delta E$ for $\eta_0 = \pi/2$ and $(2n + 1) \Delta E$ for $\eta_0 = 0$. The unnormalised ground state in both cases is

$$\psi_\eta^{\text{gs}}(\delta\eta) = \exp \left[-\frac{1}{2} \mathcal{B} \sqrt{N} \delta\eta^2 \right], \quad (10.22)$$

except for odd N when expanding about $\eta_0 = \pi/2$, as the above state then

^{*}The η_0 -dependence of the oscillator length and energy scale has been suppressed from notation. This will be a general notational convention for quantities directly or indirectly dependent on \mathcal{F}_{η_0} from now on, including \mathcal{B}_{η_0} and \mathcal{F}_{η_0} itself.

has incorrect parity and is hence unphysical. In that case, the first excited state of the harmonic oscillator represents the physical ground state. For simplicity, we focus on even numbers of particles hereafter.

10.4 GROUND-STATE OVERLAPS WITH LIMITING NEMATIC STATES

This section derives scaling laws with respect to N of ground-state overlaps with the limiting nematic states, as encountered in the quadratic Zeeman treatment of Chapter 9. The ground states of the previous chapter retained an amount of mean-field-like character, in that their overlaps with the limiting large- $|q|$ nematic states, closely related to mean-field states, were independent of N , as evidenced by Eqs. (9.25) and (9.32). The resulting overlap expressions were given in terms of u -factors, defined in Eq. (9.23) without reference to any N -dependent quantities. As the overlap between any two mean-field states, characterised by linearly independent order parameters, i.e., not equal up to a phase, tends to 0 with increasing N ,[†] this may be interpreted as the ground state containing a robust mean-field component. Since the ground-state overlap with the limiting nematic state tends to 1 with increasing $|q|$, this mean-field component alone becomes a good approximation to the full ground state at large $|q|$.

The situation is different with the alternative potential (10.1) of the present chapter. For $g_1 > 0$ ($g_1 < 0$) the overlap of the ground state with the z -oriented biaxial (uniaxial) nematic state is still the biggest among mean-field states, but even this tends to zero as an inverse power of N . The aim of the present section is deriving the N dependence of the largest mean-field overlaps, with emphasis on the leading-order terms of the obtained expressions.

[†]Even more is true when considering coherent mean-field states, $|\sqrt{N}\boldsymbol{\chi}\rangle \equiv \exp[-\frac{N}{2} + \sqrt{N}\chi_\alpha \hat{a}_\alpha^\dagger] |0\rangle$ with $\boldsymbol{\chi}$ a unit-norm complex vector, since $|\langle \sqrt{N}\boldsymbol{\rho} | \sqrt{N}\boldsymbol{\chi} \rangle| = \exp[N(\operatorname{Re}\boldsymbol{\rho}^\dagger \boldsymbol{\chi} - 1)]$. This tends to zero with increasing N even when $\boldsymbol{\rho} = e^{i\varphi}\boldsymbol{\chi}$ for a real non-zero phase φ , and remains 1 only when $\boldsymbol{\rho} = \boldsymbol{\chi}$. With fixed-particle-number mean-field states, $|\boldsymbol{\chi}_N\rangle \equiv (N!)^{-1/2}(\chi_\alpha \hat{a}_\alpha^\dagger)^N |0\rangle$, the overlap is $\langle \boldsymbol{\rho}_N | \boldsymbol{\chi} \rangle = (\boldsymbol{\rho}^\dagger \boldsymbol{\chi})^N$ and tends to 0 when $|\boldsymbol{\rho}^\dagger \boldsymbol{\chi}| < 1$ and remains 1 when $\boldsymbol{\rho} = \boldsymbol{\chi}$. When $\boldsymbol{\rho} = e^{i\varphi}\boldsymbol{\chi}$ for real non-zero φ , the finite- N overlap is $e^{-iN\varphi}$ which has no well-defined infinite- N limit. In the rotor treatment this ambiguity is circumvented by considering only real $\boldsymbol{\chi}$ and wave-function (anti)symmetrisation.

When considering expansions about $\eta_0 = 0, \pi/2$, most of the expressions involving the matrices $A(\eta), B(\eta)$ of Eq. (10.15) simplify dramatically as

$$A(\eta_0) = \frac{\lambda}{|g_2|} \mathcal{F}_{\eta_0} \mathbb{1}, \quad (10.23)$$

with \mathcal{F}_{η_0} defined under Eq. (10.21). This further implies that Eq. (10.17) simplifies to

$$\hat{S} = -\frac{N}{2\mathcal{F}} \hat{\mathbf{x}}^2 \quad (10.24)$$

and that the matrix $C(\eta_0)$ of Eq. (10.19) simplifies to

$$C(\eta_0) = \frac{|g_2|}{\lambda\mathcal{F}} \sqrt{1 + 2\mathcal{F}} \mathbb{1}. \quad (10.25)$$

The \mathbf{x} -dependent factor of the ground state of the non-similarity-transformed Hamiltonian (10.16) is proportional to $e^S \psi_0(\mathbf{x})$, with the latter factor defined in Eq. (10.19). It is given, up to constant factors, by

$$\psi_x^{\text{gs}}(\mathbf{x}) = \exp \left[-\frac{N}{2\mathcal{F}} \left(1 + \sqrt{1 + 2\mathcal{F}} \right) \mathbf{x}^2 \right] \equiv \exp \left[-\frac{1}{2} N \mathcal{A} \mathbf{x}^2 \right]. \quad (10.26)$$

The uniaxial and biaxial limiting states of the previous chapter are given in the new coordinates, up to constant factors, by

$$\psi_0^{\text{lim}}(\eta, \mathbf{x}) = \eta^{-1} \delta(\eta) \delta^{(2)}(\mathbf{x}) \quad \text{uniaxial} \quad (10.27)$$

$$\psi_{\pi/2}^{\text{lim}}(\eta, \mathbf{x}) = \delta\left(\eta - \frac{\pi}{2}\right) \delta^{(2)}(\mathbf{x}) \quad \text{biaxial} \quad (10.28)$$

where we have not performed the (anti)symmetrisation in the uniaxial case, since we shall again integrate over only half of the sphere in that case. This yields equivalent results and allows for a more streamlined derivation.

At this point notice that all of the considered wave functions, both the physical ground states as well as the limiting states, are independent of φ , are isotropic in \mathbf{x} , and have a product structure with a factor depending solely on η and another factor depending solely on the \mathbf{x} coordinate, for which the general notation $\psi(\eta, \mathbf{x}) = \psi_\eta(\delta\eta) \psi_x(\mathbf{x})$ will be used. These properties will come handy in simplifying expressions for the overlaps.

The latter are again defined as

$$\langle \psi_1 | \psi_2 \rangle \equiv \frac{\langle \psi_1 | \psi_2 \rangle}{\sqrt{\langle \psi_1 | \psi_1 \rangle \langle \psi_2 | \psi_2 \rangle}} \quad (10.29)$$

and we are particularly interested in calculating $\langle \psi^{\text{gs}} | \psi^{\text{lim}} \rangle$ with ψ^{lim} defined in Eq. (10.28) and where ψ^{gs} are rotor ground states whose η - and \mathbf{x} -dependent factors are given in Eqs. (10.22) and (10.26), respectively.

In calculating the unnormalised overlaps $\langle \psi_1 | \psi_2 \rangle$, one finally needs the form of the dot products $\boldsymbol{\Omega}_1 \cdot \boldsymbol{\Omega}_2$ when the $\boldsymbol{\Omega}_i$ are parametrised as $\boldsymbol{\Omega}_i = \boldsymbol{\Omega}_i(\eta_i, \mathbf{x}_i, \varphi_i)$. Denoting $\Delta\varphi \equiv \varphi_2 - \varphi_1$ and $\mathbf{x}'_2 \equiv R(\Delta\varphi)\mathbf{x}_2$, where $R(\cdot)$ is again a rotation matrix, one obtains, after using some trigonometric identities, the expression:

$$\begin{aligned} \boldsymbol{\Omega}_1 \cdot \boldsymbol{\Omega}_2 &= (\cos(\eta_1 - \eta_2) \cos^2 \Delta\varphi + \cos(\eta_1 + \eta_2) \sin^2 \Delta\varphi) \times \\ &\times \sqrt{(1 - \mathbf{x}_1^2)(1 - \mathbf{x}_2^2)} + \mathbf{x}_1 \cdot \mathbf{x}'_2 \end{aligned} \quad (10.30)$$

The unnormalised overlap expression is then, schematically,

$$\begin{aligned} \langle \psi_1 | \psi_2 \rangle &= \mathcal{C} \int_0^\pi d(\Delta\varphi) \int_0^\pi d\eta_1 d\eta_2 \sin \eta_1 \sin \eta_2 \\ &\times \int_{\mathcal{D}} d\mathbf{x}_1 d\mathbf{x}_2 \sqrt{(1 - \mathbf{x}_1^2)(1 - \mathbf{x}_2^2)} (\boldsymbol{\Omega}_1 \cdot \boldsymbol{\Omega}_2)^N \\ &\times \psi_{1\eta}^*(\delta\eta_1) \psi_{1x}^*(\mathbf{x}_1) \psi_{2\eta}(\delta\eta_2) \psi_{2x}(\mathbf{x}_2) \end{aligned} \quad (10.31)$$

where the ranges of coordinates and the integration measure, described above and below Eq. (10.12), respectively, were taken into account. \mathcal{D} denotes the unit disk. As in the negative- q case of the previous chapter, the integral over one of the angles φ_1, φ_2 has been performed, leaving an integral over the variable $\Delta\varphi$ which appears in $(\boldsymbol{\Omega}_1 \cdot \boldsymbol{\Omega}_2)^N$. The performed angular integral, along with factors from the integration measure, is the source of the constant factor \mathcal{C} , which in this case just equals 4π . However, since \mathcal{C} obviously cancels from the normalised overlaps in Eq. (10.29), the notation emphasises that any wave-function-independent factors arising from further simplifications may be absorbed into \mathcal{C} and thus effectively ignored, as we shall do in the following. On account of tight localisation in \mathbf{x} of all wave functions considered, the

$\sqrt{1 - \mathbf{x}}$ factors may also be ignored. Finally, the $\Delta\varphi$ integral is performed after the \mathbf{x}_2 integral so that the integration variable in the latter may be changed to $\mathbf{x}'_2 = R(\Delta\varphi)\mathbf{x}_2$ which does not affect the integration measure nor the \mathbf{x} -isotropic wave functions considered. Renaming the integration variable back to \mathbf{x}_2 , this amounts to substituting \mathbf{x}'_2 in the overlap expression (10.30) with \mathbf{x}_2 , a step we will implicitly perform in all overlap calculations.

Expression (10.31) may be further simplified and made more amenable to analytical manipulation, but the specific simplifications admitted depend on the value of η_0 about which we're expanding, and the two values must be considered separately. We first consider the simpler case of $\eta_0 = \pi/2$, applicable when $g_1 > 0$.

10.4.1 LIMITING-STATE OVERLAPS AT $\eta_0 = \pi/2$

In this case, the first factor of the first term of Eq. (10.30), which we denote by f , may be simplified by letting $\eta_i = \frac{\pi}{2} + \delta\eta_i$ and expanding the cosines to second order in $\delta\eta_i$ as follows:

$$\begin{aligned} f &\equiv \cos(\eta_1 - \eta_2) \cos^2 \Delta\varphi + \cos(\eta_1 + \eta_2) \sin^2 \Delta\varphi \\ &\simeq \cos 2\Delta\varphi \left(1 - \frac{1}{2}(\delta\eta_1^2 + \delta\eta_2^2) \right) + \delta\eta_1 \delta\eta_2. \end{aligned} \quad (10.32)$$

Since it is part of an expression exponentiated to the large number N , the main contributions to the overlap integrals will come from the region where $|\cos 2\Delta\varphi|$ is close to 1, similarly to the negative- q calculation of the previous chapter. Introduce variables $\delta\eta_{\pm} \equiv (\delta\eta_1 \pm \delta\eta_2)/\sqrt{2}$. Letting $\Delta\varphi = \varphi_0 + \delta\varphi$ with $\varphi_0 = 0, \pi/2$ and expanding $\cos 2\Delta\varphi$ in $\delta\varphi$, f of Eq. (10.32) may be approximated by

$$f \simeq \pm [1 - 2\delta\varphi^2 - \delta\eta_{\mp}^2], \quad (10.33)$$

where the upper (lower) sign corresponds to expansion about $\varphi_0 = 0$ ($\varphi_0 = \pi/2$). Consider now the full expression for $\mathbf{\Omega}_1 \cdot \mathbf{\Omega}_2$ in Eq. (10.30) with f replaced by its simplified form. Replace \mathbf{x}'_2 by \mathbf{x}_2 , as justified below Eq. (10.31), and introduce variables $\mathbf{x}_{\pm} \equiv (\mathbf{x}_1 \pm \mathbf{x}_2)/\sqrt{2}$. Expanding the square roots,

one finds

$$\mathbf{\Omega}_1 \cdot \mathbf{\Omega}_2 \simeq \pm [1 - 2\delta\varphi^2 - \delta\eta_{\mp}^2 - \mathbf{x}_{\mp}^2] \quad (10.34)$$

with the signs as in Eq. (10.33). Since we are considering only even values of N for simplicity, as mentioned below Eq. (10.22), this also implies

$$(\mathbf{\Omega}_1 \cdot \mathbf{\Omega}_2)^N \simeq \exp [-N (2\delta\varphi^2 + \delta\eta_{\mp}^2 + \mathbf{x}_{\mp}^2)]. \quad (10.35)$$

Due to the tight localisation of the above expression and the wave functions, all integration limits may be extended to infinity. As it turns out, we may actually evaluate the overlaps to within terms of relative order $N^{-1/2}$. For this level of accuracy, we need to expand the η -dependent measure factors as $\sin \eta_1 \sin \eta_2 = 1 - \frac{1}{2} (\delta\eta_1^2 + \delta\eta_2^2) = 1 - \frac{1}{2} (\delta\eta_+^2 + \delta\eta_-^2)$. With this, the unnormalised overlap expression (10.31) becomes

$$\begin{aligned} \langle \psi_1 | \psi_2 \rangle &= \mathcal{C} \sum_{\pm} \int_{-\infty}^{\infty} d\delta\varphi e^{-2N\delta\varphi^2} \\ &\times \int_{-\infty}^{\infty} d\delta\eta_1 d\delta\eta_2 \left(1 - \frac{1}{2} (\delta\eta_+^2 + \delta\eta_-^2) \right) e^{-N\delta\eta_{\pm}^2} \psi_{1\eta}^*(\delta\eta_1) \psi_2(\delta\eta_2) \\ &\times \int_{\mathbb{R}^2} d\mathbf{x}_1 d\mathbf{x}_2 e^{-N\mathbf{x}_{\pm}^2} \psi_{1x}^*(\mathbf{x}_1) \psi_{2x}(\mathbf{x}_2). \end{aligned} \quad (10.36)$$

It is not difficult to see that the \pm contributions to the outer sum are equal when $\psi_{1,2}$ above are taken to be ψ^{lim} or ψ^{gs} . For our purposes, the sum can thus be converted to a factor of 2 and absorbed into \mathcal{C} . Furthermore, the $\delta\varphi$ integral is independent of the wave functions and may also be absorbed into \mathcal{C} . We shall consider \mathcal{C} set to 1 from now on, since it cancels from final expressions.

The rest of the integral then factorises. Define

$$\begin{aligned} \langle \psi_1 | \psi_2 \rangle_{\eta} &= \int_{-\infty}^{\infty} d\delta\eta_1 d\delta\eta_2 \left(1 - \frac{1}{2} (\delta\eta_+^2 + \delta\eta_-^2) \right) e^{-N\delta\eta_{\pm}^2} \psi_{1\eta}^*(\delta\eta_1) \psi_2(\delta\eta_2), \\ \langle \psi_1 | \psi_2 \rangle_x &= \int_{\mathbb{R}^2} d\mathbf{x}_1 d\mathbf{x}_2 e^{-N\mathbf{x}_{\pm}^2} \psi_{1x}^*(\mathbf{x}_1) \psi_{2x}(\mathbf{x}_2), \end{aligned} \quad (10.37)$$

so that $\langle \psi_1 | \psi_2 \rangle = \langle \psi_1 | \psi_2 \rangle_\eta \langle \psi_1 | \psi_2 \rangle_x$. Furthermore, define

$$(\psi_1 | \psi_2)_c \equiv \frac{\langle \psi_1 | \psi_2 \rangle_c}{\sqrt{\langle \psi_1 | \psi_1 \rangle_c \langle \psi_2 | \psi_2 \rangle_c}} \quad (10.38)$$

where c is either η or x . The total overlap, as defined in Eq. (10.29), is then given by $(\psi_1 | \psi_2) = (\psi_1 | \psi_2)_\eta (\psi_1 | \psi_2)_x$.

Recalling that $\psi_x^{\text{gs}}(\mathbf{x}) = \exp[-\frac{N}{2}\mathcal{A}\mathbf{x}^2]$, with \mathcal{A} defined in Eq. (10.26), and $\psi_x^{\text{lim}}(\mathbf{x}) = \delta^{(2)}(\mathbf{x})$, one may directly invoke results of Sec. 9.4 to ascertain that

$$(\psi^{\text{gs}} | \psi^{\text{lim}})_x = \frac{\sqrt{\mathcal{A}(\mathcal{A}+2)}}{\mathcal{A}+1}. \quad (10.39)$$

Now recall that $\psi_\eta^{\text{gs}}(\delta\eta) = \exp[-\frac{\mathcal{B}\sqrt{N}}{2}\delta\eta^2]$, with \mathcal{B} defined above Eq. (10.22), and that the limiting wave function, when rewritten in terms of $\delta\eta$ rather than η , is in this case $\psi_\eta^{\text{lim}}(\delta\eta) = \delta(\delta\eta)$. The η integrals involving delta functions are straightforward and equal

$$\begin{aligned} \langle \psi^{\text{lim}} | \psi^{\text{lim}} \rangle_\eta &= 1 \\ \langle \psi^{\text{gs}} | \psi^{\text{lim}} \rangle_\eta &= \int_{-\infty}^{\infty} d\delta\eta \left(1 - \frac{1}{2}\delta\eta^2\right) e^{-\frac{1}{2}(N+\mathcal{B}\sqrt{N})\delta\eta^2} \\ &= \sqrt{\frac{2\pi}{N}} \left(1 - \frac{\mathcal{B}}{2\sqrt{N}} + \mathcal{O}(N^{-1})\right) \end{aligned} \quad (10.40)$$

Finally, $\langle \psi^{\text{gs}} | \psi^{\text{gs}} \rangle_\eta$ is a Gaussian integral over $\delta\eta_1$ and $\delta\eta_2$, with the integrand's exponent equal to $-N\delta\eta_-^2 - \frac{\mathcal{B}\sqrt{N}}{2}(\delta\eta_1^2 + \delta\eta_2^2) = -\left(N + \frac{\mathcal{B}\sqrt{N}}{2}\right)\delta\eta_-^2 - \frac{\mathcal{B}\sqrt{N}}{2}\delta\eta_+^2$. Since $d\delta\eta_1 d\delta\eta_2 = d\delta\eta_+ d\delta\eta_-$, the Gaussian integral is now straightforward and yields

$$\langle \psi^{\text{gs}} | \psi^{\text{gs}} \rangle_\eta = \frac{2\pi}{\sqrt{2\mathcal{B}}} N^{-3/4} \left(1 - \frac{2 + \mathcal{B}^2}{4\mathcal{B}\sqrt{N}} + \mathcal{O}(N^{-1})\right) \quad (10.41)$$

Assembling the above factors into $(\psi^{\text{gs}} | \psi^{\text{lim}})_\eta$ and multiplying by $(\psi^{\text{gs}} | \psi^{\text{lim}})_x$ finally yields

$$(\psi^{\text{gs}} | \psi^{\text{lim}}) = \frac{\sqrt{\mathcal{A}(\mathcal{A}+2)}}{\mathcal{A}+1} (2\mathcal{B})^{1/4} N^{-1/8} \left(1 + \frac{2 - 3\mathcal{B}^2}{8\mathcal{B}\sqrt{N}} + \mathcal{O}(N^{-1})\right). \quad (10.42)$$

This expression tends to 0 as $N^{-1/8}$ with increasing N , in marked contrast to the situation in the presence of the quadratic Zeeman field. While computationally accessible particle numbers are hardly in the large- N regime, the numerical results shown in the (a) subpanel of Fig. 10.2 qualitatively support our analytical conclusions as all overlaps are seen to decrease with increasing N . The relative error of expression (10.42) with respect to the numerically obtained overlaps is just under 10% at the parameter values and range of N of Fig. 10.2, and slowly decreases with N . The agreement is thus expected to become better for larger values of N .

10.4.2 LIMITING-STATE OVERLAPS AT $\eta_0 = 0$

In this case the f component of the general positional overlap, as defined in the first line of Eq. (10.32), may again be simplified by expanding the cosines to second order in η_i , which themselves are tightly localised about zero, yielding

$$f \simeq 1 - \frac{1}{2} (\eta_1^2 + \eta_2^2 - 2\eta_1\eta_2 \cos 2\Delta\varphi) \quad (10.43)$$

Following reasoning analogous to that of the previous subsection, the exponentiated dot product is found to be well approximated by

$$(\mathbf{\Omega}_1 \cdot \mathbf{\Omega}_2)^N \simeq \exp \left[-\frac{N}{2} (\eta_1^2 + \eta_2^2 - 2\eta_1\eta_2 \cos 2\Delta\varphi + 2\mathbf{x}_-^2) \right]. \quad (10.44)$$

Combining this with appropriately extending integration limits to infinity and approximating the sines appearing in the integration measure by $\sin \eta_i \simeq \eta_i$, allows the unnormalised overlap expression of Eq. (10.31) to be rewritten as

$$\begin{aligned} \langle \psi_1 | \psi_2 \rangle &= \mathcal{C} \int_0^{2\pi} d\zeta \int_0^\infty d\eta_1 d\eta_2 \eta_1 \eta_2 e^{-\frac{N}{2} (\eta_1^2 + \eta_2^2 - 2\eta_1 \eta_2 \cos \zeta)} \psi_{1\eta}^*(\eta_1) \psi_{2\eta}(\eta_2) \\ &\times \int_{\mathbb{R}^2} d\mathbf{x}_1 d\mathbf{x}_2 e^{-N\mathbf{x}_-^2} \psi_{1x}^*(\mathbf{x}_1) \psi_{2x}(\mathbf{x}_2) \end{aligned} \quad (10.45)$$

where ζ corresponds to $2\Delta\varphi$. Note that the lower integration limits of the η integrals cannot be extended beyond 0 as η here has the character of a radial

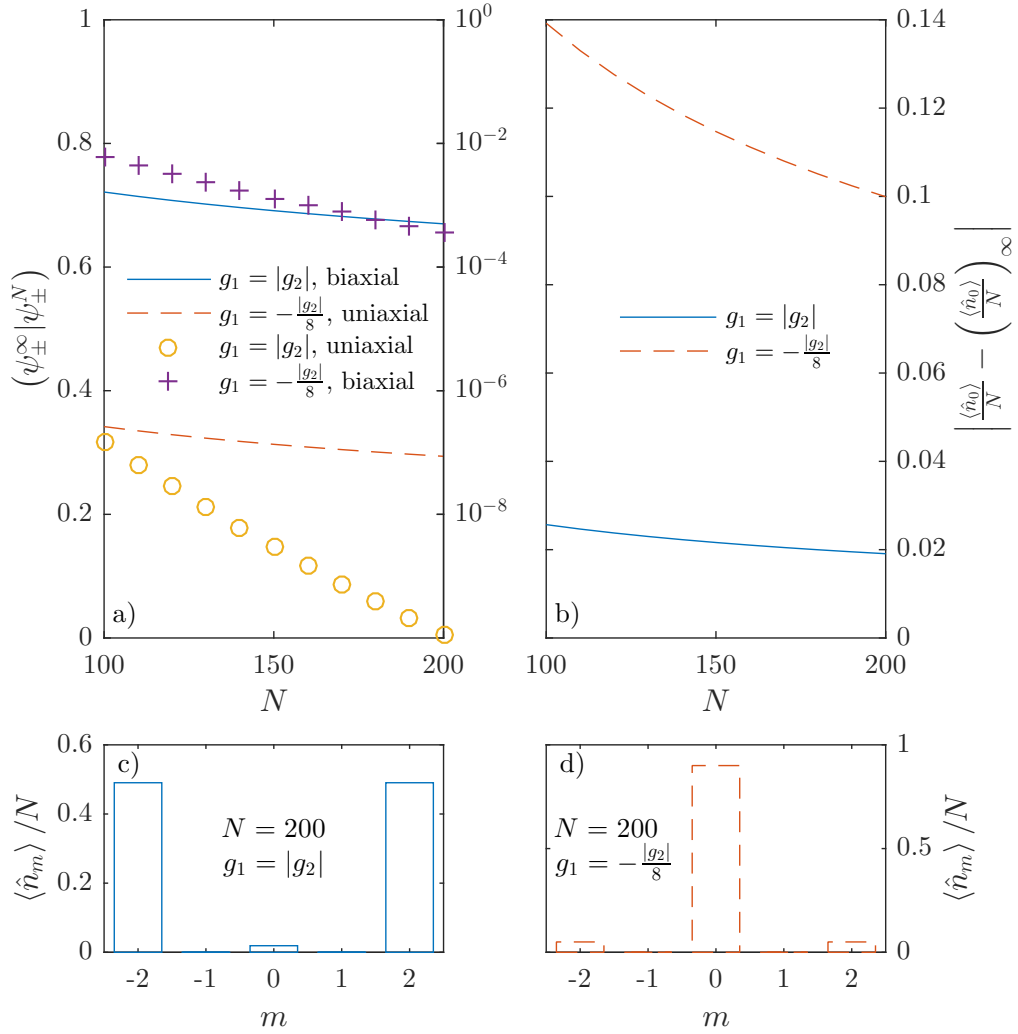


Figure 10.2: (a) The absolute value of overlaps between the limiting states $|\psi_{\pm}^{\infty}\rangle$ and numerically computed ground states. The left linear axis corresponds to the bigger overlaps, represented by lines, and the right logarithmic axis to the smaller overlaps, represented by markers. (b) The numerically computed expectation value of the fraction of particles in the $m = 0$ single-particle magnetic sublevel. (See the end of Sec. 10.5 for details and explanation of notation.) Both (a) and (b) are plotted with respect to particle number N at $\lambda = 10|g_2|$. (c) and (d) show relative occupations of individual single-particle magnetic sublevels at $N = 200$ for positive and negative g_1 , respectively.

coordinate. Additionally, extending the limits to $-\infty$ would demonstrably make the norm of any state 0.

Again set \mathcal{C} to 1 and let $\langle \psi_1 | \psi_2 \rangle = \langle \psi_1 | \psi_2 \rangle_\eta \langle \psi_1 | \psi_2 \rangle_x$ with

$$\begin{aligned}\langle \psi_1 | \psi_2 \rangle_\eta &= \int_0^{2\pi} d\zeta \int_0^\infty d\eta_1 d\eta_2 \eta_1 \eta_2 e^{-\frac{N}{2}(\eta_1^2 + \eta_2^2 - 2\eta_1 \eta_2 \cos \zeta)} \psi_{1\eta}^*(\eta_1) \psi_{2\eta}(\eta_2), \\ \langle \psi_1 | \psi_2 \rangle_x &= \int_{\mathbb{R}^2} d\mathbf{x}_1 d\mathbf{x}_2 e^{-N\mathbf{x}_\pm^2} \psi_{1x}^*(\mathbf{x}_1) \psi_{2x}(\mathbf{x}_2),\end{aligned}\quad (10.46)$$

as well as $(\psi_1 | \psi_2) = (\psi_1 | \psi_2)_\eta (\psi_1 | \psi_2)_x$, with the factors defined by Eq. (10.38). In analogy with previous calculations, $(\psi^{\text{gs}} | \psi^{\text{lim}})_x$ can again be seen to be given by $\sqrt{\mathcal{A}(\mathcal{A} + 2)}/(\mathcal{A} + 1)$.

Recalling $\psi_\eta^{\text{lim}} = \eta^{-1} \delta(\eta)$ and $\psi_\eta^{\text{gs}} = \exp\left[-\frac{\sqrt{N\mathcal{B}}}{2}\eta^2\right]$, the simpler unnormalised overlaps, involving ψ^{lim} , are found to be:

$$\begin{aligned}\langle \psi^{\text{lim}} | \psi^{\text{lim}} \rangle_\eta &= 2\pi \\ \langle \psi^{\text{gs}} | \psi^{\text{lim}} \rangle_\eta &= 2\pi \int_0^\infty du e^{-(N + \mathcal{B}\sqrt{N})u} = \frac{2\pi}{N + \mathcal{B}\sqrt{N}}.\end{aligned}\quad (10.47)$$

The form of the final unnormalised overlap is

$$\langle \psi^{\text{gs}} | \psi^{\text{gs}} \rangle_\eta = \int_0^{2\pi} d\zeta \int_0^\infty d\eta_1 d\eta_2 \eta_1 \eta_2 e^{-\frac{1}{2}((N + \mathcal{B}\sqrt{N})(\eta_1^2 + \eta_2^2) - 2N\eta_1 \eta_2 \cos \zeta)}.\quad (10.48)$$

The inner integral is of a less frequently encountered form, compared to Gaussian integrals over all of Euclidean space, but one that nevertheless also admits a closed-form solution. For positive α and real β such that $|\beta| \leq \alpha$, one has

$$\begin{aligned}\mathcal{I}_{\alpha,\beta} \equiv \int_0^\infty d\eta_1 d\eta_2 \eta_1 \eta_2 e^{-\frac{1}{2}(\alpha(\eta_1^2 + \eta_2^2) - 2\beta\eta_1 \eta_2)} &= \\ \frac{1}{\alpha^2 - \beta^2} \left[1 + \frac{\beta}{\sqrt{\alpha^2 - \beta^2}} \left(\frac{\pi}{2} + \arctan \frac{\beta}{\sqrt{\alpha^2 - \beta^2}} \right) \right].\end{aligned}\quad (10.49)$$

In the case of Eq. (10.48), we may set $\alpha = N + \mathcal{B}\sqrt{N}$ and $\beta = N \cos \zeta$.

Denote thus

$$g(\zeta) \equiv \mathcal{I}_{N+\mathcal{B}\sqrt{N}, N \cos \zeta} = \frac{1}{\gamma(\zeta)} \left[1 + \tau(\zeta) \left(\frac{\pi}{2} + \arctan \tau(\zeta) \right) \right] \quad (10.50)$$

where $\gamma(\zeta) \equiv N^2 \left(\sin^2 \zeta + \frac{2\mathcal{B}}{\sqrt{N}} + \frac{\mathcal{B}^2}{N} \right)$ corresponds to $\alpha^2 - \beta^2$ and $\tau(\zeta) \equiv \cos \zeta / \sqrt{\sin^2 \zeta + \frac{2\mathcal{B}}{\sqrt{N}} + \frac{\mathcal{B}^2}{N}}$ to $\beta / \sqrt{\alpha^2 - \beta^2}$ of Eq. (10.49). The function $g(\zeta)$ is even, periodic with period 2π , heavily peaked about $\zeta = n\pi, n \in \mathbb{Z}$, and is essentially zero elsewhere. For symmetry reasons we thus shift ζ integration boundaries to $[-\pi, \pi]$. Since $\tau(\zeta)$ is very large in the vicinity of $\zeta = 0$, we may use the asymptotic expansion $\arctan x \simeq \frac{\pi}{2} - x^{-1}$. This yields

$$g(\zeta) \simeq \pi \frac{\tau(\zeta)}{\gamma(\zeta)} = N^{-2} \pi \frac{\cos \zeta}{\left(\sin^2 \zeta + \frac{2\mathcal{B}}{\sqrt{N}} + \frac{\mathcal{B}^2}{N} \right)^{\frac{3}{2}}} \equiv \tilde{g}(\zeta) \quad (10.51)$$

The effective function $\tilde{g}(\zeta)$ agrees with $g(\zeta)$ remarkably well for $|\zeta| \lesssim \frac{\pi}{2}$. In the range $\frac{\pi}{2} < |\zeta| < \pi$, however, the asymptotic expansion becomes unwarranted, and $\tilde{g}(\zeta)$ takes on large negative values, while $g(\zeta)$ is effectively zero. One may nevertheless still use the simpler asymptotic $\tilde{g}(\zeta)$ to extract the leading-order behaviour of $\langle \psi^{\text{gs}} | \psi^{\text{gs}} \rangle_\eta = \int d\zeta g(\zeta)$ with respect to N . This is achieved by integrating only over $[-\zeta_0, \zeta_0]$ with $\zeta_0 \sim \frac{\pi}{2}$. Neglecting terms of relative order N^{-1} and utilising the indefinite integral

$$\int d\zeta \cos \zeta (\sin^2 \zeta + a)^{-3/2} = \frac{\sin \zeta}{a \sqrt{a + \sin^2 \zeta}} \quad (10.52)$$

allows one to find

$$\begin{aligned} \langle \psi^{\text{gs}} | \psi^{\text{gs}} \rangle_\eta &= N^{-2} \pi \int_{-\zeta_0}^{\zeta_0} d\zeta \frac{\cos \zeta}{\left(\sin^2 \zeta + \frac{2\mathcal{B}}{\sqrt{N}} \right)^{\frac{3}{2}}} \\ &= 2\pi N^{-2} \frac{\sin \zeta_0}{\frac{2\mathcal{B}}{\sqrt{N}} \sqrt{\sin^2 \zeta_0 + \frac{2\mathcal{B}}{\sqrt{N}}}} = \frac{\pi}{\mathcal{B}} N^{-\frac{3}{2}} \left(1 + \frac{2\mathcal{B}}{\sqrt{N} \sin^2 \zeta_0} \right)^{-\frac{1}{2}} \\ &= \frac{\pi}{\mathcal{B}} N^{-\frac{3}{2}} \left(1 + \mathcal{O} \left(N^{-\frac{1}{2}} \right) \right). \end{aligned} \quad (10.53)$$

Putting all of the factors together finally yields

$$\langle \psi^{\text{gs}} | \psi^{\text{lim}} \rangle = \frac{\sqrt{2\mathcal{B}\mathcal{A}(\mathcal{A}+2)}}{\mathcal{A}+1} N^{-\frac{1}{4}} \left(1 + \mathcal{O}\left(N^{-\frac{1}{2}}\right) \right) \quad (10.54)$$

Again, the overlaps steadily tend to zero with increasing N , once more demonstrating the non-mean-field nature of the ground states. Compared to the numerically obtained results in Fig. 10.2, the above leading-order expansion overestimates the results by about 20%, most likely reflecting the fact that some of the approximations enacted are not entirely applicable for such low particle numbers, though the discrepancy does get smaller with increasing N .

10.5 MAGNETIC SUBLEVEL OCCUPATIONS

In this section we demonstrate that, even though the rotor ground states have been shown to differ significantly from mean-field-like states, some qualitative aspects of the exact quantum treatment agree with the effects of the order-by-disorder mechanism in the related continuum problem. Notably, the ground-state magnetic sublevel occupation expectation values $\langle \hat{n}_m \rangle = \langle \hat{a}_m^\dagger \hat{a}_m \rangle$ are in good qualitative agreement.

Since we are working with unnormalised states, the expectation value of $\hat{\mathcal{O}}$ in state $|\psi\rangle$ is defined as $\langle \hat{\mathcal{O}} \rangle \equiv \langle \psi | \hat{\mathcal{O}} | \psi \rangle / \langle \psi | \psi \rangle$. To calculate $\langle \hat{n}_m \rangle$, first consider general matrix elements of operators of the form $\hat{b}_\alpha^\dagger \hat{b}_\beta$. These are particularly simple in the rotor framework and are given by

$$\begin{aligned} \langle \psi_1 | \hat{b}_\alpha^\dagger \hat{b}_\beta | \psi_2 \rangle &= \int d\Omega_1 d\Omega_2 \langle \Omega_{1N} | \hat{b}_\alpha^\dagger \hat{b}_\beta | \Omega_{2N} \rangle \psi_1^*(\Omega_1) \psi_2(\Omega_2) \\ &= N \int d\Omega_1 d\Omega_2 (\Omega_1 \cdot \Omega_2)^{N-1} \Omega_{1\alpha} \psi_1^*(\Omega_1) \Omega_{2\beta} \psi_2(\Omega_2) \\ &\simeq N \langle \hat{\Omega}_\alpha \psi_1 | \hat{\Omega}_\beta \psi_2 \rangle. \end{aligned} \quad (10.55)$$

The second equality follows from the definition $|\Omega_N\rangle \equiv \frac{1}{\sqrt{N!}} \left(\Omega_\alpha \hat{b}_\alpha^\dagger \right)^N |0\rangle$, while in the last approximate equality, the exponent $N-1$ is approximated by N .

The rotor ground state ψ^{gs} is independent of φ . Referring to the definition of current coordinates in Eq. (10.10) and the fact that the \mathbf{x} variable is localised on a scale $\sim N^{-1/2}$, this implies, by symmetry,

$$\langle \hat{b}_2^\dagger \hat{b}_2 \rangle \simeq N \frac{\langle \hat{\Omega}_2 \psi^{\text{gs}} | \hat{\Omega}_2 \psi^{\text{gs}} \rangle}{\langle \psi^{\text{gs}} | \psi^{\text{gs}} \rangle} \sim 1 \sim \langle \hat{b}_3^\dagger \hat{b}_3 \rangle. \quad (10.56)$$

Furthermore, $\langle \hat{b}_2^\dagger \hat{b}_2 + \hat{b}_3^\dagger \hat{b}_3 \rangle = \langle \hat{n}_1 + \hat{n}_{-1} \rangle$. Since $\sum_{m=-2}^2 \langle \hat{n}_m \rangle = N$, at least one of the $\langle \hat{n}_m \rangle$ has to be of order N and thus the occupations of the $m = \pm 1$ sublevels can safely be neglected. We also have $\langle \hat{n}_0 \rangle = \langle \hat{b}_1^\dagger \hat{b}_1 \rangle$ and $\langle \hat{b}_4^\dagger \hat{b}_4 + \hat{b}_5^\dagger \hat{b}_5 \rangle = \langle \hat{n}_2 + \hat{n}_{-2} \rangle$. Since the original Hamiltonian, in terms of the $\hat{a}_m^{(\dagger)}$ operators, is invariant under the single-particle sublevel interchange such that $m \rightarrow -m$, and we are considering the \hat{F}_z null space, we also expect $\langle \hat{n}_2 \rangle = \langle \hat{n}_{-2} \rangle \simeq (N - \langle \hat{n}_0 \rangle)/2$. We thus only need to calculate $\langle \hat{b}_1^\dagger \hat{b}_1 \rangle$ and infer the occupations through the simple relations listed above.

We first do so at $g_1 < 0$, where the ground state is localised about $\eta_0 = 0$. To be thorough, we shall attempt to calculate $\langle \psi^{\text{gs}} | \hat{b}_1^\dagger \hat{b}_1 | \psi^{\text{gs}} \rangle$ as given in the second line of Eq. (10.55), rather than in the approximate form on the third line. The resulting integral is equivalent to that for $\langle \psi^{\text{gs}} | \psi^{\text{gs}} \rangle$ with the integrand multiplied by $\mathcal{L} \equiv N(\boldsymbol{\Omega}_1)_1(\boldsymbol{\Omega}_2)_1/(\boldsymbol{\Omega}_1 \cdot \boldsymbol{\Omega}_2)$. Recall from the coordinate definitions in Eq. (10.10) that $\boldsymbol{\Omega}_1 = \cos \eta \sqrt{1 - \mathbf{x}^2}$ and from Eqs. (10.43) and (10.44) that $\boldsymbol{\Omega}_1 \cdot \boldsymbol{\Omega}_2 \simeq 1 - \frac{1}{2}(\eta_1^2 + \eta_2^2 - 2\eta_1\eta_2 \cos \zeta + 2\mathbf{x}_-^2)$. Expanding to relative order $N^{-1/2}$ yields $\mathcal{L} \simeq N(1 - \eta_1\eta_2 \cos \zeta)$. $\langle \psi^{\text{gs}} | \hat{b}_1^\dagger \hat{b}_1 | \psi^{\text{gs}} \rangle$ again factors into $\langle \psi^{\text{gs}} | \hat{b}_1^\dagger \hat{b}_1 | \psi^{\text{gs}} \rangle_\eta$ and $\langle \psi^{\text{gs}} | \hat{b}_1^\dagger \hat{b}_1 | \psi^{\text{gs}} \rangle_x$. Since \mathcal{L} does not depend on $\mathbf{x}_{1,2}$, $\langle \psi^{\text{gs}} | \hat{b}_1^\dagger \hat{b}_1 | \psi^{\text{gs}} \rangle_x = \langle \psi^{\text{gs}} | \psi^{\text{gs}} \rangle_x$, implying $\langle \hat{b}_1^\dagger \hat{b}_1 \rangle = \langle \psi^{\text{gs}} | \hat{b}_1^\dagger \hat{b}_1 | \psi^{\text{gs}} \rangle_\eta / \langle \psi^{\text{gs}} | \psi^{\text{gs}} \rangle_\eta$. The other factor equals

$$\begin{aligned} \langle \psi^{\text{gs}} | \hat{b}_1^\dagger \hat{b}_1 | \psi^{\text{gs}} \rangle_\eta &= \int_0^{2\pi} d\zeta \int_0^\infty d\eta_1 d\eta_2 \eta_1 \eta_2 \mathcal{L} e^{-\frac{1}{2}((N+\mathcal{B}\sqrt{N})(\eta_1^2 + \eta_2^2) - 2N\eta_1\eta_2 \cos \zeta)} = \\ N \langle \psi^{\text{gs}} | \psi^{\text{gs}} \rangle_\eta - N \int_0^{2\pi} d\zeta \int_0^\infty d\eta_1 d\eta_2 \eta_1^2 \eta_2^2 \cos \zeta e^{-\frac{1}{2}((N+\mathcal{B}\sqrt{M})(\eta_1^2 + \eta_2^2) - 2N\eta_1\eta_2 \cos \zeta)} \\ &\equiv N \langle \psi^{\text{gs}} | \psi^{\text{gs}} \rangle_\eta - N\mathcal{K}. \end{aligned} \quad (10.57)$$

On the second line we have formally replaced \sqrt{N} with \sqrt{M} , considered independent from N , to simplify the following step, after which we will set $M = N$

again. Writing $\eta_1\eta_2 \cos \zeta$ in the suggestive form $-\frac{1}{2}((\eta_1^2 + \eta_2^2 - 2\eta_1\eta_2 \cos \zeta) - (\eta_1^2 + \eta_2^2))$, we find $\mathcal{K} = \left(\frac{\partial}{\partial N} - \frac{1}{\sqrt{M}}\frac{\partial}{\partial \mathcal{B}}\right) \langle \psi^{\text{gs}} | \psi^{\text{gs}} \rangle_\eta$, had $\langle \psi^{\text{gs}} | \psi^{\text{gs}} \rangle_\eta$ also been evaluated with \sqrt{N} substituted by \sqrt{M} . The term arising from the $\frac{\partial}{\partial N}$ derivation is of lower order and may be neglected, and M may be renamed back to N . Referring to the form of $\langle \psi^{\text{gs}} | \psi^{\text{gs}} \rangle_\eta$ in Eq. (10.53), showing that $\langle \psi^{\text{gs}} | \psi^{\text{gs}} \rangle_\eta \propto \mathcal{B}^{-1}$, we may infer

$$\mathcal{K} \simeq -\frac{1}{\sqrt{N}}\frac{\partial}{\partial \mathcal{B}} \langle \psi^{\text{gs}} | \psi^{\text{gs}} \rangle_\eta = \frac{\langle \psi^{\text{gs}} | \psi^{\text{gs}} \rangle_\eta}{\mathcal{B}\sqrt{N}}. \quad (10.58)$$

Putting the above results together finally yields

$$\langle \hat{n}_0 \rangle = \left\langle \hat{b}_1^\dagger \hat{b}_1 \right\rangle = \frac{\langle \psi^{\text{gs}} | \hat{b}_1^\dagger \hat{b}_1 | \psi^{\text{gs}} \rangle_\eta}{\langle \psi^{\text{gs}} | \psi^{\text{gs}} \rangle_\eta} = N - \frac{\sqrt{N}}{\mathcal{B}} + \mathcal{O}(1) \quad (10.59)$$

and, by the previous discussion,

$$\langle \hat{n}_2 \rangle = \langle \hat{n}_{-2} \rangle = \frac{\sqrt{N}}{2\mathcal{B}} + \mathcal{O}(1). \quad (10.60)$$

In the large- N limit, the \sqrt{N} terms become negligible compared to N and essentially all particles occupy the $m = 0$ sublevel. Note that this is exactly the sublevel distribution arising in the related continuum problem through Order by Disorder.

The above occupation expressions are in agreement with trends discernible from numerical results. Subpanel (b) of Fig. 10.2 shows the numerically computed expectation value of the fraction of particles in the $m = 0$ single-particle magnetic sublevel with respect to particle number N at $\lambda = 10|g_2|$. For compactness, the quantity actually plotted is $\left| \frac{\langle \hat{n}_0 \rangle}{N} - \left(\frac{\langle \hat{n}_0 \rangle}{N} \right)_\infty \right|$ where $\langle \cdot \rangle$ denotes the ground-state expectation value and $(\cdot)_\infty$ denotes taking the limit of $N \rightarrow \infty$. $\left(\frac{\langle \hat{n}_0 \rangle}{N} \right)_\infty$ is predicted analytically. As we have just shown, it equals 1 for negative g_1 . For positive g_1 , it turns out to be 0, as will be shown shortly. Numerical results also confirm that $\langle \hat{n}_0 \rangle = N - \langle \hat{n}_2 + \hat{n}_{-2} \rangle$ to a very good approximation, with $\langle \hat{n}_1 + \hat{n}_{-1} \rangle$ already being negligible for the values of N shown in Fig 10.2. Qualitative features of the sublevel particle distributions are visible in subpanels (c) and (d) of Fig 10.2, showing relative

occupations of individual single-particle magnetic sublevels, labelled by m , at $N = 200$ and $\lambda = 10|g_2|$, for both signs of g_1 , as obtained through exact diagonalisation.

The fractional occupation expectation differences decrease with N for both signs of g_1 , indicating the correct trend. Compared to the numerical results in Fig. 10.2(b), expression (10.59), appropriate for $g_1 < 0$, overestimates $\frac{\langle \hat{n}_0 \rangle}{N}$ by about 0.03, but gets better with increasing N .

For $g_1 > 0$, i.e., when expanding about $\eta_0 = \pi/2$, truncating expressions at the lowest order suffices, and yields $(\boldsymbol{\Omega}_1)_1(\boldsymbol{\Omega}_2)_1/(\boldsymbol{\Omega}_1 \cdot \boldsymbol{\Omega}_2) \simeq \pm \delta\eta_1 \delta\eta_2 = \pm (\delta\eta_+^2 - \delta\eta_-^2)/2$. We may also set the sines appearing in the integration measure to 1. \boldsymbol{x} again factors out of the problem. One finds

$$\begin{aligned} \langle \psi^{\text{gs}} | \hat{b}_1^\dagger \hat{b}_1 | \psi^{\text{gs}} \rangle_\eta &= \frac{N}{2} \int_{-\infty}^{\infty} d\delta\eta_+ d\delta\eta_- (\delta\eta_+^2 - \delta\eta_-^2) e^{-(N + \frac{\mathcal{B}\sqrt{N}}{2})\delta\eta_-^2 - \frac{\mathcal{B}\sqrt{N}}{2}\delta\eta_+^2} \\ &\simeq \frac{\sqrt{N}}{2\mathcal{B}} \langle \psi^{\text{gs}} | \psi^{\text{gs}} \rangle_\eta \end{aligned} \quad (10.61)$$

and consequently $\langle \hat{n}_0 \rangle = \sqrt{N}/2\mathcal{B} + \mathcal{O}(1)$. This overestimates the results of Fig. 10.2(b) by about 0.02, with the relative discrepancy slowly decreasing with N . The qualitative conclusion of agreement with continuum results, however, remains the same.

The final picture that emerges is that of a system that may be treated at the quantum level with only very mild approximations, shows distinct features, not seen in the mean-field treatment, and yet follows the same qualitative patterns. In particular, the single-particle sublevel occupation values are fully consistent with those determined by a Bogoliubov-theory order-by-disorder mechanism in the continuum. This follows from an application of degenerate perturbation theory, yielding an effective Hamiltonian for the classically degenerate η degree of freedom, which may be viewed as a fully quantum counterpart to the (beyond-)mean-field phenomenon of Order by Disorder.

11

CONCLUSION

This thesis has presented new results on a pair of systems with strong experimental links to cold atoms, putting particular emphasis on how the fluctuation-induced phenomenon of Order by Disorder arises and manifests itself in them. Both have been found to feature the phenomenon in a manner that affords further physical interpretation.

In the dice lattice at half-flux, this takes the form of what seem like fluctuation-mediated interactions between the extended mean-field domain walls. These domain walls already take centre stage at the mean-field level, before taking into account fluctuations, and closely relate the mean-field treatment of the full Bose-Hubbard Hamiltonian (2.1) to that of the XY model in the same geometry and the corresponding results by Korshunov.^{61,63,62} The two types of domain walls also provide a convenient means of classifying members of the greatly degenerate mean-field ground-state manifold. Its extensive degeneracy may be interpreted to originate from a completely flat single-particle spectrum, including a ground-state band exhibiting a vast degeneracy, that the interactions fail to completely lift. An order-by-disorder analysis has been performed by calculating the Bogoliubov excitation spectra of the four smallest-unit-cell mean-field states. State (b) of Fig. 3.1 has been found to

be universally selected as the true ground state, both at zero temperature, and even more robustly so at finite temperature. Bogoliubov spectra have been calculated and summed up for another set of mean-field states. These were periodic, having a large unit cell, for the most part resembling state (a) of Fig. 3.1, with two domain walls of the same type inserted at variable separations. These were enforced to be small compared to the unit-cell size. The zero-point contributions to the free energy are consistent with a picture wherein type-I domain walls interact attractively and type-II domain walls repel each other. This is consistent with state (b), having the highest density of type-II domain walls, always being lowest in energy, and state (c), having the highest density of type-I domain walls, always being highest in energy.

These results alone suggest a rather broad range of options for further work on the dice lattice, that include studying finite temperature behaviour and interactions between intersecting domain walls of different types. As we demonstrate in the following appendix, there is another class of mean-field states, closely related to that of domain walls inserted into state (a), that does not exhibit translational symmetry, but rather rotational symmetry about a point. These were discovered only after the publication of the work on the dice lattice, presented in this thesis. On the basis of the domain-wall-interactions picture, they should not pose a threat to state (b) as the lowest-energy state. However, their point-like nature is peculiar and one may even hope to form an effective Hamiltonian governing their dynamics, along the lines of the lowest Landau-level study by Möller and Cooper.⁸⁵ While the author admits that this may seem optimistic, the dice lattice at half-flux appears to host no shortage of curious and surprising low-energy phenomena in its various phases. These all seem to be traceable, in one way or another, back to the exceptional localisation mechanism of Aharonov-Bohm cages. Whatever the outcomes of future studies of the dice lattice, it thus seems highly unlikely that they would not be interesting.

The other system considered was that of a tightly confined spin-2 condensate. Besides demonstrating the correspondence between the mean-field notion of Order by Disorder and a full quantum computation for a specific external potential, a considerable number of pages has been devoted to the main an-

alytical tool, the rotor mapping. This has been instrumental in deriving, for the first time, non-mean-field analytical results for tightly confined condensates in the presence of a quadratic Zeeman field for spin-1 species, and, in the publication discussed and expanded upon in this thesis, spin-2 species as well. While generalising the mapping includes transferring the domain of our effective description from a regular 2-sphere to a geometrically much less intuitive 4-sphere, and giving up favourable representation-theoretic properties that significantly reduce the amount of algebra in the spin-1 setting, the shift proves entirely manageable. This makes the rotor mapping an attractive tool with which to study even higher-spin condensates. On the other hand, rotor mappings may be fruitfully applied to systems other than those consisting of spinors. A prominent example of this is the two-dimensional Bose-Hubbard mapping of Anglin et al.,⁸ recast into the rotor formalism by Barnett et al.¹² and adapted to the present treatment in Sec. 8.1. According to the algebraically motivated rule of thumb of Chapter 8, the rotor mapping is likely to offer significant simplifications whenever the system Hamiltonian is expressible in terms of creation/annihilation operator bilinears $\hat{\mathbf{a}}^\dagger M \hat{\mathbf{a}}$, such that the matrix M is largely similar to an imaginary antisymmetric matrix. It is not easy to conjure up such systems, but the author believes they will be discovered spontaneously and be analysed in the rotor framework accordingly. Finally it should be mentioned that the feasibility of calculations in the special Hermitianising basis of Eq. (7.12) is currently being investigated for the rotor mapping, and that the preliminary observations seem very promising.

After extensively introducing the rotor mapping as the main calculational tool and treating several examples, the previous two chapters of this thesis applied the mapping to the specific problem of tightly confined spin-2 condensates. Analytical results for the low-energy spectra in the presence of a non-zero quadratic Zeeman field were derived. This includes excitations about a fragmented condensate in the large negative- Nq regime, that does not admit a Bogoliubov analysis and has consequently evaded an analytical description to date. Where it is stable, Bogoliubov theory appears to agree with the mapping in general, i.e., including its applications to the spin-1 sys-

tem and the double-well Bose-Hubbard Hamiltonian. This is also the case for the large-positive- Nq regime. In both cases, the effective rotor Hamiltonians were found to be those of independent one-dimensional harmonic oscillators, yielding spectra in excellent agreement with an exact-diagonalisation numerical study, admitting up to about 300 particles. Ground-state wave-function overlaps with the limiting large- $N|q|$ ground states were also considered, and analytical expressions for them derived. The latter were verified to reproduce the numerically computed overlaps to first order in an asymptotic expansion, yielding good agreement at large $|q|$.

One of the features that was naïvely expected to be seen in the overlap plots with respect to q was ground states approaching the limiting large- $N|q|$ states in a particular manner, depending on the region of the spin-2 diagram, determined by the effective spin interaction constants g_i . Notably, one would expect the uniaxial state to be approached faster with increasing q and the biaxial state slower with increasing $-q$ in the uniaxial region, compared to the speed of the respective approaches in the biaxial region. This, however, is not observed, and the deeper in the biaxial region we are, the faster both limiting states are seen to be approached with increasing $|q|$. This was then seen to originate from the quadratic Zeeman field breaking too much of the original Hamiltonian's symmetry and has prompted studying a new external field that leaves the mean-field degeneracy among nematic states entirely intact. It was demonstrated to lead to an order-by-disorder mechanism in the continuum, highly analogous to the calculation at zero field, but selecting exactly the opposite states in the two nematic subregions at large enough potential magnitudes. A parallel rotor analysis was then carried out in a new set of coordinates. The effective Hamiltonian was separated into a zeroth-order and a first-order part. The zeroth-order part was seen to not depend on one of the coordinates at all, leading to a highly degenerate zeroth-order ground-state manifold, lifted by the first order perturbation. This is argued to be an exact manifestation of the order-by-disorder phenomenon. Finally, a number of analytical predictions were made and found to be consistent with the numerics. While the obtained ground state is demonstrably non-mean-field, its spin-sublevel occupation values qualitatively agree with those

of the mean-field analysis. These features make the spin-2 condensate with the modified quadratic Zeeman potential an interesting one to attempt to realise experimentally. For $g_1 > 0$, the selected state is also seen to be fragmented. Issues of crossover between the continuum mean-field state and the highly consistent tightly bound non-mean-field state, with respect to trap size, could also be addressed in the future, both experimentally and theoretically. Finally, the rotor-framework study of dynamics of the effective low-energy Hamiltonian appears to be an interesting problem, possibly exhibiting a dynamical instability in an appropriate configuration, representing another possible avenue of further research on this curious system.



ENUMERATION OF POSSIBLE VORTEX-LATTICE STATES IN THE DICE LATTICE

This appendix exhaustively lists all the mean-field vortex lattices that may be realised through exclusive repetition of the triple gauge-invariant-phase-difference link, consisting of phase differences of magnitude Φ_s , Φ_m , and Φ_l , summarised in Eq. (3.8). From Eq. (3.3) it may be seen that, at fixed sublattice densities, all such states yield the same mean-field energy. Following Korshunov,⁶² one can further demonstrate that given uniform sublattice densities, this energy is necessarily the lowest attainable. It has so far not been rigorously proved that uniform sublattice-density states globally minimise the mean-field energy. However, they are demonstrably local minima. Additionally, their high level of symmetry, further enhanced by the highly regular phase profiles they admit, and physical intuition from other systems with repulsive interactions favouring spatially uniform states, such as condensates in the continuum or on the square lattice, suggest the uniform sublattice density states as virtually the only realistic candidates for a global minimum

of the mean-field energy. All of Chapter 4 has been written under the assumption that they indeed are global minima, and we continue under that assumption here. In the author’s opinion, a rigorous proof of their global minimisation property should also be found in the not-too-distant future.

With the key assumption set out, let us briefly re-examine the phase-difference magnitudes Φ_i appearing in what we will refer to as the “Korshunov link.” These are given by the system of equations:

$$\begin{aligned}
2\Phi_s + 2\Phi_l &= \pi && \text{type 1 vortex} \\
-\Phi_s + 2\Phi_m + \Phi_l &= \pi && \text{type 2 vortex} \\
\sin \Phi_s + \sin \Phi_m &= \sin \Phi_l && \text{continuity equation}
\end{aligned} \tag{A.1}$$

where the first two equations provide the two ways these phases may provide an Aharonov-Bohm phase of $\pm\pi$ upon encircling a plaquette, and the third is the continuity equation. A simpler and more convenient way to think about the resulting vortex lattices is in terms of, as the term suggests, vortices themselves. The first order of business will be to demonstrate that chains of like vortices in consistent states, formed solely out of a repeated Korshunov link, are necessarily all of length three. Before that, however, a note on the terminology used is in order.

A.1 TERMINOLOGY

Hub and rim *sites* are defined as in Chapter 2. Sites are connected by *edges*. A *plaquette* is surrounded by four edges, and the three edges, adjacent to a rim site, form a *link*. The words “edge” and “link” will be used to mean either a physical feature of the lattice, or the values of phase differences across such a feature, when no confusion can arise. Additionally, the phase differences Φ_s , Φ_m , and Φ_l will occasionally be referred to as the *single*, *double*, and *triple edge*, respectively, in accordance with the number of arrowheads usually attributed to each in graphical representations. A *Korshunov link* is defined to be any rotation of a link consisting of an inward single edge, an inward double edge, and an outward triple edge, or an outward single edge,

an outward double edge, and an inward triple edge.

Vortices are considered pinned to plaquette centres and are said to have positive vorticity if the phase differences across edges surrounding the plaquette sum up to $+\pi$ in the counter-clockwise direction. On the other hand, if they sum up to $-\pi$, the vortices are said to have negative vorticity. From now on, positive-vorticity vortices will be referred to and represented as *black* vortices, and the negative-vorticity ones as *white* vortices.

Two derived lattices will be of interest. The first is the lattice of vortices. Since these are pinned to plaquettes, this will be the standard dual lattice, in which sites and plaquettes are exchanged, and the sites of the dual lattice are connected by an edge iff the corresponding plaquettes of the original lattice shared an edge. The dual lattice of the dice lattice is the Kagome lattice, discernible from figures below. In addition, again dualising the Kagome lattice yields the original dice lattice.

The dual-lattice sites are occupied by black or white vortices, and the word “vortex” will again be taken to mean either the dual-lattice site itself or the actual vortex occupying the site. *Chains* of vortices are sequences of dual-lattice sites in which every contiguous pair of sites in the sequence is connected by an edge and no site appears more than once. We will mostly be interested in chains of vortices of the same colour. When a vortex is said to be part of an unqualified chain, this refers to the longest chain of vortices of the same colour containing it that may be formed.

The other lattice of interest will be the honeycomb lattice of rim sites, in which hub sites are entirely discarded, and two rim sites are connected by an edge if they appeared as corners of the same plaquette in the original lattice. This lattice is “dual” to the Kagome vortex lattice in a non-standard, non-invertible sense. Replacing *edges* of the honeycomb lattice with sites, and letting every pair of such new sites be connected iff the corresponding edges of the original lattice intersected at a site, yields the Kagome lattice. This will come handy in Sec. A.3.

Finally, the class of states where every link is a Korshunov link, in which we are interested, will occasionally be called “Korshunov states.” Furthermore,

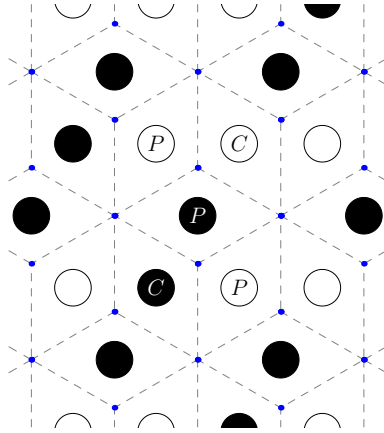


Figure A.1: Basic neighbouring properties of vortices.

the small unit-cell periodic vortex lattices of Fig 3.1 will simply be referenced by their single-letter labels in the figure, with particularly frequent references to state (a).

A.2 KORSHUNOV STATES CONSIST OF VORTEX CHAINS OF LENGTH THREE

Let us now show that Korshunov states can only form chains of vortices of like colour of length three. We begin with a few qualitative observations about the states that we already know to contain only such chains of length three, such as the state (a) of Fig. 3.1, with any number of consistently inserted type-I or type-II domain walls.

1. Every vortex is either at one of the ends of a chain, in which case we shall refer to it as a peripheral, or P vortex, or at the centre of a chain, in which case we shall call it a central, or C vortex.
2. Due to the geometry of the Kagome lattice every vortex has 4 neighbours.
3. A P vortex has a neighbour of the same colour, while the rest of the neighbours have to be of the opposite colour. Again due to the geometry of the Kagome lattice, whose relevant features and the corre-

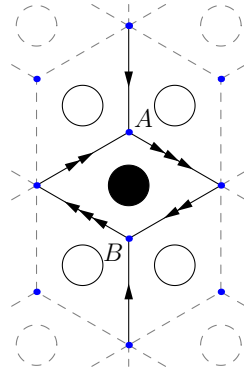


Figure A.2: An inconsistent chain of length 1.

sponding notation are shown in figure A.1, two of these have to be neighbours, so they cannot both be central. The remaining oppositely coloured vortex also has to be peripheral, as its chain has only two other neighbouring vortices to which it can expand. If it were a C vortex we would have thus obtained a white triangle, which we shall shortly show to not qualify as a chain of length three. Every P vortex hence has 2 P neighbours of the opposite colour and a C neighbour of the same colour.

With these properties in mind, let us now adopt an agnostic stance as to whether any other length of chains besides 3 is possible. It is useful to consider a third division of vortices into two groups, depending on whether the Aharonov-Bohm phase $\pm\pi$ of a vortex originated from two Φ_l and two Φ_s phases on the edges of its plaquette, oriented in the same fashion, or from two Φ_m and one Φ_l phase, oriented in the same fashion, and an oppositely oriented Φ_s phase. We will refer to such vortices as type-1 and type-2 vortices, respectively, as summarised in the first two lines of Eq. (A.1).

We can now start listing the observations that will eventually lead to the demonstration that all Korshunov states possess exclusively chains of length three:

1. An edge between two vortices will contribute in the positive direction to one of the vortices and in the negative direction to the other. Hence

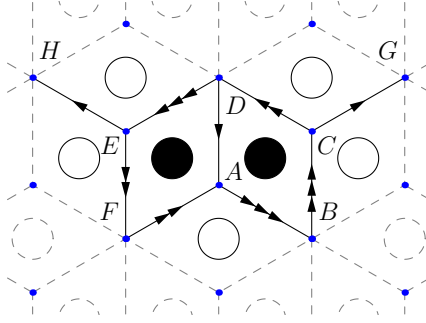


Figure A.3: An inconsistent chain of length 2.

the only edge that can appear between two vortices of the same colour is the single edge Φ_s , as it is the only one that features in the first two lines of Eq. (A.1) with both signs.

2. This eliminates the possibility of having a triangle of contiguous vortices of the same colour. Such a triangle surrounds a Korshunov link. Hence there are also double and triple edges between sites of equal colour, which is impossible.
3. Suppose we had a chain of length 1, i.e., an isolated vortex of a particular colour, say black. The situation is shown in Fig. A.2. All of the black vortex' neighbours must be white, but some are also neighbours to each other. Thus the edge between them must be Φ_s . Since the edges around rim sites A and B comprise a Korshunov link, the edges bordering the black vortex must be double or triple. Additionally one can quickly see that, due to the continuity equation (A.1), the double and triple edge must always contribute to the black vortex' vorticity in the same direction. From the first two lines of Eq. (A.1) one can derive that $\Phi_l + \Phi_m = \frac{3\pi}{4}$. By adding or subtracting these it is impossible to obtain π , which thus yields a contradiction, implying that chains of length 1 are not allowed.
4. Now suppose we have a chain of length two. This is illustrated in Fig. A.3. This time we demand that the sum of edge phase differences along the path $ABCDEF$, i.e., around *two plaquettes*, has to equal 2π .

Since the edges AD , CG and EH have to be single due to neighbouring plaquettes of equal colour, sections FAB , BCD and DEF again contribute $\pm \frac{3\pi}{4}$ each, out of which we cannot form 2π , again yielding a contradiction.

5. We know that chains of length three are consistent, so what remains to be done is check that chains of length more than that are inconsistent. We can observe that a chain of n black vortices must have $n - 1$ single edges between neighbouring black vortices and two more single edges between the two white vortices terminating the chain, which altogether prescribes the locations of $n + 1$ single edges. The continuity equation then implies that this will yield $n + 1$ contributions of magnitude $\frac{3\pi}{4}$ to the n -vortex complex. For consistency, these contributions must add up to $n\pi$. The maximum vorticity that can be formed this way is $\Omega = \frac{3(n+1)}{4}\pi$. Since $n > 3 \Rightarrow 3n + 3 < 4n \Rightarrow \Omega < n\pi$, no open chains of length more than three are possible. Temporarily allowing for closed chains, the difference in the case of those is found to be even more pronounced, so we may conclude this part of the discussion.

Note that the above discussion establishes a necessary condition. A state cannot be a Korshunov state if it possesses vortex chains of lengths other than three. That every state, exhibiting exclusively vortex chains of length three, can be obtained through repetition of only the Korshunov link, has not been demonstrated. However, in the following section, the necessary condition, or rather an even less specific, but related condition, is applied to narrow down the set of Korshunov-state candidates, for which the realisation through Korshunov links may be more easily verified.

A.3 EXHAUSTIVE LIST OF KORSHUNOV STATES

We now proceed to show that all valid Korshunov states are geometrically equivalent to a state, obtained from state (a) through insertions of type-I and type-II domain walls, or to a point defect and circular domain walls around it. By geometrically equivalent, we mean that the two states are related by

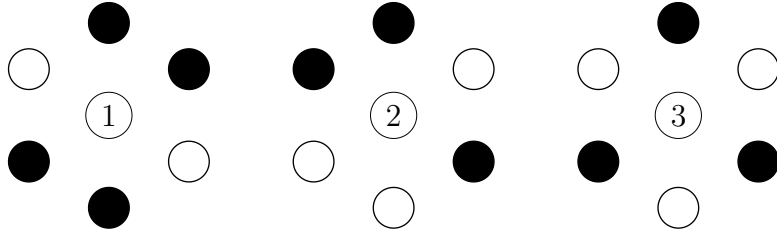


Figure A.4: The three types of hexagons occurring in the related honeycomb lattice problem.

translations, rotations, reflections, and time (colour) inversion.

Working with vortex chains rather than the Korshunov links giving rise to them already presents a simplification, but the problem may be simplified even further. Consider the derived honeycomb lattice, consisting of the original lattice’s rim sites, introduced in Sec. A.1. If one populates such a lattice by placing a black dot on rim sites, surrounded by more black vortices than white ones, and vice versa, it can be shown that a necessary condition for having only vortex chains of length exactly three is that there are no chains longer than two on this new lattice. This is a somewhat more manageable problem. Even though it isn’t a sufficient condition, as it allows for like-colour triangular vortex clusters and situations as in Fig. A.2, a consistent vortex lattice may always be reconstructed from the simpler honeycomb problem’s solution. Furthermore, all solutions of the full dice problem corresponding to the same honeycomb image are related to each other by type II domain walls.

Barring the cases of triangular clusters and Fig. A.2, one can see that a chain of length n on the honeycomb lattice implies a chain of length $n + 1$ on the Kagome vortex lattice. This can be seen by recalling that the vortex Kagome lattice corresponds to the edges of the honeycomb lattice. For two adjacent honeycomb sites of the same colour, admissible vortex configurations will have a vortex of the same colour on the edge between the honeycomb sites. The situation where only this edge vortex is of the opposite colour is also possible, but this is exactly the case of Fig. A.2, which we have explicitly excluded. For the present application, all honeycomb chains must thus be of length 2.

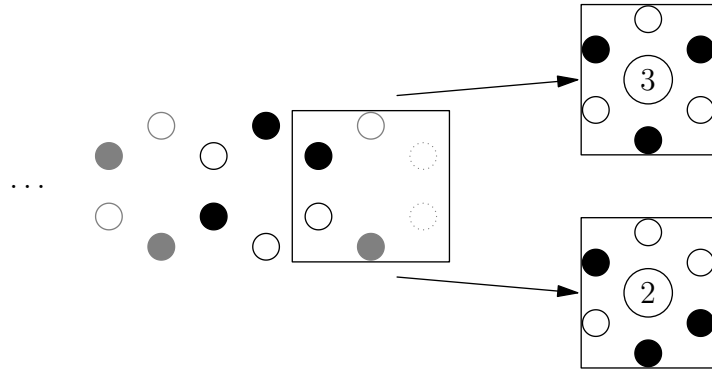


Figure A.5: Possible ways of continuing a chain of type 2 hexagons.

Let's first find all the possible configurations of the honeycomb lattice sites. Only three types of hexagons, up to rotation, reflection and colour inversion symmetry, shown in fig A.4, can occur in the honeycomb lattice. All others imply chains of length more than 2. Considering which types of hexagons can appear next to each other eventually yields a complete description of the ground states. Let us thus write down some key observations:

1. Starting with a hexagon of type 3, there is a unique, easy way to colour *all* the surrounding sites such that all chains are of length 2, shown in fig A.6d. Hence we can have at most one hexagon of type 3 per configuration.
2. Now suppose we have a hexagon of type 2, as shown in fig. A.5. We can uniquely determine the colours of the sites of the hexagon to its left, which turns out to be a colour-inverted type 2 hexagon, but have two choices for the hexagon on its right. One of them is a type 3 hexagon. If we encounter this, we already know that the rest of the state is uniquely determined. The other choice is another colour inverted type 2 hexagon, after which we are faced with the same choices for the next hexagon on the right. Restricting to states without type 3 hexagons, this means that type 2 hexagons can only appear within infinite rows of type 2 hexagons. Denote these type 2 rows.
3. The neighbouring row of a type 2 row can either be another type 2 row,

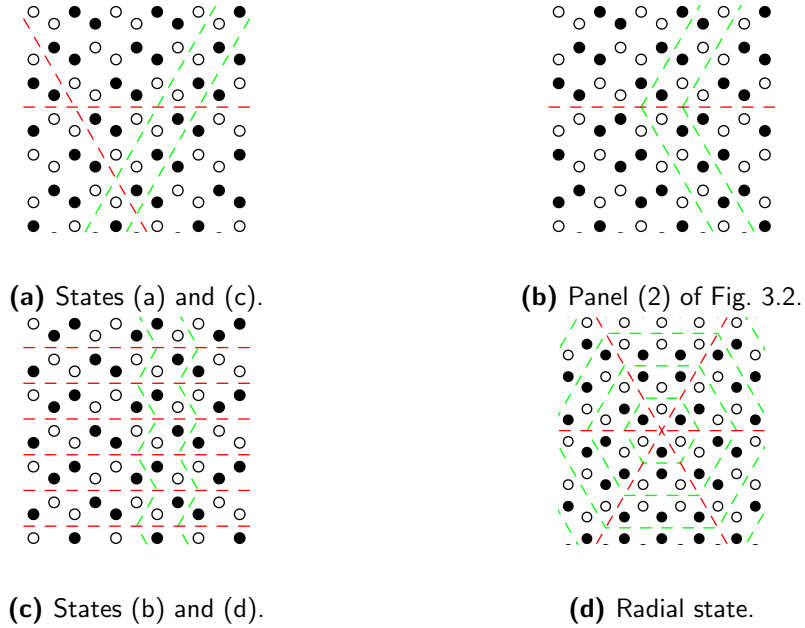


Figure A.6: Honeycomb lattice images of different mean-field states, listed in the subcaptions, up to geometrical transformations. Red lines indicate the position of type I-domain walls/type 2 rows or, in the first image, locations where they may be inserted, and green lines mark tubes or, equivalently, locations where type-II domain walls may be inserted.

or an infinite row of type 1 hexagons. Call such a row a type 1 row, accordingly.

4. Furthermore, a neighbouring row of a type 1 row may be either a type 2 row or a type 1 row.
5. There is a unique honeycomb image consisting only of type 1 hexagons.

The last three properties can be very easily verified by drawing a few hexagrams. This completely determines the possible honeycomb images: an arbitrary sequence of type 1 and type 2 rows, or a type 3 hexagon-induced radial image.

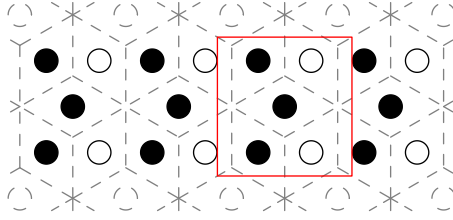
Note that should we have an image composed solely of type 1 rows and a single type 2 row, the region, consisting exclusively of type 1 hexagons, on one side of the type 2 row would correspond to the mirrored and colour-inverted type 1 hexagon region on the other side of the type 2 row. This heavily resembles a type-I domain wall. Indeed, the honeycomb image of

state (a) consists entirely of type-I hexagons, and acquires a single type 2 row when a Type-I domain wall is inserted, coinciding with location of the type 2 row.

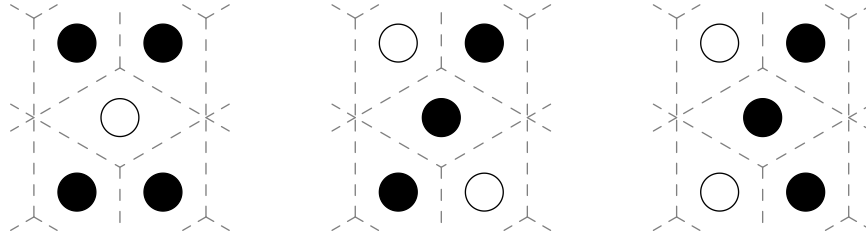
The correspondence is not accidental, as we are about to show. A good organising principle for enumerating all the vortex lattice states, corresponding to a given honeycomb image, is locating what we'll call *tubes*: double lines of equally coloured honeycomb sites. In Fig. A.6a, these are indicated by dashed green lines. We'll furthermore refer to the nearest equal-colour pairs of honeycomb sites that form the walls of the tube as its *joints*. Note that tubes may be harder to identify in the presence of type 2 rows, as they bend and change colour when crossing them. This is illustrated in Fig.A.6b. They are particularly well concealed when there are many type 2 rows, as in Fig.A.6c, but are nevertheless well defined.

Consider now a horizontal black tube. The sections of the dice lattice that a single joint of the tube can represent are shown in Fig. A.7. Subfigure A.7b is eliminated immediately as it contains a chain of length 1. The remaining representations in Figs. A.7c and A.7d and their mirror images are admissible. The situation is, however, only consistent if every joint of the tube represents this same pattern. This is also true for bending tubes, where the pattern needs to be mirrored and colour-inverted every time the tube passes a type 2 row. Assuming any other configuration leads to a contradiction in a very small number of steps, as can easily be verified.

Given a honeycomb image, we may in fact fully specify the underlying vortex lattice by choosing a joint pattern for each tube. Note that, if this is done in order for contiguous tubes, the previous tube determines the “chirality” of the next tube’s joint pattern. We are, however, free to choose whether our joints will form straight vortex chains, or crooked ones. As may again be verified graphically, choosing all but one of the tubes to have straight joints, and the remaining tube to have crooked joints, is completely analogous to inserting a type-II domain wall into state (a) at the position of the crooked-joint tube. This may be further used to show that type 2 rows satisfy all the properties of a Type-I domain wall, and may hence be considered completely equivalent.



(a) An example dice-lattice vortex configuration that yields a black tube in the honeycomb image.



(b) Inconsistent link. (c) Straight consistent link. (d) Crooked consistent link.

Figure A.7

Recalling that state (a) yields the honeycomb image without any type 2 rows, the following is seen to be true: Apart from the radial states, commented on briefly, vortex-lattice states exhibiting exclusively chains of length three correspond exactly to state (a) with an arbitrary number of consistently inserted domain walls of both types, up to geometric transformations. Recall that we are specifically interested in Korshunov states and that we have only demonstrated the chain-length condition to be a necessary one. In this case, however, we know from Chapter 3 and previous work by Korshunov^{61,63,62} that these vortex lattices *can* be constructed in terms of the Korshunov link, and that the constructions are unique.

The radial state, shown in Fig. A.6d, is a new, previously unanticipated feature. A consistent Korshunov link construction may be found, for arbitrarily inserted type-II circular domain walls, meaning that these are not an artefact of the honeycomb analysis, but correspond to legitimate members of the degenerate set of dice-lattice mean-field ground states. While the interacting-domain-walls interpretation of fluctuation zero-point energy contributions of Sec. 4.4 does not appear to favour such states, particularly

when type-II domain walls are present, this would still need to be explicitly verified. They should also be taken into account with any future calculations at finite temperature. For now, their existence implies that the mean-field degeneracy is even greater than previously anticipated on the basis of the remainder of Korshunov states.

The above analysis shows that the arbitrarily geometrically transformed radial states, with any number of radial type-II domain walls inserted, and the mean-field states of Chapter 3, completely parametrise the space of Korshunov states.

REFERENCES

- [1] C. C. Abilio, P. Butaud, Th. Fournier, B. Pannetier, J. Vidal, S. Tedesco, and B. Dalzotto. Magnetic Field Induced Localization in a Two-Dimensional Superconducting Wire Network. *Phys. Rev. Lett.*, 83:5102–5105, Dec 1999. doi: 10.1103/PhysRevLett.83.5102. URL <http://link.aps.org/doi/10.1103/PhysRevLett.83.5102>.
- [2] A.A. Abrikosov. The magnetic properties of superconducting alloys. *Journal of Physics and Chemistry of Solids*, 2(3):199 – 208, 1957. ISSN 0022-3697. doi: [http://dx.doi.org/10.1016/0022-3697\(57\)90083-5](http://dx.doi.org/10.1016/0022-3697(57)90083-5). URL <http://www.sciencedirect.com/science/article/pii/0022369757900835>.
- [3] M. Aidelsburger, M. Atala, M. Lohse, J. T. Barreiro, B. Paredes, and I. Bloch. Realization of the Hofstadter Hamiltonian with Ultracold Atoms in Optical Lattices. *Phys. Rev. Lett.*, 111:185301, Oct 2013. doi: 10.1103/PhysRevLett.111.185301. URL <http://link.aps.org/doi/10.1103/PhysRevLett.111.185301>.
- [4] K. Aikawa, A. Frisch, M. Mark, S. Baier, A. Rietzler, R. Grimm, and F. Ferlaino. Bose-Einstein Condensation of Erbium. *Phys. Rev. Lett.*, 108:210401, May 2012. doi: 10.1103/PhysRevLett.108.210401. URL <http://link.aps.org/doi/10.1103/PhysRevLett.108.210401>.
- [5] M. H. Anderson, J. R. Ensher, M. R. Matthews, C. E. Wieman, and E. A. Cornell. Observation of Bose-Einstein Condensation in a Dilute Atomic Vapor. *Science*, 269(5221):198–201, 1995. doi: 10.1126/science.269.5221.198. URL <http://www.sciencemag.org/content/269/5221/198.abstract>.
- [6] P. W. Anderson. Absence of Diffusion in Certain Random Lattices.

- Phys. Rev.*, 109:1492–1505, Mar 1958. doi: 10.1103/PhysRev.109.1492.
URL <http://link.aps.org/doi/10.1103/PhysRev.109.1492>.
- [7] P. W. Anderson. *Progress in Low Temperature Physics*, pages 1–43. North-Holland, 1967.
- [8] J. R. Anglin, P. Drummond, and A. Smerzi. Exact quantum phase model for mesoscopic Josephson junctions. *Phys. Rev. A*, 64:063605, Nov 2001. doi: 10.1103/PhysRevA.64.063605. URL <http://link.aps.org/doi/10.1103/PhysRevA.64.063605>.
- [9] V. Bargmann. On a Hilbert space of analytic functions and an associated integral transform part I. *Communications on Pure and Applied Mathematics*, 14(3):187–214, 1961. ISSN 1097-0312. doi: 10.1002/cpa.3160140303. URL <http://dx.doi.org/10.1002/cpa.3160140303>.
- [10] Ryan Barnett, Ari Turner, and Eugene Demler. Classifying Novel Phases of Spinor Atoms. *Phys. Rev. Lett.*, 97:180412, Nov 2006. doi: 10.1103/PhysRevLett.97.180412. URL <http://link.aps.org/doi/10.1103/PhysRevLett.97.180412>.
- [11] Ryan Barnett, Jay D. Sau, and S. Das Sarma. Antiferromagnetic spinor condensates are quantum rotors. *Phys. Rev. A*, 82:031602, Sep 2010. doi: 10.1103/PhysRevA.82.031602. URL <http://link.aps.org/doi/10.1103/PhysRevA.82.031602>.
- [12] Ryan Barnett, Hoi-Yin Hui, Chien-Hung Lin, Jay D. Sau, and S. Das Sarma. Quantum rotor theory of spinor condensates in tight traps. *Phys. Rev. A*, 83:023613, Feb 2011. doi: 10.1103/PhysRevA.83.023613. URL <http://link.aps.org/doi/10.1103/PhysRevA.83.023613>.
- [13] Ryan Barnett, Stephen Powell, Tobias Graß, Maciej Lewenstein, and S. Das Sarma. Order by disorder in spin-orbit-coupled Bose-Einstein condensates. *Phys. Rev. A*, 85:023615, Feb 2012. doi: 10.1103/PhysRevA.85.023615. URL <http://link.aps.org/doi/10.1103/PhysRevA.85.023615>.

- [14] D. Bercioux, D. F. Urban, H. Grabert, and W. Häusler. Massless Dirac-Weyl fermions in a \mathcal{T}_3 optical lattice. *Phys. Rev. A*, 80:063603, Dec 2009. doi: 10.1103/PhysRevA.80.063603. URL <http://link.aps.org/doi/10.1103/PhysRevA.80.063603>.
- [15] Jean-Paul Blaizot and Georges Ripka. *Quantum theory of finite systems*. MIT press Cambridge, 1986.
- [16] H. M. J. M. Boesten, A. J. Moerdijk, and B. J. Verhaar. Dipolar decay in two recent Bose-Einstein condensation experiments. *Phys. Rev. A*, 54:R29–R32, Jul 1996. doi: 10.1103/PhysRevA.54.R29. URL <http://link.aps.org/doi/10.1103/PhysRevA.54.R29>.
- [17] Satyendra Nath Bose. Plancks Gesetz und Lichtquantenhypothese. *Zeitschrift für Physik*, 26:178, 1924.
- [18] C. C. Bradley, C. A. Sackett, J. J. Tollett, and R. G. Hulet. Evidence of Bose-Einstein Condensation in an Atomic Gas with Attractive Interactions. *Phys. Rev. Lett.*, 75:1687–1690, Aug 1995. doi: 10.1103/PhysRevLett.75.1687. URL <http://link.aps.org/doi/10.1103/PhysRevLett.75.1687>.
- [19] G. Breit and I. I. Rabi. Measurement of Nuclear Spin. *Phys. Rev.*, 38:2082–2083, Dec 1931. doi: 10.1103/PhysRev.38.2082.2. URL <http://link.aps.org/doi/10.1103/PhysRev.38.2082.2>.
- [20] G. Bressi, G. Carugno, R. Onofrio, and G. Ruoso. Measurement of the Casimir Force between Parallel Metallic Surfaces. *Phys. Rev. Lett.*, 88:041804, Jan 2002. doi: 10.1103/PhysRevLett.88.041804. URL <http://link.aps.org/doi/10.1103/PhysRevLett.88.041804>.
- [21] A. A. Burkov and Eugene Demler. Vortex-Peierls States in Optical Lattices. *Phys. Rev. Lett.*, 96:180406, May 2006. doi: 10.1103/PhysRevLett.96.180406. URL <http://link.aps.org/doi/10.1103/PhysRevLett.96.180406>.
- [22] H. B. G. Casimir and D. Polder. The Influence of Retardation on the London-van der Waals Forces. *Phys. Rev.*, 73:360–372, Feb 1948. doi:

- 10.1103/PhysRev.73.360. URL <http://link.aps.org/doi/10.1103/PhysRev.73.360>.
- [23] V. Cataudella and R. Fazio. Glassy dynamics of Josephson arrays on a dice lattice. *EPL (Europhysics Letters)*, 61(3):341, 2003. URL <http://stacks.iop.org/0295-5075/61/i=3/a=341>.
- [24] Claude Cohen-Tannoudji and Jacques Dupont-Roc. Experimental Study of Zeeman Light Shifts in Weak Magnetic Fields. *Phys. Rev. A*, 5:968–984, Feb 1972. doi: 10.1103/PhysRevA.5.968. URL <http://link.aps.org/doi/10.1103/PhysRevA.5.968>.
- [25] Franco Dalfovo, Stefano Giorgini, Lev P. Pitaevskii, and Sandro Stringari. Theory of Bose-Einstein condensation in trapped gases. *Rev. Mod. Phys.*, 71:463–512, Apr 1999. doi: 10.1103/RevModPhys.71.463. URL <http://link.aps.org/doi/10.1103/RevModPhys.71.463>.
- [26] K. B. Davis, M. O. Mewes, M. R. Andrews, N. J. van Druten, D. S. Durfee, D. M. Kurn, and W. Ketterle. Bose-Einstein Condensation in a Gas of Sodium Atoms. *Phys. Rev. Lett.*, 75:3969–3973, Nov 1995. doi: 10.1103/PhysRevLett.75.3969. URL <http://link.aps.org/doi/10.1103/PhysRevLett.75.3969>.
- [27] Hui Deng, Hartmut Haug, and Yoshihisa Yamamoto. Exciton-polariton Bose-Einstein condensation. *Rev. Mod. Phys.*, 82:1489–1537, May 2010. doi: 10.1103/RevModPhys.82.1489. URL <http://link.aps.org/doi/10.1103/RevModPhys.82.1489>.
- [28] Albert Einstein. Quantentheorie des einatomigen idealen Gases. In *Sitzungsberichte der Preussischen Akademie der Wissenschaften, Physikalisch-mathematische Klasse*, pages 261–267, 1924.
- [29] Albert Einstein. Quantentheorie des einatomigen idealen Gases. 2. Abhandlung. In *Sitzungsberichte der Preussischen Akademie der Wissenschaften, Physikalisch-mathematische Klasse*, pages 3–14, 1925.
- [30] N. Elstner and H. Monien. Dynamics and thermodynamics of the Bose-Hubbard model. *Phys. Rev. B*, 59:12184–12187, May 1999. doi:

- 10.1103/PhysRevB.59.12184. URL <http://link.aps.org/doi/10.1103/PhysRevB.59.12184>.
- [31] Matthew P. A. Fisher, Peter B. Weichman, G. Grinstein, and Daniel S. Fisher. Boson localization and the superfluid-insulator transition. *Phys. Rev. B*, 40:546–570, Jul 1989. doi: 10.1103/PhysRevB.40.546. URL <http://link.aps.org/doi/10.1103/PhysRevB.40.546>.
- [32] J. K. Freericks and H. Monien. Phase diagram of the Bose-Hubbard Model. *EPL (Europhysics Letters)*, 26(7):545, 1994. URL <http://stacks.iop.org/0295-5075/26/i=7/a=012>.
- [33] Dale G. Fried, Thomas C. Killian, Lorenz Willmann, David Landhuis, Stephen C. Moss, Daniel Kleppner, and Thomas J. Greytak. Bose-Einstein Condensation of Atomic Hydrogen. *Phys. Rev. Lett.*, 81:3811–3814, Nov 1998. doi: 10.1103/PhysRevLett.81.3811. URL <http://link.aps.org/doi/10.1103/PhysRevLett.81.3811>.
- [34] Takeshi Fukuhara, Seiji Sugawa, and Yoshiro Takahashi. Bose-Einstein condensation of an ytterbium isotope. *Phys. Rev. A*, 76:051604, Nov 2007. doi: 10.1103/PhysRevA.76.051604. URL <http://link.aps.org/doi/10.1103/PhysRevA.76.051604>.
- [35] J. Garrison and R. Chiao. *Quantum Optics*. Oxford Graduate Texts. OUP Oxford, 2008. ISBN 9780198508861. URL <https://books.google.co.uk/books?id=RCoSDAAAQBAJ>.
- [36] Rudolf Gati, Børge Hemmerling, Jonas Fölling, Michael Albiez, and Markus K. Oberthaler. Noise Thermometry with Two Weakly Coupled Bose-Einstein Condensates. *Phys. Rev. Lett.*, 96:130404, Apr 2006. doi: 10.1103/PhysRevLett.96.130404. URL <http://link.aps.org/doi/10.1103/PhysRevLett.96.130404>.
- [37] Li Ge, Fei Zhou, and Yu Shi. Correlated spontaneous symmetry breaking induced by zero-point fluctuations in a quantum mixture. *Phys. Rev. A*, 89:043623, Apr 2014. doi: 10.1103/PhysRevA.89.043623. URL <http://link.aps.org/doi/10.1103/PhysRevA.89.043623>.

- [38] Fabrice Gerbier, Artur Widera, Simon Fölling, Olaf Mandel, and Immanuel Bloch. Resonant control of spin dynamics in ultracold quantum gases by microwave dressing. *Phys. Rev. A*, 73:041602, Apr 2006. doi: 10.1103/PhysRevA.73.041602. URL <http://link.aps.org/doi/10.1103/PhysRevA.73.041602>.
- [39] J. M. Gerton, C. A. Sackett, B. J. Frew, and R. G. Hulet. Dipolar relaxation collisions in magnetically trapped ${}^7\text{Li}$. *Phys. Rev. A*, 59:1514–1516, Feb 1999. doi: 10.1103/PhysRevA.59.1514. URL <http://link.aps.org/doi/10.1103/PhysRevA.59.1514>.
- [40] N Goldman, G Juzeliūnas, P Öhberg, and I B Spielman. Light-induced gauge fields for ultracold atoms. *Reports on Progress in Physics*, 77(12):126401, 2014. URL <http://stacks.iop.org/0034-4885/77/i=12/a=126401>.
- [41] Markus Greiner, Olaf Mandel, Tilman Esslinger, Theodor W. Hansch, and Immanuel Bloch. Quantum phase transition from a superfluid to a Mott insulator in a gas of ultracold atoms. *Nature*, 415(6867):39–44, January 2002. ISSN 0028-0836. URL <http://dx.doi.org/10.1038/415039a>.
- [42] Axel Griesmaier, Jörg Werner, Sven Hensler, Jürgen Stuhler, and Tilman Pfau. Bose-Einstein Condensation of Chromium. *Phys. Rev. Lett.*, 94:160401, Apr 2005. doi: 10.1103/PhysRevLett.94.160401. URL <http://link.aps.org/doi/10.1103/PhysRevLett.94.160401>.
- [43] D. S. Hall, M. R. Matthews, C. E. Wieman, and E. A. Cornell. Measurements of Relative Phase in Two-Component Bose-Einstein Condensates. *Phys. Rev. Lett.*, 81:1543–1546, Aug 1998. doi: 10.1103/PhysRevLett.81.1543. URL <http://link.aps.org/doi/10.1103/PhysRevLett.81.1543>.
- [44] Charles E. Hecht. The possible superfluid behaviour of hydrogen atom gases and liquids. *Physica*, 25(7):1159 – 1161, 1959. ISSN 0031-8914. doi: [http://dx.doi.org/10.1016/0031-8914\(59](http://dx.doi.org/10.1016/0031-8914(59)

- 90035-7. URL <http://www.sciencedirect.com/science/article/pii/0031891459900357>.
- [45] Christopher L. Henley. Ordering by disorder: Ground-state selection in fcc vector antiferromagnets. *Journal of Applied Physics*, 61(8):3962–3964, 1987. doi: 10.1063/1.338570. URL <http://link.aip.org/link/?JAP/61/3962/1>.
- [46] Christopher L. Henley. Ordering due to disorder in a frustrated vector antiferromagnet. *Phys. Rev. Lett.*, 62:2056–2059, Apr 1989. doi: 10.1103/PhysRevLett.62.2056. URL <http://link.aps.org/doi/10.1103/PhysRevLett.62.2056>.
- [47] Tin-Lun Ho. Spinor Bose Condensates in Optical Traps. *Phys. Rev. Lett.*, 81:742–745, Jul 1998. doi: 10.1103/PhysRevLett.81.742. URL <http://link.aps.org/doi/10.1103/PhysRevLett.81.742>.
- [48] Tin-Lun Ho and Sung Kit Yip. Fragmented and Single Condensate Ground States of Spin-1 Bose Gas. *Phys. Rev. Lett.*, 84:4031–4034, May 2000. doi: 10.1103/PhysRevLett.84.4031. URL <http://link.aps.org/doi/10.1103/PhysRevLett.84.4031>.
- [49] Kôdi Husimi. Some Formal Properties of the Density Matrix. In *Proc. Phys. Math. Soc. Jpn.* 22, pages 264–314, 1940.
- [50] D. Jaksch and P. Zoller. The cold atom Hubbard toolbox . *Annals of Physics*, 315(1):52 – 79, 2005. ISSN 0003-4916. doi: <http://dx.doi.org/10.1016/j.aop.2004.09.010>. URL <http://www.sciencedirect.com/science/article/pii/S0003491604001782>. Special Issue.
- [51] D. Jaksch, C. Bruder, J. I. Cirac, C. W. Gardiner, and P. Zoller. Cold Bosonic Atoms in Optical Lattices. *Phys. Rev. Lett.*, 81:3108–3111, Oct 1998. doi: 10.1103/PhysRevLett.81.3108. URL <http://link.aps.org/doi/10.1103/PhysRevLett.81.3108>.
- [52] H. H. Jen and S.-K. Yip. Fragmented many-body states of a spin-2 Bose gas. *Phys. Rev. A*, 91:063603, Jun 2015. doi: 10.1103/PhysRevA.

- 91.063603. URL <http://link.aps.org/doi/10.1103/PhysRevA.91.063603>.
- [53] K. Jensen, V. M. Acosta, J. M. Higbie, M. P. Ledbetter, S. M. Rochester, and D. Budker. Cancellation of nonlinear Zeeman shifts with light shifts. *Phys. Rev. A*, 79:023406, Feb 2009. doi: 10.1103/PhysRevA.79.023406. URL <http://link.aps.org/doi/10.1103/PhysRevA.79.023406>.
- [54] B.D. Josephson. Possible new effects in superconductive tunnelling. *Phys. Lett.*, 1(7):251 – 253, 1962. ISSN 0031-9163. doi: [http://dx.doi.org/10.1016/0031-9163\(62\)91369-0](http://dx.doi.org/10.1016/0031-9163(62)91369-0). URL <http://www.sciencedirect.com/science/article/pii/0031916362913690>.
- [55] Gregor Jotzu, Michael Messer, Remi Desbuquois, Martin Lebrat, Thomas Uehlinger, Daniel Greif, and Tilman Esslinger. Experimental realization of the topological Haldane model with ultracold fermions. *Nature*, 515(7526):237–240, November 2014. ISSN 0028-0836. URL <http://dx.doi.org/10.1038/nature13915>.
- [56] Kenichi Kasamatsu, Makoto Tsubota, and Masahito Ueda. Vortices in multicomponent Bose-Einstein condensates. *International Journal of Modern Physics B*, 19(11):1835–1904, 2005. doi: 10.1142/S0217979205029602. URL <http://www.worldscientific.com/doi/abs/10.1142/S0217979205029602>.
- [57] Yuki Kawaguchi and Masahito Ueda. Spinor Bose-Einstein condensates. *Physics Reports*, 520(5):253 – 381, 2012. ISSN 0370-1573. doi: <http://dx.doi.org/10.1016/j.physrep.2012.07.005>. URL <http://www.sciencedirect.com/science/article/pii/S0370157312002098>.
- [58] J.R. Klauder and E.C.G. Sudarshan. *Fundamentals of Quantum Optics*. Dover books on physics. Dover Publications, 2006. ISBN 9780486450087. URL <https://books.google.co.uk/books?id=rbSfWTrKwnAC>.
- [59] Nille N. Klausen, John L. Bohn, and Chris H. Greene. Nature of spinor Bose-Einstein condensates in rubidium. *Phys. Rev. A*, 64:053602, Oct

2001. doi: 10.1103/PhysRevA.64.053602. URL <http://link.aps.org/doi/10.1103/PhysRevA.64.053602>.
- [60] Masato Koashi and Masahito Ueda. Exact eigenstates and magnetic response of spin-1 and spin-2 Bose-Einstein condensates. *Phys. Rev. Lett.*, 84:1066–1069, Feb 2000. doi: 10.1103/PhysRevLett.84.1066. URL <http://link.aps.org/doi/10.1103/PhysRevLett.84.1066>.
- [61] S. E. Korshunov. Vortex ordering in fully frustrated superconducting systems with a dice lattice. *Phys. Rev. B*, 63:134503, Feb 2001. doi: 10.1103/PhysRevB.63.134503. URL <http://link.aps.org/doi/10.1103/PhysRevB.63.134503>.
- [62] S. E. Korshunov. Fluctuation-induced vortex pattern and its disordering in the fully frustrated XY model on a dice lattice. *Phys. Rev. B*, 71:174501, May 2005. doi: 10.1103/PhysRevB.71.174501. URL <http://link.aps.org/doi/10.1103/PhysRevB.71.174501>.
- [63] S. E. Korshunov and B. Douçot. Structure of the superconducting state in a fully frustrated wire network with dice lattice geometry. *Phys. Rev. B*, 70:134507, Oct 2004. doi: 10.1103/PhysRevB.70.134507. URL <http://link.aps.org/doi/10.1103/PhysRevB.70.134507>.
- [64] L. Landau. Theory of the Superfluidity of Helium II. *Phys. Rev.*, 60:356–358, Aug 1941. doi: 10.1103/PhysRev.60.356. URL <http://link.aps.org/doi/10.1103/PhysRev.60.356>.
- [65] L. Landau. Theory of the Superfluidity of Helium II. *J. Phys. USSR*, 5:71–100, 1941.
- [66] L.D. Landau and E.M. Lifshitz. *Quantum Mechanics: Non-relativistic Theory*. Butterworth Heinemann. Butterworth-Heinemann, 1977. ISBN 9780750635394. URL <http://books.google.co.uk/books?id=J9ui6KwC4mMC>.
- [67] C. K. Law, H. Pu, and N. P. Bigelow. Quantum spins mixing in spinor Bose-Einstein condensates. *Phys. Rev. Lett.*, 81:5257–5261, Dec 1998.

- doi: 10.1103/PhysRevLett.81.5257. URL <http://link.aps.org/doi/10.1103/PhysRevLett.81.5257>.
- [68] Anthony J. Leggett. BEC: The alkali gases from the perspective of research on liquid helium. *AIP Conference Proceedings*, 477(1):154–169, 1999. doi: <http://dx.doi.org/10.1063/1.59354>. URL <http://scitation.aip.org/content/aip/proceeding/aipcp/10.1063/1.59354>.
- [69] Anthony J. Leggett. Bose-Einstein condensation in the alkali gases: Some fundamental concepts. *Rev. Mod. Phys.*, 73:307–356, Apr 2001. doi: 10.1103/RevModPhys.73.307. URL <http://link.aps.org/doi/10.1103/RevModPhys.73.307>.
- [70] M. Lewenstein and L. You. Quantum Phase Diffusion of a Bose-Einstein Condensate. *Phys. Rev. Lett.*, 77:3489–3493, Oct 1996. doi: 10.1103/PhysRevLett.77.3489. URL <http://link.aps.org/doi/10.1103/PhysRevLett.77.3489>.
- [71] Maciej Lewenstein, Anna Sanpera, Veronica Ahufinger, Bogdan Damski, Aditi Sen(De), and Ujjwal Sen. Ultracold atomic gases in optical lattices: mimicking condensed matter physics and beyond. *Advances in Physics*, 56(2):243–379, 2007. doi: 10.1080/00018730701223200. URL <http://www.tandfonline.com/doi/abs/10.1080/00018730701223200>.
- [72] Xiaopeng Li, Stefan S. Natu, Arun Paramekanti, and S. Das Sarma. Chiral magnetism and spontaneous spin Hall effect of interacting Bose superfluids. *Nat Commun*, 5:–, October 2014. URL <http://dx.doi.org/10.1038/ncomms6174>.
- [73] Y. Liu, E. Gomez, S. E. Maxwell, L. D. Turner, E. Tiesinga, and P. D. Lett. Number Fluctuations and Energy Dissipation in Sodium Spinor Condensates. *Phys. Rev. Lett.*, 102:225301, Jun 2009. doi: 10.1103/PhysRevLett.102.225301. URL <http://link.aps.org/doi/10.1103/PhysRevLett.102.225301>.

- [74] Y. Liu, S. Jung, S. E. Maxwell, L. D. Turner, E. Tiesinga, and P. D. Lett. Quantum Phase Transitions and Continuous Observation of Spinor Dynamics in an Antiferromagnetic Condensate. *Phys. Rev. Lett.*, 102:125301, Mar 2009. doi: 10.1103/PhysRevLett.102.125301. URL <http://link.aps.org/doi/10.1103/PhysRevLett.102.125301>.
- [75] F. London. The λ -Phenomenon of Liquid Helium and the Bose-Einstein Degeneracy. *Nature*, 141:643–644, April 1938. doi: 10.1038/141643a0.
- [76] Mingwu Lu, Nathaniel Q. Burdick, Seo Ho Youn, and Benjamin L. Lev. Strongly Dipolar Bose-Einstein Condensate of Dysprosium. *Phys. Rev. Lett.*, 107:190401, Oct 2011. doi: 10.1103/PhysRevLett.107.190401. URL <http://link.aps.org/doi/10.1103/PhysRevLett.107.190401>.
- [77] K. W. Madison, F. Chevy, W. Wohlleben, and J. Dalibard. Vortex Formation in a Stirred Bose-Einstein Condensate. *Phys. Rev. Lett.*, 84:806–809, Jan 2000. doi: 10.1103/PhysRevLett.84.806. URL <http://link.aps.org/doi/10.1103/PhysRevLett.84.806>.
- [78] K. W. Madison, F. Chevy, V. Bretin, and J. Dalibard. Stationary states of a rotating bose-einstein condensate: Routes to vortex nucleation. *Phys. Rev. Lett.*, 86:4443–4446, May 2001. doi: 10.1103/PhysRevLett.86.4443. URL <http://link.aps.org/doi/10.1103/PhysRevLett.86.4443>.
- [79] Ettore Majorana. Atomi orientati in campo magnetico variabile. *Il Nuovo Cimento*, 9(2):43–50, 1932. ISSN 0029-6341. doi: 10.1007/BF02960953. URL <http://dx.doi.org/10.1007/BF02960953>.
- [80] M. R. Matthews, B. P. Anderson, P. C. Haljan, D. S. Hall, C. E. Wieman, and E. A. Cornell. Vortices in a Bose-Einstein Condensate. *Phys. Rev. Lett.*, 83:2498–2501, Sep 1999. doi: 10.1103/PhysRevLett.83.2498. URL <http://link.aps.org/doi/10.1103/PhysRevLett.83.2498>.
- [81] N. D. Mermin and H. Wagner. Absence of Ferromagnetism or Antiferromagnetism in One- or Two-Dimensional Isotropic Heisenberg Models.

- Phys. Rev. Lett.*, 17:1133–1136, Nov 1966. doi: 10.1103/PhysRevLett.17.1133. URL <http://link.aps.org/doi/10.1103/PhysRevLett.17.1133>.
- [82] Louis Michel. Symmetry defects and broken symmetry. Configurations hidden symmetry. *Rev. Mod. Phys.*, 52:617–651, Jul 1980. doi: 10.1103/RevModPhys.52.617. URL <http://link.aps.org/doi/10.1103/RevModPhys.52.617>.
- [83] Hirokazu Miyake, Georgios A. Siviloglou, Colin J. Kennedy, William Cody Burton, and Wolfgang Ketterle. Realizing the Harper Hamiltonian with Laser-Assisted Tunneling in Optical Lattices. *Phys. Rev. Lett.*, 111:185302, Oct 2013. doi: 10.1103/PhysRevLett.111.185302. URL <http://link.aps.org/doi/10.1103/PhysRevLett.111.185302>.
- [84] U. Mohideen and Anushree Roy. Precision Measurement of the Casimir Force from 0.1 to 0.9 μm . *Phys. Rev. Lett.*, 81:4549–4552, Nov 1998. doi: 10.1103/PhysRevLett.81.4549. URL <http://link.aps.org/doi/10.1103/PhysRevLett.81.4549>.
- [85] G. Möller and N. R. Cooper. Correlated Phases of Bosons in the Flat Lowest Band of the Dice Lattice. *Phys. Rev. Lett.*, 108:045306, Jan 2012. doi: 10.1103/PhysRevLett.108.045306. URL <http://link.aps.org/doi/10.1103/PhysRevLett.108.045306>.
- [86] Hendrik J. Monkhorst and James D. Pack. Special points for Brillouin-zone integrations. *Phys. Rev. B*, 13:5188–5192, Jun 1976. doi: 10.1103/PhysRevB.13.5188. URL <http://link.aps.org/doi/10.1103/PhysRevB.13.5188>.
- [87] Tohru Morita and Tsuyoshi Horiguchi. Lattice Green’s function for the diatomic lattices. *J. Math. Phys.*, 13(8):1243–1252, 1972. doi: <http://dx.doi.org/10.1063/1.1666129>. URL <http://scitation.aip.org/content/aip/journal/jmp/13/8/10.1063/1.1666129>.
- [88] Oliver Morsch and Markus Oberthaler. Dynamics of Bose-Einstein condensates in optical lattices. *Rev. Mod. Phys.*, 78:179–215, Feb 2006.

- doi: 10.1103/RevModPhys.78.179. URL <http://link.aps.org/doi/10.1103/RevModPhys.78.179>.
- [89] Erich J. Mueller, Tin-Lun Ho, Masahito Ueda, and Gordon Baym. Fragmentation of Bose-Einstein condensates. *Phys. Rev. A*, 74:033612, Sep 2006. doi: 10.1103/PhysRevA.74.033612. URL <http://link.aps.org/doi/10.1103/PhysRevA.74.033612>.
- [90] J. Mur-Petit, M. Guilleumas, A. Polls, A. Sanpera, M. Lewenstein, K. Bongs, and K. Sengstock. Dynamics of $F = 1$ ^{87}Rb condensates at finite temperatures. *Phys. Rev. A*, 73:013629, Jan 2006. doi: 10.1103/PhysRevA.73.013629. URL <http://link.aps.org/doi/10.1103/PhysRevA.73.013629>.
- [91] Y. Nakamura, J. Takahashi, and Y. Yamanaka. Formulation for the zero mode of a Bose-Einstein condensate beyond the Bogoliubov approximation. *Phys. Rev. A*, 89:013613, Jan 2014. doi: 10.1103/PhysRevA.89.013613. URL <http://link.aps.org/doi/10.1103/PhysRevA.89.013613>.
- [92] Titus Neupert, Luiz Santos, Claudio Chamon, and Christopher Mudry. Fractional Quantum Hall States at Zero Magnetic Field. *Phys. Rev. Lett.*, 106:236804, Jun 2011. doi: 10.1103/PhysRevLett.106.236804. URL <http://link.aps.org/doi/10.1103/PhysRevLett.106.236804>.
- [93] Tetsuo Ohmi and Kazushige Machida. Bose-Einstein condensation with internal degrees of freedom in alkali atom gases. *Journal of the Physical Society of Japan*, 67(6):1822–1825, 1998. doi: 10.1143/JPSJ.67.1822. URL <http://dx.doi.org/10.1143/JPSJ.67.1822>.
- [94] Matjaž Payrits and Ryan Barnett. Order-by-disorder degeneracy lifting of interacting bosons on the dice lattice. *Phys. Rev. A*, 90:013608, Jul 2014. doi: 10.1103/PhysRevA.90.013608. URL <http://link.aps.org/doi/10.1103/PhysRevA.90.013608>.
- [95] Matjaž Payrits and Ryan Barnett. Quantum rotor theory of systems of spin-2 bosons. *Phys. Rev. A*, 94:023605, Aug 2016. doi:

- 10.1103/PhysRevA.94.023605. URL <http://link.aps.org/doi/10.1103/PhysRevA.94.023605>.
- [96] Oliver Penrose and Lars Onsager. Bose-Einstein Condensation and Liquid Helium. *Phys. Rev.*, 104:576–584, Nov 1956. doi: 10.1103/PhysRev.104.576. URL <http://link.aps.org/doi/10.1103/PhysRev.104.576>.
- [97] F. Pereira Dos Santos, J. Léonard, Junmin Wang, C. J. Barrelet, F. Perales, E. Rasel, C. S. Unnikrishnan, M. Leduc, and C. Cohen-Tannoudji. Bose-Einstein Condensation of Metastable Helium. *Phys. Rev. Lett.*, 86:3459–3462, Apr 2001. doi: 10.1103/PhysRevLett.86.3459. URL <http://link.aps.org/doi/10.1103/PhysRevLett.86.3459>.
- [98] C.J. Pethick and H. Smith. *Bose-Einstein Condensation in Dilute Gases*. Cambridge University Press, 2nd edition, 2008. ISBN 9780521846516.
- [99] Sylvain Petit, Julien Robert, Solène Guitteny, Pierre Bonville, Claudia Decorse, Jacques Ollivier, Hannu Mutka, Michel J. P. Gingras, and Isabelle Mirebeau. Order by disorder or energetic selection of the ground state in the XY pyrochlore antiferromagnet $\text{Er}_2\text{Ti}_2\text{O}_7$: An inelastic neutron scattering study. *Phys. Rev. B*, 90:060410, Aug 2014. doi: 10.1103/PhysRevB.90.060410. URL <http://link.aps.org/doi/10.1103/PhysRevB.90.060410>.
- [100] Nguyen Thanh Phuc, Yuki Kawaguchi, and Masahito Ueda. Fluctuation-induced and symmetry-prohibited metastabilities in spinor Bose-Einstein condensates. *Phys. Rev. A*, 88:043629, Oct 2013. doi: 10.1103/PhysRevA.88.043629. URL <http://link.aps.org/doi/10.1103/PhysRevA.88.043629>.
- [101] Nguyen Thanh Phuc, Yuki Kawaguchi, and Masahito Ueda. Quantum Mass Acquisition in Spinor Bose-Einstein Condensates. *Phys. Rev. Lett.*, 113:230401, Dec 2014. doi: 10.1103/PhysRevLett.113.

230401. URL <http://link.aps.org/doi/10.1103/PhysRevLett.113.230401>.
- [102] C. Raman, J. R. Abo-Shaeer, J. M. Vogels, K. Xu, and W. Ketterle. Vortex Nucleation in a Stirred Bose-Einstein Condensate. *Phys. Rev. Lett.*, 87:210402, Nov 2001. doi: 10.1103/PhysRevLett.87.210402. URL <http://link.aps.org/doi/10.1103/PhysRevLett.87.210402>.
- [103] Matteo Rizzi, Vittorio Cataudella, and Rosario Fazio. Phase diagram of the Bose-Hubbard model with \mathcal{T}_3 symmetry. *Phys. Rev. B*, 73:144511, Apr 2006. doi: 10.1103/PhysRevB.73.144511. URL <http://link.aps.org/doi/10.1103/PhysRevB.73.144511>.
- [104] A. Robert, O. Sirjean, A. Browaeys, J. Poupard, S. Nowak, D. Borion, C. I. Westbrook, and A. Aspect. A Bose-Einstein Condensate of Metastable Atoms. *Science*, 292(5516):461–464, 2001. ISSN 0036-8075. doi: 10.1126/science.1060622. URL <http://science.sciencemag.org/content/292/5516/461>.
- [105] K. A. Ross, Y. Qiu, J. R. D. Copley, H. A. Dabkowska, and B. D. Gaulin. Order by Disorder Spin Wave Gap in the XY Pyrochlore Magnet $\text{Er}_2\text{Ti}_2\text{O}_7$. *Phys. Rev. Lett.*, 112:057201, Feb 2014. doi: 10.1103/PhysRevLett.112.057201. URL <http://link.aps.org/doi/10.1103/PhysRevLett.112.057201>.
- [106] Hiroki Saito and Masahito Ueda. Diagnostics for the ground-state phase of a spin-2 Bose-Einstein condensate. *Phys. Rev. A*, 72:053628, Nov 2005. doi: 10.1103/PhysRevA.72.053628. URL <http://link.aps.org/doi/10.1103/PhysRevA.72.053628>.
- [107] A. Sala, D. López Núñez, J. Martorell, L. De Sarlo, T. Zibold, F. Gerbier, A. Polls, and B. Juliá-Díaz. Shortcut to adiabaticity in spinor condensates. *ArXiv e-prints*, July 2016. URL <https://arxiv.org/abs/1607.04119>.
- [108] Luca Salasnich and Flavio Toigo. Zero-point energy of ultracold atoms. *Physics Reports*, 640:1 – 29, 2016. ISSN 0370-1573. doi:

<http://dx.doi.org/10.1016/j.physrep.2016.06.003>. URL <http://www.sciencedirect.com/science/article/pii/S0370157316301338>.

Zero-point energy of ultracold atoms.

- [109] L. Santos, M. Fattori, J. Stuhler, and T. Pfau. Spinor condensates with a laser-induced quadratic Zeeman effect. *Phys. Rev. A*, 75:053606, May 2007. doi: 10.1103/PhysRevA.75.053606. URL <http://link.aps.org/doi/10.1103/PhysRevA.75.053606>.
- [110] L.S. Schulman. *Techniques and Applications of Path Integration*. Dover Books on Physics. Dover Publications, 2012. ISBN 9780486137025. URL <https://books.google.co.uk/books?id=PsODcDKAEmIC>.
- [111] I.E. Segal and G.W. Mackey. *Mathematical Problems of Relativistic Physics*. Lectures in Applied Mathematics Series, Vol 2. American Mathematical Society, 1967. ISBN 9780821890578. URL <https://books.google.co.uk/books?id=lfwinKX-EhEC>.
- [112] E. Serret, P. Butaud, and B. Pannetier. Vortex correlations in a fully frustrated two-dimensional superconducting network. *EPL (Europhysics Letters)*, 59(2):225, 2002. URL <http://stacks.iop.org/0295-5075/59/i=2/a=225>.
- [113] E.F. Shender. Antiferromagnetic garnets with fluctuationally interacting sublattices. *J. Exp. Theor. Phys.*, 83(1):326, July 1982. URL <http://www.jetp.ac.ru/cgi-bin/e/index/e/56/1/p178?a=list>.
- [114] K. Sheshadri, H. R. Krishnamurthy, R. Pandit, and T. V. Ramakrishnan. Superfluid and Insulating Phases in an Interacting-Boson Model: Mean-Field Theory and the RPA. *EPL (Europhysics Letters)*, 22(4): 257, 1993. URL <http://stacks.iop.org/0295-5075/22/i=4/a=004>.
- [115] J. Söding, D. Guéry-Odelin, P. Desbiolles, G. Ferrari, and J. Dalibard. Giant spin relaxation of an ultracold cesium gas. *Phys. Rev. Lett.*, 80:1869–1872, Mar 1998. doi: 10.1103/PhysRevLett.80.1869. URL <http://link.aps.org/doi/10.1103/PhysRevLett.80.1869>.

- [116] Jun Liang Song, Gordon W. Semenoff, and Fei Zhou. Uniaxial and biaxial spin nematic phases induced by quantum fluctuations. *Phys. Rev. Lett.*, 98:160408, Apr 2007. doi: 10.1103/PhysRevLett.98.160408. URL <http://link.aps.org/doi/10.1103/PhysRevLett.98.160408>.
- [117] D. M. Stamper-Kurn, M. R. Andrews, A. P. Chikkatur, S. Inouye, H.-J. Miesner, J. Stenger, and W. Ketterle. Optical Confinement of a Bose-Einstein Condensate. *Phys. Rev. Lett.*, 80:2027–2030, Mar 1998. doi: 10.1103/PhysRevLett.80.2027. URL <http://link.aps.org/doi/10.1103/PhysRevLett.80.2027>.
- [118] Dan M. Stamper-Kurn and Masahito Ueda. Spinor Bose gases: Symmetries, magnetism, and quantum dynamics. *Rev. Mod. Phys.*, 85:1191–1244, Jul 2013. doi: 10.1103/RevModPhys.85.1191. URL <http://link.aps.org/doi/10.1103/RevModPhys.85.1191>.
- [119] D.M. Stamper-Kurn and W. Ketterle. Spinor condensates and light scattering from Bose-Einstein condensates. In R. Kaiser, C. Westbrook, and F. David, editors, *Coherent atomic matter waves*, volume 72 of *Les Houches - Ecole d'Ete de Physique Theorique*, pages 139–217. Springer Berlin Heidelberg, 2001. ISBN 978-3-540-41047-8. doi: 10.1007/3-540-45338-5_2. URL http://dx.doi.org/10.1007/3-540-45338-5_2.
- [120] L.K. Stergioulas and A. Vourdas. The Bargmann analytic representation in signal analysis . *Journal of Computational and Applied Mathematics*, 167(1):183 – 192, 2004. ISSN 0377-0427. doi: <http://dx.doi.org/10.1016/j.cam.2003.10.002>. URL <http://www.sciencedirect.com/science/article/pii/S0377042703008963>.
- [121] Willian C. Stwalley and L. H. Nosanow. Possible "new" quantum systems. *Phys. Rev. Lett.*, 36:910–913, Apr 1976. doi: 10.1103/PhysRevLett.36.910. URL <http://link.aps.org/doi/10.1103/PhysRevLett.36.910>.
- [122] Kai Sun, Zhengcheng Gu, Hosho Katsura, and S. Das Sarma. Nearly flatbands with nontrivial topology. *Phys. Rev. Lett.*, 106:236803, Jun

2011. doi: 10.1103/PhysRevLett.106.236803. URL <http://link.aps.org/doi/10.1103/PhysRevLett.106.236803>.
- [123] Bill Sutherland. Localization of electronic wave functions due to local topology. *Phys. Rev. B*, 34:5208–5211, Oct 1986. doi: 10.1103/PhysRevB.34.5208. URL <http://link.aps.org/doi/10.1103/PhysRevB.34.5208>.
- [124] Yosuke Takasu, Kenichi Maki, Kaduki Komori, Tetsushi Takano, Kazuhito Honda, Mitsutaka Kumakura, Tsutomu Yabuzaki, and Yoshiro Takahashi. Spin-Singlet Bose-Einstein Condensation of Two-Electron Atoms. *Phys. Rev. Lett.*, 91:040404, Jul 2003. doi: 10.1103/PhysRevLett.91.040404. URL <http://link.aps.org/doi/10.1103/PhysRevLett.91.040404>.
- [125] Evelyn Tang, Jia-Wei Mei, and Xiao-Gang Wen. High-temperature fractional quantum Hall states. *Phys. Rev. Lett.*, 106:236802, Jun 2011. doi: 10.1103/PhysRevLett.106.236802. URL <http://link.aps.org/doi/10.1103/PhysRevLett.106.236802>.
- [126] M. Tesei, R. Théron, and P. Martinoli. Frustration phenomena in Josephson junction arrays on a dice lattice. *Physica C: Superconductivity*, 437 - 438(0):328 – 330, 2006. ISSN 0921-4534. doi: <http://dx.doi.org/10.1016/j.physc.2005.12.090>. URL <http://www.sciencedirect.com/science/article/pii/S0921453405008695>.
- [127] Ari M. Turner, Ryan Barnett, Eugene Demler, and Ashvin Vishwanath. Nematic order by disorder in spin-2 Bose-Einstein condensates. *Phys. Rev. Lett.*, 98:190404, May 2007. doi: 10.1103/PhysRevLett.98.190404. URL <http://link.aps.org/doi/10.1103/PhysRevLett.98.190404>.
- [128] Shun Uchino, Michikazu Kobayashi, and Masahito Ueda. Bogoliubov theory and Lee-Huang-Yang corrections in spin-1 and spin-2 Bose-Einstein condensates in the presence of the quadratic Zeeman effect. *Phys. Rev. A*, 81:063632, Jun 2010. doi: 10.1103/PhysRevA.81.063632. URL <http://link.aps.org/doi/10.1103/PhysRevA.81.063632>.

- [129] Masahito Ueda. Many-body theory of dilute Bose-Einstein condensates with internal degrees of freedom. *Phys. Rev. A*, 63:013601, Dec 2000. doi: 10.1103/PhysRevA.63.013601. URL <http://link.aps.org/doi/10.1103/PhysRevA.63.013601>.
- [130] Masahito Ueda. Bose gases with nonzero spin. *Annual Review of Condensed Matter Physics*, 3(1):263–283, 2012. doi: 10.1146/annurev-conmatphys-020911-125033. URL <http://dx.doi.org/10.1146/annurev-conmatphys-020911-125033>.
- [131] Masahito Ueda and Masato Koashi. Theory of spin-2 Bose-Einstein condensates: Spin correlations, magnetic response, and excitation spectra. *Phys. Rev. A*, 65:063602, May 2002. doi: 10.1103/PhysRevA.65.063602. URL <http://link.aps.org/doi/10.1103/PhysRevA.65.063602>.
- [132] D. van Oosten, P. van der Straten, and H. T. C. Stoof. Quantum phases in an optical lattice. *Phys. Rev. A*, 63:053601, Apr 2001. doi: 10.1103/PhysRevA.63.053601. URL <http://link.aps.org/doi/10.1103/PhysRevA.63.053601>.
- [133] Julien Vidal, Rémy Mosseri, and Benoit Douçot. Aharonov-Bohm cages in two-dimensional structures. *Phys. Rev. Lett.*, 81:5888–5891, Dec 1998. doi: 10.1103/PhysRevLett.81.5888. URL <http://link.aps.org/doi/10.1103/PhysRevLett.81.5888>.
- [134] J. Villain, R. Bidaux, J. P. Carton, and R. Conte. Order as an effect of disorder. *Journal de Physique*, 41(11):1263–1272, 1980. ISSN 0302-0738. doi: 10.1051/jphys:0198000410110126300. URL <http://dx.doi.org/10.1051/jphys:0198000410110126300>.
- [135] Fa Wang and Ying Ran. Nearly flat band with Chern number $c = 2$ on the dice lattice. *Phys. Rev. B*, 84:241103, Dec 2011. doi: 10.1103/PhysRevB.84.241103. URL <http://link.aps.org/doi/10.1103/PhysRevB.84.241103>.
- [136] Stefan Wessel and Matthias Troyer. Supersolid Hard-Core Bosons on the Triangular Lattice. *Phys. Rev. Lett.*, 95:127205, Sep 2005. doi: 10.

- 1103/PhysRevLett.95.127205. URL <http://link.aps.org/doi/10.1103/PhysRevLett.95.127205>.
- [137] Yi-Zhuang You, Zhu Chen, Xiao-Qi Sun, and Hui Zhai. Superfluidity of Bosons in Kagome Lattices with Frustration. *Phys. Rev. Lett.*, 109:265302, Dec 2012. doi: 10.1103/PhysRevLett.109.265302. URL <http://link.aps.org/doi/10.1103/PhysRevLett.109.265302>.
- [138] Vivien Zapf, Marcelo Jaime, and C. D. Batista. Bose-Einstein condensation in quantum magnets. *Rev. Mod. Phys.*, 86:563–614, May 2014. doi: 10.1103/RevModPhys.86.563. URL <http://link.aps.org/doi/10.1103/RevModPhys.86.563>.
- [139] Wanzhou Zhang, Yuan Yang, Lijuan Guo, Chengxiang Ding, and Tony C. Scott. Trimer superfluid and supersolid on two-dimensional optical lattices. *Phys. Rev. A*, 91:033613, Mar 2015. doi: 10.1103/PhysRevA.91.033613. URL <http://link.aps.org/doi/10.1103/PhysRevA.91.033613>.
- [140] Gong-Ping Zheng, Lei-Kuan Xu, Shuai-Feng Qin, Wen-Tian Jian, and J.-Q. Liang. An order-by-disorder process in the cyclic phase of spin-2 condensate with a weak magnetic field. *Annals of Physics*, 334:341 – 350, 2013. ISSN 0003-4916. doi: <http://dx.doi.org/10.1016/j.aop.2013.04.012>. URL <http://www.sciencedirect.com/science/article/pii/S000349161300078X>.
- [141] Erez Zohar, J Ignacio Cirac, and Benni Reznik. Quantum simulations of lattice gauge theories using ultracold atoms in optical lattices. *Reports on Progress in Physics*, 79(1):014401, 2016. URL <http://stacks.iop.org/0034-4885/79/i=1/a=014401>.